NASA Contractor Report 191008

Navier-Stokes Analysis of Airfoils With Leading Edge Ice Accretions

Mark G. Potapczuk
University of Akron
Akron, Ohio

February 1993

NASA

National Aeronautics and
Space Administration

(NASA-CR-191008) NAVIER-STOKES
ANALYSIS OF AIRFOILS WITH LEADING
EDGE ICE ACCRETIONS Final Report
(Akron Univ.) 206 p

N93-22822

Unclas

G3/02   0153127

TABLE OF CONTENTS

NAVIER-STOKES ANALYSIS OF AIRFOILS WITH LEADING EDGE ICE ACCRETIONS

Mark G. Potapczuk
University of Akron
Akron, Ohio 44325

ABSTRACT

A numerical analysis of the flowfield characteristics and the performance degradation of an airfoil with leading edge ice accretions was performed. The important fluid dynamic processes were identified and calculated. Among these were the leading edge separation bubble at low angles of attack, complete separation on the low pressure surface resulting in premature stall, drag rise due to the ice shape, and the effects of angle of attack on the separated flow field. Comparisons to experimental results were conducted to confirm these calculations.

A computer code which solves the Navier-Stokes equations in two dimensions, ARC2D, was used to perform the calculations. A Modified Mixing Length turbulence model was developed to improve capabilities in calculating the separated flow phenomena. A grid generation code, GRAPE, was used to produce grids for several ice shape and airfoil combinations.

Results indicate that the ability to predict overall performance characterisitics, such as lift and drag, at low angles of attack is excellent. Transition location is important for accurately determining separation bubble shape. Details of the flowfield in and downstream of the separated regions requires some modifications. Calculations for the stalled airfoil indicate periodic shedding of vorticity that was generated aft of the ice accretion. Time averaged pressure values produce results which compare favorably with experimental information. A turbulence model which accounts for the history effects in the flow may be justified.

CHAPTER 1

INTRODUCTION

This work details the investigation of the aerodynamics of an airfoil with leading edge ice accretions. A computational approach is employed for the prediction of the fluid dynamics and performance characteristics of such an airfoil. The method presented is based on the numerical solution of the Navier-Stokes equations in a body-fitted coordinate system. A previously existing airfoil code, along with a new turbulence model developed for this study, was adapted to incorporate the physics of a leading edge separation bubble and to account for the completely separated flow at high angles of attack. This code was used to examine the structure of the separation bubble, the development of the turbulent boundary layer aft of the bubble, and examine the effects of angle of attack on the stalled airfoil flowfield. In addition, the code was used to determine the changes to maximum lift, angle of attack at stall, and drag as a result of the presence of ice on the leading edge.

Comparisons to experimental results, for several airfoils with artificial leading edge ice shapes, are presented to verify the method and to illustrate its predictive capability. Capabilities for the quantitative analysis of airfoil performance degradation due to icing were previously limited to experimental correlations and potential flow analysis of relatively aerodynamic ice accretions. Evaluation of less benign ice shapes requires the ability to calculate separated flow regions and the resulting changes in lift, drag, and moment forces. This can be accomplished by the use of either an interactive boundary-layer approach or the solution of the Navier-Stokes equations. The former method is under evaluation by Cebeci [1]. The investigation of the use of a Navier-Stokes code thus seems justified in order to examine the

relative merits of each approach. Optimum design of ice protection systems generates the need for such computational capabilities. If the performance of an iced airfoil can be accurately predicted, then more meaningful design parameters can be considered in the development of ice protection systems. Further, if the aerodynamics of the iced airfoil are known then other analysis methods can be used to predict the ice buildup on the airfoil. This should serve to decrease the need for actual wind tunnel testing.

1.1 Description of Problem

Aircraft icing occurs when an aircraft passes through a cloud of supercooled water droplets and droplet impingement combined with heat transfer processes result in accretion of an ice mass which may cause significant performance loss to the aircraft. The severity of the icing encounter is dependant on meteorological conditions, flight conditions, aircraft geometry, pilot performance, and anti/de-icing measures employed. Prediction of aircraft capabilities under icing conditions is determined by the first three of these factors.

Meteorological conditions determine the charcterisitics of the ice itself. Typically the types of ice identified for these purposes are rime, glaze, and mixed. Temperature is the major influence on determining the type of icing encountered. At temperatures just below freezing, a clear granular ice, termed glaze ice, tends to form which can produce very non-aerodynamic shapes on the airfoil leading edge. At very cold temperatures, an opaque relatively smooth ice, termed rime ice, forms which has a more aerodynamic shape than glaze. At some intermediate temperatures, a mixture of these conditions occurs usually with a glaze ice core surrounded by a shell of rime. These ice types combined with flight conditions, length of icing encounter, and aircraft geometry determine the final ice shape and resulting aerodynamic degradation characteristics.

The presence of ice on the leading edge surfaces of an aircraft can lead to severe degradation of the aircraft performance as a result of several influences. The weight of the ice itself can require additional lift to maintain the desired altitude. At the same time, the ability of the lifting surfaces to provide that lift is reduced. Additionally, the ice accretions increase the drag forces on the aircraft resulting in increased thrust requirements. Any one of these influences can be enough to prohibit operation of an aircraft in an icing environment. Evaluation of the performance degradation due to these influences is important for specification of appropriate ice protection measures.

The weight of the ice can be accounted for as an additional payload. Thus, it should be within the scope of present design techniques to determine this influence. The increased drag and decreased lift due to the ice accretion are not so easily determined. Drag calculations require an ability to evaluate both pressure drag and skin friction. This means being able to determine the appropriate pressure distribution on a highly irregular geometry and to accurately determine the influence of the turbulent boundary layer on that surface. Lift calculations also require the ability to accurately determine pressure on the surface. These capabilities are available in existing codes only for attached flows on normal airfoil shapes.

Airfoils with leading edge ice shapes pose greater difficulties for computation due to the flow characteristics associated with the non-aerodynamic geometry of the ice accretion. The ice shape produces a leading edge separation bubble which at low angles of attack reattaches to the surface. The size of this region and the flowfield inside it are difficult to model due to the limitations of the method of modeling turbulence previuosly employed in most computer codes. The location of the reattachment point is also affected by the turbulence model, which in turn can influence the development of the reattached boundary layer downstream of the bubble. At high angles of attack, this bubble detaches from the surface and results in an unsteady flowfield characterized by periodic vortex shedding. This

leading edge separation results in premature stall of the airfoil. Accurate modelling of these phenomena is essential for determination of the performance characteristics of the airfoil during an icing encounter.

1.2 Icing Analysis Plan

The development of an iced airfoil analysis code is part of a national icing analysis effort coordinated by NASA and the FAA. In this effort, the goal is to be able to calculate the growth of ice on an airfoil and determine the aerodynamic performance degradation due to that ice. Additionally, it is desired to be able to model various de-icing and anti-icing systems in order to limit expensive icing tunnel tests. This approach requires the development of several types of codes and ultimately the tying together of these codes in an overall analysis scheme. The codes used for icing analysis are employed in a computational loop which starts with evaluation of the flowfield for a clean airfoil, moves to a calculation of the water droplet trajectories, calculates the ice buildup from those particles which impinge on the surface, and evaluates the performance degradation due to this ice growth. The new shape is then used to re-evaluate the flowfield and go through the loop again. This process would be repeated until the ice buildup reached some critical level, most likely the stall point. The computational approach developed in this study would be used for calculation of the flowfield at the start of the loop and for performance evaluation at the end of the loop.

For the overall icing analysis plan, it is essential, to be able to perform the calculations of the type reported in this work. The methods employed up to the present have either been unsuccessful or successful over a limited range of conditions. The use of a Navier-Stokes code with an appropriate turbulence model holds the promise of achieving this critical capability for icing analysis research.

CHAPTER 2

ICED AIRFOIL PERFORMANCE ANALYSIS : STATE OF THE ART

The ability to predict the performance degradation of an airfoil due to ice deposition is not presently available to the aerospace community. Several empirical studies have been completed over the years, but no well-developed method has been produced to determine the loss in lift and increase in drag associated with this phenomena. The advent of high speed computers and development of efficient numerical schemes for solving partial differential equations has provided the opportunity for further development of prediction methods for iced airfoil aerodynamic analysis. It is the objective of this investigation to utilize these recent advances in computational ability and to examine their strengths and weaknesses in relation to the icing problem. This chapter presents a brief examination of the state of the art in icing analysis up to the present. The development of computational methods in the codes employed during this investigation is also discussed.

2.1 Historical Background

The current method of ice protection, hot air bleed, was first developed in the 1940's as a result of an experimental program conducted by NACA [2]. This program consisted of numerous wind tunnel tests of iced airfoils, in an attempt to develop correlations for the associated drag rise. The correlations of Gray [3] were developed during this period and have served as the basis for predicting drag rise up until the present. Gray's correlation is known to be a very approximate method and is considered inadequate for the design of ice protection of modern general aviation aircraft and rotorcraft.

6

During the past five to ten years, work in the area of correlation development has been re-examined in an attempt to improve upon Gray's results. In 1982, Bragg [4] developed a method which accounted separately for the effects of changes in leading edge geometry and of surface roughness for rime ice profiles. He states that this method is limited to small ice accretions at low angles of attack. In 1983, another empirically based approach was attempted by Miller, Korkan, and Shaw [5]. Their conclusion was that further work was required for the development of a more general drag rise correlation. Additionally, these methods are used strictly for the prediction of global characteristics of the iced airfoil flow field. Detailed evaluation of the velocities, pressures, temperatures, or other important parameters, is not provided by the use of correlations. However, this type of information is necessary input to any method designed to predict ice accretion and growth, as envisioned for a comprehensive icing analysis program.

Analytical methods for predicting drag rise due to icing were evaluated by Peterson and Dadone [6] in 1980. Their conclusion was that then current methods underpredicted drag rise. Later, in 1982, Bragg, Gregorek, and Shaw [7] used the airfoil code of Eppler [8] to successfully predict the maximum lift coefficient $\left(C_{L\ max}\right)$ for a rime ice profile. In 1984, Bragg [9] investigated the aerodynamic characteristics of airfoils with rime and glaze ice accretions. He compared several computer codes, eventually settling on the Dvorak CLMAX code [10]. His results for rime ice were encouraging, but several difficulties were found in calculation of drag and in prediction of leading edge separation on glaze ice profiles. Bragg also used the Bristow potential flow code [11] and measured separation bubble geometry to predict Cp values on a glaze ice shape. This approach does not, of course, allow evaluation of viscous effects.

As mentioned previously, either an interactive boundary layer method or solution of the Navier-Stokes equations is necessary to produce the desired results. The interactive

boundary layer approach currently being used by Cebeci [1], shows promising preliminary results, especially for angles of attack below stall. However, some details of the flowfield, such as the reverse flow region of the separation bubble, are not predicted properly. Further, the massive separation which occurs at and above stall angles is not capable of being predicted by this method. Hence, it seems justified to employ an alternate approach, in an effort to complement the interactive boundary layer method, for situations which require the additional physical modeling provided by the Navier-Stokes equations. Thus, it may be envisioned that the less computationally expensive interactive boundary layer approach would be employed for small angles of attack and the Navier-Stokes solver would be used for the evaluation of stall. Additionally, the Navier-Stokes solver could be employed for evaluation of velocities within the separation bubble region. It was with these goals in mind that this work was undertaken.

2.2 Background of Numerical Procedures

The literature on grid generation, Navier-Stokes analysis, and turbulence modeling is quite extensive. Thus, any presentation of the sources which cover these topics will be necessarily abridged. This section is a survey of some, but by no means all, of the relevant literature regarding these topics. This material is mentioned in order to provide a context within which the methods employed are expected to operate. It is necessary to understand the limits of present analysis techniques in order to have realistic expectations for the use of those techniques in a given application. In this spirit, the following material was examined prior to and during the course of this investigation.

Grid generation codes are employed to provide a convenient means of representing a complex geometrical shape in a way which can be modeled in a rectangular finite-difference grid. These codes typically transform the standard Cartesian coordinate system, which represents physical space, into a body-fitted curvilinear coordinate system, which represents the

computatuional space within which the governing equations are solved. Typically these methods result in the x-y coordinates corresponding to the grid points in the curvilinear coordinate system. The methods differ in the form of the transformation equation which must be solved and therefore in the boundary conditions which must be specified. Initial efforts at employing body-fitted coordinate systems were conducted by Winslow [12] in 1966 and Chu [13] in 1971. Both evaluated the Laplace equation as a means of transforming the coordinates from one system to the other. In 1973, Amsden and Hirt [14] used the same equations to provide a method of generating general curvilinear grids. Thompson, Thames, and Mastin [15-17] expanded this approach, during 1974-77, to include any number of bodies in the computational space. Their methods have been used quite extensively. In 1979, Steger and Sorenson [18] provided for angle and distance control of the grid lines at the inner boundary. In the following year, Sorenson [19] extended this method to control angles and spacing at the outer boundary. This method is employed in the so-called GRAPE code which is used for this investigation and will be described later.

Other grid generation methods employ solutions of hyperbolic and parabolic partial differential equations and geometric techniques. Barth, Pulliam, and Buning [20] employed a hyperbolic grid generator, in 1985, to examine 'exotic' airfoils, including a glaze ice shape provided by the author. In 1978, Gibeling, Shamroth, and Eiseman [21] developed a geometric grid generation technique, refined by Eiseman [22] which was used by Shamroth [23] in 1985 to evaluate steady and unsteady airfoil flow fields.

Early efforts at evaluation of the Navier-Stokes equations considered incompressible laminar flow. Examples are those of Mehta and Lavan [24] and Lugt and Haussling [25], both from 1975. Mehta and Lavan solved these equations with a stream function-vorticity formulation to examine flow about an impulsively started airfoil. Lugt and Haussling also used a stream function-vorticity approach to examine flow about an abruptly started cylinder.

In an alternate approach, during 1977 Reddy and Thompson [26] applied an integro-differential formulation to the problem of incompressible flow in a doubly connected region. This was used to evaluate symmetric airfoils at zero angle of attack with a Reynolds number of less than 10^6. Similarly, during the mid-1970's, Wu and Sampath [27] and Wu, Sampath, and Sankar [28] applied an integro-differential formulation [29] to both an impulsively started airfoil and an oscillating airfoil. Finally, in 1980, Sugavanarm and Wu [30] attempted to use a two equation k-ϵ turbulence model with a vorticity-velocity formulation.

The primitive variable approach has also been employed for the evaluation of incompressible laminar flows. Harlow and Welch [31] employed the Marker And Cell (MAC) method to investigate time dependent flow of a fluid with a free surface. This approach was developed further by Hirt and Harlow [32]. Later, Hodge [33] and Hodge and Stone [34] employed a successive over relaxation (SOR) iteration approach in a body fitted curvilinear coordinate system. The alternating direction implicit (ADI) approach was used by Ghia, Hankey, and Hodge [35] to calculate incompressible driven flow in a square cavity for Reynolds numbers under 1000.

Compressible flow over airfoils has been and continues to be examined by a large number of investigators. Verhoff [36] applied MacCormack's fully explicit method [37] to this problem but was restricted by small time steps in order to maintain numerical stability. Deiwert [38] also used this method to examine transonic flow.

Implicit methods have been employed for the laminar compressible Navier-Stokes equations in an effort to avoid the stability limitations present in explicit schemes. Gibeling, Shamroth, and Eiseman [21] applied the Briley-McDonald [39] formulation to examine dynamic stall. Sankar and Tassa [40] used a similar approach to examine an oscillating airfoil in a low Reynolds number flow.

The examination of turbulent compressible flows presents an additional degree of complexity to the calculation of airfoil flow fields. The various investigators have generally employed either a zero-equation algebraic eddy viscosity model or a two-equation k-ϵ model, where an n-equation model refers to the n-number of additional partial differential equations to be solved. Recently, there has also been considerable interest in the single ordinary differential equation model of Johnson and King [41]. All of these types of models have been compared by Coakley [42] for cases of shock induced separation, and the Johnson-King model was considered to have performed favorably. A k-ϵ model that has been used by several invetigators (e.g. [23] and [43]) is described by Launder and Spalding [44]. The algebraic models most commonly used are those of Cebeci and Smith [45] and Baldwin and Lomax [46]. These models have been used sucessfully over a wide range of airfoil configurations for conditions below stall. At higher angles of attack, there have been some difficulties observed however. The models tend to overpredict the turbulence level and damp out some of the vorticity generation ocurring under these conditions. This is of particular concern for the iced airfoil condition due to the presence of the stationary separation bubble and its subsequent shedding at higher angles of attack. These considerations will be discussed in more detail in later chapters.

Early investigation of the turbulent airfoil problem was performed in 1979 by Shamroth and Gibeling [47]. The method described therein employed a mixing length type turbulence model and was used to examine airfoils at low angles of attack. This approach was employed again during the following year by Shamroth and Gibeling [48] to examine airfoils in stall and again in 1981 by Shamroth [49] to examine airfoils pitching at low incidence. Tassa and Sankar [50] in 1981 and Sankar and Tang [51] in 1985 used an algebraic mixing length model to study dynamic stall. A k-ϵ model was employed in 1985 by Shamroth [23] to investigate steady flow over a NACA0012 airfoil at low angles of attack. The basis for the

code employed in this investigation was developed by Steger [52] in 1978, who used the numerical scheme of Beam and Warming [53] and the Baldwin-Lomax turbulence model.

The code developed at the Ames Research Center by Steger, ARC2D, has been further enhanced by Pulliam [54]. Pulliam introduced a diagonalization of the blocktridiagonal inversion for the implicit operators which resulted in a computationally more efficient set of scalar tridiagonal inversions along with a series of 4x4 multiplications. Additionally, he vectorized the code to take advantage of the capabilities of CRAY type computer architecture. This code has been used to evaluate a large number of airfoils over a large range of Reynolds number and Mach number conditions [55]. ARC2D and GRAPE will be the basic numerical tools used to examine the iced airfoil flowfield and will thus be described more fully in the next chapter.

CHAPTER 3

DESCRIPTION OF COMPUTER CODES

Solution of the Navier-Stokes equations with a finite difference method for a highly irregular geometry requires the use of two separate codes. One is used for the transformation of the physical space, which holds the object of interest, into a rectangular computational space, which is more suitable for the use of a finite difference code. The other is the actual Navier-Stokes solver. Both codes in this study were supplied by the NASA Ames Research Center. The grid transformation code is called GRAPE and was written by Sorenson [19]. GRAPE is an acronym for GRid transformation Algorithm for solution of the Poisson Equation. The Navier-Stokes solver is called ARC2D and was originally written by Steger [52] and later modified by Pulliam [54].

The following sections give a description of the basic equations being solved by the two codes used in this study. The form of the equations, as implemented in the codes, is also developed from these basic equations. Much of the development presented can be found in the references cited. Inclusion of this development is for the sake of familiarizing the reader with the specific mathematical formulation of the physical systems being modeled. This presentation is thorough enough to give the flavor of the calculation methods employed, while not purporting to be an exhaustive examination of work which has been described previously.

3.1 GRAPE Code Description

The GRAPE code is based on a transformation of the physical x-y coordinate system to a body-fitted ξ-η coordinate system through the use of a Poisson equation. The equations to be solved are,

$$\xi_{xx} + \xi_{yy} = P \tag{3.1a}$$

$$\eta_{xx} + \eta_{yy} = Q \tag{3.1b}$$

where P and Q are constants which can be manipulated to control spacing and skewness of the resulting grid. Subscripts indicate differentiation with respect to the given coordinate.

If the new coordinates are defined as functions of x and y then,

$$\xi = \xi(x,y) \tag{3.2a}$$

and,

$$\eta = \eta(x,y) \tag{3.2b}$$

It is desired to obtain the x and y coordinates of the rectangular ξ-η computational grid. Thus, expressing (3.1) in terms of differentials of x and y with respect to ξ and η is necessary. The resulting partial differential equations are then solved using a computational technique described below.

The relationship between (3.1) and differentials of x and y with respect to ξ and η is obtained by employing the Jacobian of the transformation from one coordinate system to the other,

$$J = \frac{\partial(x,y)}{\partial(\xi,\eta)} \tag{3.3}$$

14

or,

$$J = x_\xi y_\eta - x_\eta y_\xi \tag{3.4}$$

Equation (3.4) can be rearranged to yield the following expressions,

$$\xi_x = y_\eta/J \tag{3.5}$$

$$\xi_y = -x_\eta/J \tag{3.6}$$

$$\eta_x = -y_\xi/J \tag{3.7}$$

$$\eta_y = x_\xi/J \tag{3.8}$$

Applying equations (3.5-3.8) to (3.1) yields,

$$\alpha x_{\xi\xi} - 2\beta x_{\xi\eta} + \gamma x_{\eta\eta} = -J^2(Px_\xi + Qx_\eta) \tag{3.9a}$$

$$\alpha y_{\xi\xi} - 2\beta y_{\xi\eta} + \gamma y_{\eta\eta} = -J^2(Py_\xi + Qy_\eta) \tag{3.9b}$$

where,

$$\alpha = x_\eta{}^2 + y_\eta{}^2 \tag{3.10}$$

$$\beta = x_\xi x_\eta + y_\xi y_\eta \tag{3.11}$$

$$\gamma = x_\xi{}^2 + y_\xi{}^2 \qquad\qquad (3.12)$$

In the GRAPE code, P, Q, and values of x and y are specified as input. The x and y values are input as a discrete set of points which can be used as is or redistributed using a curve-fit routine and a pre-defined distribution function. The boundary values correspond to the surface of the object being considered and an artificial boundary at some distance away from the object. The distance to the outer bondary is set at some value that is considered to be sufficient for free-stream conditions to prevail. The outer boundary can be specified as a C or O type grid. Equation (3.6) is solved by an iterative method employing a successive line over-relaxation solution procedure. The solution proceeds along lines that run in the ξ direction. Convergence is obtained when the absolute value of the largest correction in x and y is below some desired level. Normally the convergence criteria is set as a drop in this correction value of six orders of magnitude. If convergence is not obtained, several relaxation parameters can be changed in an effort to improve the results. Also, the point distribution at the surface can be altered in an attempt to avoid regions of high curvature. The former approach is preferred, as this does not require alteration of the input geometry specification. Further explanation of the theory underlying the GRAPE code may be found in reference [19].

GRAPE has been used successfully to produce grids for many complex geometries, including ice shapes, as seen in figure 1. The output of this code is the x and y locations of the grid points from the uniform rectangular ξ-η computational coordinate system. These locations are then used as input for the ARC2D code, specifying the locations at which the Navier-Stokes equations are to be solved.

The ability of a particular grid to provide appropriate spatial resolution for a given flow-field is a question of much debate. Some of the influential factors are: the spacing of grid
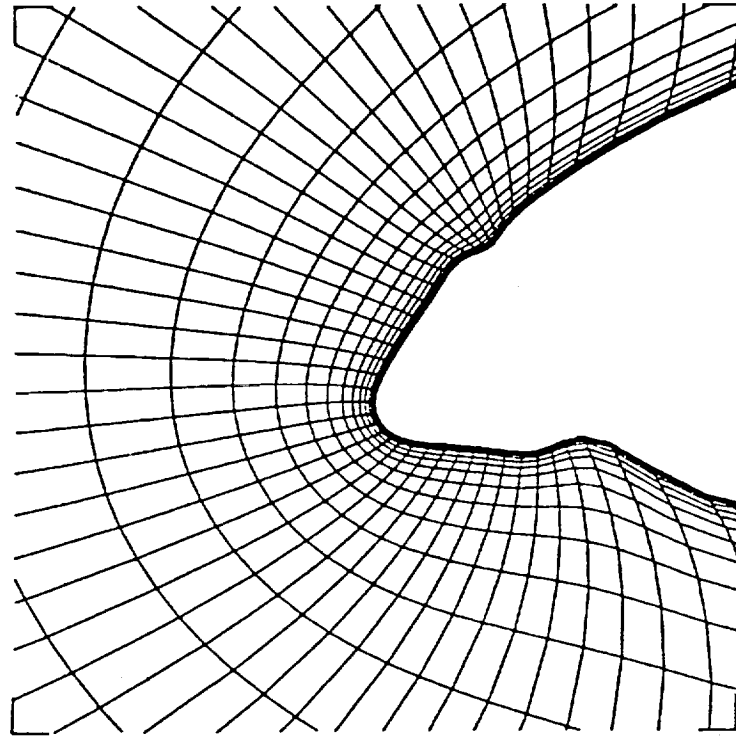
Figure 1(a) Grid for rime ice leading edge
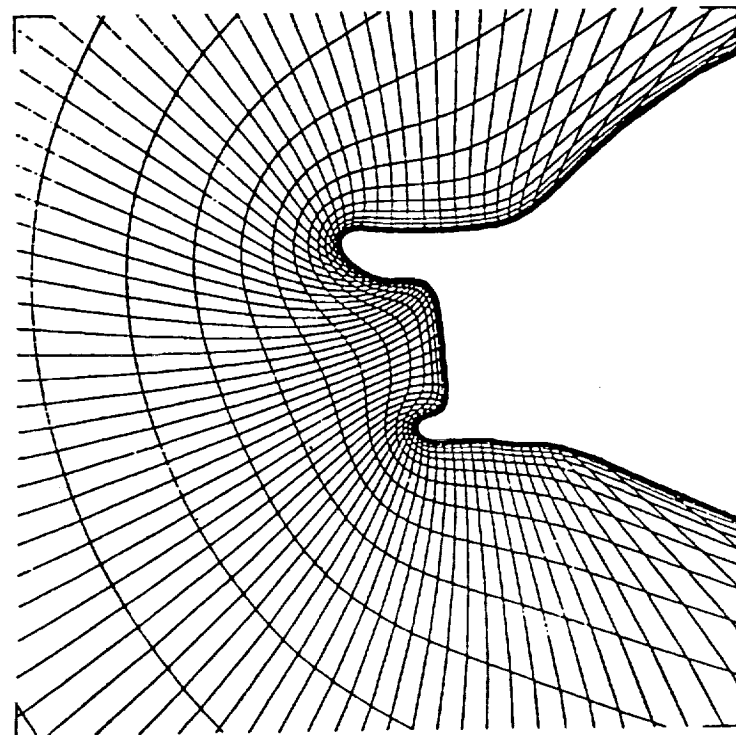
Figure 1(b) Grid for glaze ice leading edge

points near a solid surface in the normal direction, the spacing of grid points in the streamwise direction, the distance from the solid surface to the free-stream boundary, and the skewness of grid lines in regions of high curvature. Presently, the only measure of a grid quality is the degree to which the grid generation code has converged. Certainly, this allows for evaluation of how well the transformation equation has been modeled. However, the degree of convergence does not give an indication of whether the grid spacing is appropriate for resolution of the important flow phenomena. These concerns, important as they are for any computational fluid dynamics problem, are not the major emphasis of this research. As such, they will only be discussed in conjunction with specific problems that developed during the course of the research.

The grids used in this work were similar, in degree of spatial resolution, to those employed for analysis of viscous flow over a clean airfoil (see, for example, Pulliam [54]). The spacing between the inner and outer boundaries was on the order of ten chord lengths. This is considered appropriate to provide free-stream conditions at the outer boundary [55]. The spacing of the first grid point off of the airfoil surface was on the order of .00002 of a chord length. This is sufficient spacing to provide approximately twenty grid points in the airfoil boundary layer. Grid spacing around the surface was concentrated near the leading edge in order to resolve the geometry of the ice shape. This is accomplished by providing a greater number of input points in this region and altering the point distribution function mentioned earlier. The high curvature of the ice shape results in significant skewing of the grid in this region. Concentration of points near the leading edge also results in scarcity of grid lines in the wake region. This can result in improper representation of the wake and must be considered carefully when creating a grid.

3.2 ARC2D Code Description

The code selected for solving the Navier-Stokes equations, ARC2D, was originally developed at the NASA Ames Research Center, as mentioned previously. This code can be configured to solve the thin-layer Navier-Stokes equations or it can additionally include the explicit ξ and cross derivative terms.

The full equations are shown below in Cartesian coordinates.

$$Q_t + E_x + F_y = Re^{-1}\left(Ev_x + Fv_y\right) \qquad (3.13)$$

where,

$$Q = \begin{bmatrix} \rho \\ \rho u \\ \rho v \\ e \end{bmatrix}, \quad E = \begin{bmatrix} \rho u \\ \rho u^2 + P \\ \rho uv \\ u(e + P) \end{bmatrix}, \quad F = \begin{bmatrix} \rho v \\ \rho uv \\ \rho v^2 + P \\ v(e + P) \end{bmatrix}, \qquad (3.14)$$

and,

$$Ev = \begin{bmatrix} 0 \\ \tau_{xx} \\ \tau_{xy} \\ e_4 \end{bmatrix}, \quad Fv = \begin{bmatrix} 0 \\ \tau_{xy} \\ \tau_{yy} \\ f_4 \end{bmatrix}, \qquad (3.15)$$

with,

$$\tau_{xx} = \frac{\mu}{3}\left(4u_x - 2v_y\right) \qquad (3.16a)$$

$$\tau_{xy} = \mu(u_y + v_x) \tag{3.16b}$$

$$\tau_{yy} = \frac{\mu}{3}\left(-2u_x + 4v_y\right) \tag{3.16c}$$

$$e_4 = u\tau_{xx} + v\tau_{xy} + \mu \, Pr^{-1}(\gamma - 1)^{-1}\left(a^2\right)_x \tag{3.16d}$$

$$f_4 = u\tau_{xy} + v\tau_{yy} + \mu \, Pr^{-1}(\gamma - 1)^{-1}\left(a^2\right)_y \tag{3.16e}$$

$$P = (\gamma - 1)\left(e - \tfrac{1}{2}\rho(u^2 + v^2)\right) \tag{3.16f}$$

These equations are then transformed to the body-fitted coordinate system established by the grid points taken from the GRAPE code output. According to the development presented by Vinokur [56], the strong conservation law form of (3.2) can be maintained for new independent variables of the form,

$$\xi = \xi(x,y,t) \; , \quad \eta = \eta(x,y,t) \; , \quad \tau = t$$

Retaining strong conservation law form is important in that it is possible to difference the equations by a variety of stable schemes, each of which can be chosen so as to conserve mass, momentum, and energy for the total flow region. The time dependence is shown for these transformations and was not included in the GRAPE code formulation. Since only the x-y positions of the ξ-η grid are transferred from GRAPE to ARC2D, this dependence is not necessary for the GRAPE code. ARC2D uses the x-y coordinate information to form the metrics again internal to the code. The roles of the independent variables are reversed for the ARC2D code and hence the Jacobian has the form,

$$J^{-1} = x_\xi \, y_\eta - x_\eta \, y_\xi \tag{3.17}$$

The contravariant velocities are defined along the ξ and η coordinates as,

$$U = \xi_t + \xi_x u + \xi_y v \tag{3.18}$$

$$V = \eta_t + \eta_x u + \eta_y v \tag{3.19}$$

where the metrics are formed by considering the differentials of the independent variables of the two coordinate systems. The metrics describe the following relationships between the two coordinate systems.

$$\xi_x = J y_\eta \,, \quad \xi_y = -J x_\eta \,, \quad \xi_t = -x_\tau \xi_x - y_\tau \xi_y$$

$$\tag{3.20}$$

$$\eta_x = J y_\xi \,, \quad \eta_y = -J x_\xi \,, \quad \eta_t = -x_\tau \eta_x - y_\tau \eta_y$$

Applying these transformations to the governing equations (3.2) results in the following form,

$$\hat{Q}_\tau + \hat{E}_\xi + \hat{F}_\eta = Re^{-1}\left(\hat{E}v_\xi + \hat{F}v_\eta\right) \tag{3.21}$$

where,

$$\hat{Q} = J^{-1}\begin{bmatrix} \rho \\ \rho u \\ \rho v \\ e \end{bmatrix}, \quad \hat{E} = J^{-1}\begin{bmatrix} \rho U \\ \rho u U + \xi_x P \\ \rho v U + \xi_y P \\ u(e + P) - \xi_t P \end{bmatrix}, \quad \hat{F} = J^{-1}\begin{bmatrix} \rho V \\ \rho u V + \eta_x P \\ \rho v V + \eta_y P \\ v(e + P) - \eta_t P \end{bmatrix}, \quad (3.22)$$

and,

$$\hat{E}v = J^{-1}(Ev\xi_x + Fv\xi_y) \,, \quad \hat{F}v = J^{-1}(Ev\eta_x + Fv\eta_y) \tag{3.23}$$

The thin-layer form of the equations is obtained by neglecting gradients of the viscous terms in the streamwise direction (i.e. the ξ direction). This is similar to a boundary layer type assumption, however, unlike the boundary layer equations, the cross-stream pressure gradient is retained. This allows evaluation of regions with recirculation.

Selection of full or thin-layer equations is dependent on the phenomena being modeled and the suitability of the grid. If the grid does not have sufficiently fine spacing in the streamwise direction, then use of the full Navier-Stokes equations may not be warranted. For airfoils with attached boundary layers, the increased run times required for the full equations are not justified by a significant increase in accuracy. This may not be the case for a separated flow field. Therefore, due to the leading edge separation which can occur with an iced airfoil geometry, the solution of the full Navier-Stokes equations should be examined. The thin layer equations have the form,

$$\hat{Q}_\tau + \hat{E}_\xi + \hat{F}_\eta = Re^{-1}\hat{F}v_\eta \tag{3.24}$$

Employing equations (3.15) and (3.23), the right hand side of (3.24) can be rewritten in the following form,

$$Re^{-1}\hat{F}v_\eta = Re^{-1}\left(J^{-1}(Ev\eta_x + Fv\eta_y)\right)_\eta \tag{3.25}$$

22

or,

$$Re^{-1}\hat{F}v_\eta = Re^{-1} J^{-1} \begin{bmatrix} 0 \\ \tau_{xx}\eta_x + \tau_{xy}\eta_y \\ \tau_{xy}\eta_x + \tau_{yy}\eta_y \\ e_4\eta_x + f_4\eta_y \end{bmatrix} \tag{3.26}$$

where τ_{xx}, τ_{xy}, τ_{yy}, e_4, and f_4 are given in (3.16). The shear stress terms can be rewritten with the u and v derivatives expanded by the chain rule,

$$\tau_{xx} = (\lambda + 2\mu)(\xi_x u_\xi + \eta_x u_\eta) + \lambda(\xi_y v_\xi + \eta_y v_\eta) \tag{3.27}$$

$$\tau_{xy} = \mu\left((\xi_y u_\xi + \eta_y u_\eta) + (\xi_x v_\xi + \eta_x v_\eta)\right) \tag{3.28}$$

$$\tau_{yy} = (\lambda + 2\mu)(\xi_y v_\xi + \eta_y v_\eta) + \lambda(\xi_x u_\xi + \eta_x u_\eta) \tag{3.29}$$

and the transformed e_4 and f_4 terms become,

$$e_4 = u\tau_{xx} + v\tau_{xy} + \mu Pr^{-1}(\gamma - 1)^{-1}\left(\xi_x \partial_\xi a^2 + \eta_x \partial_\eta a^2\right) \tag{3.30}$$

$$f_4 = u\tau_{xy} + v\tau_{yy} + \mu Pr^{-1}(\gamma - 1)^{-1}\left(\xi_y \partial_\xi a^2 + \eta_y \partial_\eta a^2\right) \tag{3.31}$$

Substituting (3.27-29) into (3.26) yields the following relations,

$$Re^{-1}J^{-1}\left(Ev\eta_x + Fv\eta_y\right)_\eta = Re^{-1}\hat{S}_\eta \tag{3.32}$$

where,

$$\hat{S} = J^{-1} \begin{bmatrix} 0 \\[2em] \mu(\eta_x{}^2 + \eta_y{}^2)u_\eta + (\mu/3)\eta_x(\eta_x u_\eta + \eta_y v_\eta) \\[2em] \mu(\eta_x{}^2 + \eta_y{}^2)u_\eta + (\mu/3)\eta_x(\eta_x u_\eta + \eta_y v_\eta) \\[2em] \kappa Pr^{-1}(\gamma-1)^{-1}(\eta_x{}^2+\eta_y{}^2)(a_\eta)^2+(\mu/2)(\eta_x{}^2 + \eta_y{}^2)(u^2 + v^2)_\eta \\[1em] + (\mu/6)\Big(\eta_x{}^2(u^2)_\eta + \eta_y{}^2(v^2)_\eta + 2\eta_x\eta_y(uv)_\eta\Big) \end{bmatrix} \tag{3.33}$$

Finally (3.24) and (3.25) are rewritten in a more compact form,

$$\hat{Q}_\tau + \hat{E}_\xi + \hat{F}_\eta = Re^{-1}\hat{S}_\eta \tag{3.34}$$

This form of the Navier-Stokes equations can now be solved by forming an equivalent finite difference representation. Applying the implicit three point time differencing scheme of Beam and Warming [53] yields an expression of the form,

$$\Delta\hat{Q}^n = \frac{\theta\,\Delta t}{1+\phi}\left(\Delta\hat{Q}^n\right)_t + \frac{\Delta t}{1+\phi}\left(\hat{Q}^n\right)_t + \frac{\phi}{1+\phi}\,\Delta\hat{Q}^{n-1}$$

$$+ \mathcal{O}\left[\ \left(\theta - \tfrac{1}{2} - \phi\right)\Delta t^2 + \Delta t^3\ \right] \tag{3.35}$$

where $\Delta\hat{Q}^n = \hat{Q}^{n+1} - \hat{Q}^n$ and $\hat{Q}^n = \hat{Q}(n\Delta t)$. The values of θ and ϕ are chosen to provide either first or second order accuracy in time. Typically, when the code is run in a time

24

accurate mode for unsteady calculations θ is set to 1 and ϕ is set to 0. This results in second order time accuracy for these calculations. For steady-state calculations, a spatially varying time step is employed to speed convergence. In these cases, the values of θ and ϕ are set to 1 and 0.5 respectively. This yields only first order accuracy in time. This is acceptable as long as there is convergence to a steady-state solution.

The equations are further modified by employing a local time linearization as described by Pulliam [54]. The equations then take the delta form of the algorithm,

$$
\left[I + h \left(\hat{A}^n \right)_\xi + h \left(\hat{B}^n \right)_\eta - Re^{-1} h J^{-1} \left(\hat{M}^n \right)_\eta \right] \Delta \hat{Q}^n
$$

$$
= - h \left[\left(\hat{E}^n \right)_\xi + \left(\hat{F}^n \right)_\eta - Re^{-1} \left(\hat{S}^n \right)_\eta \right]
$$

(3.36)

where $\hat{A} = \partial \hat{E} / \partial \hat{Q}$, $\hat{B} = \partial \hat{F} / \partial \hat{Q}$, and $\hat{M} = \partial \hat{S} / \partial \hat{Q}$. The right hand side of (3.36) is the explicit part and the left hand side of (3.36) is the implicit part of the algorithm.

The form presented in (3.36) is for the thin-layer Navier-Stokes equations. As noted before, ARC2D has the capability to include the streamwise and cross-term derivatives as an alternative to the thin-layer approximation. This is accomplished by retaining the explicit portions of $\hat{E}v$ in the algorithm. The use of these terms was examined with respect to the iced airfoil flow-field and found to have no influence on results for the grid systems used.

The spatial differencing employed by ARC2D is second order central differencing. Upwinding is also included as an optional approach but is generally used only for resolution of shocks. The matrix resulting from application of the central differencing is a (Jmax * Kmax * 4) × (Jmax * Kmax *4) square banded matrix. This form is sparse but very computationally expensive. In order to decrease the run times, the solution process is simplified by an approximate factorization [53] of the two dimensional operator (3.36) into two

25

one-dimensional operators of the form,

$$\left[I + h \left(\hat{A}^n \right)_\xi \right]\left[I + h \left(\hat{B}^n \right)_\eta - h \, Re^{-1}J^{-1}\left(\hat{M}^n \right)_\eta \right] \Delta \hat{Q}^n$$

$$\tag{3.37}$$

$$= - h \left[\left(\hat{E}^n \right)_\xi + \left(\hat{F}^n \right)_\eta - Re^{-1}\left(\hat{S}^n \right)_\eta \right]$$

The solution algorithm now consists of two implicit operators each of which is block tridiagonal. The program flow now consists of two one-dimensional sweeps, one in the ξ-direction and one in the η-direction. The resulting procedure is more economical both in terms of run time and computer storage [54].

Artificial dissipation is added to the algorithm to ensure stability, especially for transonic flow with shocks. This is required because, in high Reynolds number viscous flows, scales of motion exist which cannot be resolved by the numerical scheme. In the actual physical problem, these high frequency waves are brought about by the interaction of the convective terms in the momentum equations. This is normally accounted for by viscous dissipation but, since the scales are not resolved by the code there is no mechanism for removing this energy from the solution.

ARC2D employs two techniques for introduction of artificial dissipation. Since ARC2D can be run as either a steady-state or unsteady code, two forms of time differencing are used as mentioned earlier. For the unsteady time-accurate mode, explicit fourth order and implicit second order smoothing with constant coefficients is included. Typically the fourth order explicit dissipation is set to zero for fine grids, such as those used in this investigation. In steady-state calculations, nonlinear artificial dissipation of mixed second and fourth order is employed. This dissipation model is based on the work of Jameson et al. [57]. A more detailed description of these models and their effect on convergence is provided by Pulliam [54].

26

3.3 The Baldwin-Lomax Turbulence Model

Theoretically, the Navier-Stokes equations fully describe the dynamics of a viscous flow, whether laminar or turbulent. In practice however, it is not feasible to evaluate the finite-difference equations on a grid fine enough to resolve all the details of the turbulent structures. This implies the need for some form of turbulence model. Typically, algebraic and two-equation models are presently being employed in aerodynamic codes. ARC2D employs an algebraic model developed by Baldwin and Lomax [46]. This model is a variation of the model developed by Cebeci and Smith [45] for boundary layer analysis. The Baldwin-Lomax model was developed to avoid the need for determination of the displacement thickness, which is a natural diagnostic of the Cebeci-Smith method but difficult to evaluate with a Navier-Stokes code such as ARC2D. This is due to the difficulty in defining the local free-stream velocity on a non-rectangular grid.

The Baldwin-Lomax model divides the turbulent boundary layer into an inner and outer region. The eddy viscosity, μ_t, is then evaluated by examination of the vorticity level in each region. The inner region encompasses the laminar sublayer and the buffer region. The outer region is the wake-like region of the boundary layer and hence is modeled by a locally constant length scale and a velocity scale dependent on the vorticity.

The form of the eddy viscosity equation in the inner region is, by dimensional reasoning, proportional to the density times a typical length scale times a typical velocity scale.

$$\mu_t = \rho \, \ell \, \mathrm{v}_{inner} \tag{3.38}$$

The length scale is given by,

$$\ell = \kappa \, \mathrm{y} \left[1 - \exp(-\mathrm{y}^+/\mathrm{A}^+) \right] \tag{3.39}$$

where κ is the von Karman constant, y is the normal distance from the wall, A^+ is the van Driest damping constant and,

$$y^+ = y \left. \frac{\sqrt{\rho |\tau|}}{\mu} \right|_w \tag{3.40}$$

The velocity scale is taken to be $v_{inner} = \ell |\omega|$, hence

$$\mu_t = \rho \, \ell^2 \, |\omega| \tag{3.41}$$

In the outer region, the eddy viscosity is given by,

$$\mu_t = K \, C_{cp} \, \rho \, F_{wake} \, F_{kleb}(y) \tag{3.42}$$

where K is the so called Clauser constant, C_{cp} is an additional empirical constant used by Baldwin-Lomax, $F_{kleb}(y)$ is a factor which tries to account for intermittancy and will be described later. F_{wake} is a function defined by Baldwin and Lomax as,

$$F_{wake} = \text{Min} \begin{cases} y_{max} \, F_{max} \\ \left(C_{wk} \, U_{diff}^2 \, y_{max} \right) / F_{max} \end{cases} \tag{3.43}$$

where F_{max} is the maximum value of the function,

$$F(y) = y \, |\omega| \left[1 - \exp(-y^+/A^+) \right] \tag{3.44}$$

along a grid line in the η-direction. The y-value at which F(y) reaches this maximum is

designated as y_{max}. The value of U_{diff} is given by,

$$U_{diff} = \left(u^2 + v^2\right)^{\frac{1}{2}}_{max} - \left(u^2 + v^2\right)^{\frac{1}{2}}_{min} \qquad (3.45)$$

This formulation results in the length scale being determined by the distribution of vorticity along a normal to the surface.

The inner region model extends outward until the value of μ_t obtained with this model equals the μ_t value obtained with the outer region model. The interface value is then taken as the average of the two model values at this point. The outer region extends from the point of equality with the inner region to a distance at which the velocity is equal to the local free stream value, which is taken to be the value at the outer boundary of the solution domain.

The effect of intermittency has been modeled by incorporation of a variation of the Klebanoff intermittency factor. This term is given by,

$$F_{kleb}(y) = \left[1 + 5.5\left(\frac{C_{kleb}\,y}{y_{max}}\right)^6\right]^{-1} \qquad (3.46)$$

where $C_{kleb} = 0.3$. The value of F_{kleb} is essentially unity for small values of y and drops to almost zero for large values. The transition from unity to zero occurs rapidly at y values close to y_{max}.

The Baldwin-Lomax model works very well for attached boundary layers and for small separated regions. Large separated regions can cause some difficulties for the model which results in improper representation of the turbulence in the region. In an attempt to rectify this problem, an alternate turbulence model has been developed which employs an approach similar to the Baldwin-Lomax model but which tries to avoid some of the difficulties encountered in the large separation regions. This is also a Modified Mixing Length (MML)

model, which bases the determination of the mixing length on the wall shear and the distance from the wall until some maximum is reached. The value of this maximum length scale is determined by evaluation of an attached boundary layer in a parametric study. The velocity scale is determined by the vorticity level and the mixing length at each point in the flow. This approach avoids the problem of trying to determine which of the local maxima of the Baldwin-Lomax F-function should be used to evaluate the viscous region on the iced airfoil. In the following chapters, the MML model will be described and compared to the Baldwin-Lomax model, especially in regard to calculation of cases at and above stall.

CHAPTER 4

MODIFICATIONS FOR ICING ANALYSIS

This chapter details the changes made to the ARC2D code in order to enhance its ability to calculate the iced airfoil flowfield. Specifically, the approach to modeling turbulence was replaced by a simple but workable model in an attempt to provide a more realistic distribution of turbulent viscosity throughout the separated flowfield that develops behind the horns of the ice shape. The modifications were made in order to calculate the separated flow aft of the horns and to allow evaluation of the premature stall of the iced airfoil.

Navier-Stokes codes have been used to evaluate separated flowfields (e.g. Mehta and Lavan [24]), but successful attempts have been confined to cases with moderate Reynolds numbers. For higher Reynolds numbers, typical of a turbulent flow, the ability to predict the maximum lift has not been demonstrated. This indicates that some attention to the turbulence model is necessary for determination of stall in an airfoil under normal operating conditions. The special circumstances of an airfoil with a leading edge ice accretion allows definite identification of the stall mechanism. An attached recirculation region aft of the horns breaks away from the surface which results in massive separation and stall. This eliminates one of the difficulties experienced in evaluation of stall on a clean airfoil. Thus, turbulence model alterations can be directed toward better evaluation of a specific flow rather than for employment in a more general and therefore more widely varying flowfield.

4.1 The Baldwin-Lomax model examined

The turbulence model originally employed in the ARC2D code is an algebraic eddy viscosity model developed by Baldwin and Lomax [46] and was described in some detail in the previous chapter. Calculations using this model for an attached boundary layer have been very successful [54]. However, the use of this model in separated boundary layers has previously resulted in some difficulties, as described by Degani and Schiff [58]. In their case, evaluation of cross-flow separation on a pointed cylinder at high angle of attack, the model suppressed secondary vortices when used as originally implemented. The difficulties experienced were attributed to the evaluation of the maximum of the F-function, described in Eq. (3.44).

The presence of multiple maxima in the F-function led to excessively large eddy viscosity values. This in turn damped out the smaller flow structures, including the secondary vortices, and resulted in the center of the main vortex being displaced from the surface. Degani and Schiff modified the Baldwin-Lomax model by essentially deciding a priori which maxima was the more significant for their calculation. Their results indicated a significant improvement in determining the details of the flow separation for the geometry being considered.

Similar problems were experienced in this study during evaluation of the iced airfoil at high angles of attack. In this case, the F-function developed a third peak, as shown in figure 2. This type of profile was due to the large value of the vorticity at the wall and the smaller, although significant, vorticity levels in the vortex being shed from the surface of the airfoil. Due to the transient nature of the flow field, this type of profile moves along the surface with the vortex, further complicating the selection of the appropriate value of F_{max}.

As a result, the turbulence levels in the flow on the upper surface have steep gradients and change along with passage of the vortex. This is shown in figures 3 and 4,
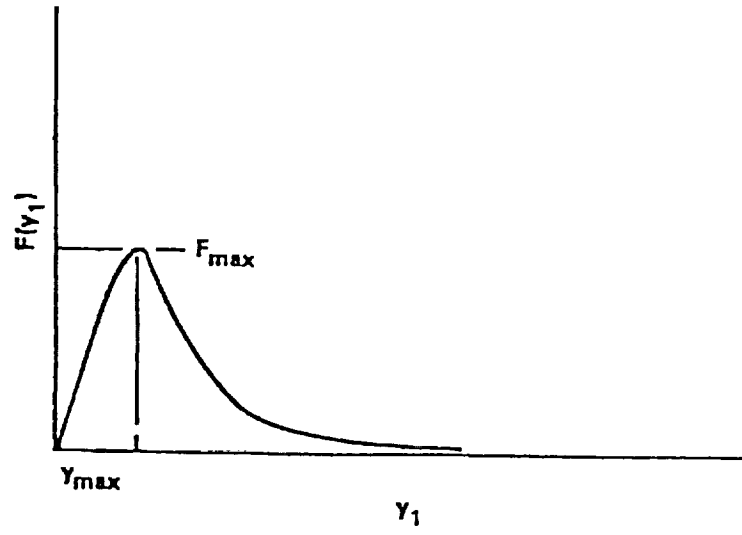
(a) Attached flow
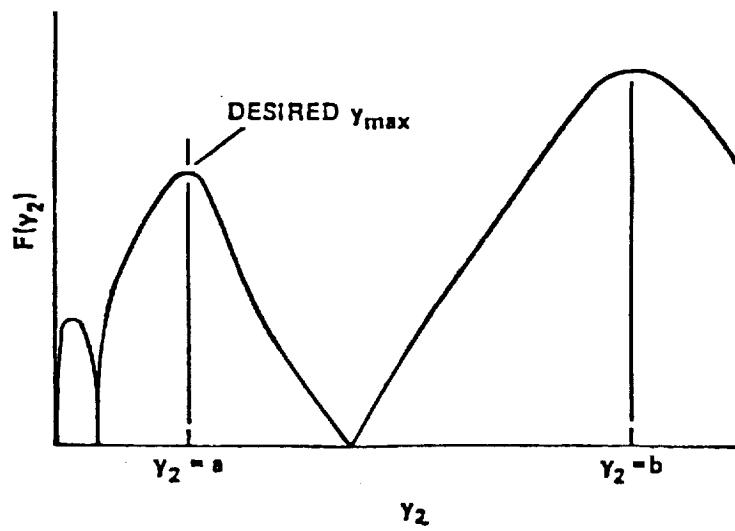
(b) Separated flow

Figure 2   F-function profiles for attached and separated flow conditions
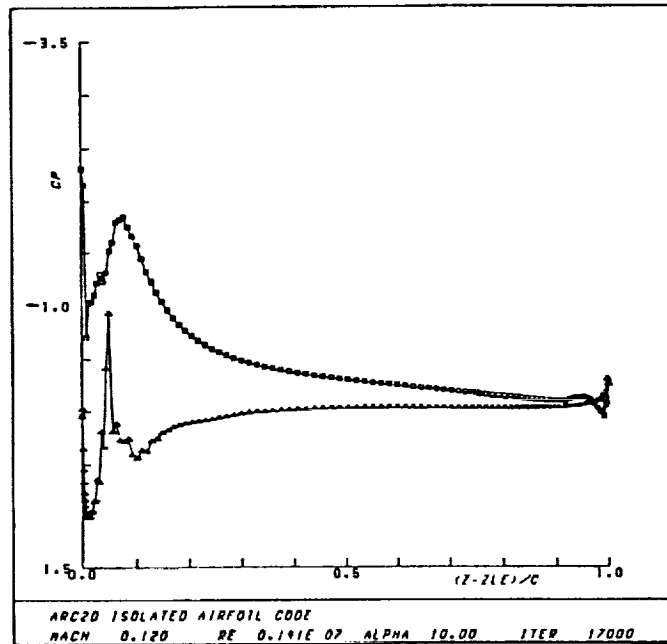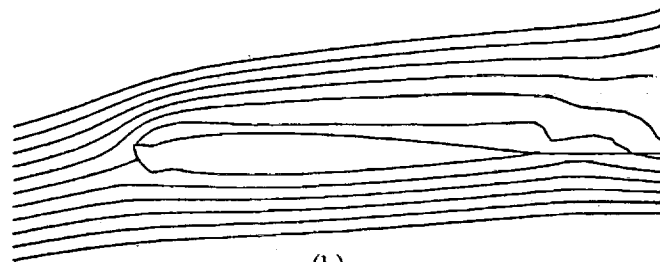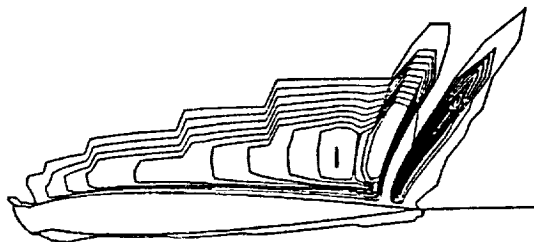
Figure 3   Unsteady flowfield at time t_o : Baldwin-Lomax model.   AOA = 10°. a) C_p distribution, b) Stream function contours, c) μ_t contours; $\mu_{t\ max} \approx 10{,}000 \mu_l$
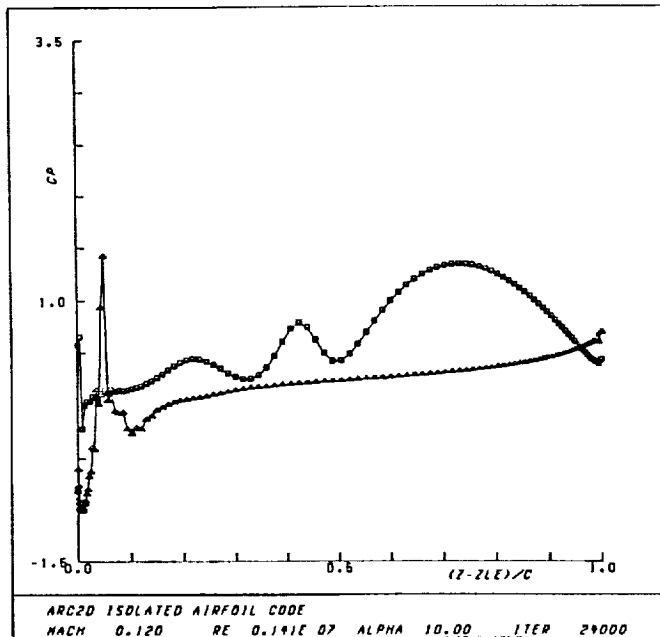
(a)
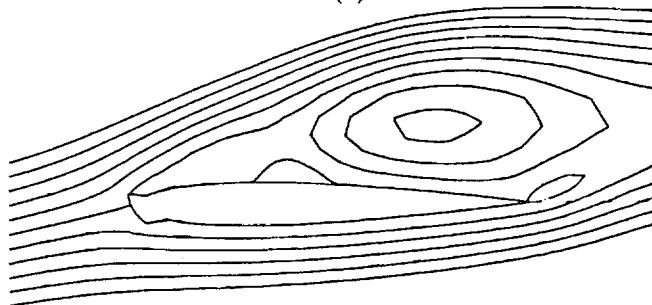
(b)
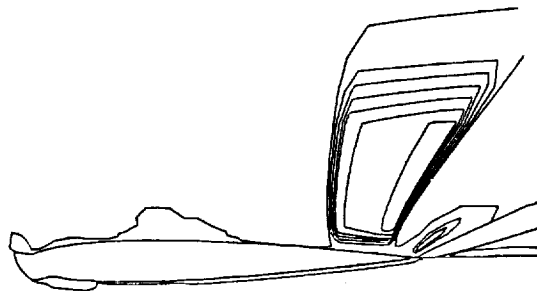
(c)

Figure 4   Unsteady flowfield at time $t_o + \Delta t$: Baldwin-Lomax model.   AOA $= 10°$.   a) C_p distribution, b) Stream function contours, c) μ_t contours; $\mu_{t\ max} \approx 7000 \mu_l$

which indicate the pressure distribution, stream function contours, and eddy viscosity levels at different points in time for an iced airfoil at an angle of attack above stall. As shown in the figures, the eddy viscosity levels increase and decrease abruptly in regions of high vorticity associated with the vortex travelling along the airfoil surface. Also apparent is the fact that the eddy viscosity levels are tied to the motion of this vortex and that points outside this region have little, if any, turbulent dissipation. It would seem more appropriate that some turbulence would remain in the regions between vortices and that the sharp gradients seen in the figures would not be present in an actual turbulent flow.

The distribution and overall level of the eddy viscosity can result in significant changes in the size and shape of vortex patterns in the flowfield, as indicated by the experience of Degani and Schiff. The size and shape of the vortices and their shedding frequency all contribute to the time-averaged pressure distribution experienced by the stalled airfoil. Thus, it is reasonable to assume that by altering the development of this vortex shedding mechanism, the pressure distribution and hence the lift of the airfoil can be adjusted. If this adjustment is approached in a rational manner, then perhaps the lift of the stalled airfoil can be determined with a higher degree of accuracy than with the present turbulence model.

With the complications of the Baldwin-Lomax model in mind and the goal of a more attractive model for separated flows, an alternate turbulence model was developed for evaluation of the iced airfoil. When selecting a new turbulence model it is appropriate to consider the degee of detail required of the model, the complexity of the model, the difficulty in implementing the model, and the resulting benefits of employing a given model. For aerodynamic codes the nature of ARC2D, the choice seems to lie between algebraic models and two equation models. Presently an effort is underway [59] to incorporate both a two equation model, that of Gorski [60], and the ordinary differential equation model of Johnson

36

and King [41] into the ARC2D code for evaluation of separated flows. Thus, in order to avoid an overlap of effort and to respond to the special circumstances of the iced airfoil conditions, an alternate approach was employed in this investigation. The model developed is essentially a mixing length model which seeks to avoid selection of the appropriate length scale based on the local maxima of an ad hoc function.

4.2 The Modified Mixing Length Model

The Modified Mixing Length (MML) model is a zero equation model based on the Prandtl mixing length hypothesis. That is to say that there are scales of motion for a turbulent flow associated with the transport of momentum much the same as the mean free path of kinetic theory characterizes the motion of gas molecules. These scales, if they can be determined, can be used to characterize the time averaged or mean flow motion of the fluid. The difficulty, of course, lies in the determination of the appropriate scales.

The MML model was developed in an attempt to model the appropriate scales of motion for a flowfield which is alternatively separated from and attached to an arbitrary geometric surface. Observation of the motion produced by this surface, as shown in figures 3 and 4, leads to some assumptions as to how the turbulence may be generated and transported in the flowfield. These assessments of the nature of the turbulent flowfield are then translated into a numerical mechanism for the introduction of turbulent viscosity into the calculation. This process requires some prior evaluation of the flowfield of interest as well as some reference to the work of other investigators which may be relevant. As such, some background for the development of this model will be presented next.

The MML model tries to address the problem of distribution of turbulent dissipation throughout a separated flowfield. In so doing, it is necessary to have some indication of the character of the flowfield being examined. An iced airfoil is typified by

regions of flow separation aft of the protruding horns (see Figure 1b). These regions increase and decrease in size with varying angle of attack (AOA). The upper surface separation region increases with increasing AOA, while the lower surface region decreases in size. The opposite occurs with decreasing AOA. At some critical AOA, the bubble no longer reattaches to the surface and a large unsteady vortex shedding pattern develops. These two different flow patterns are shown in figures 5a and 5b, respectively.

The closed separation bubble of figure 5a is modeled adequately by the Baldwin-Lomax model, as will be discussed in the next chapter. The unsteady flow pattern of figure 5b is the flow which resulted in the difficulties discussed in section 4.1. Therefore, the special circumstances of this flow were examined and modeled during the development of the MML model.

The MML model is based on the expression associated with the Prandtl mixing-length theory [61]. Basically the turbulent viscosity is taken to be,

$$\mu_t = \rho \ell^2 |\omega| \qquad (4.1)$$

The question is what to use for the evaluation of the mixing-length, ℓ. The mixing-length is dependent on distance from the wall. In an attached boundary layer there are typically three regions;

$$\ell \sim y^2 \qquad\qquad y^+ < 10 \qquad\qquad (4.2)$$

$$\ell \sim \kappa y \qquad\qquad 10 \leq y^+ \leq 100 \qquad\qquad (4.3)$$

$$\ell = \text{const.} \qquad\qquad y^+ > 100 \qquad\qquad (4.4)$$
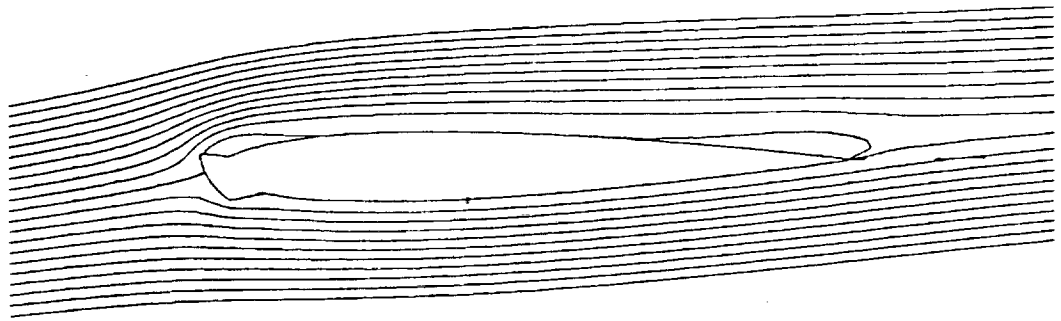
(a)
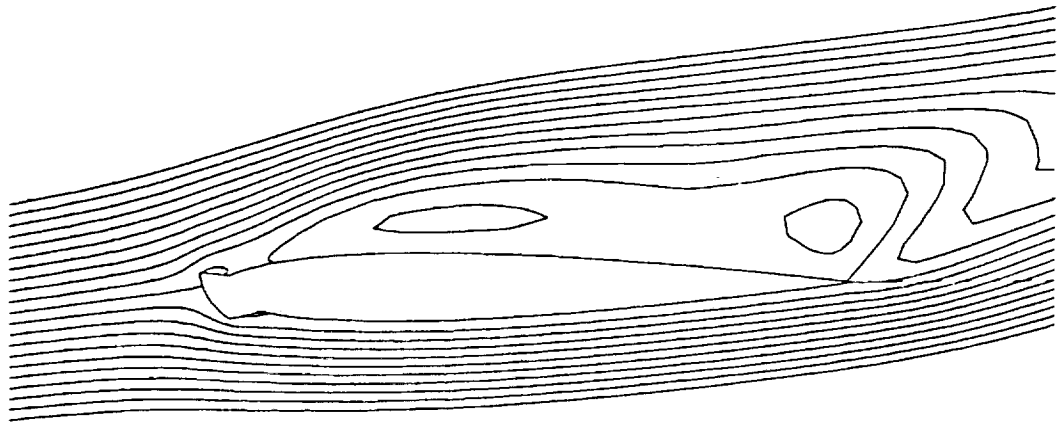
(b)

Figure 5   Stream function contours for an airfoil with ice accretion. a) Pre-stall condition,

AOA = 5° b) Post-stall condition, AOA = 7°

where,

$$y^+ = \frac{y\,u_\tau}{\nu}$$
(4.5)

and

$$u_\tau = \frac{|\tau_w|^{\frac{1}{2}}}{\rho}$$
(4.6)

and

$$\tau_w = \mu \left|\frac{\partial u}{\partial y}\right|_w$$
(4.7)

The flowfields which seem to develop on the iced airfoil above stall have three distinct regions. Very near the wall is a region of low velocity and high vorticity, distinguished from conventional attached boundary layers only by the far field boundary condition (i.e. the vortex structures in the separated region). Further out is the moderate velocity, moderate vorticity recirculation regions of the main separated flow. Above this is the high velocity, low vorticity region of the outer flow. It would seem then that the vorticity is generated at the horns and along the surface of the airfoil. This observation is in line with the expression for development of vorticity in a Newtonian fluid given by,

$$\frac{D\bar{\Omega}}{Dt} = (\bar{\Omega}\cdot\nabla)\bar{U} + \nabla \times \left(-\frac{\nabla P}{\rho}\right) + \nabla \times \left[\frac{1}{\rho} - \nabla \times \left(\mu\bar{\Omega}\right) + \nabla \left(\left(\frac{4}{3}\right)\mu\,\nabla\cdot\bar{U}\right)\right]$$
(4.8)

which is obtained by taking the curl of both sides of the equation of motion in vector form. In this expression, $\bar{\Omega}$ is the vorticity vector, $\bar{U}$ is the velocity vector, P is the pressure, ρ is

the fluid density, μ is the absolute viscosity, and $\frac{D}{Dt}$ is the substantial derivative. The first term in this equation indicates the change in vorticity in the flowfield due to strain rate. The second term is a source of vorticity due to the pressure force. The final term is the diffusion of vorticity by viscosity. In a two-dimensional flow the first term disappears and only the source and diffusion terms remain.

As a solid body passes through a viscous fluid with initially no vorticity, the pressure gradient at the surface produces vorticity tangential to the surface. This vorticity is then spread through the flow due to the viscous dissipation. The linkage between this generation and diffusion of vorticity and the level of turbulence is provided by (4.1). Thus, if the vorticity is generated near the surface, it may be reasonable to assume that the value of μ_t is associated with the flow near the surface. Also, as the vorticity is spread through the flowfield, the turbulence level develops along with it, hence the dependence of μ_t on $|\omega|$.

Equation (4.8) indicates that there is no vorticity production in the separated region due to the absence of a significant source term. Therefore, it is reasonable to conclude that there is no further enhancement of the turbulent viscosity. This is embodied in Prandtl's observation that the length scale very far from the surface is a constant, Eq. (4.4). This allows the turbulent viscosity to diminish along with the vorticity as would be expected from equation (4.8).

The MML model is based on the idea that the length scale is dependent on conditions near the surface and that its level remains constant in the separated region. The length scales are thus established by conditions at the surface and are then transported into the separated flow regions along with the mean flow. The ultimate level of the turbulent viscosity in these regions is established by the length scale and the level of vorticity. This leads to a two layer type model as employed by Cebeci-Smith and Baldwin-Lomax, with the cross over point being established by conditions near the surface.

The inner region of the MML model encompasses the laminar sublayer and the logarithmic buffer layer. There are several empirical formulas available which are used to evaluate this region. In this case, the van Driest formulation is used and is given by,

$$\ell(y) = \kappa y \left(1 - e^{(-y^+/A^+)} \right)$$

(4.9)

The outer region is based on the observation that the length scale in an attached boundary layer saturates at a level of about 0.10δ, as shown in figure 6 taken from reference [62]. For a separated flow, there is no definite boundary layer thickness, hence the length scale in this region is defined with respect to the value of y^* where,

$$y^* = \frac{\nu}{\sqrt{|\tau|/\rho}} \bigg|_w$$

(4.10)

The length scale is simply,

$$\ell = \text{const.} \times y^*$$

(4.11)

with the constant to be defined empirically.

The two regions are blended into each other through a function of the form,

$$\left(\frac{C_1}{C_2} \right) \left(\frac{y^*}{y} \right) \left[1 - \left(1 - \frac{y}{C_1 y^*} \right)^{C_2} \right]$$

(4.12)

where $C_1 y^*$ is the distance above the surface at which ℓ saturates and C_2 controls the curvature of the blending region. The form of the mixing length profile as a function of distance from the surface is shown in figure 7. Note the similarity to the ℓ curve in figure 6.
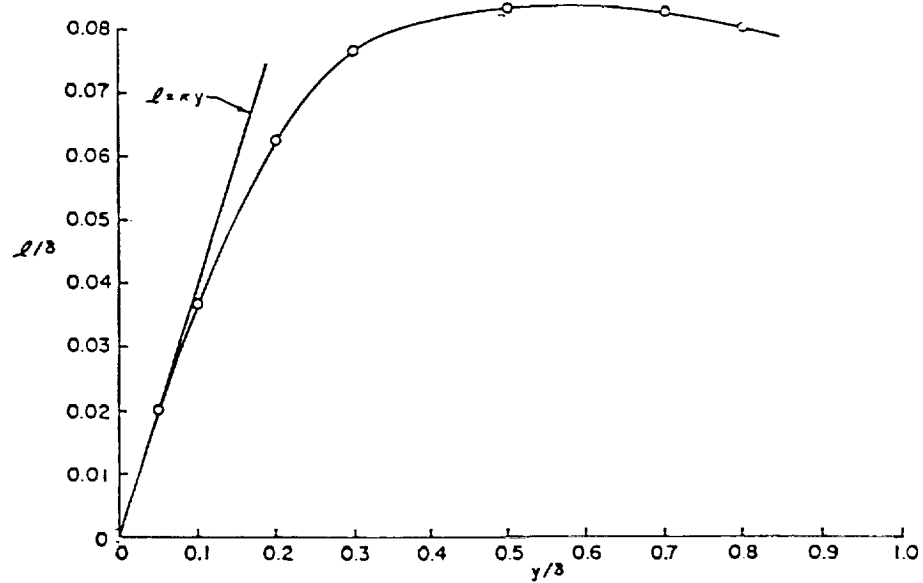
Figure 6   Length scale profile in a turbulent boundary layer. Taken from Cebeci and

Smith [62].
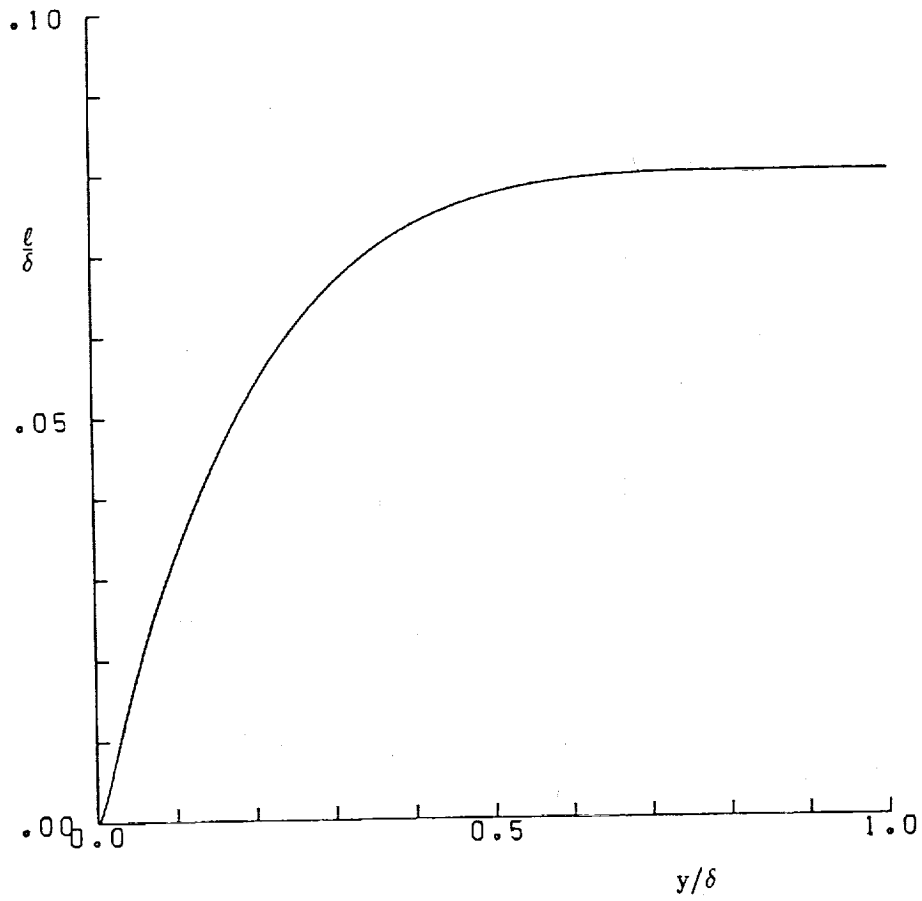
Figure 7   Mixing length profile for the MML model.

The MML model is thus defined by the following relations,

$$y^+ < C_1 \qquad \ell(y) = \kappa \frac{C_1}{C_2} y^* \left(1 - \left(1 - \frac{y^+}{C_1} \right)^{C_2} \right) \left(1 - e^{(-y^+/A^+)} \right) \qquad (4.13)$$

and,

$$y^+ > C_1 \qquad \ell(y) = \kappa \frac{C_1}{C_2} y^* \qquad (4.14)$$

where y^+ can be rewritten as,

$$y^+ = \frac{y}{y^*} \qquad (4.15)$$

From (4.14) we see that the constant in (4.11) is given by,

$$\text{const.} = \kappa \frac{C_1}{C_2} \qquad (4.16)$$

where the values of C_1 and C_2 can be varied to match empirical results.

This model is dependent on the value of τ_w and thus will in general enhance the level of turbulent viscosity near regions of separation and reattachment. On the other hand, the value of τ_w in the backflow region of a separated flow is relatively large, resulting in lower values of the turbulent viscosity. This agrees with a number of the observations of Simpson et.al. [63] regarding two-dimensional separated flows. These are that the separating shear layer behaves progressively more like a free shear mixing layer and that the part of the backflow adjacent to the surface has little Reynolds shear stress effects. There are some

observations which are not incorporated however, but these appear to be more characteristic of a closed separation bubble than of the massive separation being considered here.

As a result of the use of τ_w near regions of separation and reattachment, there is a possibility of the mixing length becoming excessively large. This is seen in figure 8a which shows $|\tau_w|^{-\frac{1}{2}}$, hence the values of y^* and ℓ, near such a region. This problem is avoided by the use of a local average for τ_w. In the model used for this investigation, the τ_w is filtered spatially using the expression,

$$\tau_{i,1} = 0.1\tau_{i-2,1} + 0.2\tau_{i-1,1} + 0.4\tau_{i,1} \\ + 0.2\tau_{i+1,1} + 0.1\tau_{i+2,1} \tag{4.17}$$

where the subscripts indicate grid points in the ξ and η directions respectively. The η-direction subscript is set at one to indicate values at the surface.

This spatial filtering assures the use of a non-zero value in the denominator of y^* by converting a profile similar to figure 8a to one more like 8b. The use of this averaging also reflects the fact that separation and reattachment are processes extending over a certain region rather than an isolated event. Hence, it is expected that the MML model will capture the physical characteristics of these processes.

4.3 Evaluation of the MML model

The MML model was developed to address some of the discrepencies resulting from use of the Baldwin-Lomax model with separated flows. The new model should also perform reasonably for attached flows, since it incorporates all the elements of mixing-length models used for attached flows. In order to evaluate this model, a number of comparisons were made

46
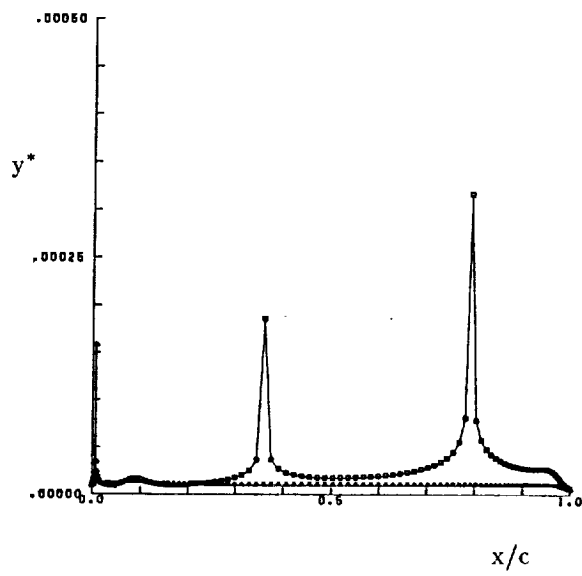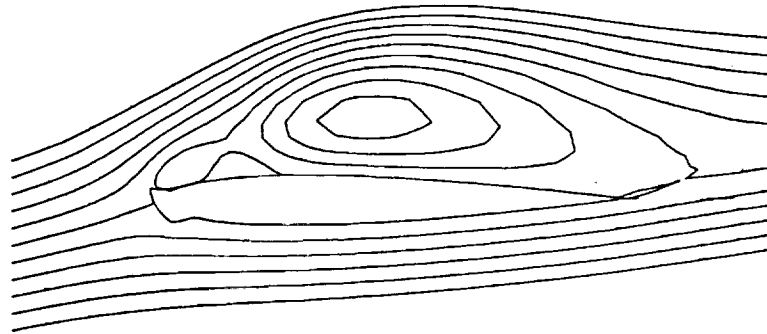
(a)
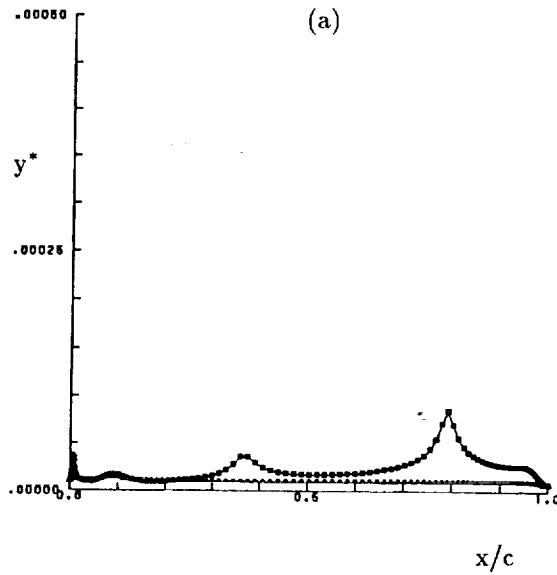
(b)

Figure 8   Distribution of y* for a separated flow condition. AOA=10° a) No spatial averaging. b) Spatially averaged.

47

between results from ARC2D using the Baldwin-Lomax model and the MML model for attached and separated flows on a NACA0012 airfoil with no ice shape. Comparisons to experimental results are also made when the latter are available.

The cases examined are 0° AOA and 15° AOA for a Mach number of 0.12 and a Reynolds number of 1.41×10^6. The grid used is shown in figure 9. There are 253 nodes in the ξ-direction and 64 nodes in the η-direction. There are 42 points along the wake cut and thus 211 points along the surface of the airfoil. The spacing of the first grid point normal to the airfoil surface is 2×10^{-5} chord lengths. This grid is similar in size and spacing to the grids used for the iced airfoil.

0° AOA-Attached flow

The attached flow at this angle of incidence is a steady flow condition and thus the code can use the form of the algorithm designed for such flows. The time step used is thus a spatially varying value which results in the optimum convergence at each point in the grid. The value of the time step input to the code is thus a parameter used in an expression such as,

$$\Delta t_o \left(\frac{1}{1 + \sqrt{J}} \right) \tag{4.18}$$

where Δt_o is the input time step and is normally chosen to be $\mathcal{O}(1)$. For the cases run here, the value of Δt_o was set at 0.9.

In evaluating the MML model, the values of C_1 and C_2 can be manipulated in order to produce results which agree with experimental information. By employing this process for the clean airfoil it is expected that the model will then be 'tuned' and ready for use with the iced airfoil. The MML model was thus used with several values of C_1 and C_2 and compared

48
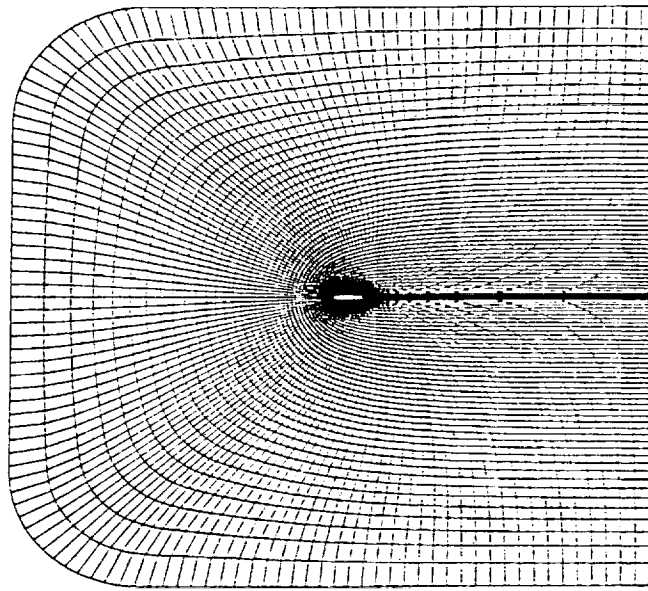
(a)
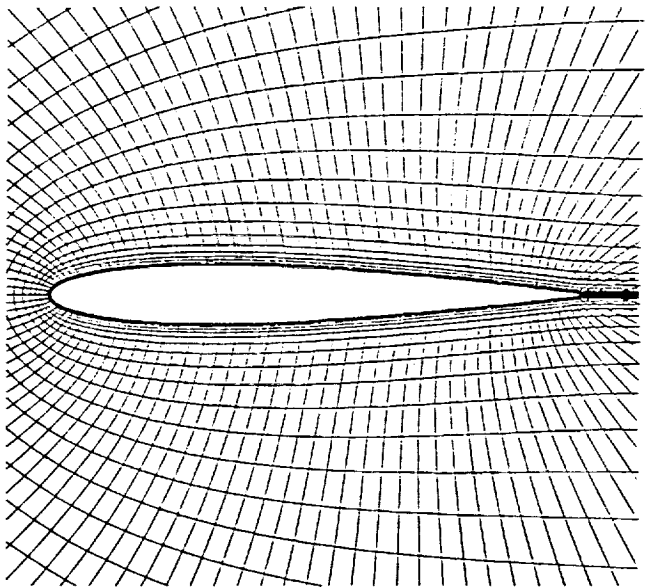
(b)

Figure 9   Grid system for NACA0012 airfoil a) Complete grid (253×64) b) Close-up of grid

near airfoil surface.

to the Baldwin-Lomax results and to experimental information. The values used for the MML model are selected such that they produce length scales similar to those near the region of transition from inner layer to outer layer as shown in Bradshaw [64]. Variation of the C_2 parameter produced overall effects similar to those of varying the C_1 parameter and results can therefore be reported for the C_1 parameter alone. The results of this comparison for drag values are shown in Table 1.

These results indicate that the MML model can have significant variations in drag as a result of varying C_1. However, the Baldwin-Lomax model produces drag values closer to experimental results. This discrepancy is examined further by looking at velocity gradients at the surface of the airfoil. The results for the Baldwin-Lomax model and the MML model, with the same C_1 values used previously, are compared in Table 2.

Evaluation Method	C_1	C_2	C_D
Baldwin-Lomax	NA	NA	0.014
MML	300	5.0	0.019
MML	1000	5.0	0.020
MML	8000	5.0	0.016
Experiment	NA	NA	0.009

Table 1   Force coefficients for several values of turbulence model parameters

Turbulence Model	C_1	$\frac{x}{C}$	$\frac{\partial u}{\partial y}$
Baldwin-Lomax	NA	0.6	2.08×10^5
MML	300	0.6	3.67×10^5
MML	1000	0.6	3.67×10^5
MML	8000	0.6	3.78×10^5

Table 2   Velocity gradients at the surface as calculated using the Baldwin-Lomax and MML turbulence models

This table indicates that the velocity gradients for the MML model are approximately twice as large as the values from the Baldwin-Lomax model. If the total velocity profile at a given location is examined, it is found that the differences are relatively minor, the relative error based on u_w being 0.01. Thus it can be seen that the values of the velocities very near the surface must be determined accurately to produce the correct drag. This is seen directly by examining the equation used to determine the frictional component of the drag. That is,

$$C_{D_v} = C_{f_v} \left(\Delta y \sin \alpha + \Delta x \cos \alpha \right) \tag{4.19}$$

where,

$$C_{f_v} = \mu \frac{\left(\dfrac{\partial u}{\partial y} - \dfrac{\partial v}{\partial x} \right)}{\left(\frac{1}{2} \rho_\infty U_\infty^2 \right)} \tag{4.20}$$

The value of μ at the wall is essentially the molecular viscosity. The geometric values are the same for both calculations as are the free stream fluid properties. The only difference between the two calculations is due to the velocity gradients. Since the wall velocity gradients are calculated by using the first two grid points off the surface, the evaluation of these points is critical. These points correspond to a height of 7×10^{-5} chord lengths above the surface. Determining how the overall turbulence level affects the velocity gradient at the wall will require further study. Even in the case of the Baldwin-Lomax model the results differ from experiment by 52 percent. Abandonment of the MML model is not warranted strictly on the basis of these results. Indeed, as later results reveal, a strong case can be made for the adoption of the MML model.

15° AOA - Separated flow

The MML model was developed with this case in mind. At 15° AOA, the NACA0012 airfoil is near $C_{L\ max}$ and under certain conditions, stall will occur. The NACA0012 airfoil has two possible modes for stall at this angle of attack. Gregory and O'Reilly [65] state that this airfoil stalls either from collapse of a short leading edge laminar separation bubble or from the rapid advance toward the leading edge of a trailing edge separation. The question of the conditions under which either mechanism occurs is not resolved by their experiment nor was it addressed in the work of Bragg [66].

As far as the calculations with ARC2D are concerned, there is no evidence of a short leading edge bubble using either turbulence model. There are differences, however, in the two calculations. The MML model produces a relatively large separation region near the trailing edge, while the Baldwin-Lomax model shows a much smaller separation region. This is shown in figures 10a and 10b, which show stream function contours for the Baldwin-Lomax model and MML model respectively. The difference between these two calculations is due to the
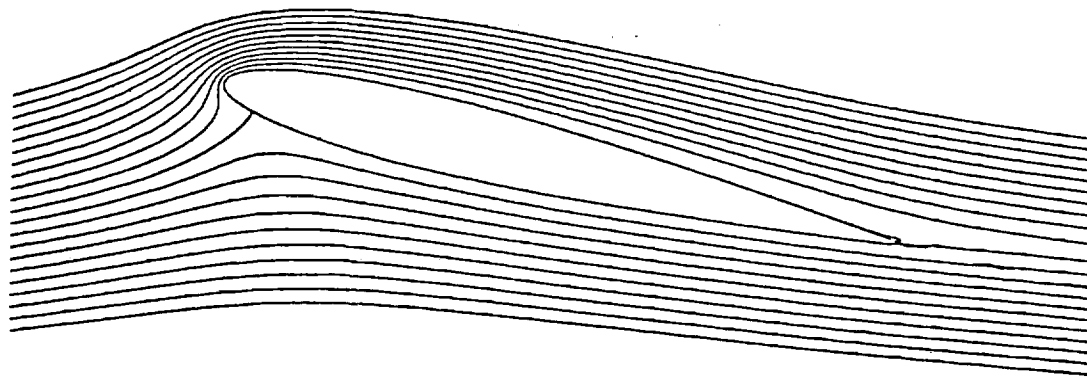
(a)
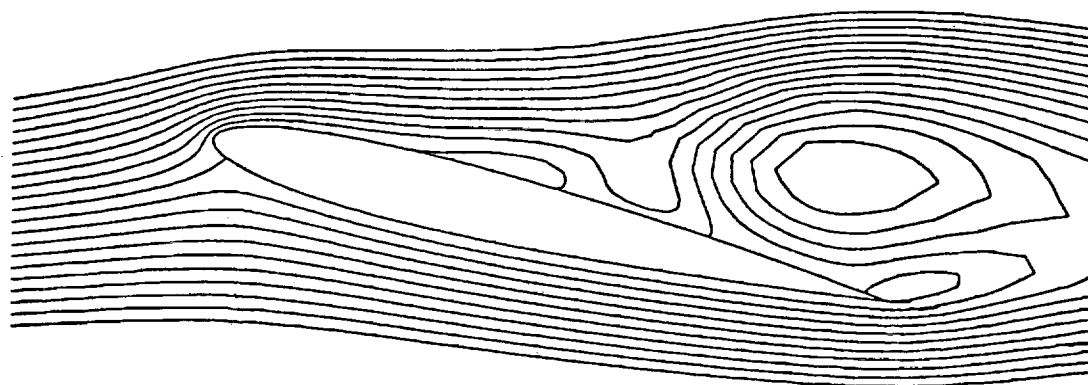
(b)

Figure 10   Stream function contours for NACA0012 airfoil. AOA = 15˚.

a) Baldwin-Lomax model, b) MML model

distribution of turbulent viscosity near the trailing edge, as seen in figures 11a and 11b. The Baldwin-Lomax model develops a large region of high μ_t values which tend to suppress the development of the trailing edge separation. On the other hand, the MML model has high values of μ_t only near the separation point, allowing the reverse flow region to develop downstream of this location.

Figure 12 shows the pressure coefficients from these two calculations compared to the experimental values of Bragg [66]. As seen, the MML model captures the alteration of the pressure development at the trailing edge much better than the Baldwin-Lomax model. This is reflected in the C_L values obtained with the two models. The Baldwin-Lomax model gives a C_L value of 1.4 while the MML model gives a C_L of 1.2. The experimental value is 1.2. Thus, while the issue of the actual mechanism for stall is not settled, it can be seen that the MML model produces a more reasonable representation of the airfoil flowfield than the Baldwin-Lomax model for high angles of attack.

Further testing

Since the MML model was able to produce results which more closely model the actual flowfield for the stall condition, it was necessary to determine the appropriate values of C_1 and C_2 to employ. A series of cases near stall were run with different C_1 and C_2 values. The cases evaluated are indicated in Table 3. The values selected as the most appropriate from this examination will then be compared to similar results from an examination of the iced airfoil at stall.

54
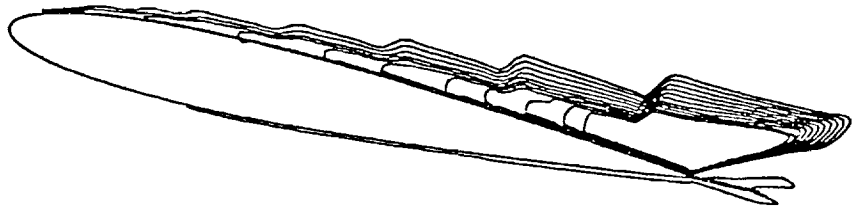
(a)
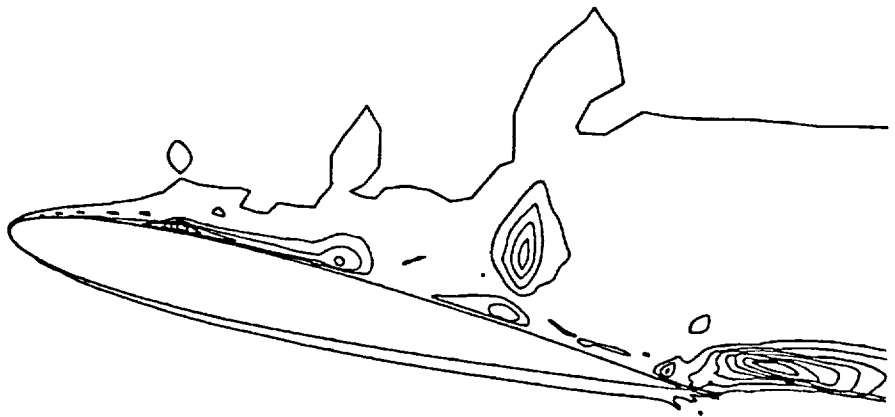
(b)

Figure 11   Eddy viscosity contours for NACA0012 airfoil. AOA=15°.

a) Baldwin-Lomax model, b) MML model
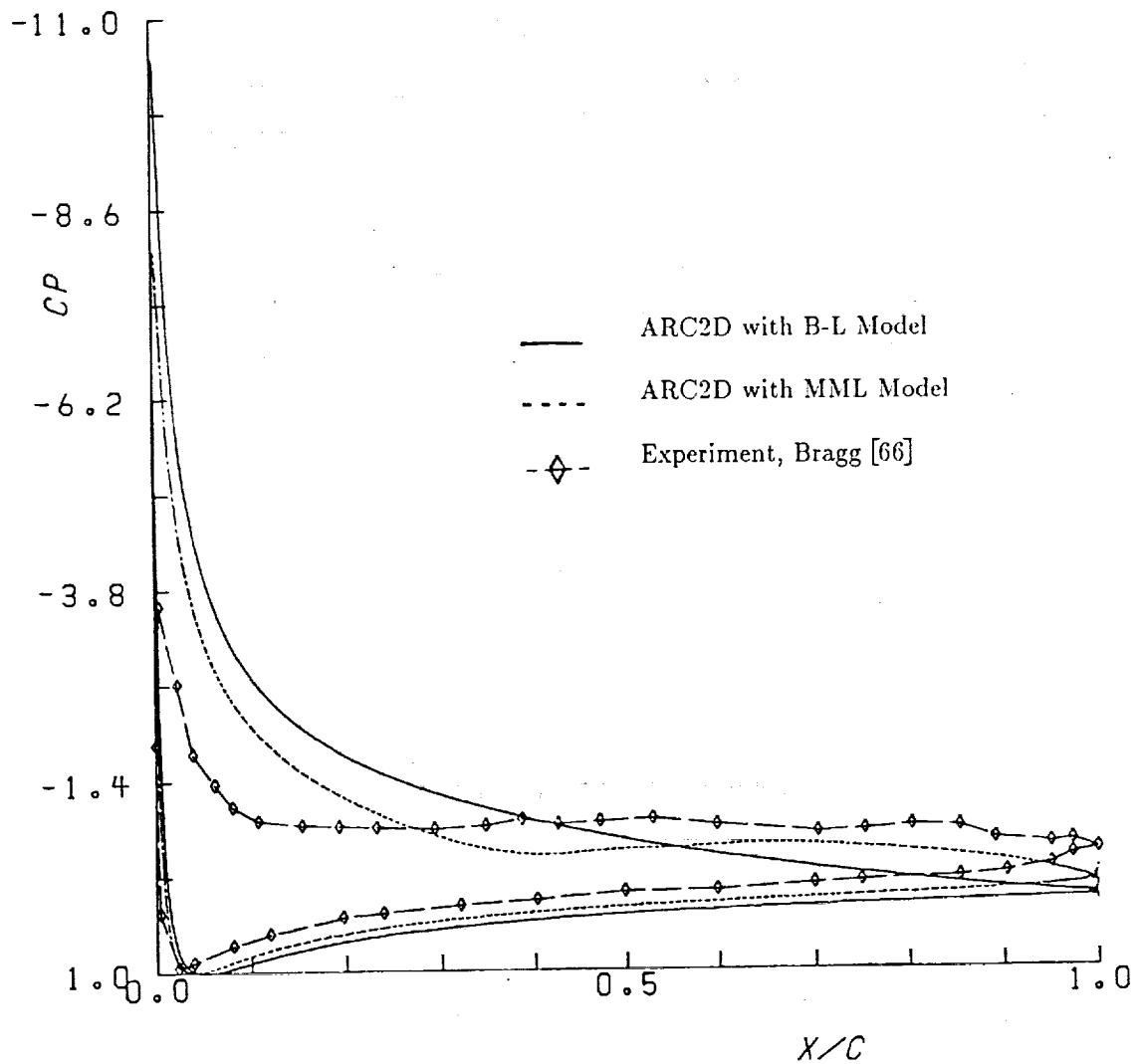
Figure 12   Pressure coefficient profiles for 15° AOA. ARC2D with either the B-L model

or the MML model versus experimental results of Bragg.

Run Number	AOA	C_1	C_2
1	14	1000	5
2	15	1000	5
3	16	1000	5
4	14	2000	5
5	15	2000	5
6	16	2000	5

Table 3   Evaluation of variation in C_1 on MML model results at several AOA values near stall

These cases were all run in the time accurate mode. Thus, the lift histories can be examined to determine if there is some unsteadiness in the flow. The lift histories for runs 1-3 are shown in figures 13-15 respectively. These results indicate unsteady behavior starting at 15° AOA. The time-averaged lift value is lower than the steady value at 14° and thus stall of the airfoil is indicated. The lift histories for runs 4-6 are shown in figures 16-18 respectively. These results indicate steady flow behavior and thus no stall of the airfoil. The resulting lift values indicate a progressive increase with AOA.

The C_L vs. AOA curve for a NACA0012 airfoil is shown in figure 19, taken from NACA TR-446 [67]. Stall of the airfoil is indicated at an AOA just above 16°. The $C_{L\ max}$ value is 1.52 and the C_L value drops off to 1.16 at 18°. These results indicate that runs 4-6
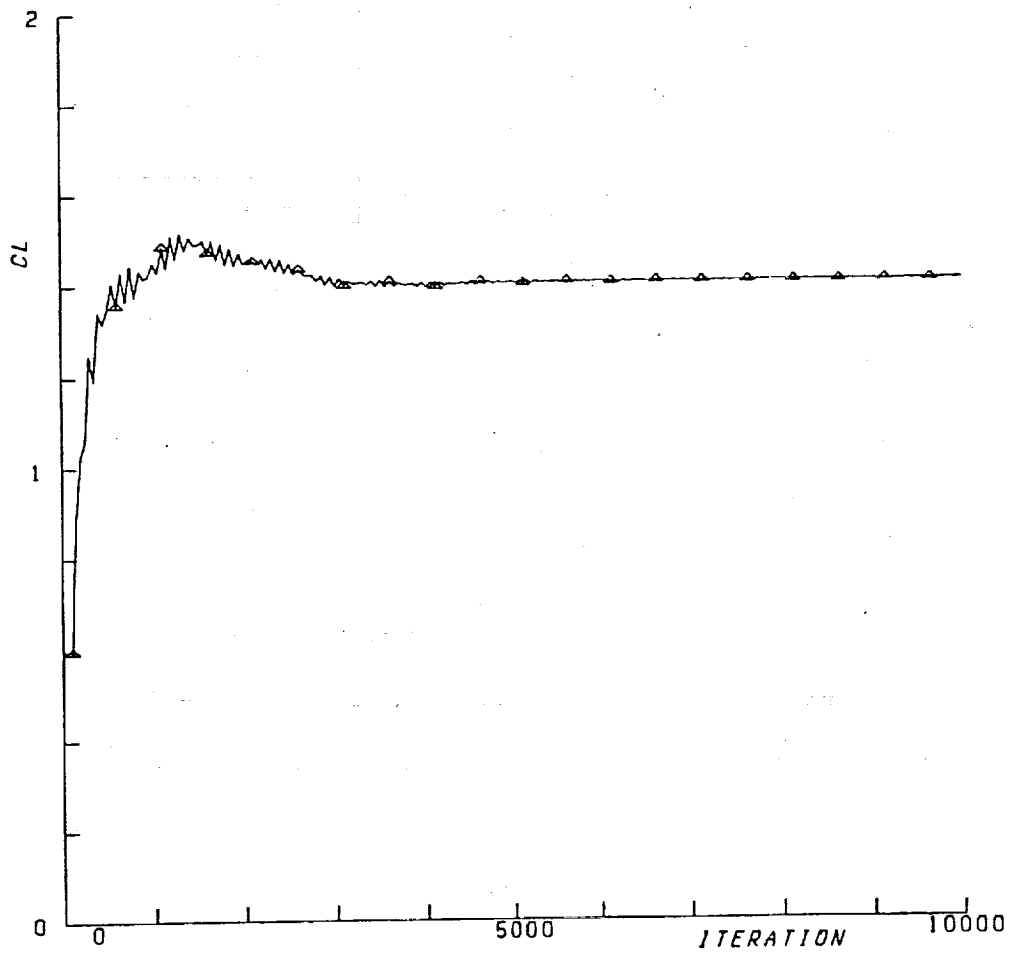
Figure 13   Lift history for run 1 : AOA 14°, $C_1 = 1000$, $C_2 = 5$.

58
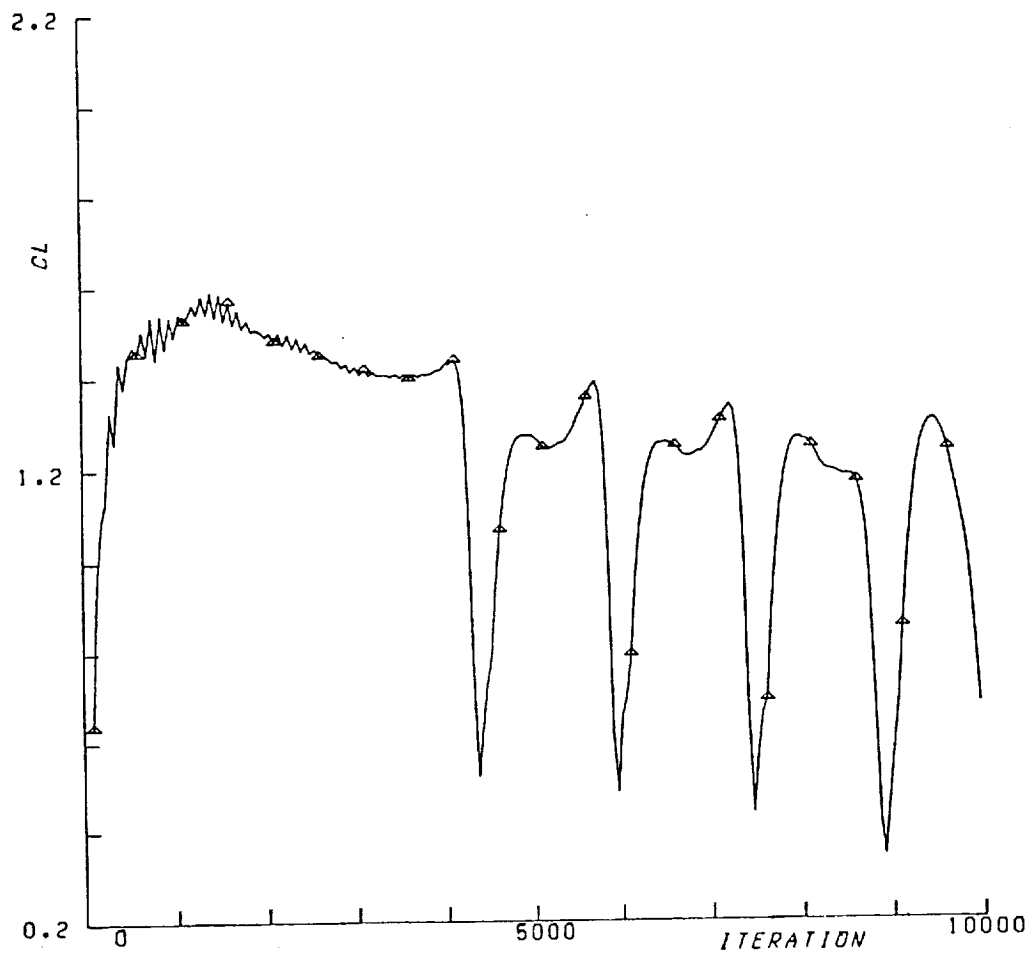
Figure 14   Lift history for run 2 : AOA 15°, $C_1 = 1000$, $C_2 = 5$.
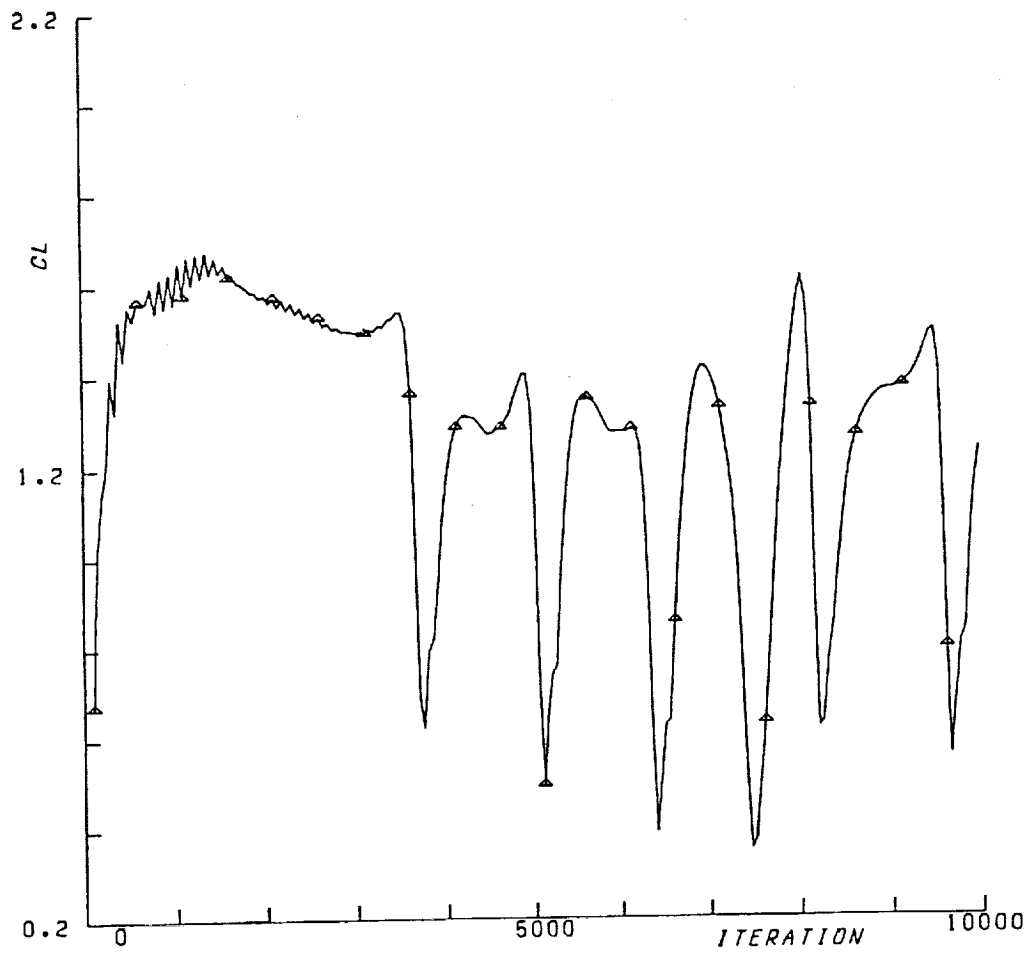
Figure 15   Lift history for run 3 : AOA 16°, $C_1 = 1000$, $C_2 = 5$.

60
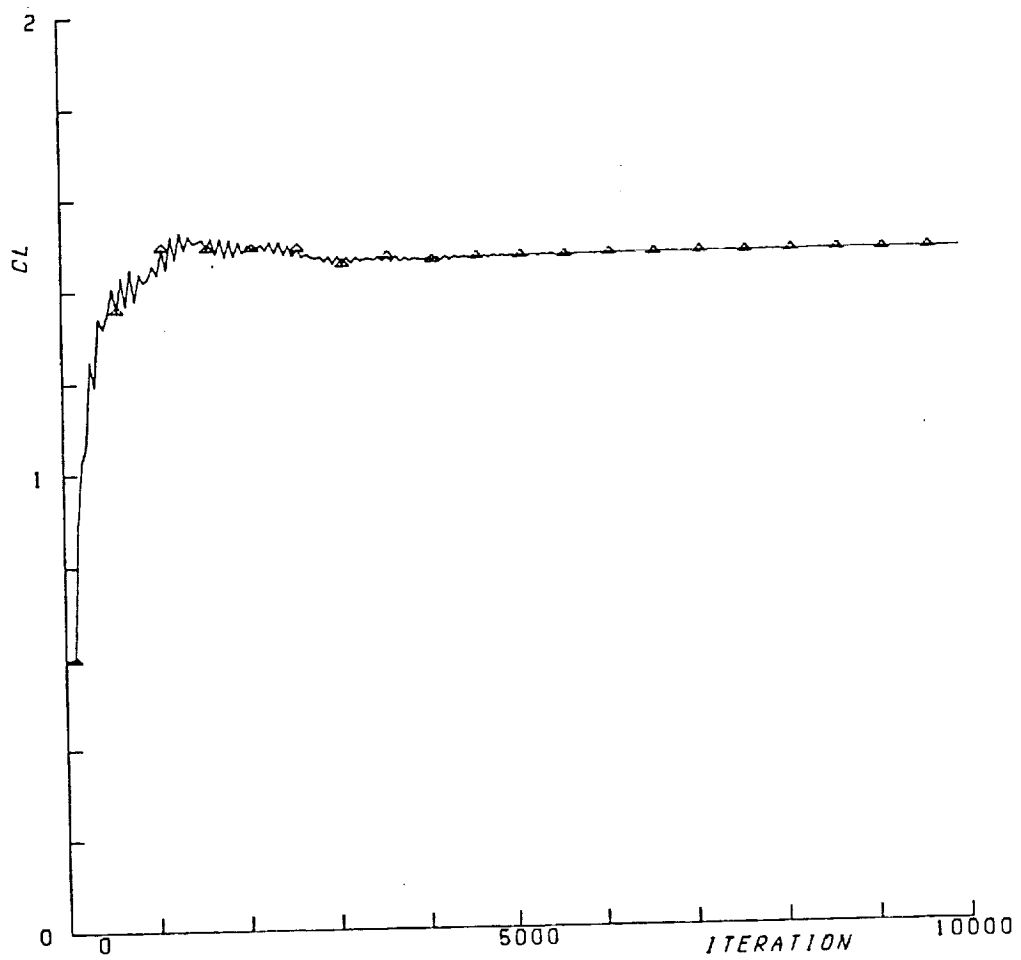
Figure 16　　　Lift history for run 4 : AOA 14°, $C_1 = 2000$, $C_2 = 5$.
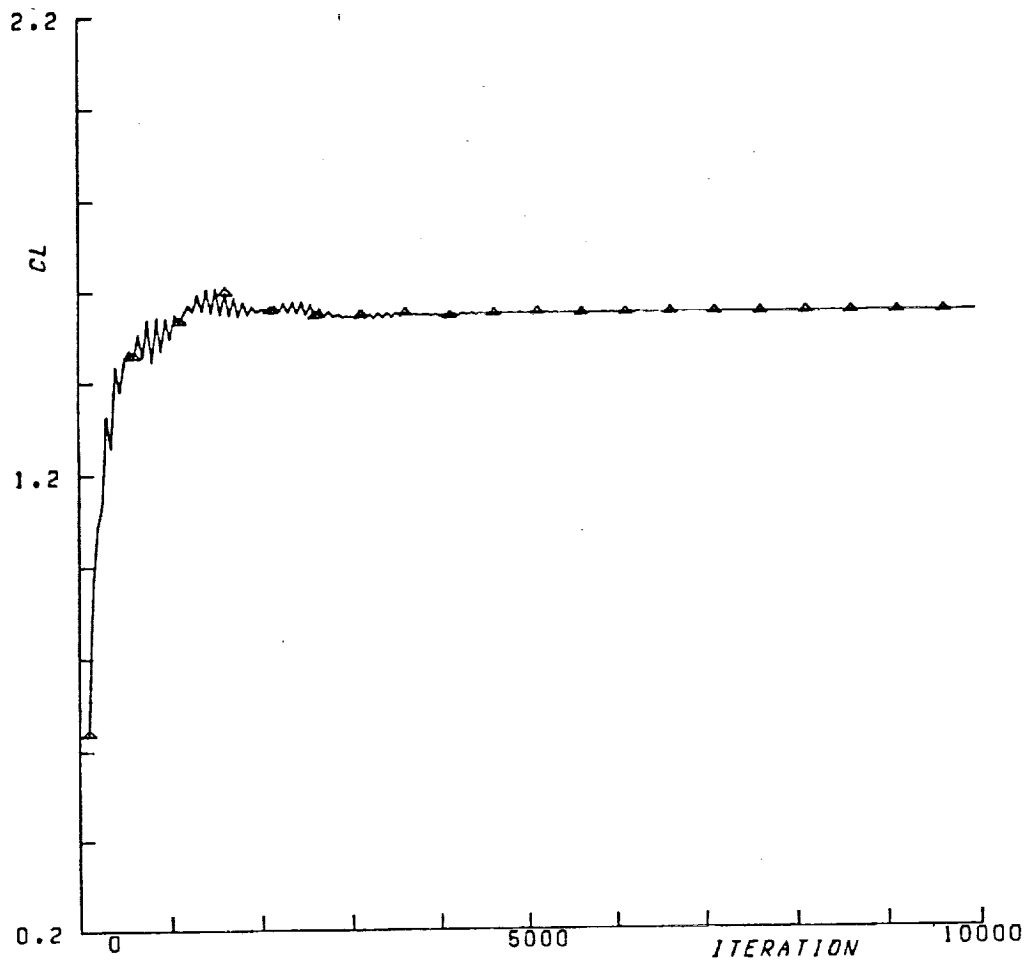
Figure 17   Lift history for run 5 : AOA 15°, $C_1 = 2000$, $C_2 = 5$.
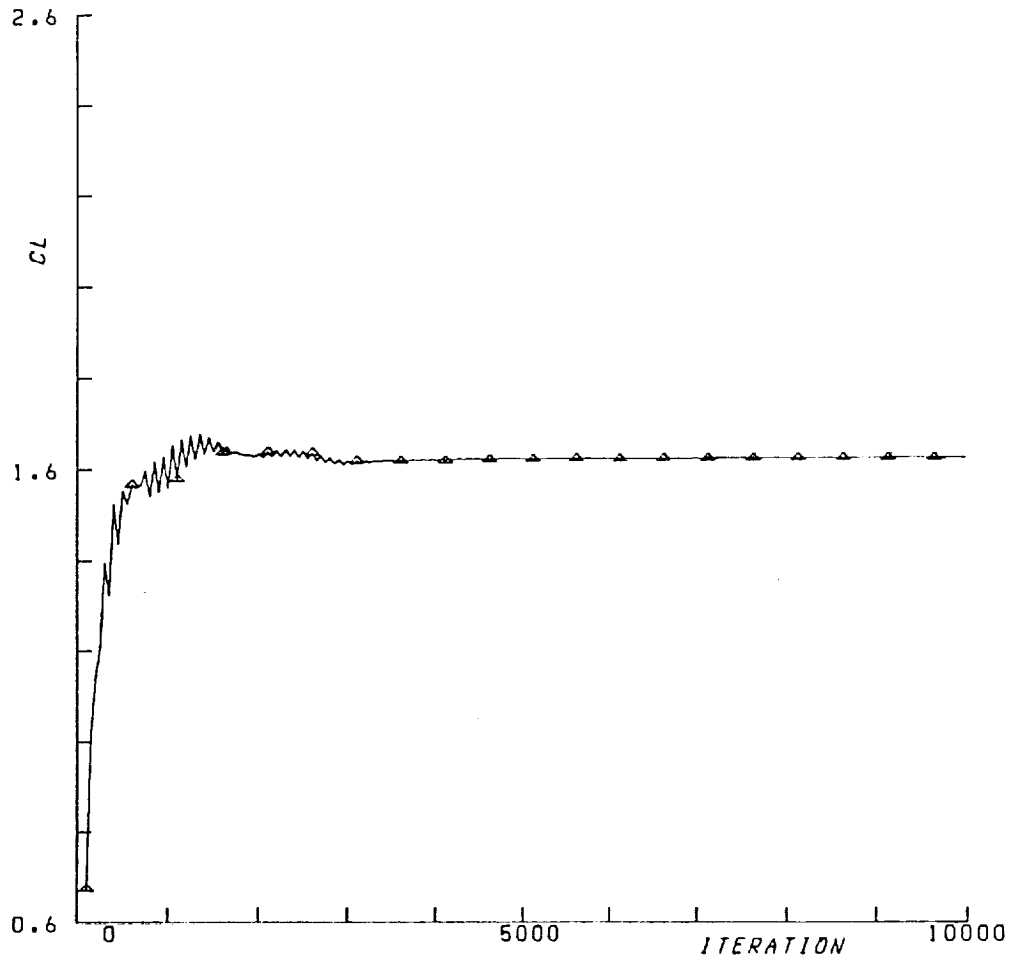
Figure 18   Lift history for run 6 : AOA 16°, $C_1 = 2000$, $C_2 = 5$.
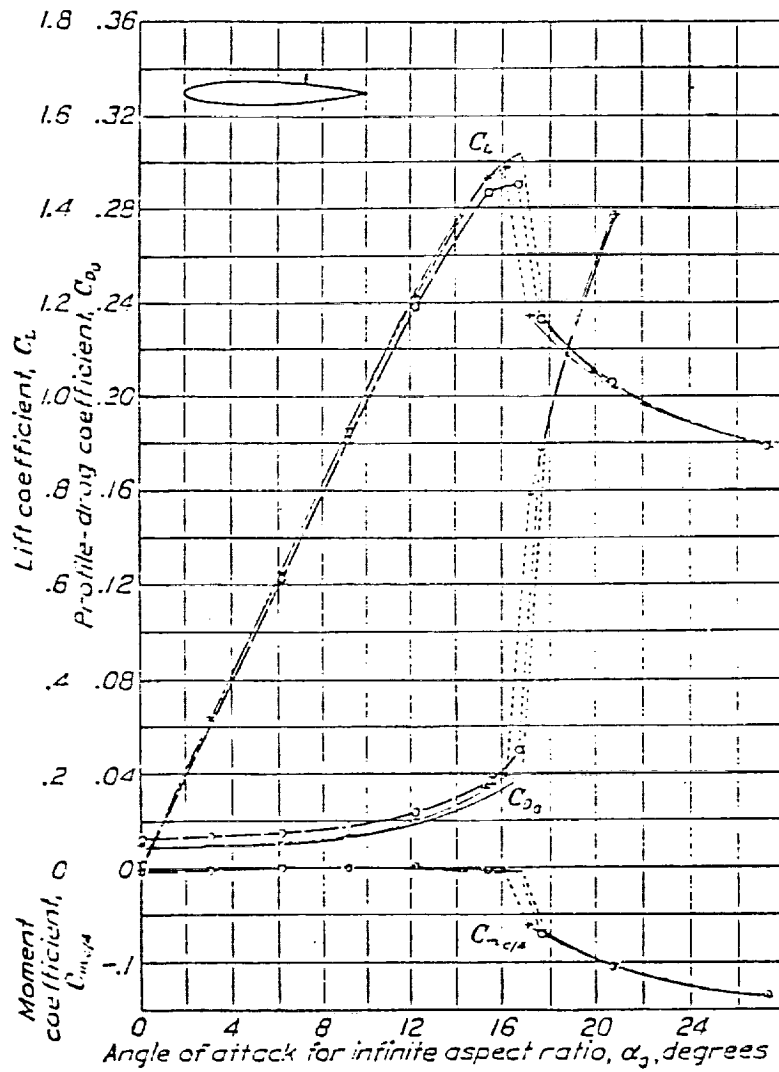
Figure 19   Lift and drag coefficients versus angle of attack for a NACA0012 airfoil.

Taken from NACA TR 446. Data taken from case with 0 protuberance

height.   ——— 0 pro. hgt.,   —o— 0.005 c,   — + —   faired

are a more accurate representation of the flowfield behavior. The value of C_1 will be set to 2000 due to better correlation with the experimental values. The C_2 value can be altered in a similar manner, with the additional effect that the velocity profiles will be altered. At this point, it is not an objective to match the velocity profiles exactly and the C_2 value will be left at 5. The velocity profiles will be discussed later along with considerations of transition location and grid refinement.

The ARC2D code was next used to evaluate the NACA0012 airfoil at 18° AOA. This should be an unsteady result with significant vortex shedding. This unsteady behavior is manifested in the lower C_L value shown in figure 19. The code was run employing the Baldwin-Lomax model, the MML model, and in an all laminar mode. The MML model used values of $C_1 = 2000$ and $C_2 = 5$, as prescribed above. The results examined are the lift histories, stream function contours, and eddy viscosity contours. Additionally the C_L and C_D values are compared to the experimental information from NACA TR 446 [67] in Table 4. The C_L and C_D values are found by time averaging over several periods of the shedding process.

Evaluation Method	C_L	C_D	S_t
Baldwin-Lomax	1.65	0.056	NA
MML	1.35	0.093	0.03
Laminar Flow	1.08	0.223	0.16
Experiment	1.16	0.19	NA

Table 4   Evaluation of turbulence modeling on post-stall performace prediction

Table 4 indicates that the MML model is better able to determine the C_L values for this post-stall behavior than the Baldwin-Lomax model. The MML model and the all laminar case results show reasonable differences from the experimental value, with the laminar case underpredicting and the MML model overpredicting the experimental value. The drag values show similar results. The Baldwin-Lomax model underpredicts drag significantly due to the attached flow behavior predicted using this model. The MML model underpredicts drag by an amount similar to the overprediction resulting from the laminar flow calculation. The laminar flow calculation results in a larger drag value due to the greater frequency of vortex shedding. It seems clear that the MML model performs better than the Baldwin-Lomax model for this case, but perhaps not any better than the use of no turbulence model altogether. The determining factor may be the evaluation of the unsteady vortex shedding phenomena.

The lift histories are shown in figures 20-22. The vortex shedding is indicated by the periodic behavior of these curves. The shedding process can be characterized by the Strouhal number, S_t, which is defined as,

$$S_t = \frac{f \, \mathcal{L} \, \sin(\alpha)}{U_\infty} \tag{4.21}$$

where f is the shedding frequency, $\mathcal{L}$ is the characterisitic length, α is the airfoil angle of attack, and U_∞ is the freestream velocity. For this case the characteristic length is the airfoil chord. The Strouhal numbers obtained from these lift histories are also shown in Table 4.

The Strouhal numbers shown correspond to behavior that has been observed experimentally. The 0.16 value of the laminar flow case is approximately the value seen during bluff-body shedding. The 0.03 value of the MML model case has been documented in

66
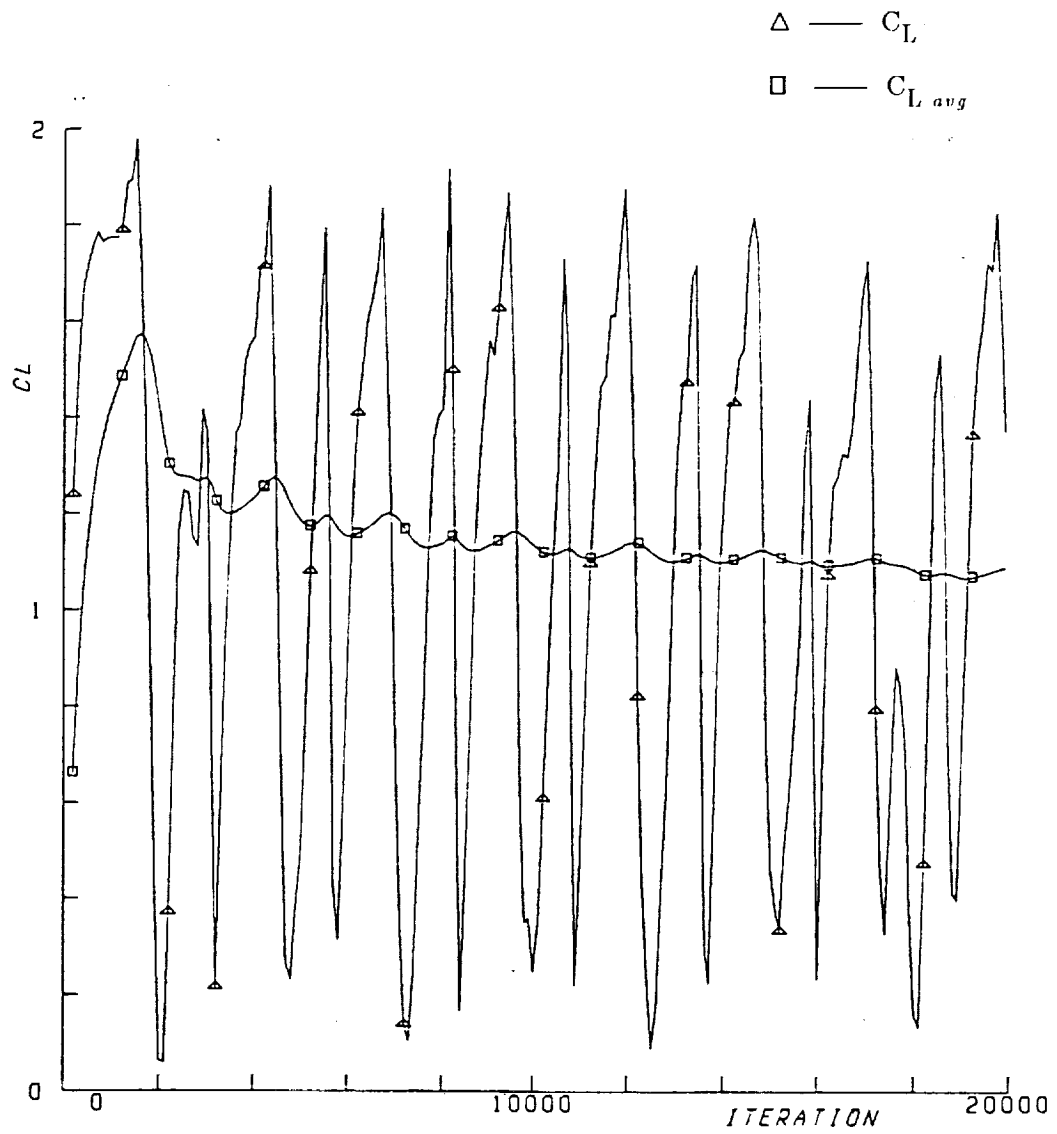
Figure 20   Lift history for NACA0012 airfoil calculation : AOA 18°, Laminar flow.
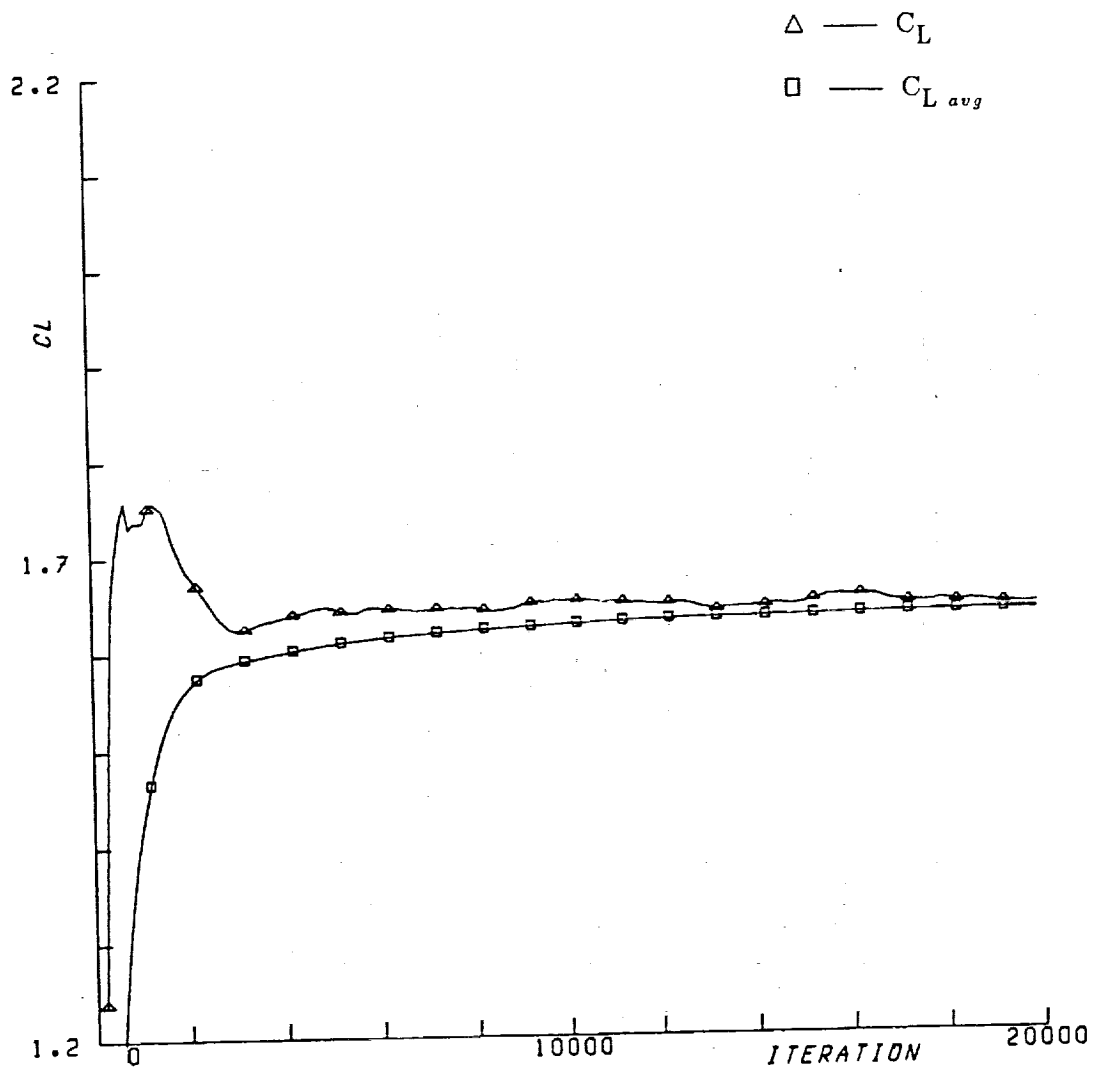
Figure 21   Lift history for NACA0012 airfoil calculation : AOA 18°, Baldwin-Lomax model.
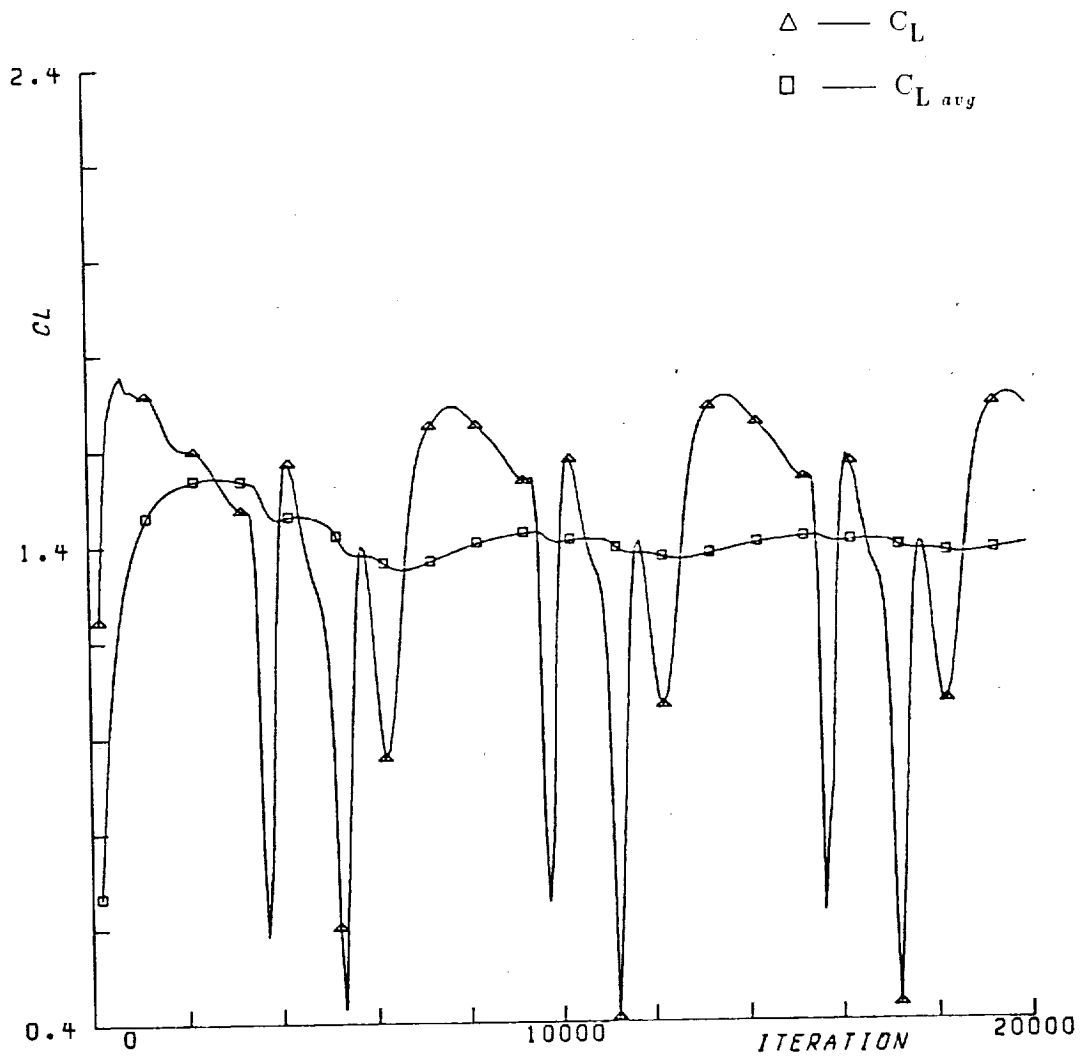
Figure 22   Lift history for NACA0012 airfoil calculation : AOA 18°, MML model.

the work of Zaman and McKinzie [68]. The result obtained from the Baldwin-Lomax model seems to miss the unsteady stall behavior at this AOA entirely. The question of what is appropriate for use in further icing calculations is unclear at this point. A study of this behavior for an iced airfoil geometry is currently underway [69]. Results of that study could shed some light on whether the MML model is operating properly.

Concluding Remarks

The results of the examination of the clean NACA0012 airfoil with the two turbulence models suggests that each model has desirable characteristics. The Baldwin-Lomax model apparently produces drag values somewhat closer to experimental results for low values of AOA. The MML model however, allows modeling of the separated flow characteristic of a stalled airfoil. Certainly, it seems that further comparisons of the two models will be necessary. Evaluation of alternate well-documented airfoil shapes should help to indicate further the strengths and weaknesses of the two models. Particularly, the interaction of turbulence model and velocity gradient at the wall should be examined further. This would require extensive comparisons of the two models to measured values of velocity gradients, pressure coefficient distributions, and integrated force coefficents.

This, however, is not the subject of the present study. For purposes of evaluation of iced airfoil performance, the pressing need is to determine the degradation of airfoil performance and to identify premature stall for a given ice shape profile. These needs translate into two requirements for the computational results. The code must be able to capture the main characteristics of the pre and post stall behavior for the iced airfoil. The pre-stall behavior includes determination of the size and shape of the attached separation bubble aft of the horns and the velocity gradients in that bubble. Additionally, the code must be able to determine the increase in drag and decrease in lift which can result from the

presence of the ice shape and the attached separation bubble. The code must also be able to determine the angle of attack at which the separation bubble detaches from the airfoil and the unsteady shedding process commences. The calculation of the value of $C_{L\ max}$ also requires the code to predict the correct size, strength, and shedding frequency of the vortex which develops at the ice shape horn.

Thus, the choice of turbulence model is still not clear at this point and the need for further testing is indicated. The ability of the MML model to capture the proper unsteady behavior near stall suggests that it may be possible to predict $C_{L\ max}$ using this model. The MML model also does not require selection of a maximum or minimum value of some variable from the mean flow field. This prevents the ambiguities found in the Baldwin-Lomax model for separated flow. The independence of this model from the solution procedure or grid structure should also allow easy transport of this model to alternate flow codes, including unstructured grid methods. The use of these two models will be further examined by using several iced airfoil geometries and will be discussed in the next chapter.

CHAPTER 5

ICED AIRFOIL PERFORMANCE EVALUATION

The tools described and developed in the previous chapters have been used to evalute the performance characteristics of several airfoil and ice shape combinations. The airfoils examined were chosen due to the availability of experimental data for verification purposes. The results for lift and drag coefficients using these airfoils have been calculated using both the Baldwin-Lomax model and MML model. Results indicate that a Navier-Stokes code coupled with the MML model can be used effectively to evaluate airfoil performance degradation due to icing. Calculations at angles of attack below stall indicate steady flow behavior with a recirculation bubble aft of the horns, when these are present in an ice accretion. At higher AOA values, the bubble separates completely and an unsteady vortex shedding process occurs. The MML model allows this process to develop and hence enables calculation of post-stall behavior. Comparisons between the Baldwin-Lomax and MML model for both pre and post stall behavior will be presented. The unsteady post-stall behavior, predicted using the MML model, will be examined in some detail.

The needs of the icing community in regard to an evaluation of iced airfoil flowfields are twofold. Performance information is needed to evaluate the effects of ice accretion. This requires global integrated results such as lift, drag, and moment coefficients. Additionally, the particle trajectory codes and ice accretion codes require information on local velocities and pressures in the iced airfoil flowfields. These local results are also used to gain a greater understanding of the characteristics of iced airfoil aerodynamics. In that regard, stream

function contours, equi-vorticity contours, and eddy viscosity contours are also useful for understanding the aerodynamic phenomena. The results have therefore been organized into the above two categories. For each airfoil/ice shape studied, both the global and local results will be examined in an effort to further understand the modeling capability of the code.

The global results are the most prominent indication of the performance loss due to icing. The experimental results of Bragg, shown in figures 23 and 24, indicate the dramatic loss in lift and increase in drag produced by a glaze ice shape. Examination of these figures indicates that the lift diverges from the clean airfoil values only as the AOA approaches stall. The drag coefficient on the other hand is affected at all values of AOA. This points out the dual effect that ice accretions have on airfoil performance. Both the pressure induced forces and the frictional forces are altered by the presence of the ice accretions. The relative importance of each effect is dependent on the ice shape and the AOA. At low angles of attack, the pressure distribution is affected due to the separation bubbles, however the resulting changes to lift and moment are not significant. The changes to drag values are significant and can be attributed to both pressure and frictional forces. At high angles of attack, the alteration to the pressure distribution is significant and leads to large changes in both quantities.

These integrated force and moment coefficients are obtained by evaluating pressures and friction forces at each grid point on the surface of the airfoil. Both of these surface force values are then resolved into normal and tangential forces which in turn are transformed into lift and drag coefficients based on AOA. Monitoring of the development, with respect to iteration number, of these coefficients is one indication of convergence of the solution. These time histories of the force coefficients are also used to indicate whether a given solution is steady or unsteady. In the case of unsteady behavior, time-averaging of the pressure distribution is used to calculate the resulting forces on the airfoil surface.

73
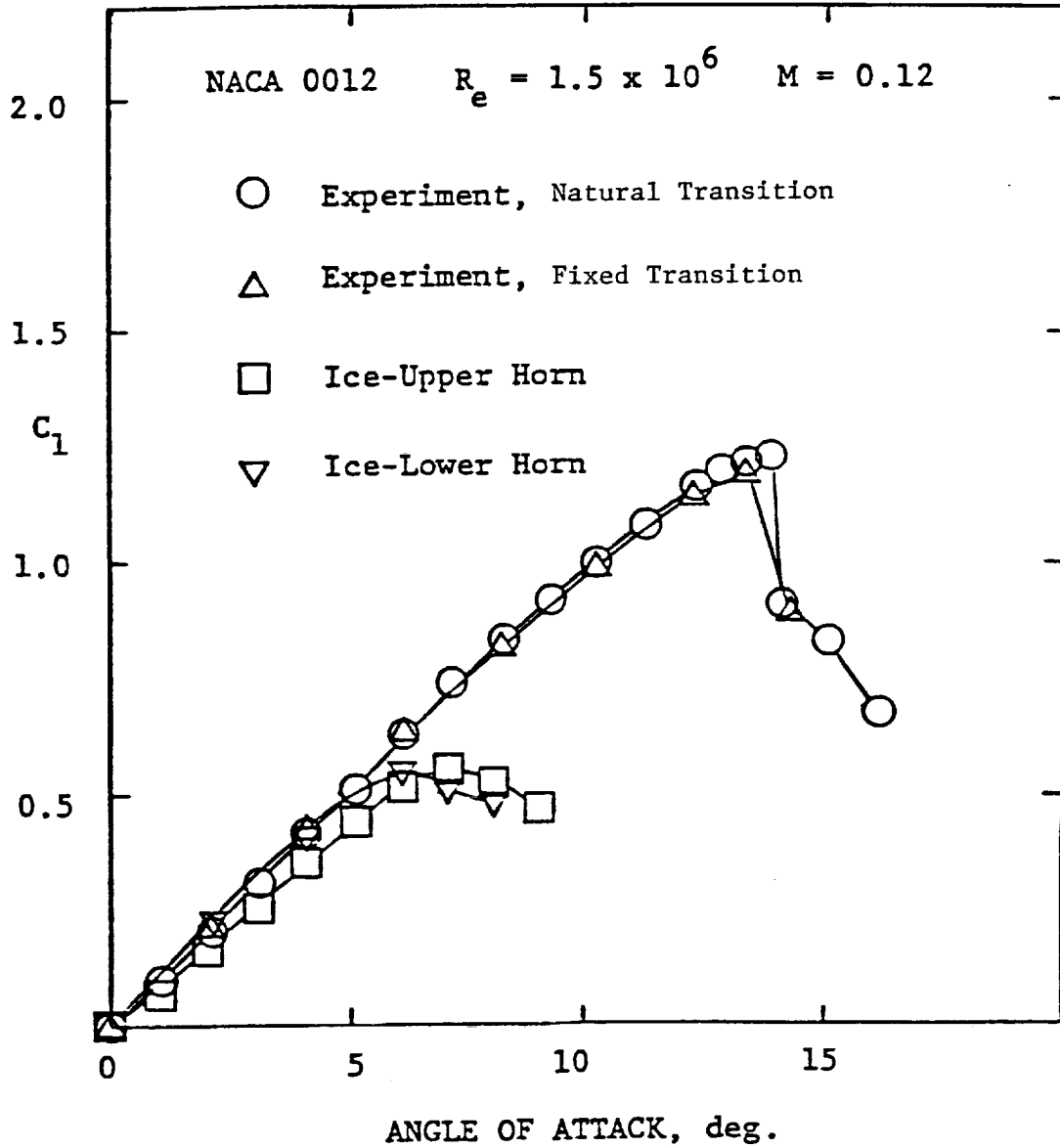
Figure 23 Lift coefficient vs. AOA for a NACA0012 airfoil with artificial glaze ice shape. Experimental results, taken from Bragg [66].
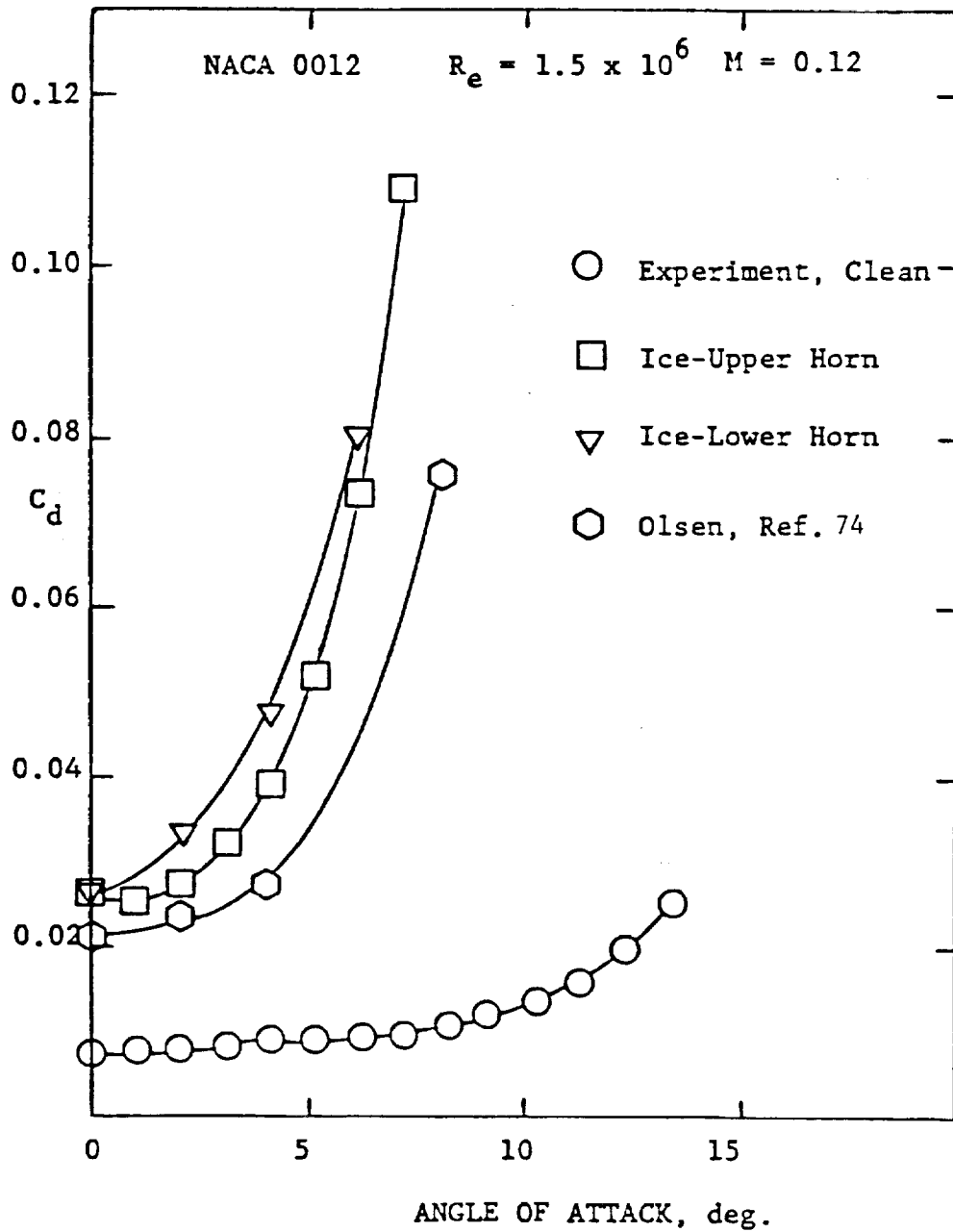
Figure 24 Drag coefficient vs. AOA for a NACA0012 airfoil with artificial glaze ice shape.

Experimental results, taken from Bragg [66].

The flowfield associated with large glaze ice conditions, such as those shown in figures 26 and 27, is characterized by a sizable disturbance to the flow just aft of the horns. This disturbance may or may not cause a significant alteration to the performance of the airfoil depending on the size of the accretion and the AOA of the airfoil. This is demonstrated most noticeably by the larger drop in $C_{L\ max}$ reported by Bragg for the glaze ice profiles. Below the threshold at which stall begins, the alteration of the flow is restricted to the region immediately surrounding the ice accretion. This results in only minor changes to the lift as compared to the clean airfoil. The correct representation of the flowfield at these AOA's is important however from the standpoint of ice shape prediction and accurate determination of the drag.

In order to provide code validation information for these lower AOA conditions, velocity and pressure measurements were taken by Bragg [66] for the NACA0012 airfoil and a glaze ice shape described below. The pressure measurements consisted of a densely packed series of pressure taps along the chord of the model, including the ice shape region and the entire upper and lower surfaces. This allowed very accurate evaluation of the C_p distribution on the airfoil and of the pressure component of the force coefficients. The velocity measurements were taken with a split-film probe which was oriented in such a way as to allow determination of the magnitude and direction of the x-component of velocity. This was essential in evaluating the characteristics of the recirculating flow within the separation bubble aft of the glaze ice horns.

Discussion of the flowfield characteristics at large values of AOA requires the definition of several terms which will be used frequently. The terms used will correspond to the definitions used by Mehta [24]. An attached separation bubble is a region bounded by a stream function contour of zero and the surface. The bifurcation point of the zero stream function contour is the separation point. The point of unification with the surface is the

76

reattachment point. A separation bubble is open or burst if it is not completely enclosed by a zero stream function contour and there is a closed contour within the region. A vortex is a region which is enclosed within equi-vorticity lines. Vortex shedding is the process of detachment of a vortex from the surface and subsequent convection into the free stream.

The unsteady flowfield behavior at large AOA's is the cause of the stall behavior reflected in the $C_{L\ max}$ value and in the divergence of the C_D curve. The three modes of stall; leading edge stall, trailing edge stall, and mixed leading-trailing edge stall; are described by Chang [69]. In the results described below, all three forms of stall have been observed. The ability of the code to indicate the type of stall and its ability to calculate correct force coefficients for these conditions, is evaluated thoroughly for the airfoil/ice shape combinations being considered in this study. A rime ice shape and two glaze ice shapes with two airfoil geometries are evaluated using ARC2D and the two turbulence models.

5.1 Ice shape geometries

The methods developed to evaluate iced airfoil performance must be independent of both the airfoil and ice shape geometry. This suggests that more than just one combination of airfoil and ice shape should be examined in order to increase confidence in the computational results. Unfortunately, there is not a large database of iced airfoil aerodynamic measurements available. The most complete information to date is that of Bragg [66] for the NACA0012 airfoil. Bragg, Zaguli, and Gregorek [70] also measured the performance characteristics of a NACA63$_A$-415 airfoil with rime and glaze ice shapes. The data from these two studies will be used to make comparisons with the computational results.

The data available for the NACA63$_A$-415 airfoil consists of pressure coefficient distributions at several angles of attack along with lift, drag, and moment coefficients for these same AOA's. There was no investigation of the velocity profiles along the surface or in the

77

wake. The data available for the NACA0012 airfoil consists of both types of information just mentioned in addition to normal Reynolds stress $\left(\overline{u'^2} \right)$ profiles at several locations. The force coefficient values for the NACA0012 airfoil are available for AOA's well past stall, while those for the NACA63$_A$-415 are not. Thus, the global results will be presented for all three airfoil/ice-shape geometries while the local results will be concentrated on comparisons using the NACA0012 airfoil.

Rime ice shape for the NACA63$_A$-415

The rime ice shape selected for use with the code corresponds to the R7 ice shape, described by Bragg et al. [70], and is shown in figure 25. This shape was selected for analysis because it appeared to have the profile least altered by the ice accretion. Indeed, at high AOA's, this shape increased the lift of the airfoil over the range measured. This shape actually seemed to act as a leading edge flap. It was thus felt that this shape would provide an interesting test for the computational method.

Glaze ice shape for the NACA63$_A$-415

The glaze ice shape selected for use with the code corresponds to the G3 ice shape, described by Bragg et al. [70], and is shown in figure 26. This shape was selected as a test for both the GRAPE code and the ARC2D code. The large concave region provided a critical test for the grid generation code. If this shape can be modeled accurately, then it is expected that the GRAPE code will be sufficient for the evaluation of most ice shapes. The large stagnation region between the horns and the rapid acceleration around these structures should also provide an important test of the ARC2D code.
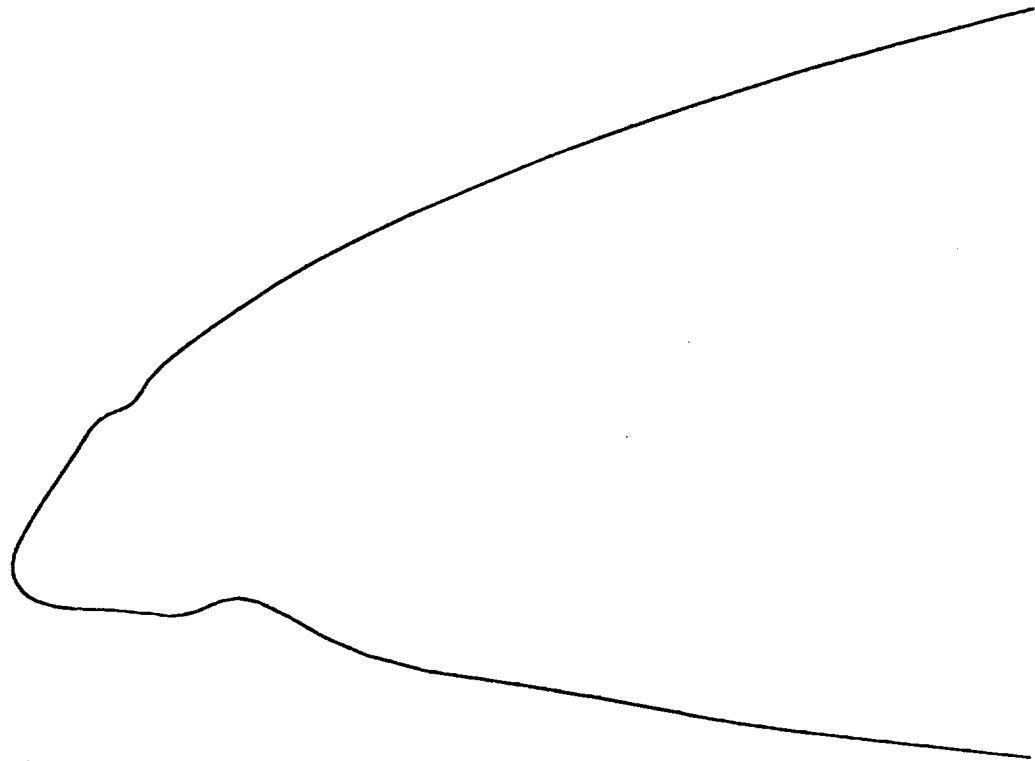
(a)
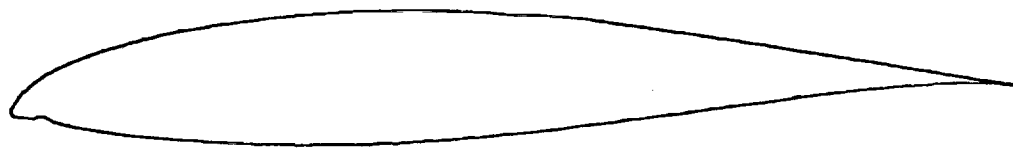
(b)

Figure 25 Rime ice shape for the NACA63$_A$- 415 airfoil. (a) Close-up of leading edge.
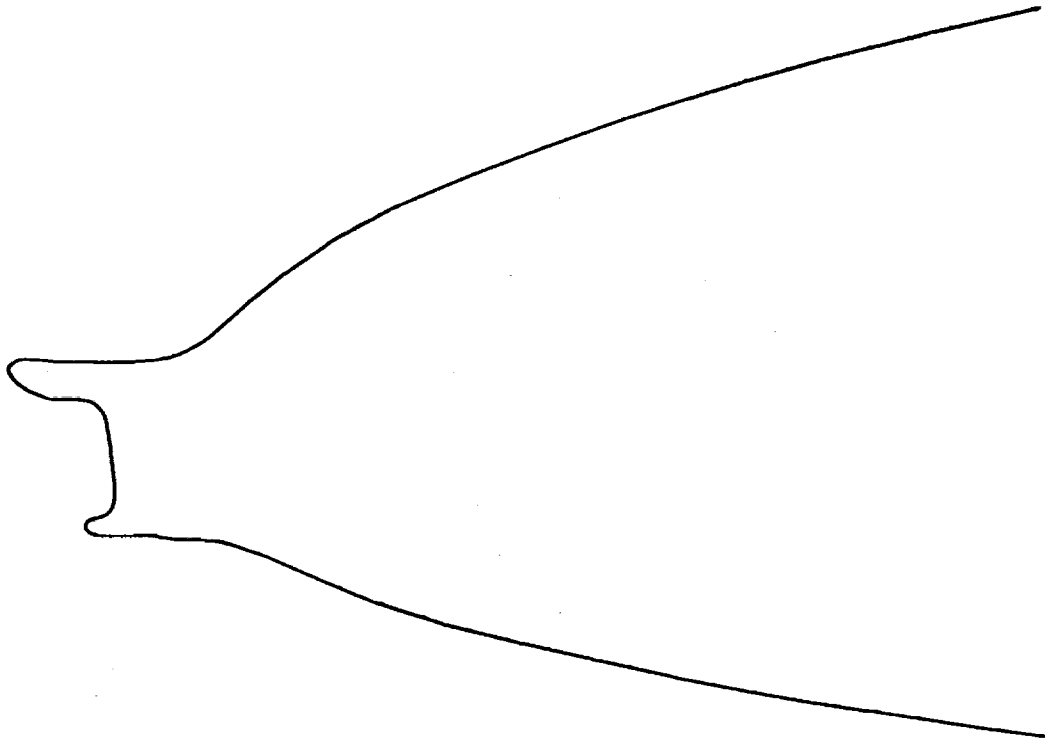
(b) Overall profile.

(a)

(b)

Figure 26 Glaze ice shape for the NACA63$_A$- 415 airfoil. (a) Close-up of leading edge.

(b) Overall profile.

Glaze ice shape for the NACA0012

This shape is the only ice geometry employed in Bragg's later study [66] and represents a 5-minute glaze ice accretion. In this case, the geometry was a simulated ice shape and is shown in figure 27. This shape will be referred to as the G1 ice shape. The well-defined geometry, consisting of circular arcs and line segments, facillitates modeling in performance codes and allows for incorporation of the geometric detail deemed appropriate by the analyst. This geometry is the result of a coordination of effort between experimentalist and analyst typical of the icing program at NASA.

5.2 Evaluation of Iced Airfoil Calculations

This section examines the results of the ARC2D calculations for the ice shape geometries just defined. Comparisons are made to experimental information where available. The two turbulence models are compared in order to determine if there is any advantage obtained by use of the MML model for separated flow calculations.

NACA63$_A$-415, R7 ice shape

This shape was tested in the NASA IRT wind tunnel and was run at a nominal Reynolds number of 5×10^6 and a nominal Mach number of 0.14. The data were taken up to an AOA of 14.6 degrees. Comparisons between data and computations for C_L and C_D are shown in figures 28 and 29 respectively. Computed results are shown for both the Baldwin-Lomax and MML turbulence models.

The lift calculations agree remarkably well with the experimental results up to an AOA of approximately 12.5°. The value of $C_{L\ max}$ was not determined experimentally for this shape. As seen in figure 28, the measured lift continues to increase over all AOA's evaluated, with the exception of the value at 13.6° AOA. Examination of the pressure coefficient
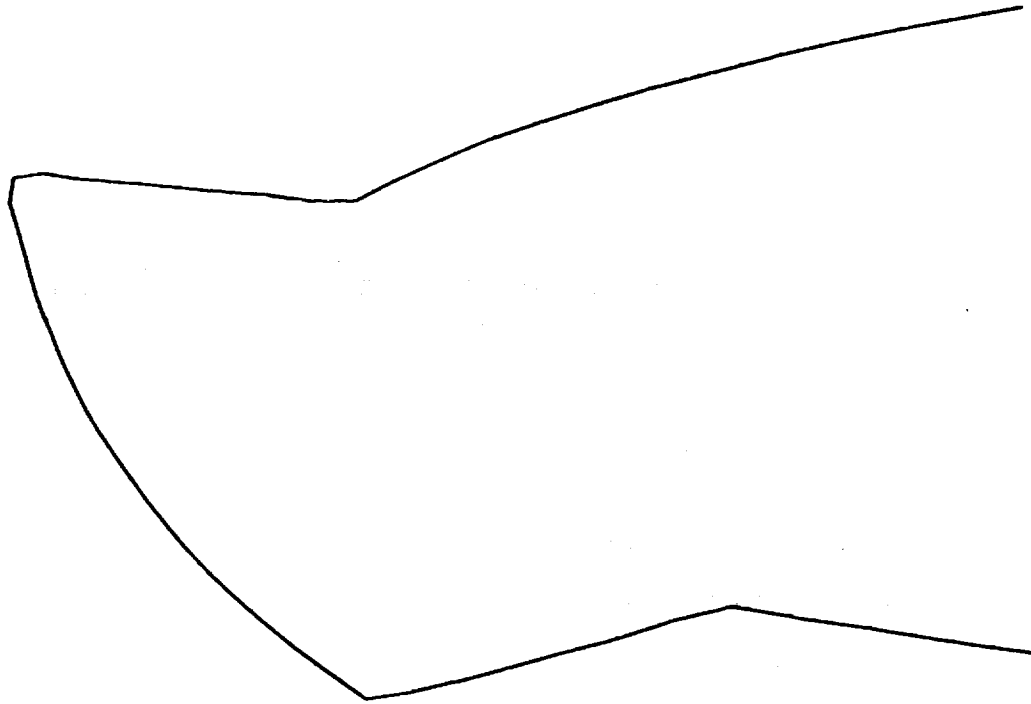
(a)
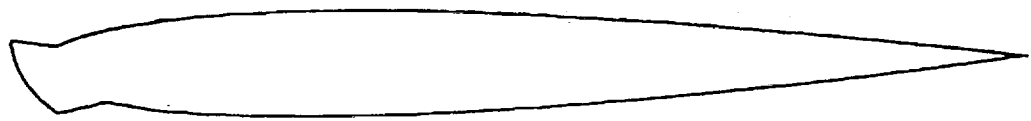
(b)

Figure 27 Glaze ice shape for the NACA0012 airfoil. (a) Close-up of leading edge.

(b) Overall profile.
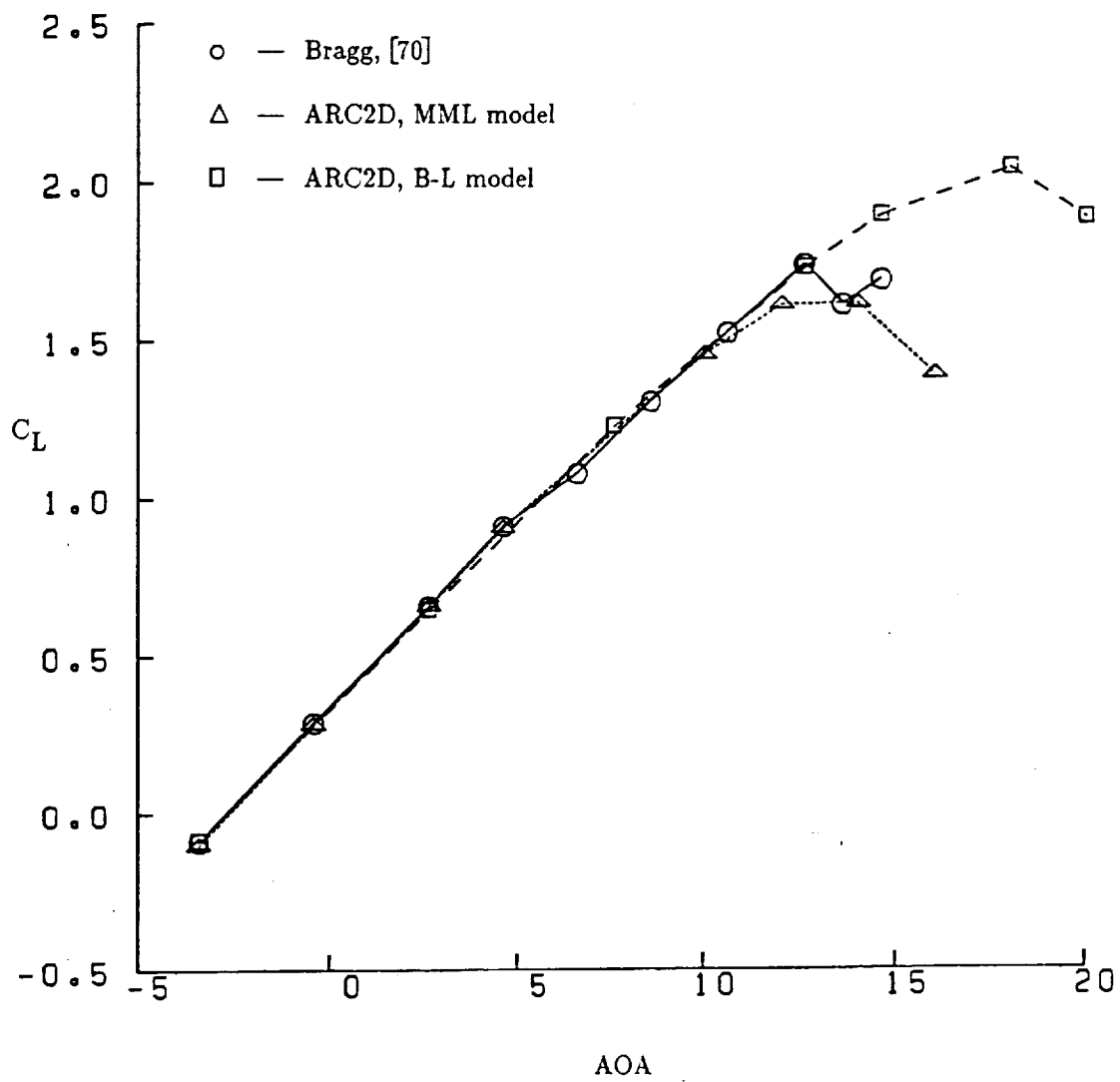
Figure 28 Lift coefficient vs. AOA for NACA63$_A$- 415 airfoil with R7 ice shape.

Comparison of ARC2D results using both turbulence models to

experimental results of Bragg.
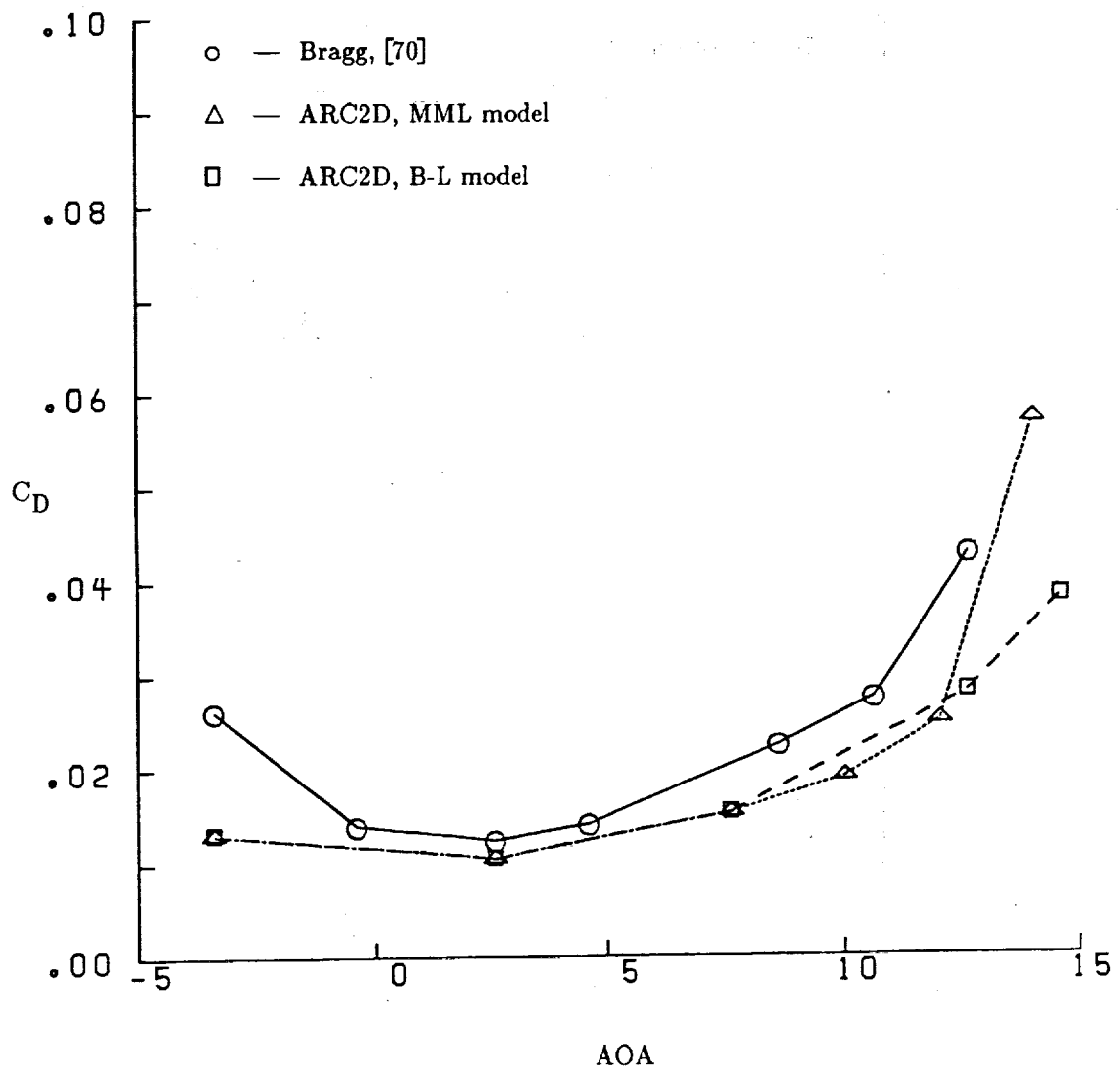
Figure 29 Drag coefficient vs. AOA for NACA63$_A$- 415 airfoil with R7 ice shape.

Comparison of ARC2D results using both turbulence models to

experimental results of Bragg.

distributions for this airfoil at AOA values near 13.6°, as seen in figures 30-32, does not indicate a collapse of the pressure peak near the leading edge nor is a trailing edge separation indicated. It is suspected that some error in the evaluation of the data has resulted in this low C_L value. As a consequence of this experimental behavior, the ARC2D calculations were performed in the steady-state mode for AOA values up to 13°.

If, however, the value of $C_{L\ max}$ were desired, a time-accurate calculation at larger AOA would be required. This was attempted using both models and resulted in the upper part of the C_L curves shown in figure 28. As seen, the Baldwin-Lomax model produces a $C_{L\ max}$ of 18° AOA while the MML model yields a value of 14°. It would be interesting to determine which prediction produces a more accurate $C_{L\ max}$ value. In any case, this is a first attempt at prediction of iced airfoil performance prior to experiment.

The drag values shown in figure 29 indicate good agreement between calculation and experiment. The two turbulence models agree well except at large AOA values where the MML model appears to give higher values. This is due to earlier separation predicted by the MML model. The C_D values at low AOA's are slightly underpredicted by both calculations. Poor resolution of the near-wall behavior is most likely at fault. Use of a smaller grid spacing near the wall is suggested. It is anticipated that alteration of the C_2 value in equation (4.13) of the MML model may also affect the velocity gradient since this value alters the rate at which the mixing length approaches its limiting value. Future studies of these effects are suggested in order to verify this speculation.

The type of stall that occurs for this airfoil and ice shape is indicated by examination of the C_p distribution and stream function contours for results past $C_{L\ max}$. The pressure distribution shows no drop in the pressure peak near the leading edge, as seen in figure 33. There is however a significant bulging of the C_p values near the trailing edge. Thus, a trailing edge separation is indicated. In fact, examination of the stream function contours, figure 34,
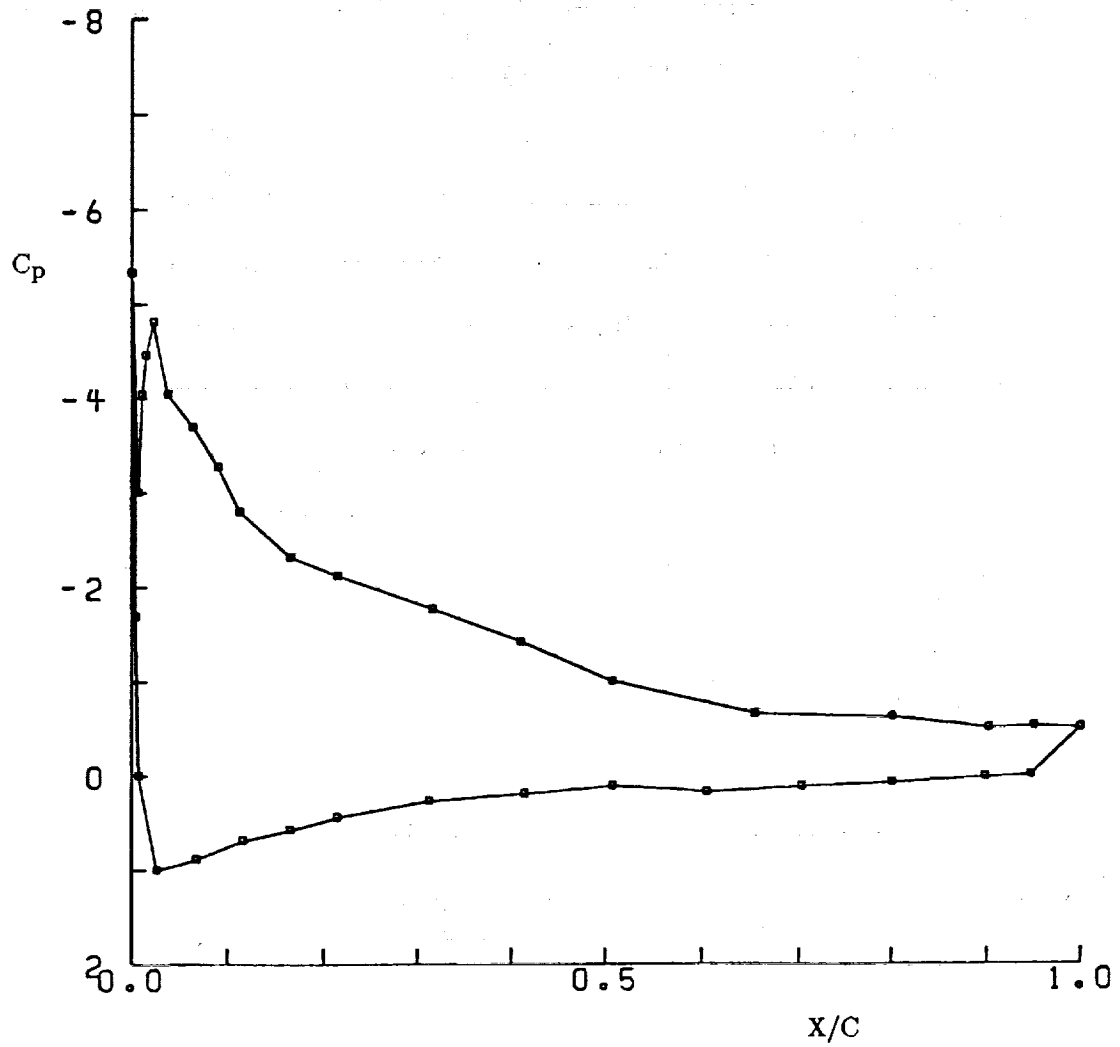
Figure 30 Pressure coefficient distribution for $NACA63_A$- 415 airfoil with R7 ice shape.

$M_\infty = 0.14$, Re $= 5.0 \times 10^6$, AOA $= 12.6°$. Bragg [70]
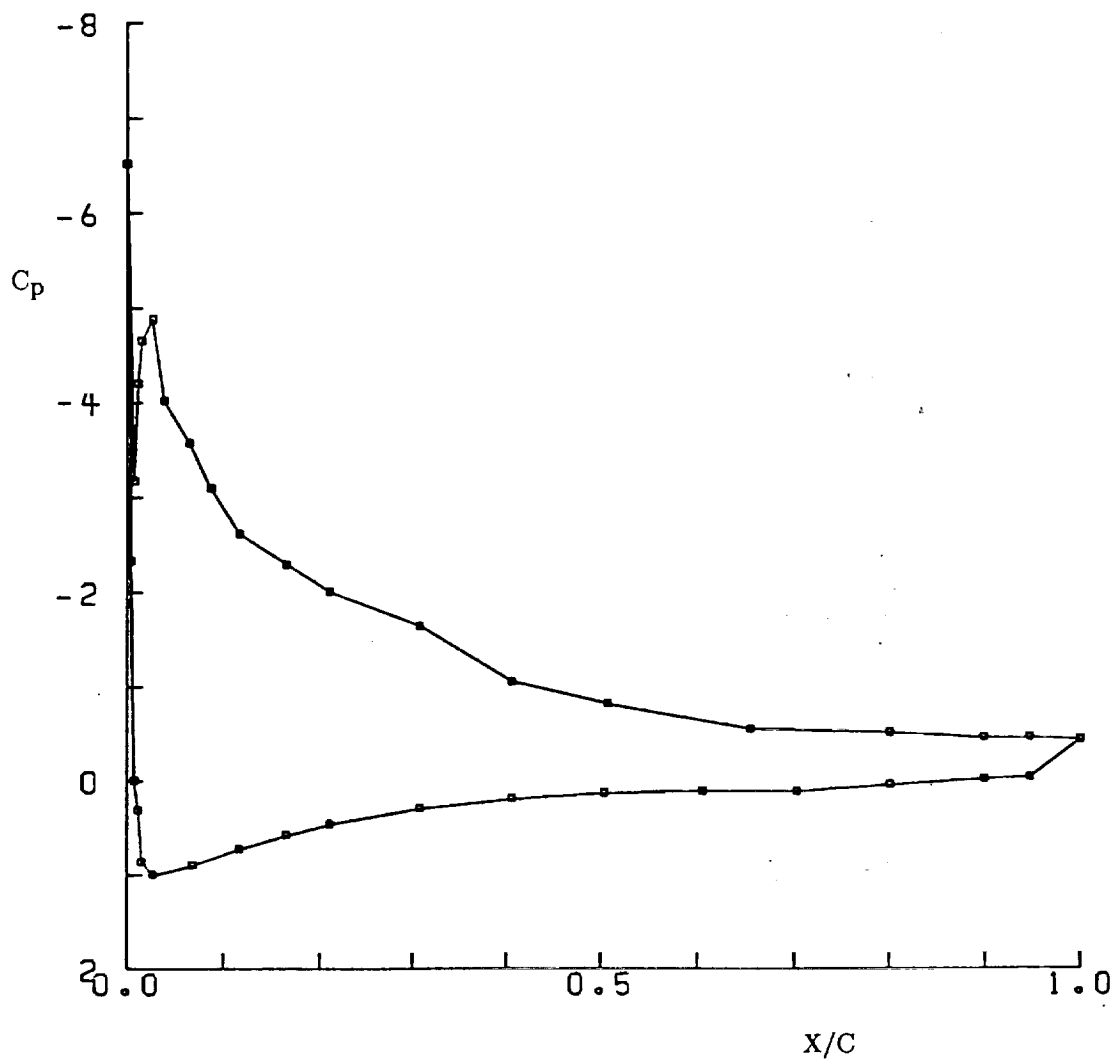
Figure 31 Pressure coefficient distribution for NACA63$_A$- 415 airfoil with R7 ice shape.

$M_\infty = 0.14$, Re $= 5.0 \times 10^6$, AOA $= 13.6°$. Bragg [70]
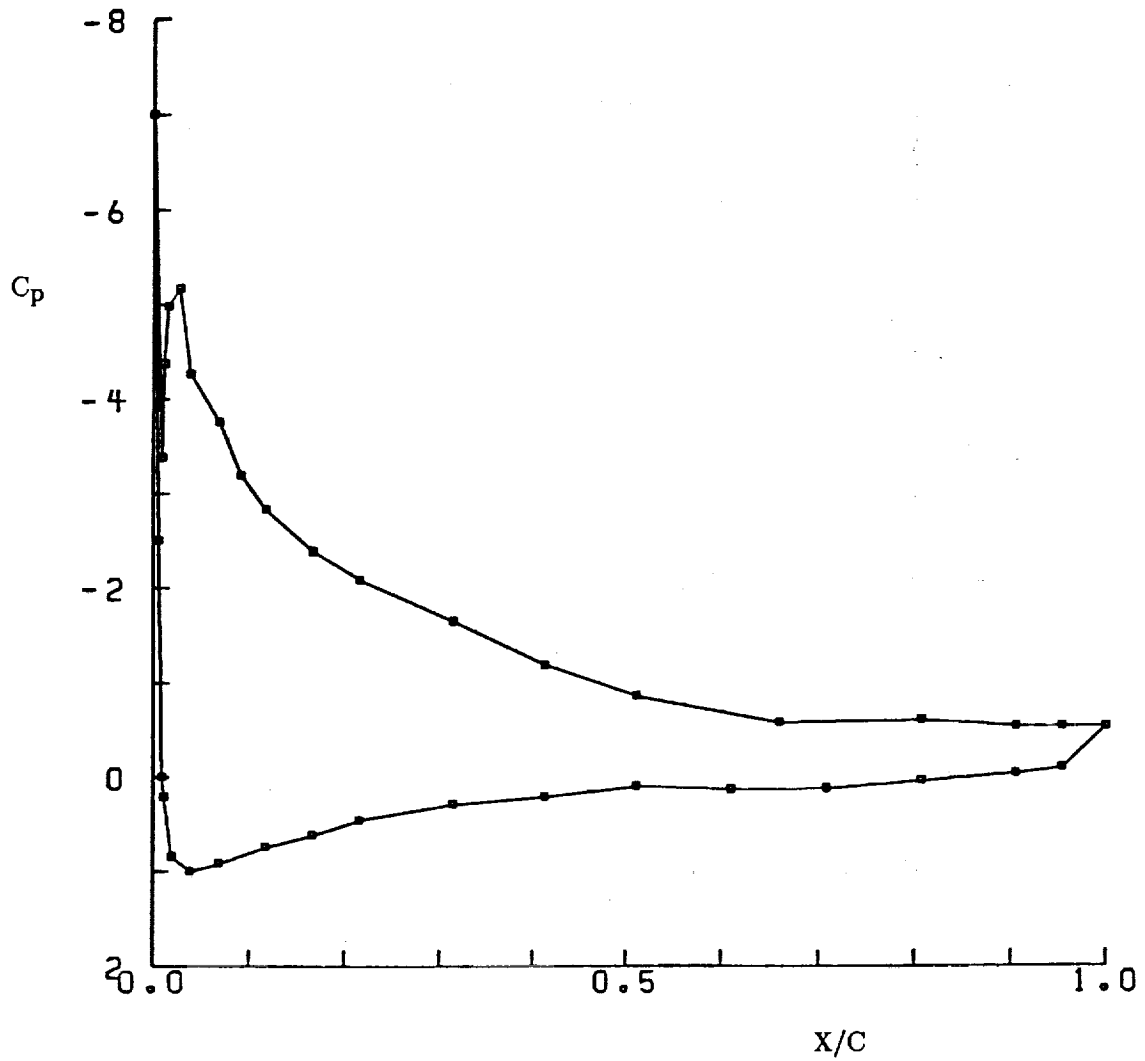
Figure 32   Pressure coefficient distribution for NACA63$_A$- 415 airfoil with R7 ice shape.

$M_\infty = 0.14$, Re = 5.0×10^6, AOA = 14.6°.   Bragg [70]
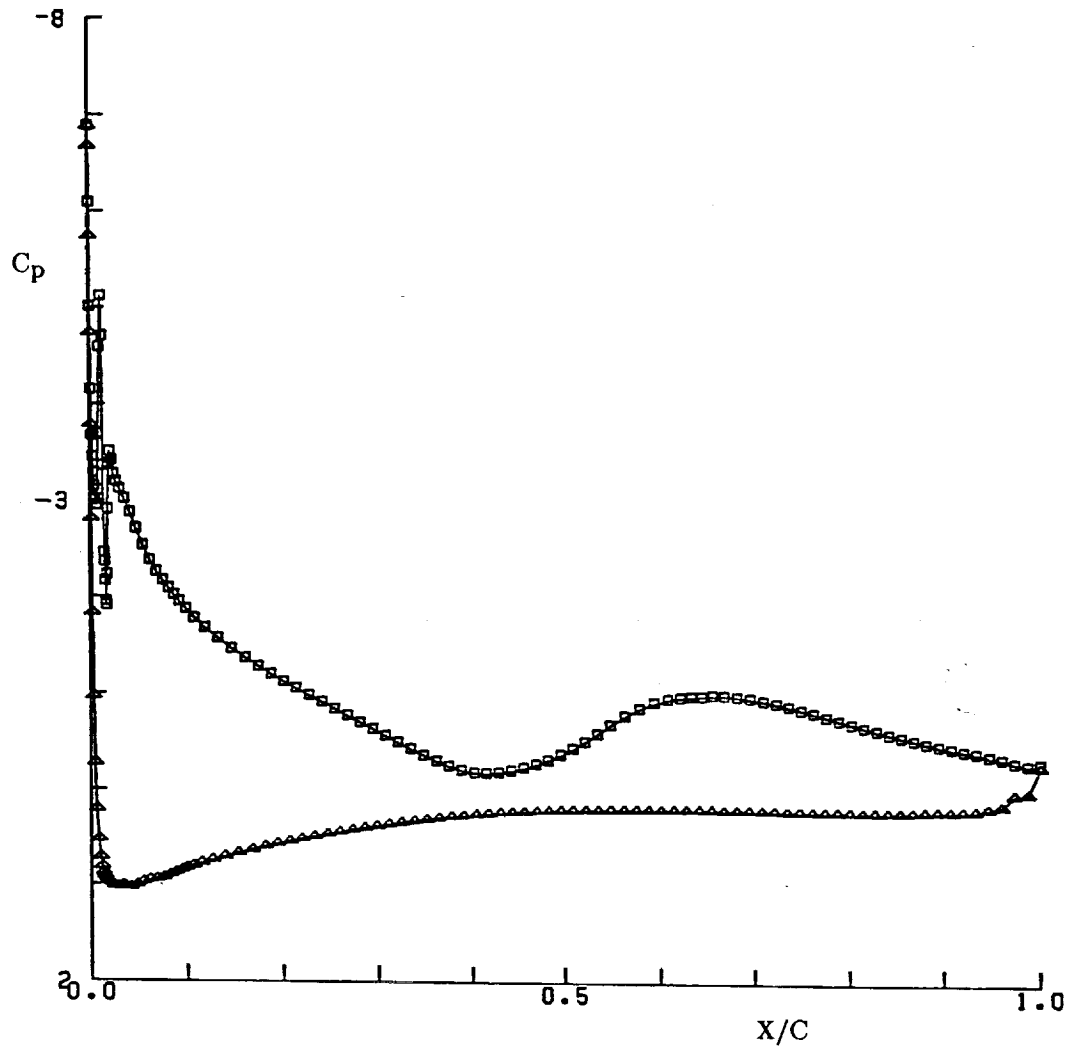
Figure 33 Pressure coefficient distribution for NACA63$_A$- 415 airfoil with R7 ice shape.

$M_\infty = 0.14$, Re $= 5.0 \times 10^6$, AOA $= 16°$.
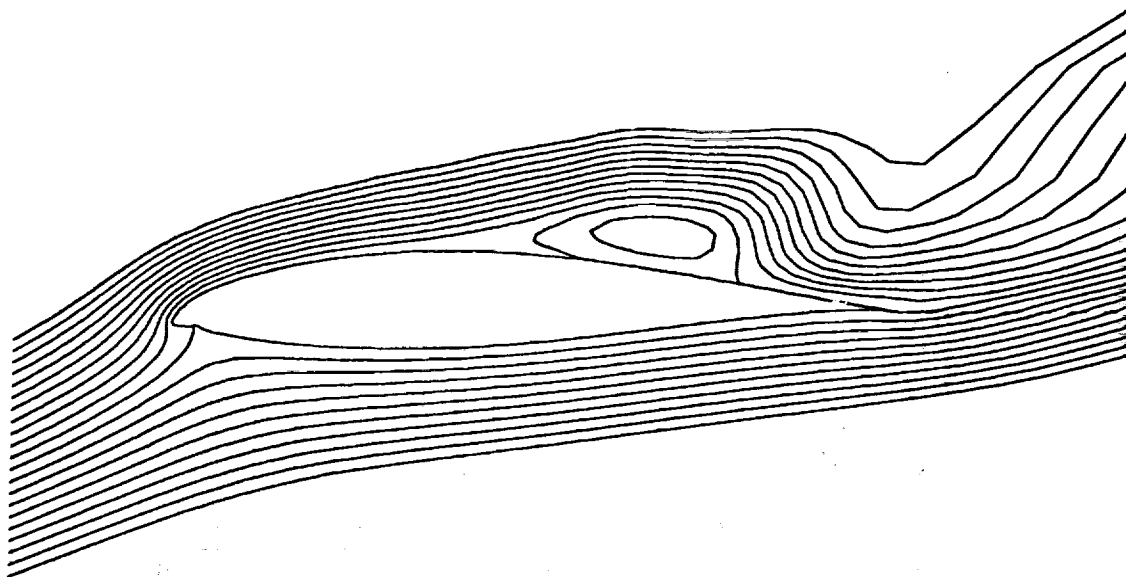
Figure 34 Stream function contours for the NACA63$_A$ - 415 airfoil with R7 ice shape.

AOA = 16°.

plainly indicates the existance of a reverse flow region at the trailing edge. This behavior is evident with either turbulence model. However, the Baldwin-Lomax model suppresses this behavior until 18° AOA, while the MML model indicates separation at a lower AOA.

The contours of eddy viscosity at these AOA's indicate why this occurs. The Baldwin-Lomax model produces $(\mu_t/\mu)_{max}$ values of approximately 2000, as seen in figure 35(a), with the largest values being centered inside the reverse flow region. The MML model produces $(\mu_t/\mu)_{max}$ values of approximately 1000, as seen in figure 35(b), with the largest values being centerd at the separation region. The larger values of the Baldwin-Lomax model tend to suppress the development of these separation regions and results in delayed prediction of stall. The relaxation of eddy viscosity values aft of the separation point, as found with use of the MML model, allows for development of the reverse flow region. This in turn, results in prediction of the physically correct lower stall angle.

NACA63$_\mathrm{A}$-415, G3 ice shape

This shape was also tested in the NASA IRT wind tunnel with nominal Reynolds and Mach numbers of 5×10^6 and 0.14 respectively. The data was taken for AOA values up to 11.6°. The experimental drag values are only available for AOA values up to 7.6°, due to limitations in the test procedure. Comparisons between data and computations for C_L and C_D are shown in figures 36 and 37 respectively with computed results for both the Baldwin-Lomax and MML models included.

The lift coeffcents do not agree well with the experiment for this shape. Both models predict lower C_L values than experiment for AOA values from 6° to 12°. The Baldwin-Lomax model starts to yield values of C_L higher than the experimental value at 12° AOA. The computed results indicate separation at this AOA. As in the case of the R7 ice shape, the two turbulence models yield significantly different flowfields. The Baldwin-Lomax model

91

$$\left(\frac{\mu_t}{\mu}\right)_{max} \approx 2000$$

U_∞

(a)

$$\left(\frac{\mu_t}{\mu}\right)_{max} \approx 1000$$

U_∞

(b)
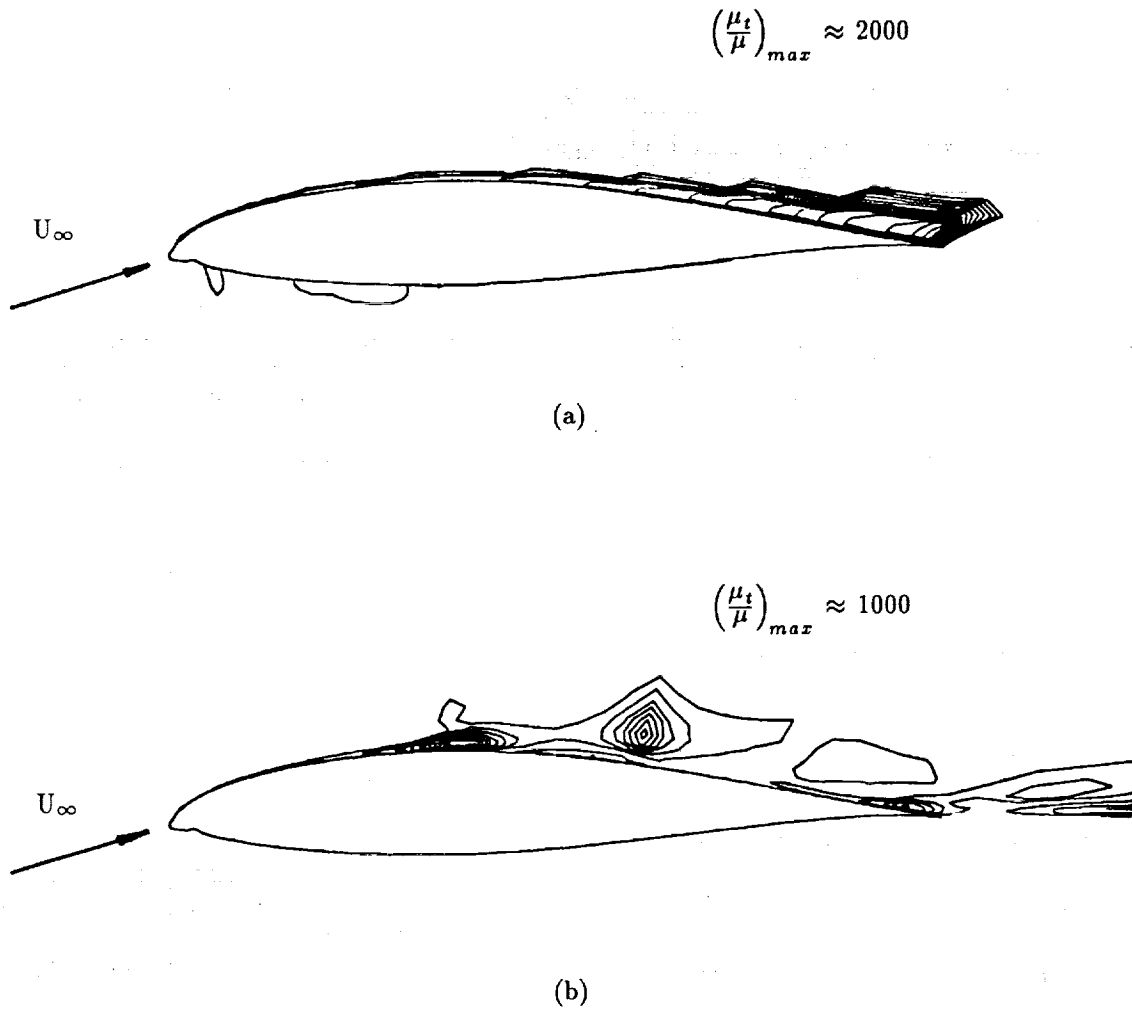
Figure 35 Eddy viscosity contours for the NACA63$_A$- 415 airfoil with R7 ice shape, AOA = 16°, (a) Baldwin-Lomax model, (b) MML model.
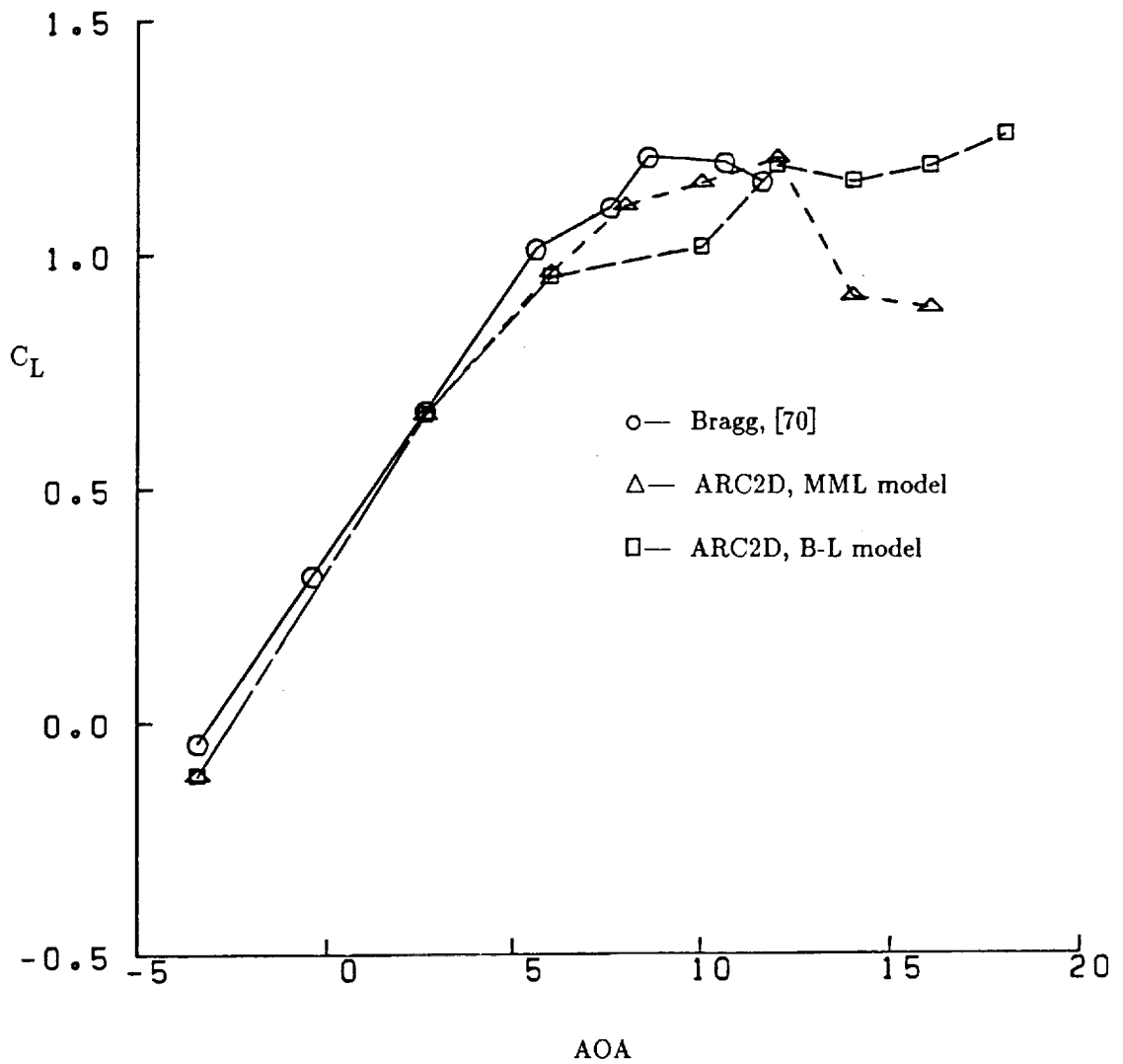
Figure 36 Lift coefficient vs. AOA for NACA63$_A$- 415 airfoil with G3 ice shape.

Comparison of ARC2D results using both turbulence models to

experimental results of Bragg.

93
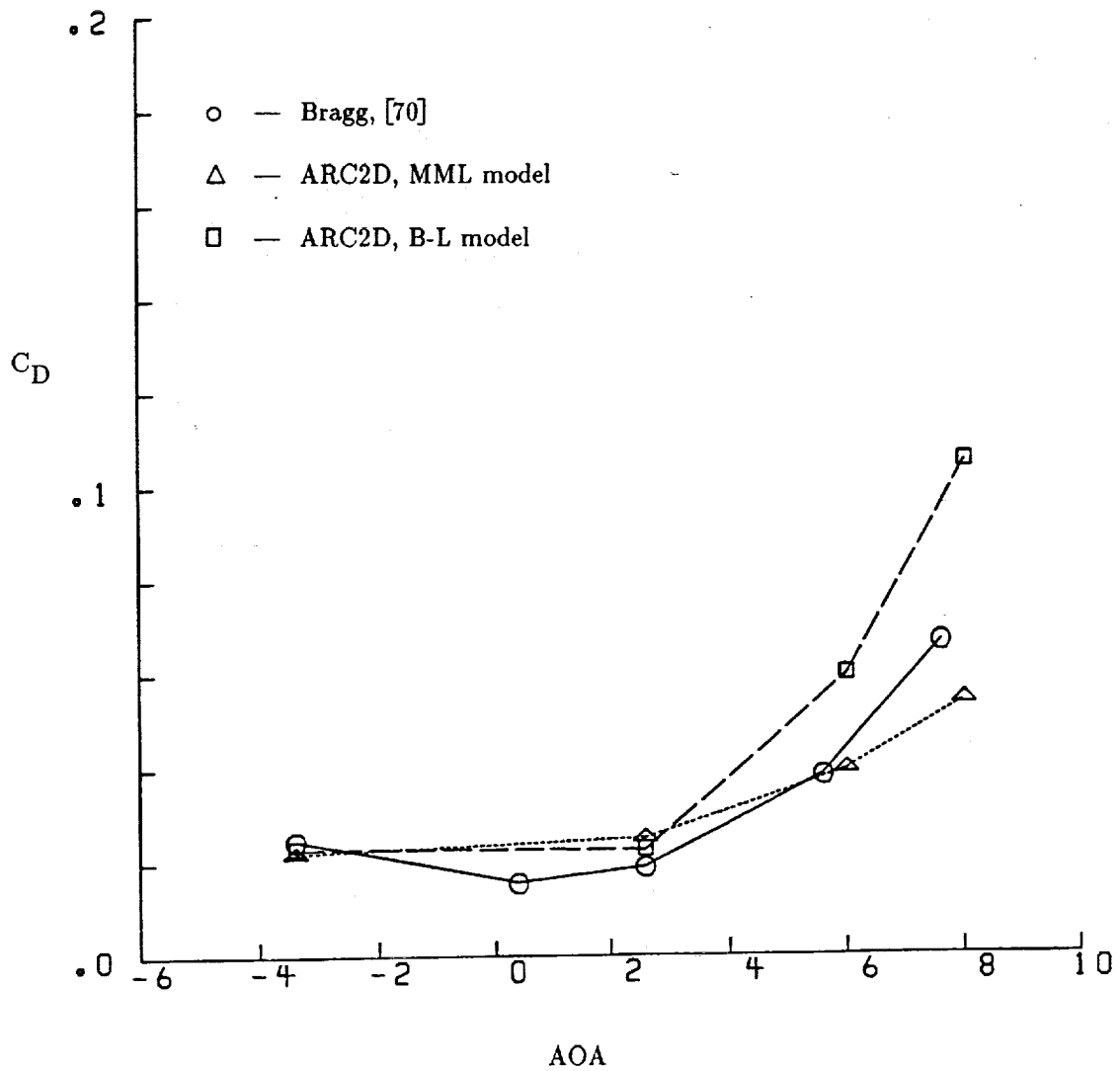
Figure 37 Drag coefficient vs. AOA for NACA63$_A$- 415 airfoil with G3 ice shape.

Comparison of ARC2D results using both turbulence models to

experimental results of Bragg.

produces a much smaller separation region than the MML model. This is again due to the differences in magnitude and distribution of eddy viscosity values as calculated by the alternate models. The μ_t values determine the size of the boundary layer, which in turn influences the pressure distribution on the airfoil and hence the force coefficient values for these flow conditions. Additionally, these dissimilar turbulent viscosities produce different values of C_f, which can result in further differences of the force coefficients.

The computational results, using both turbulence models for AOA at $C_{L\ max}$, are compared to experiment in Table 5.

	$C_{L\ max}$	AOA
Experiment	1.2	8.6
Baldwin - Lomax	1.25	18.0
MML Model	0.94	12.0

Table 5   Calculated stall conditions using either turbulence model.

Comparison to experimental conditions.

As these values indicate, the stall angle is more accurately evaluated by use of the MML model. The value of $C_{L\ max}$ is found by the Baldwin-Lomax model but this would seem to be fortuitous, since it is at the wrong angle of attack. The reason for this result is somewhat different than for the previous case. The maximum values of μ_t obtained with the MML

a-2

model are approximately 2500 and are distributed throughout the flowfield, as seen in figure 38(b). The Baldwin-Lomax model, on the other hand, produces values which are close to 10 in some regions (i.e. near the leading and trailing edges) and close to 10,000 in other regions (i.e. at mid-chord locations), as seen in figure 38(a). This large variation in μ_t values corresponds to the motion of the separation bubble over the surface. The small values are due to selection of F_{max} at a very small y value, while the large μ_t values are due to selection of F_{max} at a very large y value. The MML model, on the other hand, tends to correctly concentrate μ_t values in regions of high vorticity. This results in a more realistic distribution of μ_t throughout the flowfield. A similar μ_t distribution is seen in the results of Majumdar and Rodi [71] for circular cylinders.

Interestingly, calculations using either turbulence model indicate the same mode of stall behavior. This is seen in figure 39(a) which shows the stream function contours for 8° AOA, that is, just prior to stall. The figure shows two separation regions on the airfoil at both the leading and trailing edge. This corresponds to the C_p distribution obtained by Bragg, as shown in figure 40. As the AOA increases, the size of both these regions increases. Finally, at 10°-12° AOA, the two recirculation regions join and stall occurs, as shown in figures 39 (b) and (c). These results are from the use of the MML model. The Baldwin-Lomax model produces similar results, except at higher AOA values.

The C_p distribution obtained using the MML model at 8° AOA is also shown in figure 40. As seen, the pressure distributions indicate that the calculated leading edge separation bubble is smaller than the measured bubble. This in turn alters the pressure distribution downstream of the leading edge. Evidently this leads to a larger calculated separation region at the trailing edge than actually occurs. Also, the influence of the trailing edge separation appears to alter the lower surface pressure distribution in that region. All of these differences lead to a much lower value of lift than measurements indicate.

$$\left(\frac{\mu_t}{\mu}\right)_{max} \approx 10,000$$

U_∞

(a)

$$\left(\frac{\mu_t}{\mu}\right)_{max} \approx 2500$$

U_∞
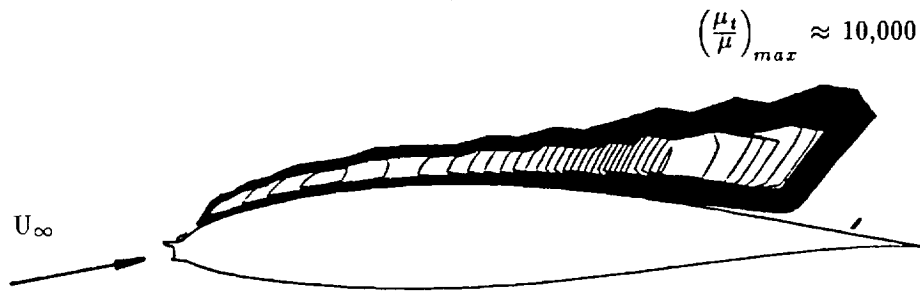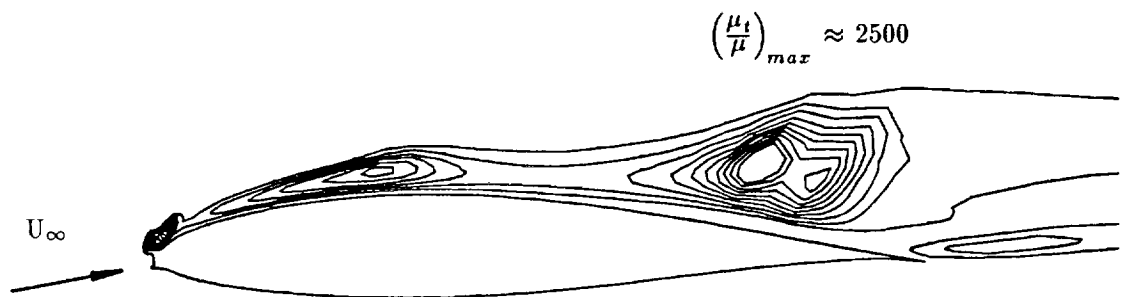
(b)

Figure 38 Eddy viscosity contours for the NACA63$_A$- 415 airfoil with G3 ice shape, AOA = 10°, (a) Baldwin-Lomax model, (b) MML model.

(a)

(b)

(c)
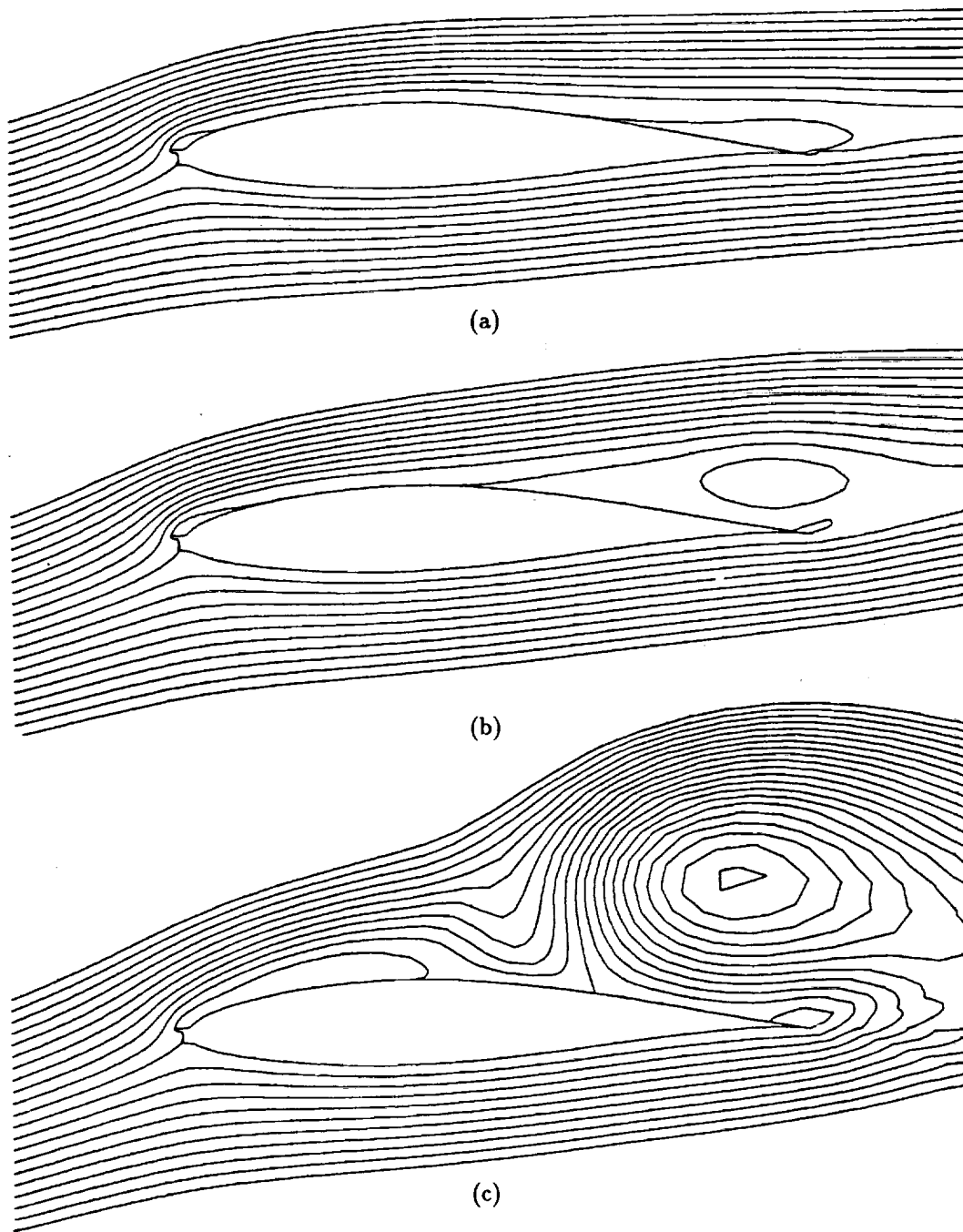
Figure 39 Stream function contours for the NACA63$_A$- 415 airfoil with G3 ice shape.

(a) 8° AOA, (b) 10° AOA, (c) 12° AOA
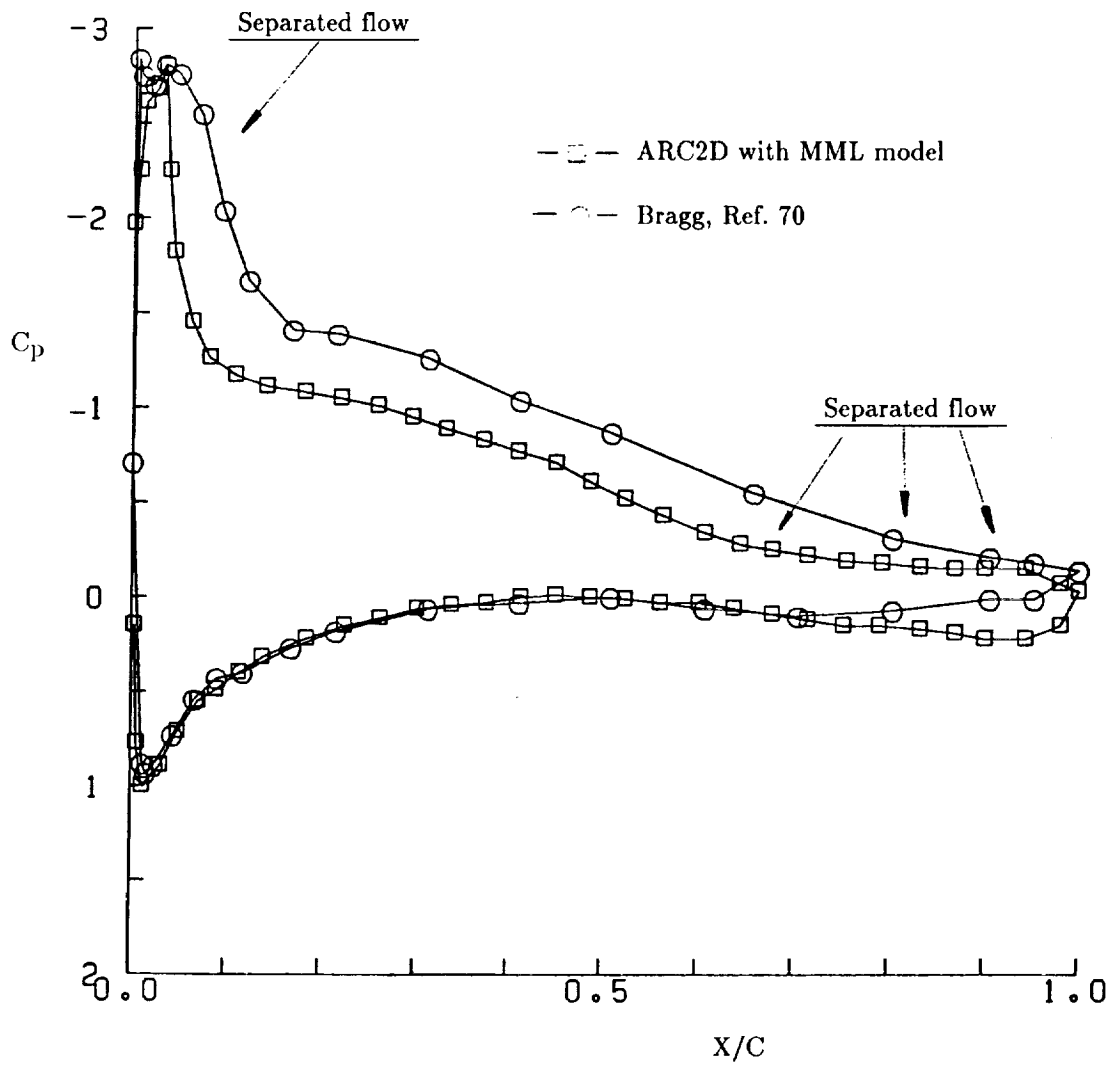
Figure 40 Pressure coefficient distribution for NACA63$_A$- 415 airfoil with G3 ice shape.

$M_\infty = 0.14$, Re $= 5.0\times10^6$, AOA $= 8°$.

The inaccuracy of the C_p values near the leading edge may be produced by a lack of grid resolution in the separation bubble region. The complex nature of the flowfield in this region requires a significant number of points in both the streamwise and transverse directions. The measured pressure values imply a local edge velocity somewhat lower than for an attached flow case. The calculated values do not reflect this behavior and indicate that the local edge velocities are close to those for attached flow. Yet, the stream function contours in figure 39(a) plainly indicate that a separation region has been calculated. The measured results also imply that the velocity gradient is close to zero in this region. The calculated results indicate a large value for the velocity gradient and thus a strong reverse flow region is suspected. Comparisons of velocities in this region are not available for this airfoil, but they were measured for the next case and will be discussed further in the next section.

Despite the differences shown in the lift values, the drag results show a remarkable degree of agreement. At the largest AOA's, the Baldwin-Lomax model produces drag values higher than the measured values. This is due to the large values of μ_t calculated by this model. The pressure drag is not a major factor for the Baldwin-Lomax calculations since the flow has not separated at the AOA values shown in the figure. The lower values of the MML model are a result of lower μ_t values and seem to reproduce the measured values very well. The inaccuracies in modeling the separation bubble may be the reason for disagreement between the MML model and experiment at these lower AOA values. At higher AOA values, the flow separates and the C_D values are dominated by pressure forces. Experimental drag values were not obtained at these higher angle of attack conditions and thus no comparisons could be made.

The results of this section indicate that the difficulties in modeling separated flow behavior may lie in the grid resolution in those regions where separation occurs, such as the leading edge horn, and in the turbulence modeling. More detailed information on the velocities

in these regions could help in diagnosing the problems in the calculations. A more detailed dataset was obtained in the test by Bragg [66] on a NACA 0012 airfoil. Results of the ARC2D calculations will be compared to Bragg's data in the next section.

NACA0012, G1 ice shape

This artificial ice shape was tested by Bragg [66] at the Ohio State subsonic wind tunnel. His tests were conducted at a nominal Reynolds number of 1.4×10^6 and a nominal Mach number of 0.12. The results of this experimental program included lift and drag data as well as pressure distributions and velocity profiles. The lift values were obtained by integration of the pressure data over the surface of the airfoil. The drag data was obtained from a total pressure survey made in the airfoil wake. Comparisons between the experimental C_L and C_D values and the computed results are shown in Figs. 41 and 42. Both the Baldwin-Lomax and MML models were used.

The lift results indicate the differences between the two turbulence models. The Baldwin-Lomax model predicts continued increase of the lift past the experimental $C_{L_{max}}$ value. At 8° AOA, the MML model predicts unsteady vortex shedding while the Baldwin-Lomax model predicts a large attached recirculation bubble resulting in the higher C_L value. At 10° AOA, both models predict unsteady behavior but with different C_L and C_D values. This is due to the large value of the pressure peak associated with the recirculation region being shed from the upper surface. The pressure peak predicted by the MML model is smaller and when integrated with respect to time produces more reasonable lift and drag values for the ice shape/airfoil combination.

The size of the recirculation region can be altered by changing the values of C_1 and C_2 in the MML model, as shown in the study of the clean NACA0012 airfoil. This indicates

101
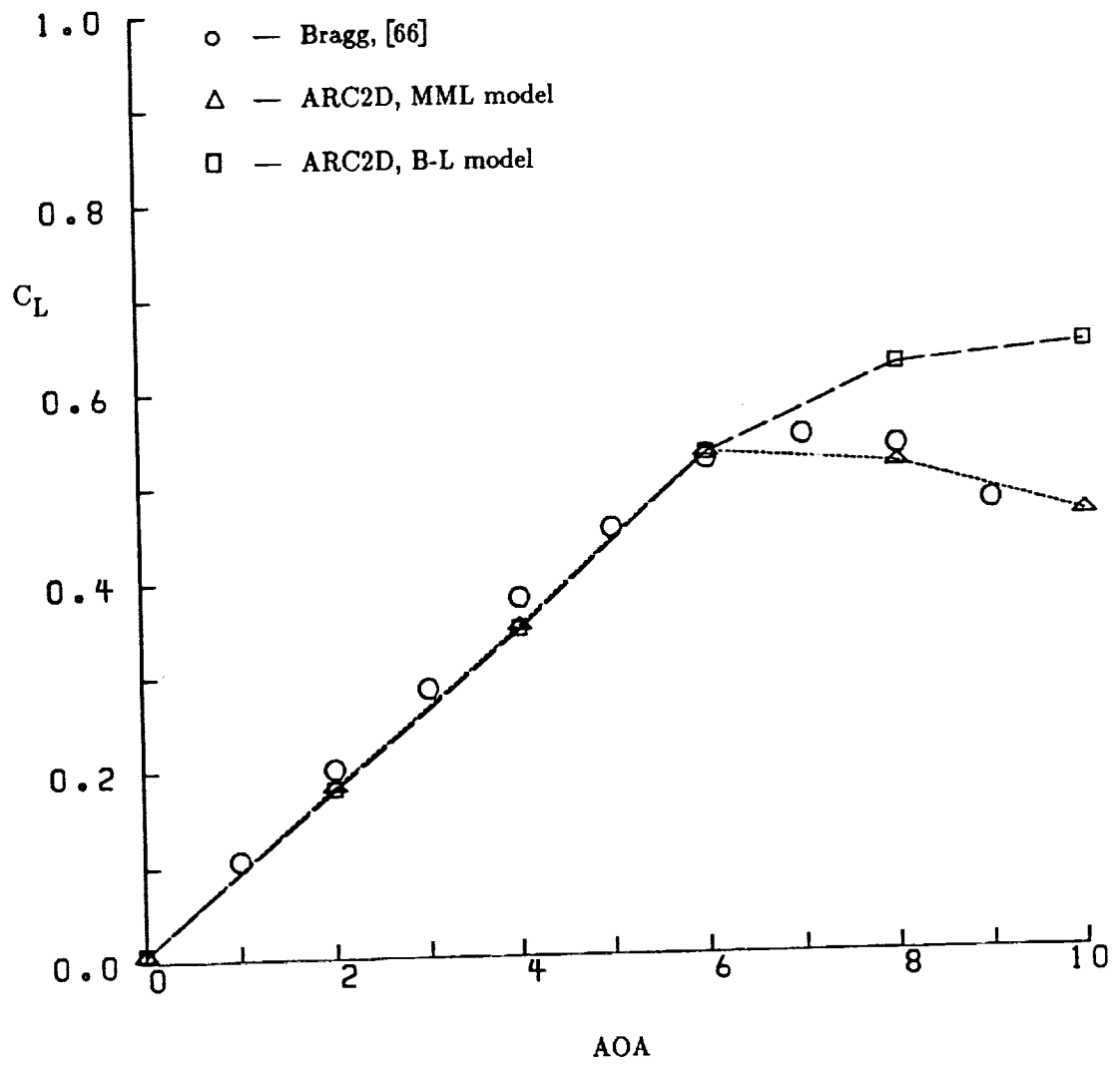
Figure 41 Lift coefficient vs. AOA for NACA0012 airfoil with G1 ice shape.
Comparison of ARC2D results using both turbulence models to
experimental results of Bragg.
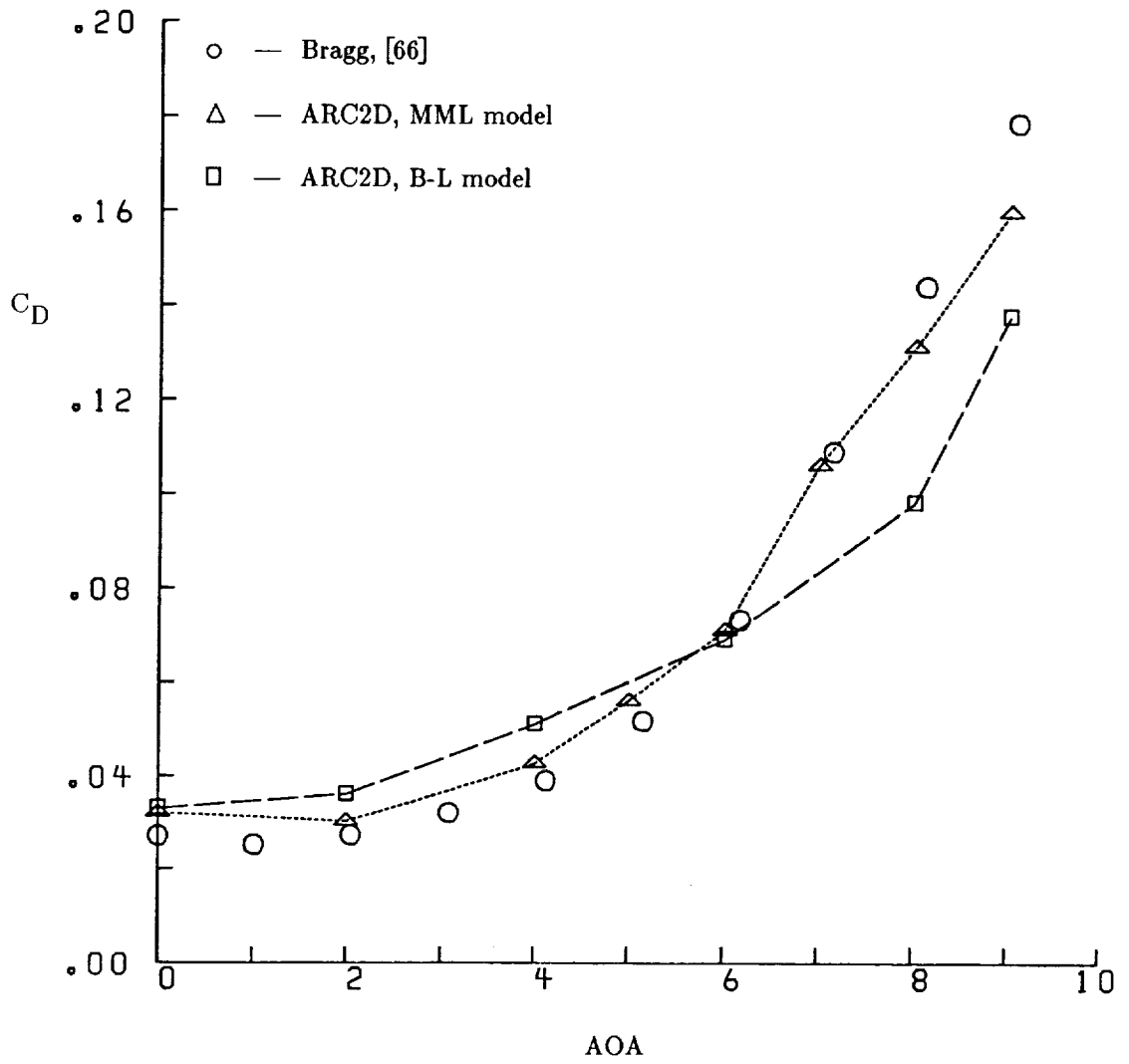
Figure 42 Drag coefficient vs. AOA for NACA0012 airfoil with G1 ice shape.

Comparison of ARC2D results using both turbulence models to

experimental results of Bragg.

that correct determination of the vortex size and shedding frequency may lead to a better evaluation of the performance characteristics of the iced airfoil near stall conditions.

In an effort to evaluate this effect, the C_1 values of 1000 and 2000 were used for several AOA's near stall. The results for 8° AOA are shown in figures 43-46, which indicate pressure coefficients and lift histories for the two C_1 values. The lower C_1 value results in a larger vortex, as seen in a comparison of figures 43 and 45. The shedding frequencies are indicated in figures 44 and 46. These results show that the C_1 value of 1000 yields a time averaged lift coefficient of 0.46 and a C_1 value of 2000 yields a time averaged lift coefficient of 0.47. The experimental value, taken from Bragg [66] for this AOA, was found to be 0.54. Thus, this term does not seem to influence the magnitude of the lift at this angle of attack.

However, examination of the lift histories reveals some differences due to C_1 values. These plots indicate a periodic behavior of the lift. Contour plots of the stream function, figure 47, show the development of a large recirculation region originating at the leading edge, moving along the upper surface of the airfoil and eventually shedding off the trailing edge of the airfoil. The shedding frequency is characterized by the Strouhal number and was found to be 0.0100 and 0.0088 for each C_1 value, respectively. The work of Zaman and McKinzie [68] indicates that there is a low frequency oscillation in the flow over an airfoil at conditions near stall. They speculate that this oscillation is due to the periodic formation and breakdown of a large separation bubble. The frequency of the oscillation resulted in a Strouhal number of 0.02, which is an order of magnitude lower than the normal value associated with bluff-body shedding, but surprisingly close to the values mentioned above. They state, that at higher incidence angles they are able to produce the more conventional bluff-body shedding frequency. Their results suggest another area of potential computational investigation, that is, the higher frequency shedding at larger AOA's.
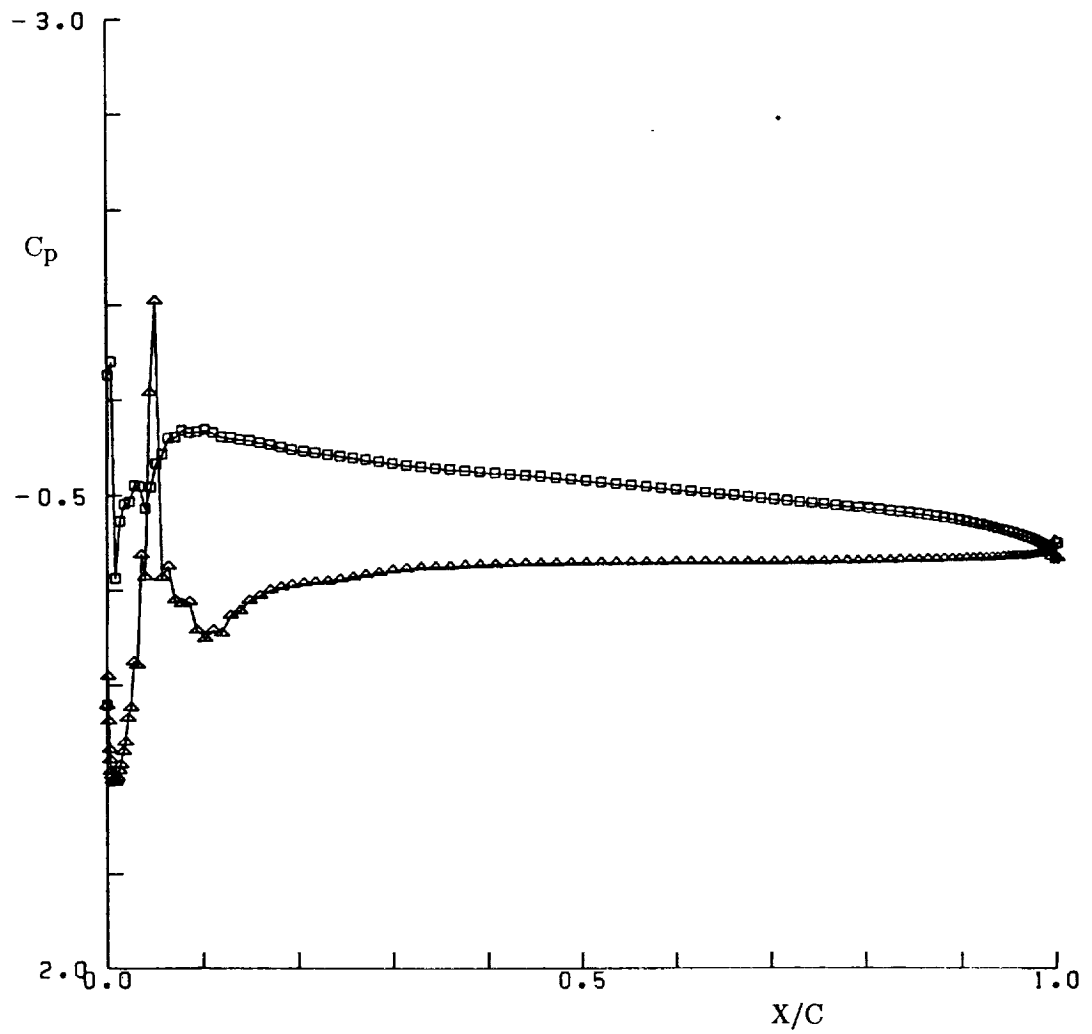
Figure 43 Pressure coefficient distribution for NACA0012 airfoil with G1 ice shape.

$M_\infty = 0.12$, $Re = 1.4\times10^6$, AOA = 8°. $C_1 = 1000$
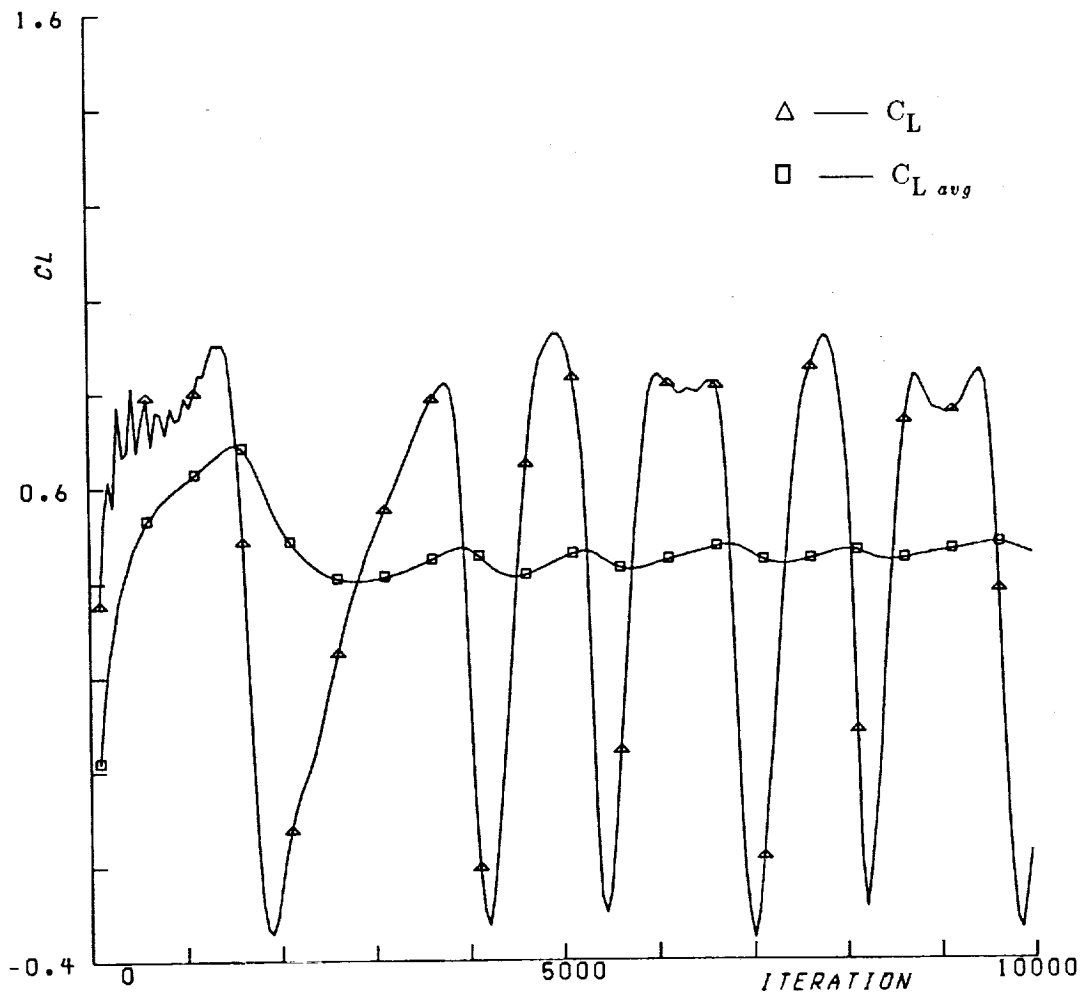
Figure 44   Lift history for NACA0012 airfoil with G1 ice shape.

$M_\infty = 0.12$, $Re = 1.4 \times 10^6$, AOA = 8°. $C_1 = 1000$
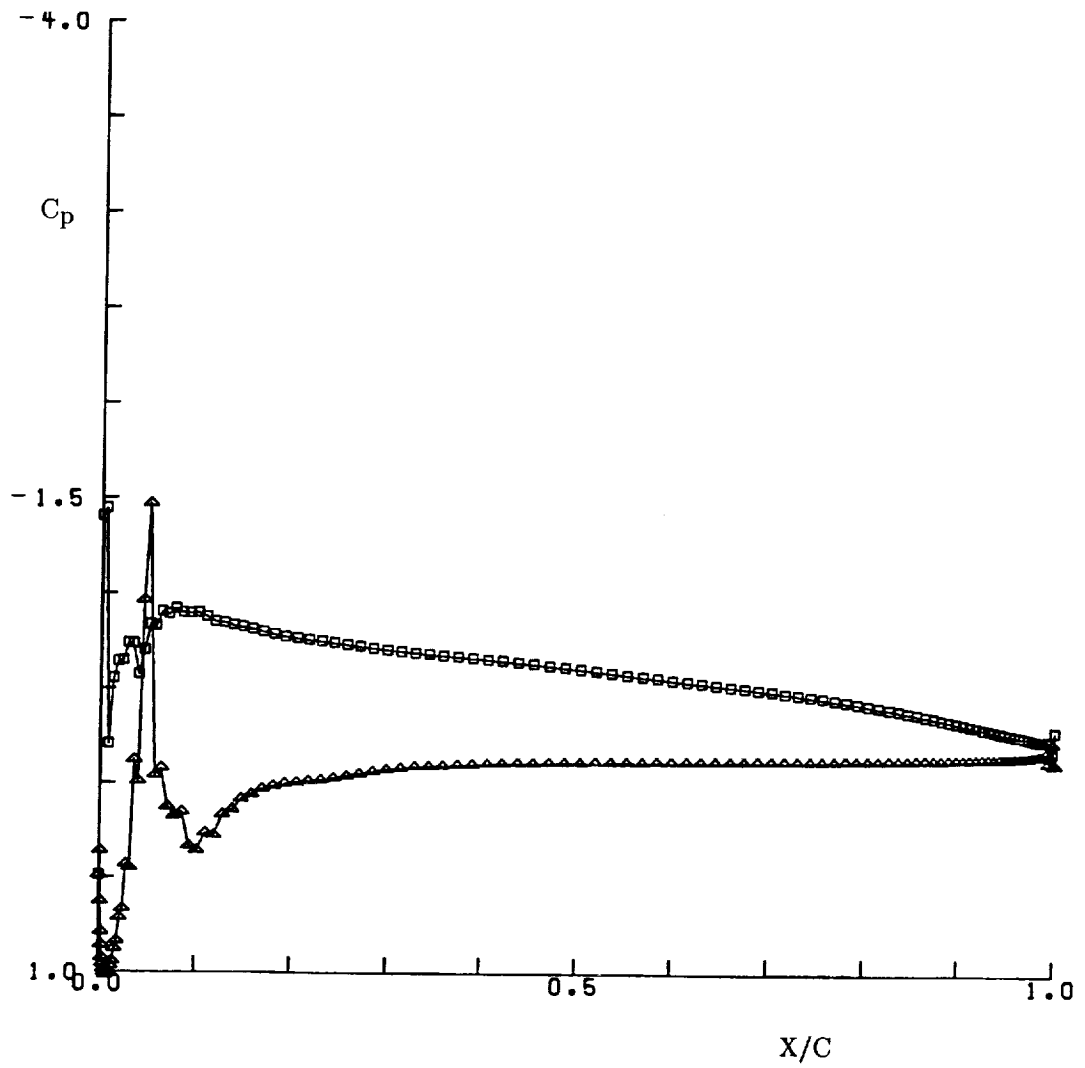
Figure 45 Pressure coefficient distribution for NACA0012 airfoil with G1 ice shape.

$M_\infty = 0.12$, $Re = 1.4 \times 10^6$, AOA = 8°. $C_l = 2000$
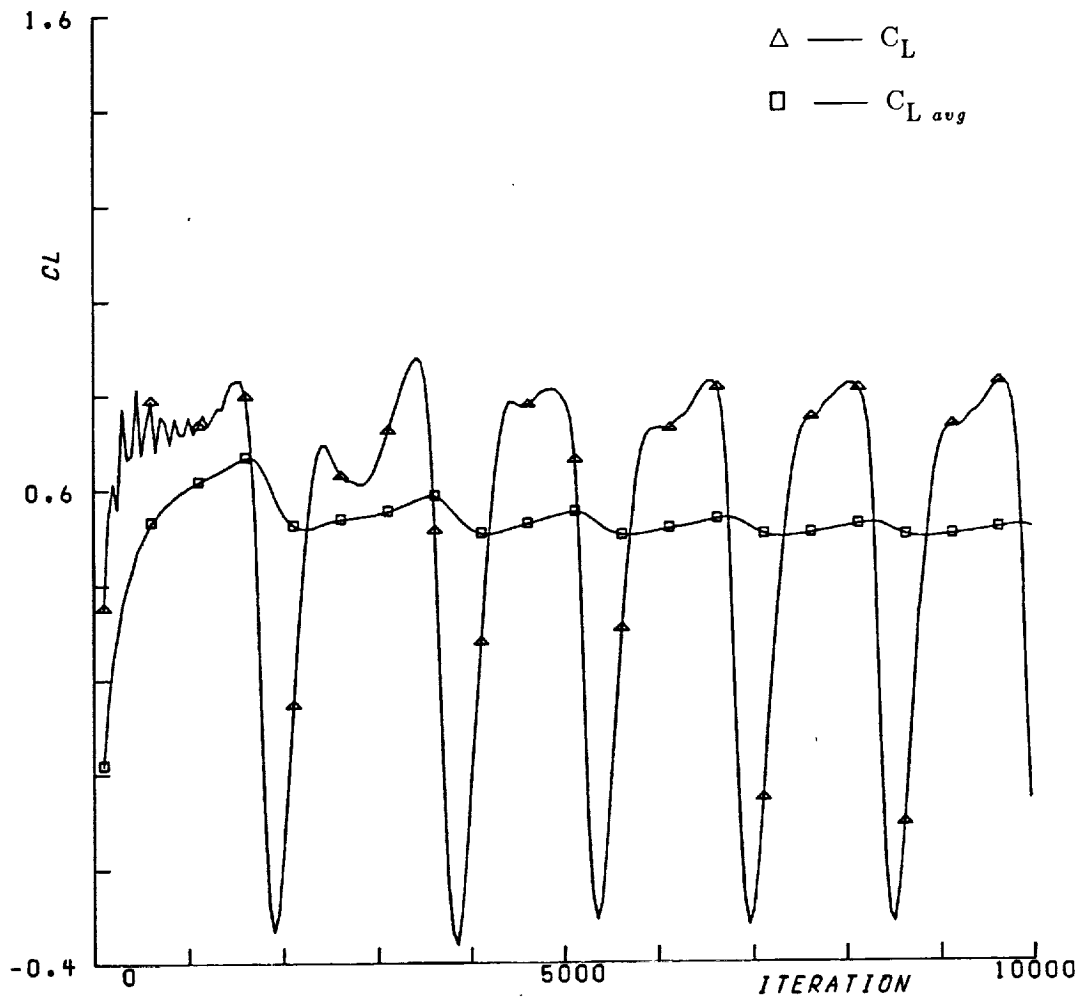
Figure 46   Lift history for NACA0012 airfoil with G1 ice shape.

$M_\infty = 0.12$, $Re = 1.4 \times 10^6$, $AOA = 8°$. $C_1 = 2000$
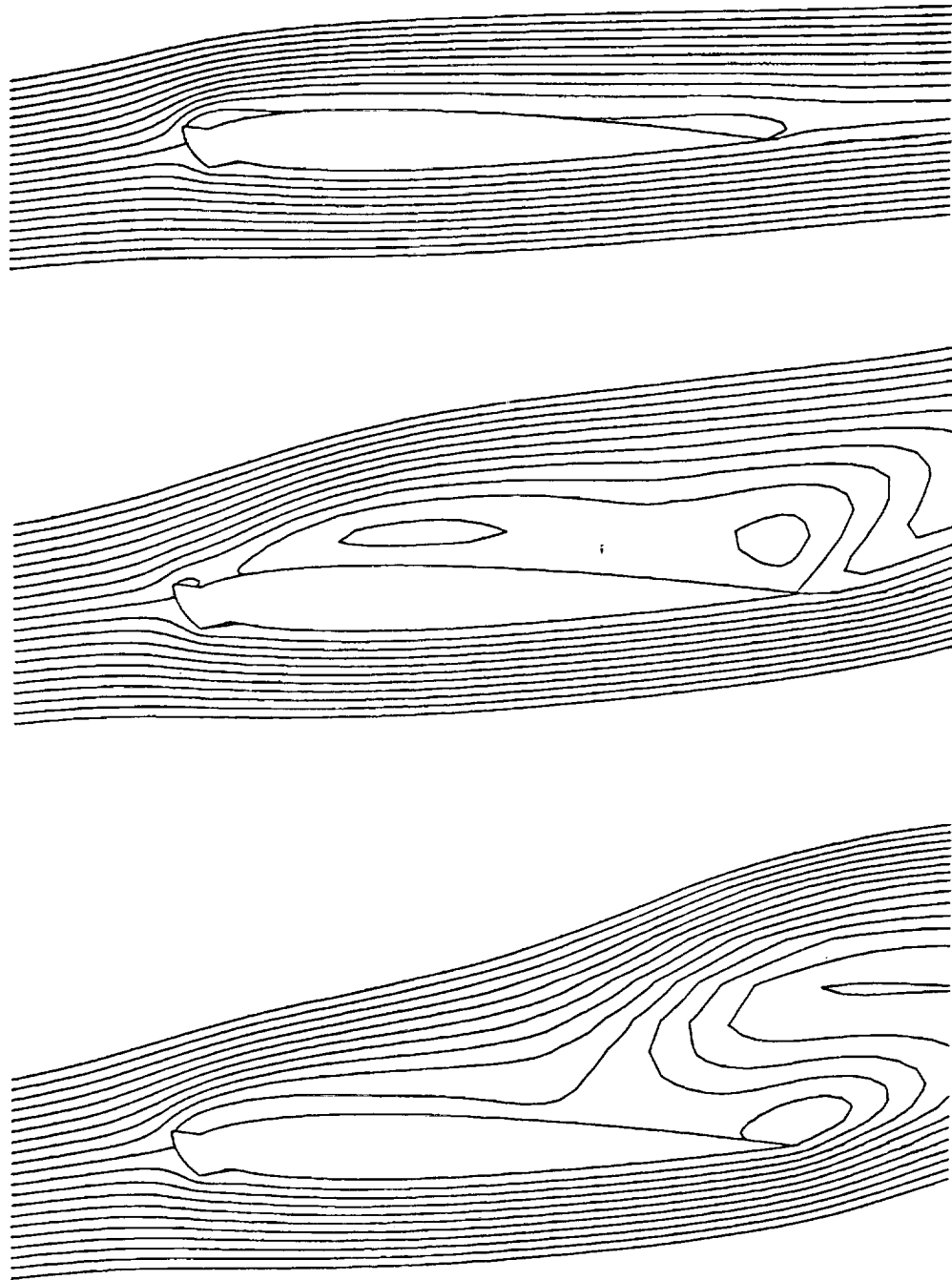
Figure 47 Stream function contours for the NACA0012 airfoil with G1 ice shape

AOA = 8°.

The computational results for the iced airfoil correspond to the description given by Zaman and McKinzie. Thus, the Strouhal number may be used to adjust the C_1 and C_2 values for a given airfoil geometry. The criterion is that at AOA values near stall the Strouhal number should be approximately 0.02 and at higher values of AOA the Strouhal number should be approximately 0.2. The point at which to switch from requiring a value of 0.02 to a value of 0.2 is not readily apparent. This is an area requiring further investigation both from the computational and experimental viewpoints.

The behavior at higher AOA values was examined in order to obtain some insight into this problem. At 10° AOA, the Strouhal numbers resulting from use of C_1 values of 1000 and 2000 are 0.016 and 0.017 respectively. These appear to be in the range associated with the low frequency shedding phenomena. It is not clear, from these results, which C_1 value is preferred. The time-averaged lift values for these two cases are 0.576 and 0.460 respectively. The lift measured by Bragg was 0.479 at 9° AOA with the slope of the lift versus alpha curve being negative. Thus it would seem that for this case the C_1 value of 2000 is preferred.

These results indicate that the vortex shedding is essentially an inviscid phenomena which is modified by the presence of viscosity in the flowfield. Referring back to the equation for vorticity generation (i.e. Eq. 4.8), these results suggest that the mechanism for vorticity generation must be the severe pressure gradient near the horn. The resulting recirculating region which develops enhances the turbulence levels, which in turn leads to increased dissipation of the energy in that region. If the increase in μ_t is too large then the development of the recirculation region is impaired. This leads to the alteration in Strouhal number indicated above. Similarly, if the viscous dissipation is too low, then the recirculation region grows too rapidly and the resulting force coefficients are larger than expected, as indicated in the 10° AOA case. The questions then are: how well does the MML model predict stall

behavior and what values of C_1 and C_2 are appropriate? A study of these effects is being planned and will serve as the basis for continuing work on this problem [72].

Local Results - Pre Stall Conditions

Pressure coefficient distributions for 0°, 2°, and 4° AOA are shown in figures 48-50. Comparisons between computed and experimental results indicate substantial agreement, with the exception of the region near the glaze ice horn. The computed results have a large pressure spike in this region which is not found in the experimental results. The pressure taps in the experiment are spaced at every one percent chord starting at the tip of the horn. Thus, it is unlikely that the spike is there and is not being measured. Examination of the computational grid indicates that the tip of the horn is represented by three grid points in a triangular arrangement. The fluid is thus forced to turn a corner which has an angle greater than 180°, which is not the case for the actual ice shape. This suggests that further grid refinement may be required to eliminate this pressure spike. An alternate grid code is presently being evaluated for this purpose, but was unavailable for use in this investigation.

The experimental results show a flat pressure profile corresponding to the recirculation region. This means that the flowfield is adjusting to the concave region aft of the horn by filling it with low-velocity recirculating fluid. The shear layer which lies on top of this stagnant region is thus flowing over a virtual surface which is more aerodynamic than the actual iced airfoil geometry. The computer code captures this recirculation region but does not adjust the pressure field appropriately.

The code does allow variation of the pressure in the direction normal to the surface, however, it does not seem to capture this feature of the flow. This is indicated in figure 51, which shows the static pressure contours in the recirculation region. The low pressure levels found near the horn do not extend into the recirculation region as the experimental results

111
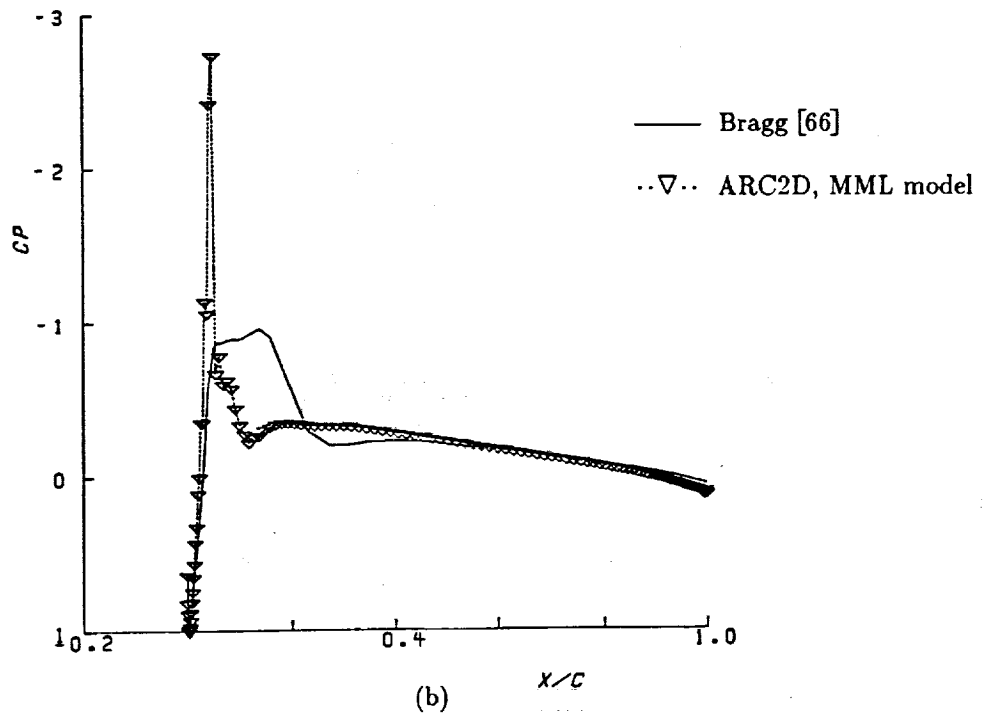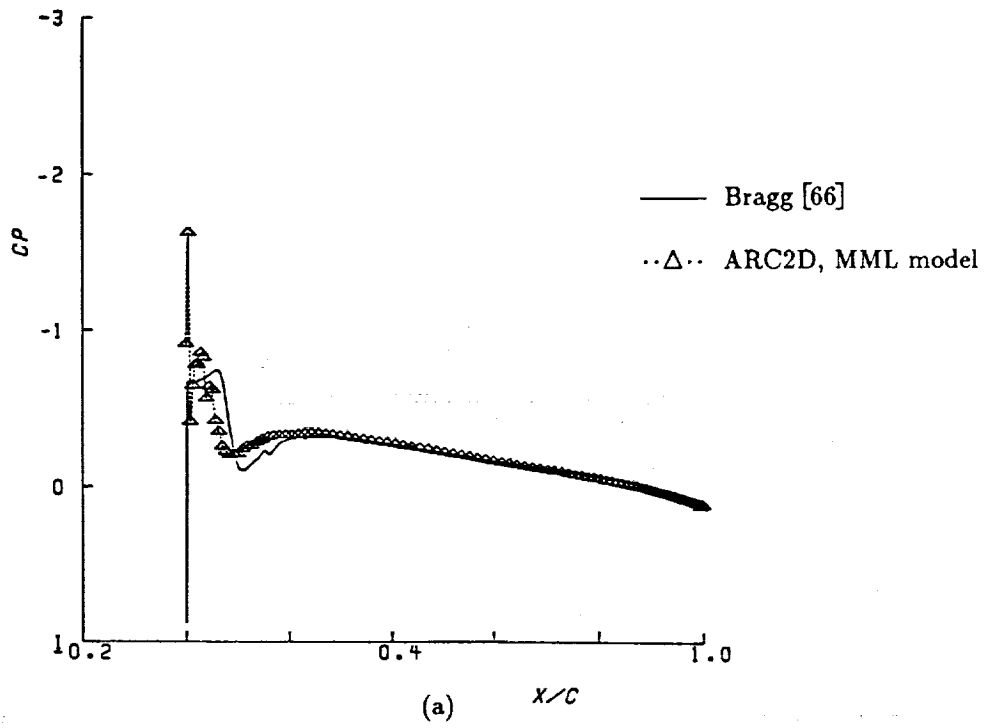
Figure 48 Pressure coefficient distribution for NACA0012 airfoil with G1 ice shape.

$M_\infty = 0.12$, $Re = 1.4 \times 10^6$, AOA = 0°. (a - upper surface, b - lower surface)

112
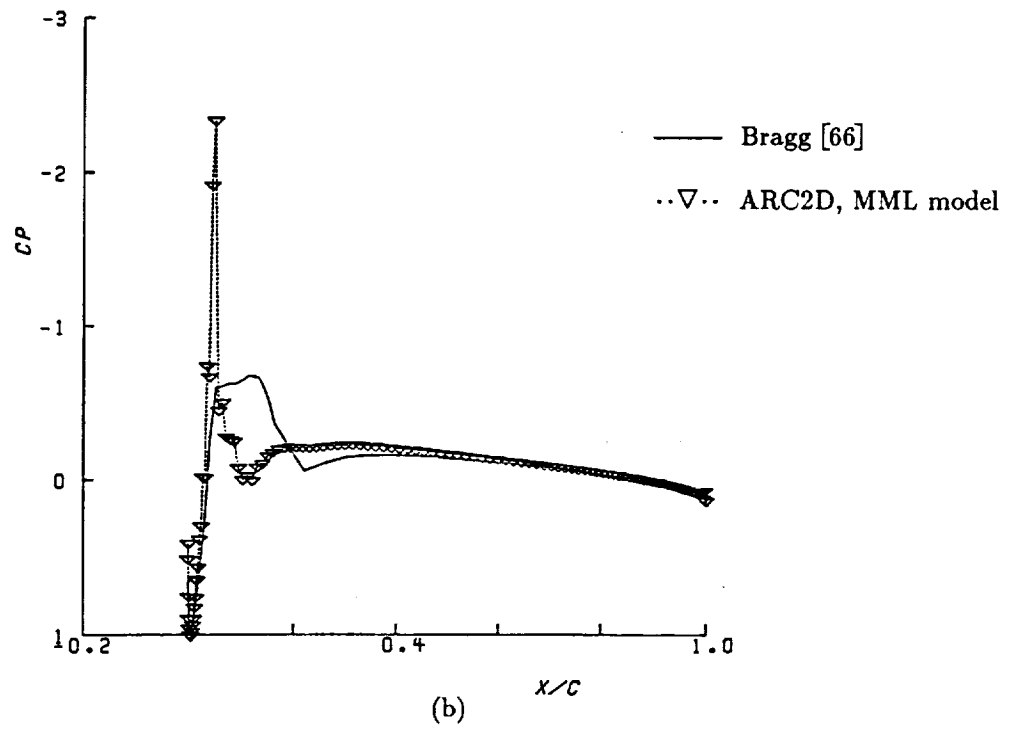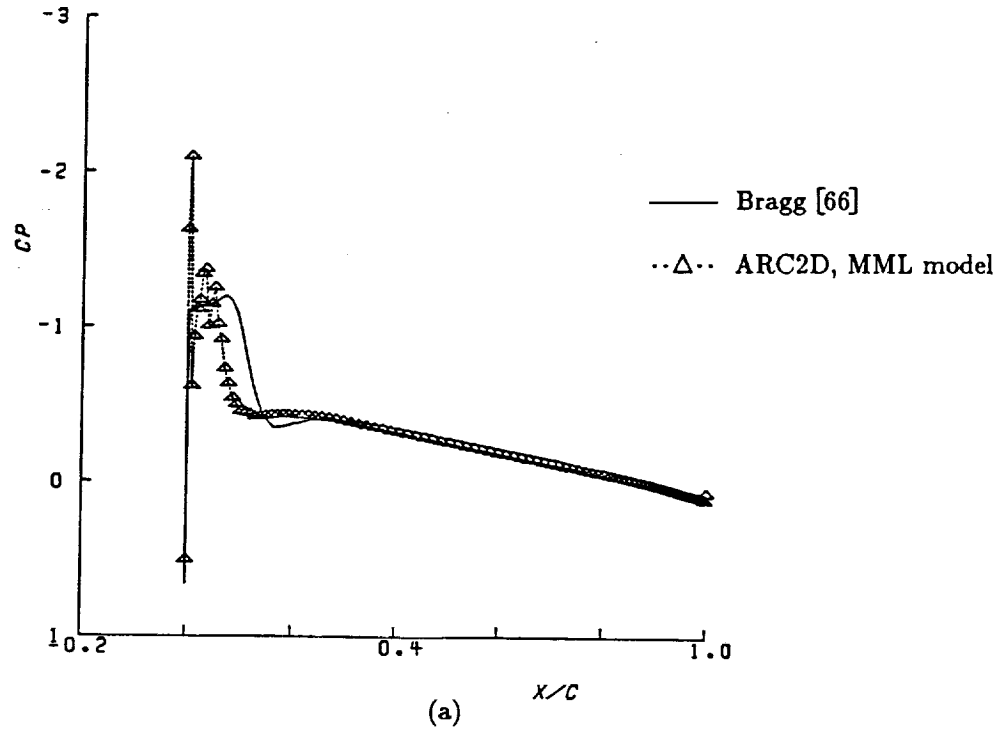
Figure 49 Pressure coefficient distribution for NACA0012 airfoil with G1 ice shape.

$M_\infty = 0.12$, $Re = 1.4 \times 10^6$, $AOA = 2°$. (a - upper surface, b - lower surface)
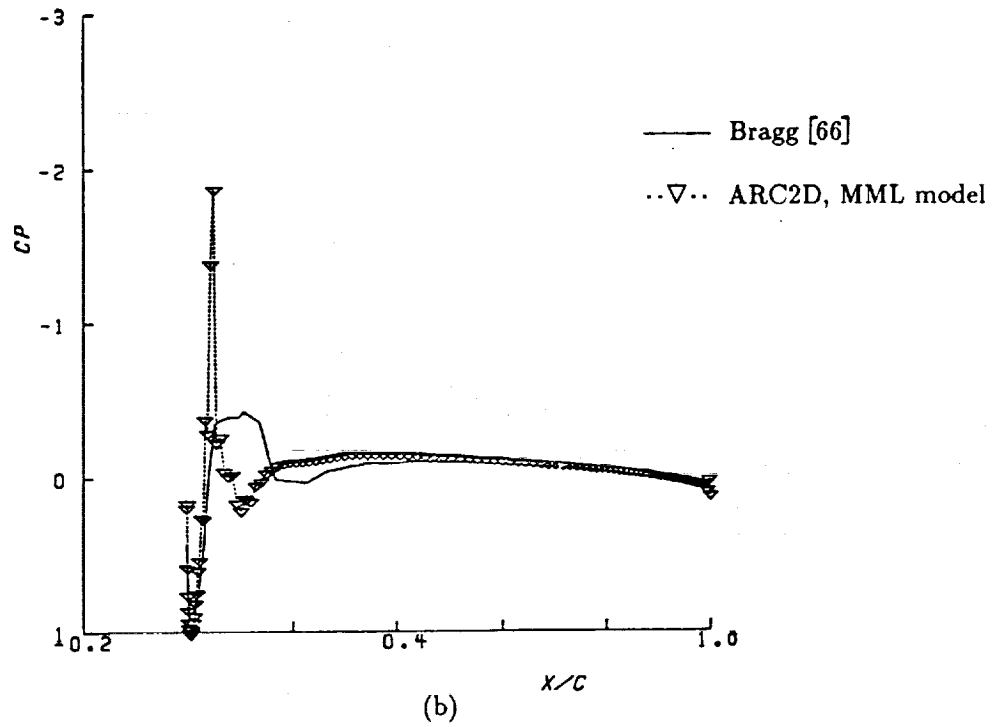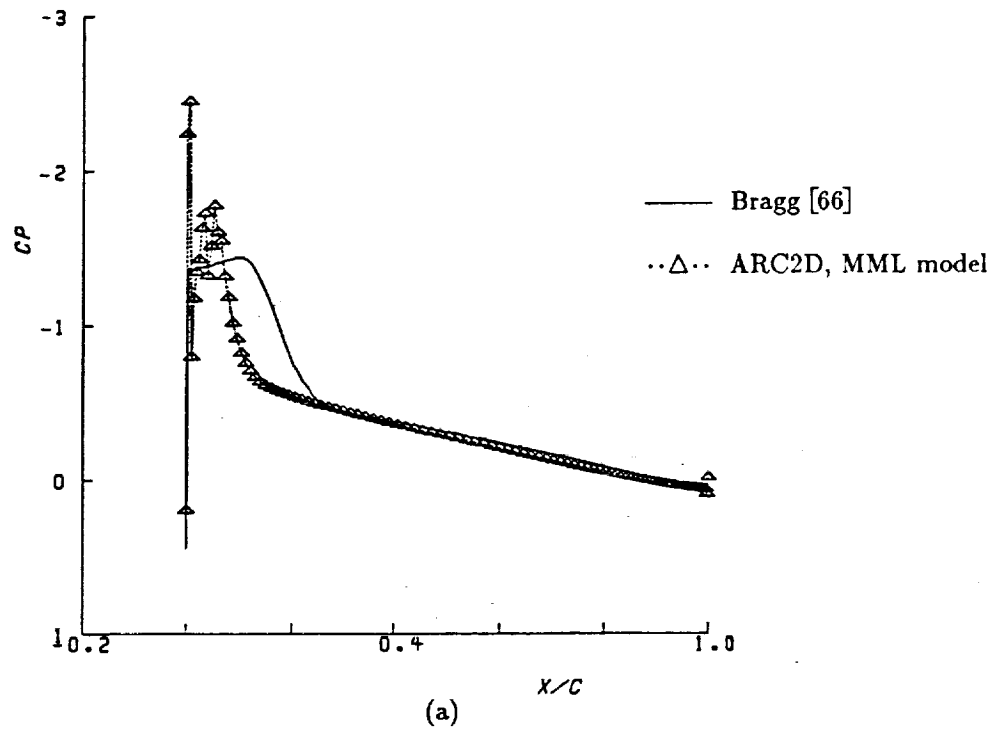
Figure 50 Pressure coefficient distribution for NACA0012 airfoil with G1 ice shape.

$M_\infty = 0.12$, Re $= 1.4 \times 10^6$, AOA $= 4°$. (a - upper surface, b - lower surface)
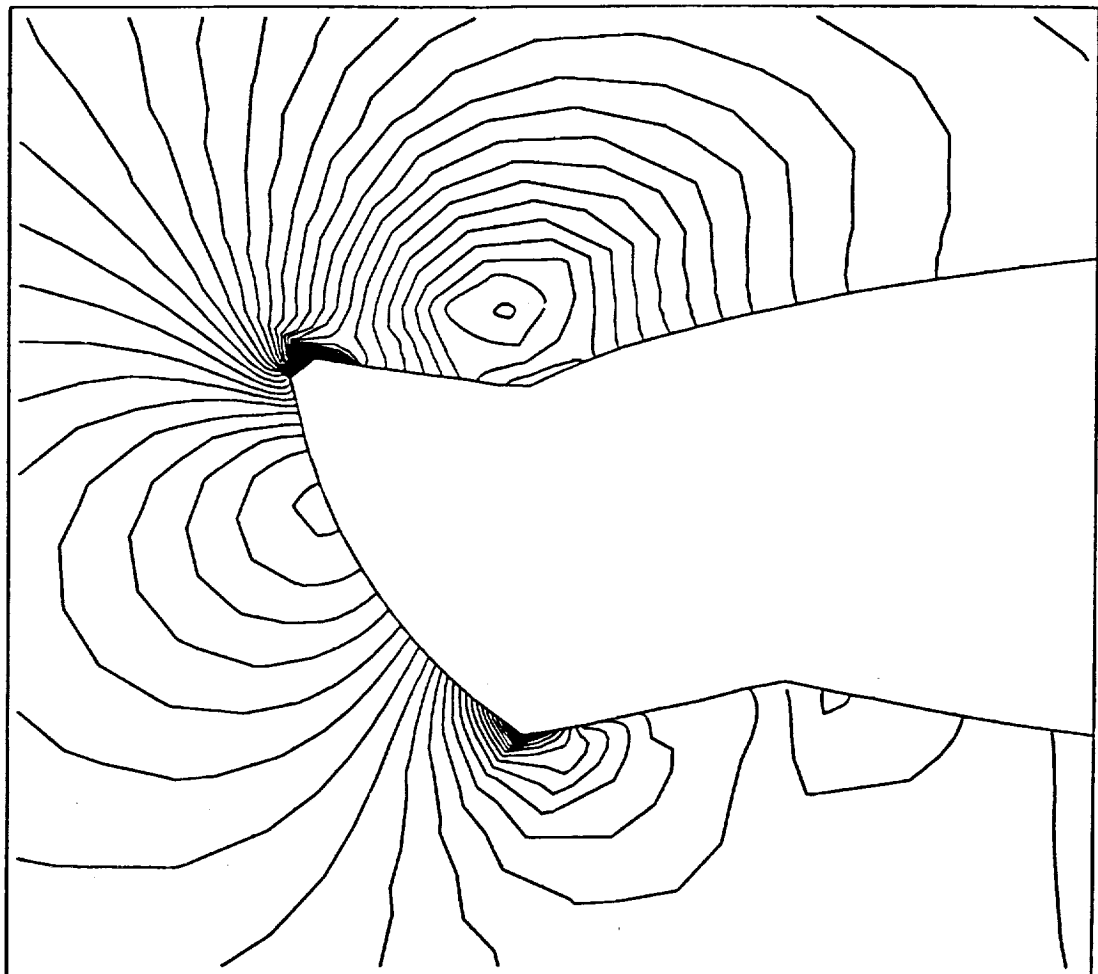
Figure 51   Static pressure contours in the recirculation region behind the horn

for 4° AOA.

would suggest. The experimental results do imply that the pressure gradient in the η-direction may be as important as the ξ-direction gradient. Hence the viscous terms in the ξ-direction, especially the v_ξ terms, may also be of some importance. These terms are neglected in the thin-layer form of the Navier-Stokes equations. The ARC2D code has the capability to include the explicit portion of these terms. When this option is employed, there is no significant difference to the solution. This suggests again that the grid resolution in this region is insufficient. It is expected that an alternate grid will resolve this problem along with the pressure spike at the tip of the horn.

The velocity profiles also suggest a need for greater grid resolution in the recirculation region. The velocity profiles obtained using ARC2D are compared to experimental values in figures 52-54. These figures show the velocity profiles within the recirculation region for AOA values of 0°, 2°, and 4° respectively. Notice the differences in height of the zero-velocity point and in location of reattachment. The height of the reverse flow region, defined as the distance from the surface to the zero-velocity line, can be as large as 2-3 percent chord. The grid resolution in this region is not as fine as it is near the surface. This is true for resolution in both the η and ξ directions. The results presented in figures 52-54 were obtained using the Baldwin-Lomax model. The turbulence model selection does not seem to play as important a role as either the transition location or the grid resolution. Further investigation of the turbulence model role in the development of the attached bubble is required.

The free shear layer, extending from the separation point to the reattachment point, should have the same grid resolution as the boundary layer. The fact that it does not means that certain aspects of the flow physics are not being modeled correctly. This is also reflected in figures 52-54, by examining the velocity gradients near the upper edge of the reverse flow regions. The code tends to underpredict the velocity gradient along with the distance of the

116
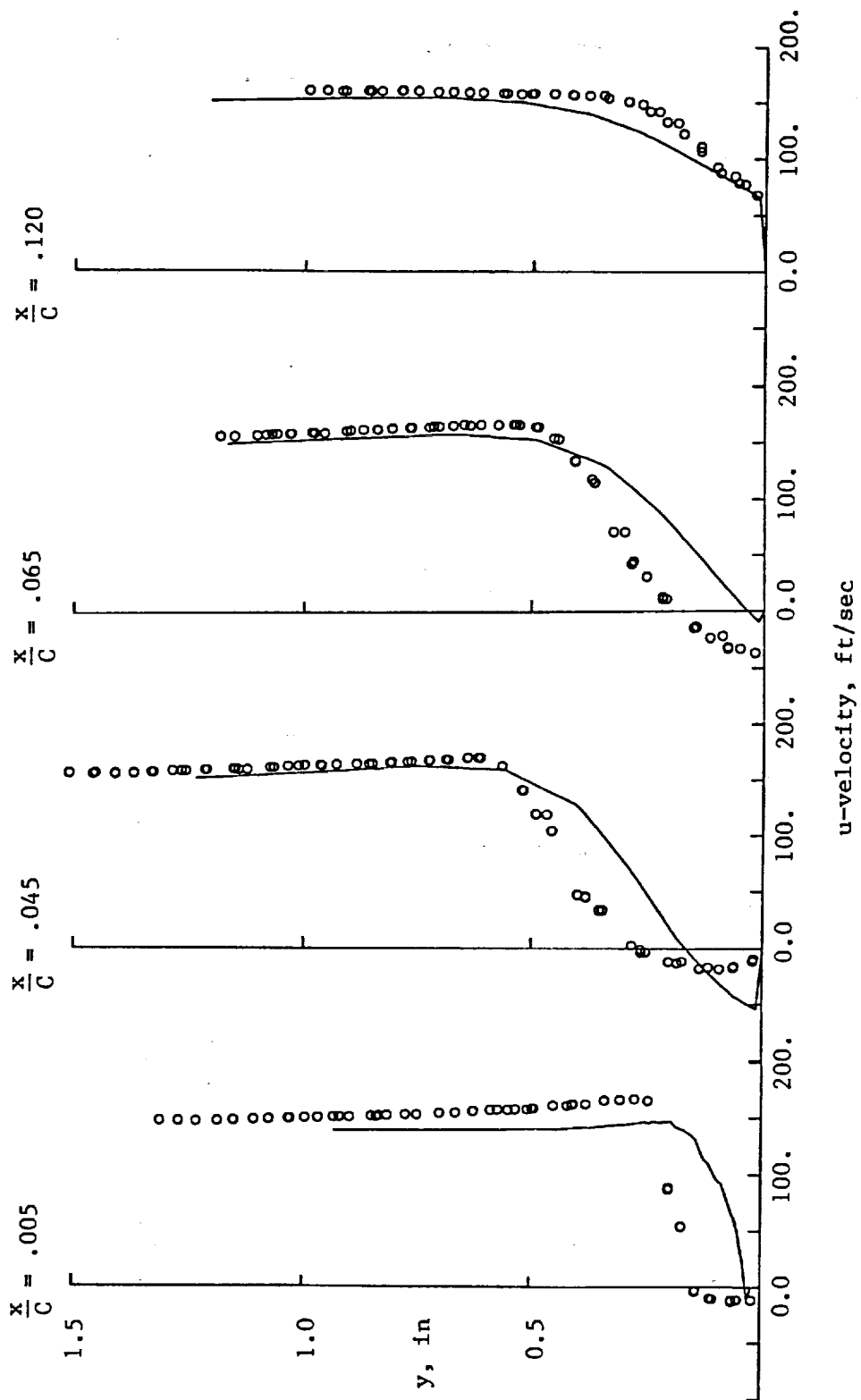
Figure 52   Velocity profiles in the recirculation region aft of the horn

———— ARC2D,   o   Experiment, AOA = 0°
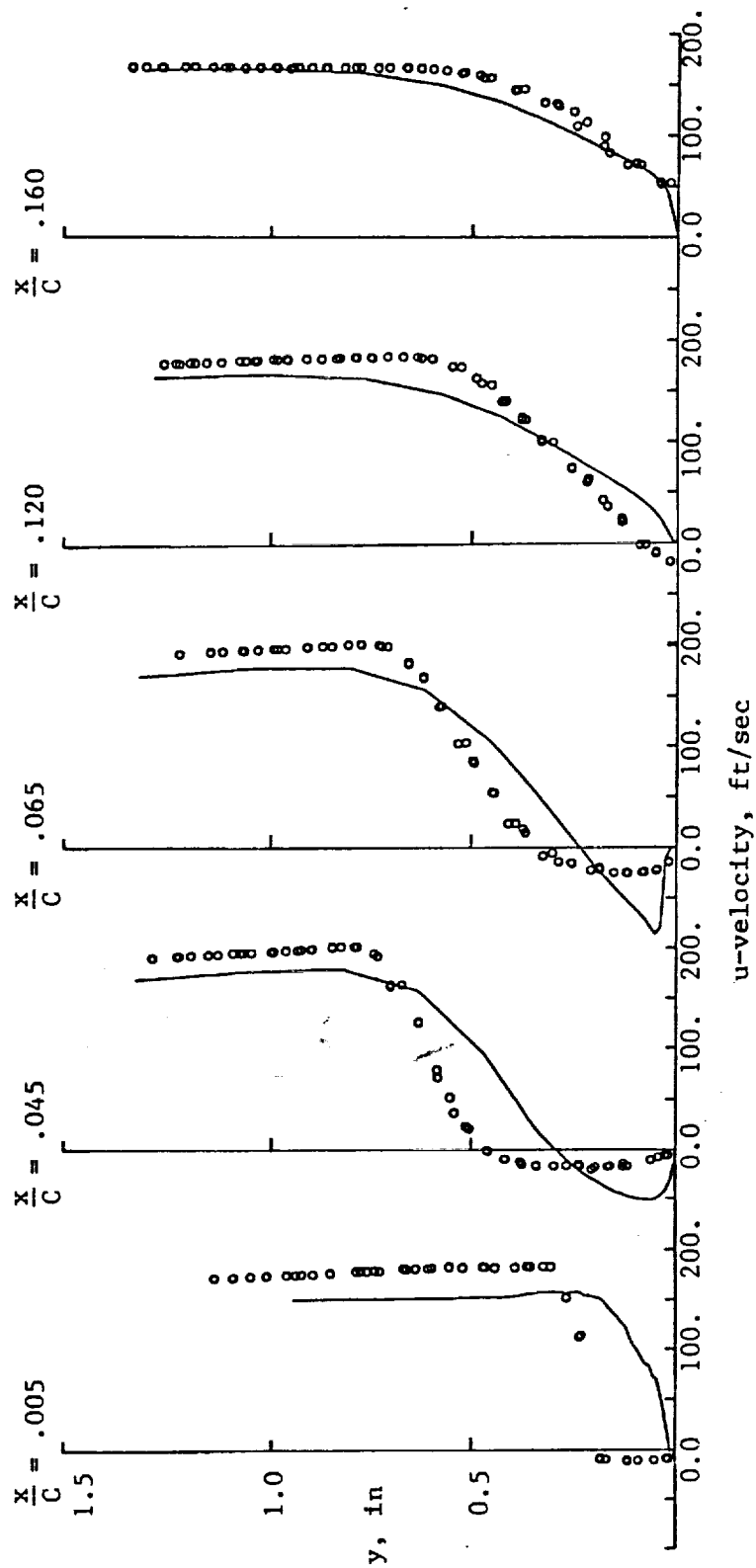
Figure 53   Velocity profiles in the recirculation region aft of the horn

———— ARC2D,   o   Experiment,   AOA = 2°
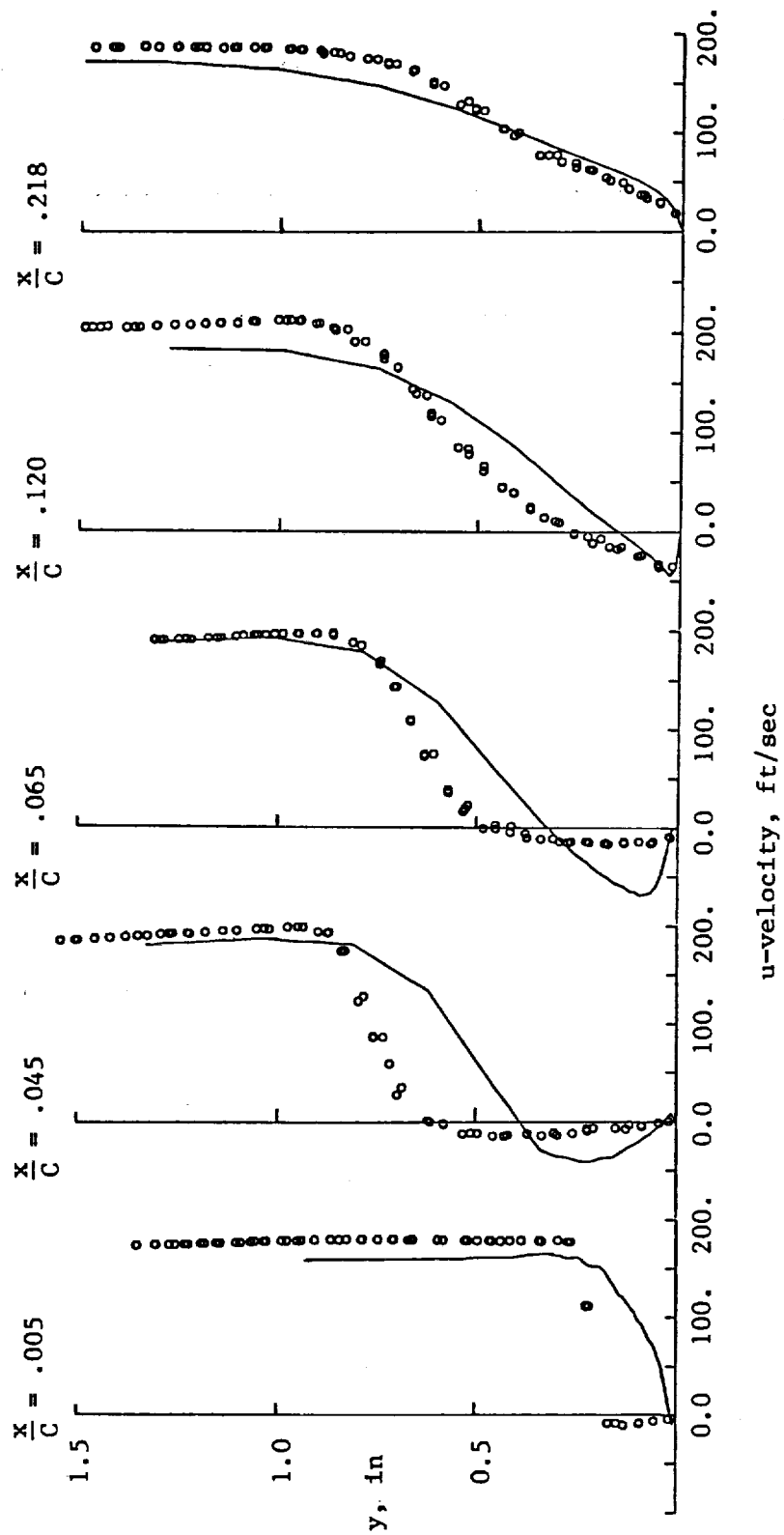
Figure 54   Velocity profiles in the recirculation region aft of the horn

———— ARC2D,   o   Experiment, AOA = 4°

free shear layer from the surface. This inability to capture the shear layer behavior is consistent with the overprediction of the pressure spike mentioned previously.

Correct representation of the flow in these recirculation regions also requires specification of the transition region. Presently, the ARC2D code has a very rudimentary single-location transition specification. As described by Mehta [73], 'the process of transition from laminar to turbulent flow is not a well-defined problem because of the sensitivity to poorly defined initiating disturbances'. He goes on to state that the main requirements for numerical solution to the compressible Navier-Stokes equations in regard to the transition process are 'that (1) the discretization errors do not contaminate physical phenomena such as instabilities, that is, the finest scales in the transition process are adequately resolved in space and time; and (2) the introduction of artificial boundaries owing to the limited size of the computational domain does not interfere with the physical upstream influence, the ellipticity of the Navier-Stokes equations.'

From these comments, it is apparent that appropriate representation of transition is necessary for correct modeling of the recirculation region aft of the glaze horns. Since the code presently does not have a sophisticated transition model, the effect of transition specification was examined by simply altering the location and noting the changes in the velocity profiles. This was done for the 0° AOA case by moving the transition location from the tip of the horn, as was the case in figures 52-54, to a point approximately in the center of the separation bubble. The results are shown in figure 55.

Moving the transition location further aft has two effects on the separation bubble. The modeling of the shear layer velocity gradient is improved and the magnitudes of the reverse flow velocities are overpredicted. The improvement to the shear layer velocity gradient can be attributed to a more realistic representation of the dissipation in that region. The use of the downstream transition location more accurately represents the free shear behavior, as
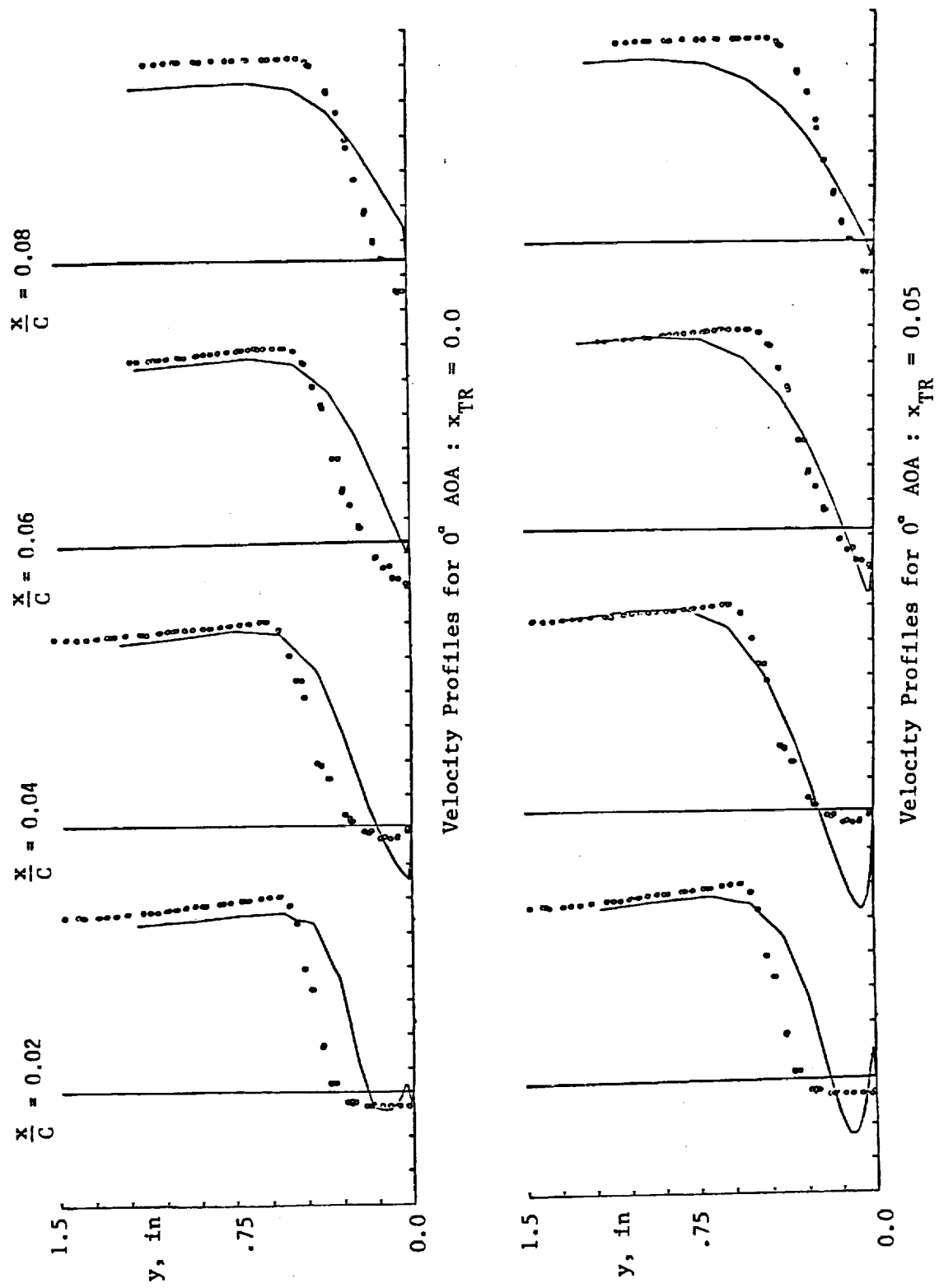
Figure 55   Velocity profiles in the recirculation region aft of the horn

——— ARC2D,   o   Experiment, AOA = 0°

121

described by Mehta. The overprediction of the reverse flow velocities is due to the approach used by ARC2D in defining laminar and turbulent regions.

The code first calculates turbulent viscosities for all constant-ξ lines from the leading edge to the trailing edge. The transition points on the upper and lower surfaces are then identified and all turbulent viscosity values from the leading edge to these transition points are reset to zero. If the transition location is in the center of a separation bubble then turbulent fluid re-laminarizes as it flow toward the forward portion of the bubble in the reverse flow region. This decrease in dissipation leads to an inappropriate enhancement of the velocities in that region.

The behavior described by Simpson et al. [63] for a two-dimensional turbulent separated flow seems more realistic. He indicates that the mean backflow in the detachment region of the separation bubble is a result of incursions of turbulent fluid from the overlying shear layer. The use of a laminar flow region in this part of the bubble is inappropriate. Also, the use of a turbulence model based on the mean flow velocity profiles seems precluded by this description. Thus, at this time no readily available method will adequately describe the detachment region. The lack of such a model requires the selection of some transition location which produces the most acceptable results from the standpoint of performance evaluation. It seems that a transition location halfway through the separation region produces a better shear layer evaluation and reattachment point prediction. Thus, selection of this point for transition location is recommended at this time. Future work could be directed at improvement of the model with respect to the type of intermittant behavior described by Simpson.

Local Results - Post Stall Behavior

The ice accretion geometry and angle of attack play a critical role in altering the maximum lift and inducing the onset of stall. The results of flow visualization studies

indicate, for the NACA0012 airfoil and G1 ice shape, that the separation bubble near the horns grows with increasing incidence until at approximately 6° − 7° AOA the entire upper surface exhibits alternating forward and reverse flow. Results from the computations also indicate a significant change at 6° − 7° AOA. As mentioned earlier, the MML model predicts unsteady flow at 6° AOA while the Baldwin-Lomax model predicts the onset of unsteady flow at 10° AOA. Therefore, the MML model will be used exclusively for evaluation of the post stall behavior described in this section.

At lower AOA's, the separation bubble size is a function of AOA but it exhibits an essentially steady size and shape. At 6° AOA, the bubble grows to encompass the entire surface and continues growing in strength until it is swept from the surface by the main flow. This flow is periodic in nature with new bubbles being generated at the leading edge to replace those being shed at the trailing edge. This shedding process is present for a large range of AOAs above stall. This sequence is captured in figures 56-74, for a 10° AOA case. The lift history for this process is shown in figure 75.

These figures show the development of the bubble at various stages of growth and subsequent shedding over several cycles. The figures shown are the stream function and equivorticity contours at selected time points in the computation. Initially, the separated flow region encompasses the entire upper surface of the airfoil, as seen in figure 56. The equivorticity contours, on the other hand appear more concentrated near the horn. This is the point in the process just after one shedding cycle and just prior to the next cycle. At this point, the lift of the airfoil is just past its maximum. The zero stream function contour has just separated from the surface and the lift is starting to decrease. A small region of counterclockwise (i.e. positive) rotating fluid is seen at the trailing edge. The high lift value is due to the large amount of circulation within the larger, negative vortex which is still present on the upper surface.
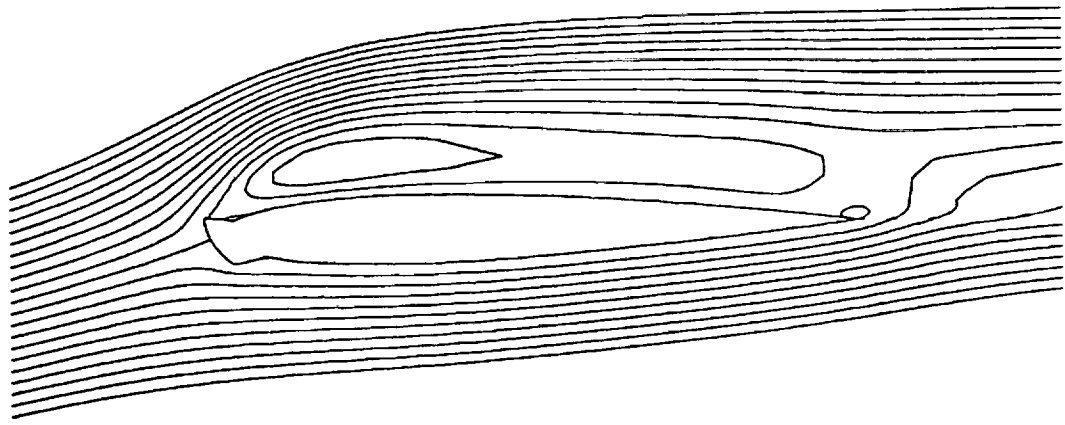
(a)
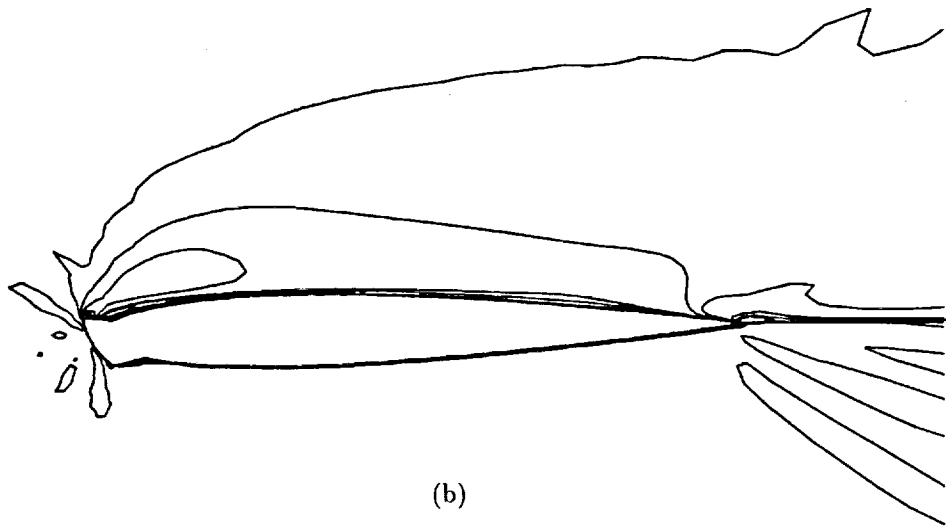
(b)

Figure 56   Vortex development on the NACA0012 airfoil with G1 ice shape; AOA = 8°,

t=t₀;   (a) stream function contours, (b) equi-vorticity contours
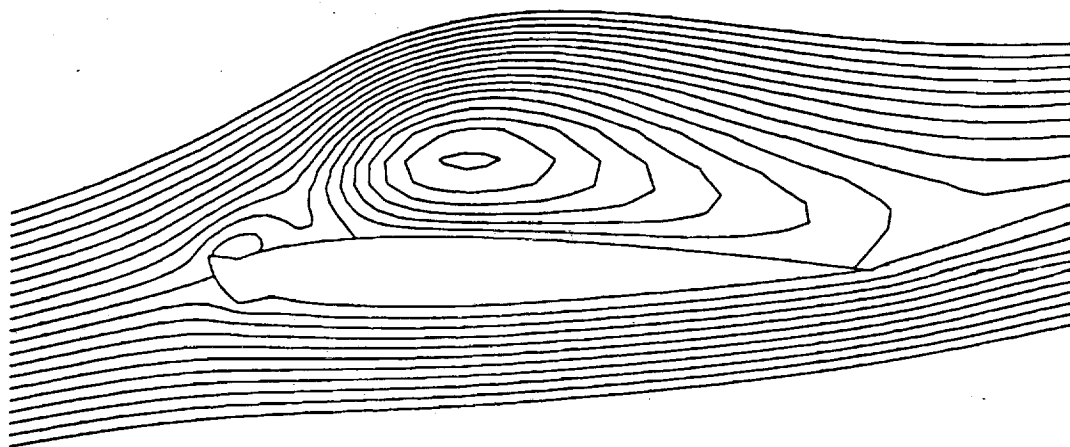
(a)
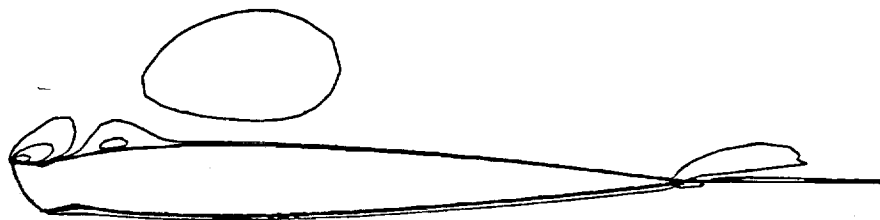
(b)

Figure 57   Vortex development on the NACA0012 airfoil with G1 ice shape; AOA=8°,

t=t$_0$+300Δt; (a) stream function contours, (b) equi-vorticity contours
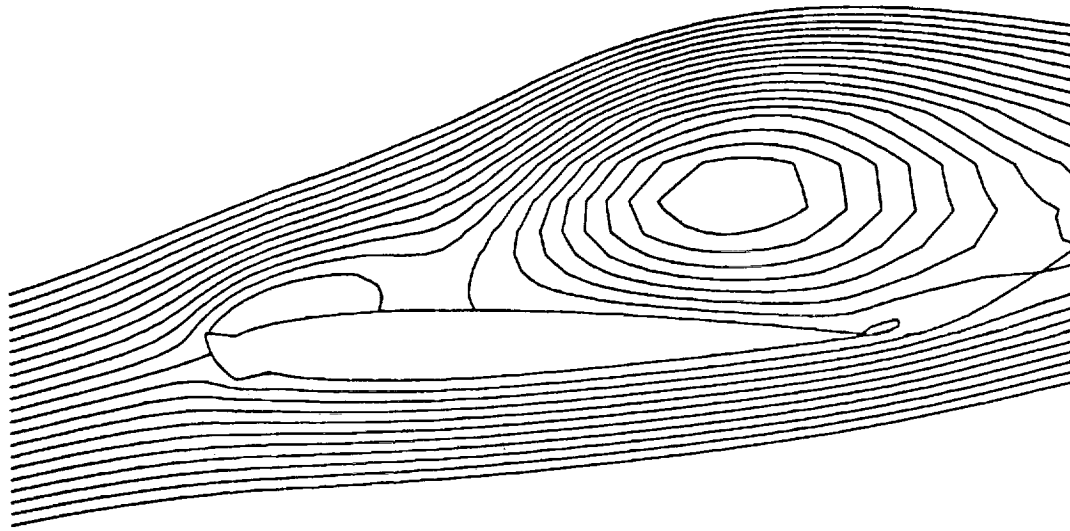
(a)

(b)

Figure 58   Vortex development on the NACA0012 airfoil with G1 ice shape; AOA=8°,

t=t$_0$ + 600Δt ;   (a) stream function contours, (b) equi-vorticity contours
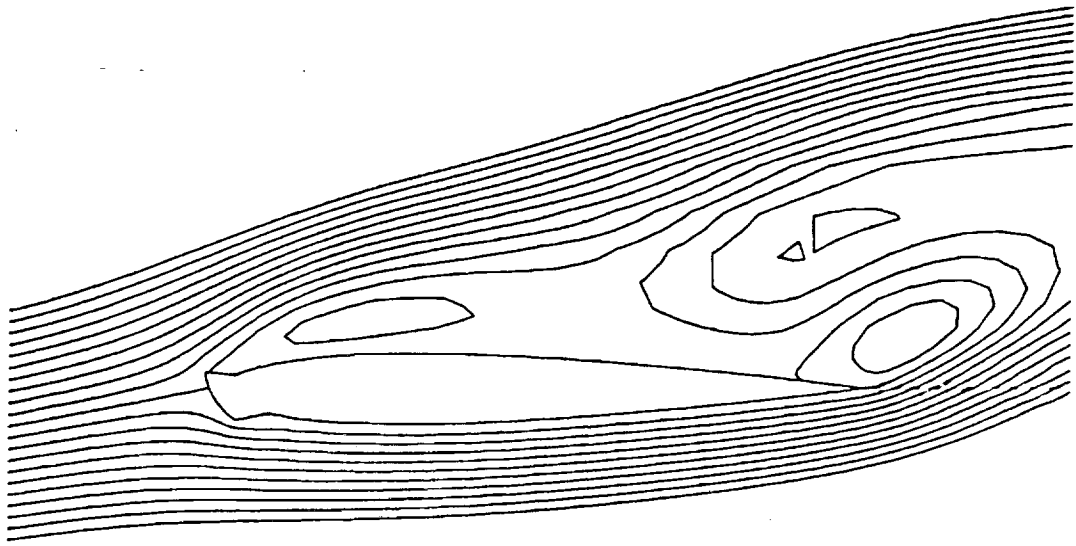
(a)
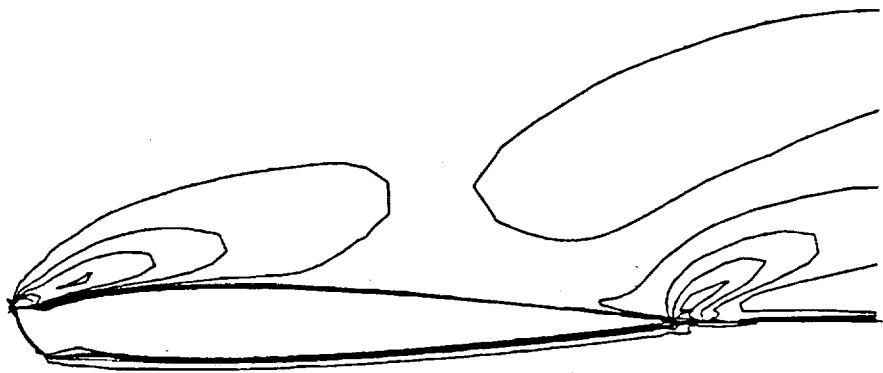
(b)

Figure 59   Vortex development on the NACA0012 airfoil with G1 ice shape; AOA=8°,

t=t$_0$ + 900Δt ;   (a) stream function contours, (b) equi-vorticity contours
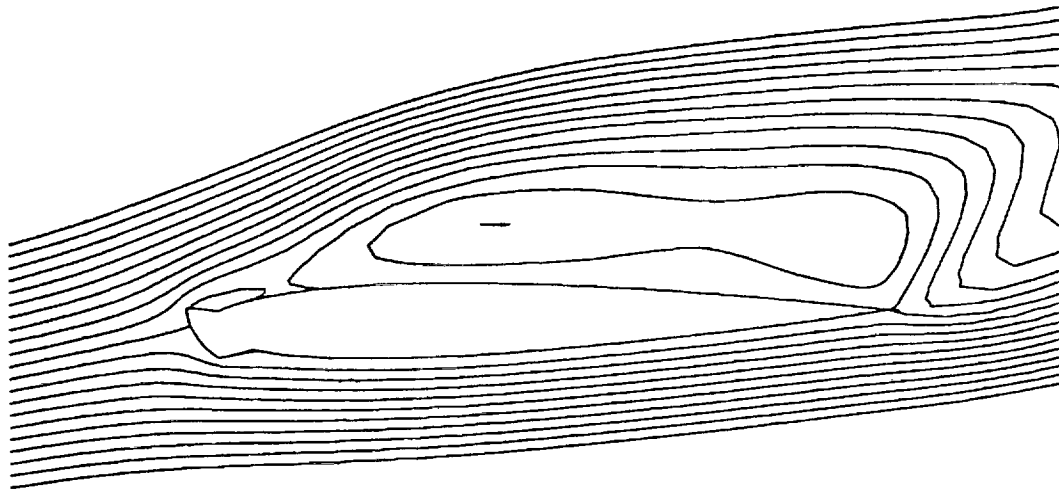
(a)
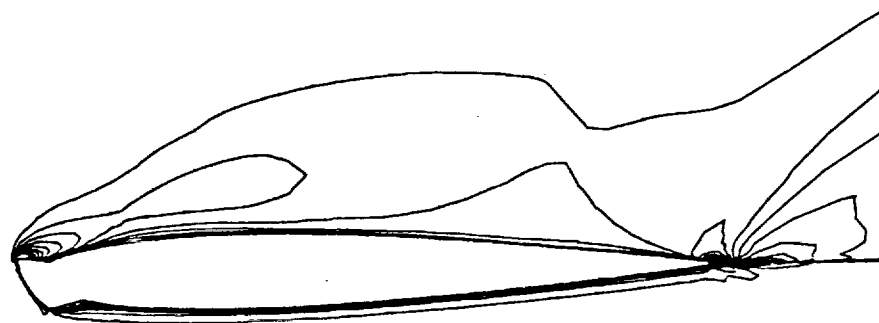
(b)

Figure 60   Vortex development on the NACA0012 airfoil with G1 ice shape; AOA=8°,

t=t$_0$+1200Δt; (a)stream function contours, (b)equi-vorticity contours
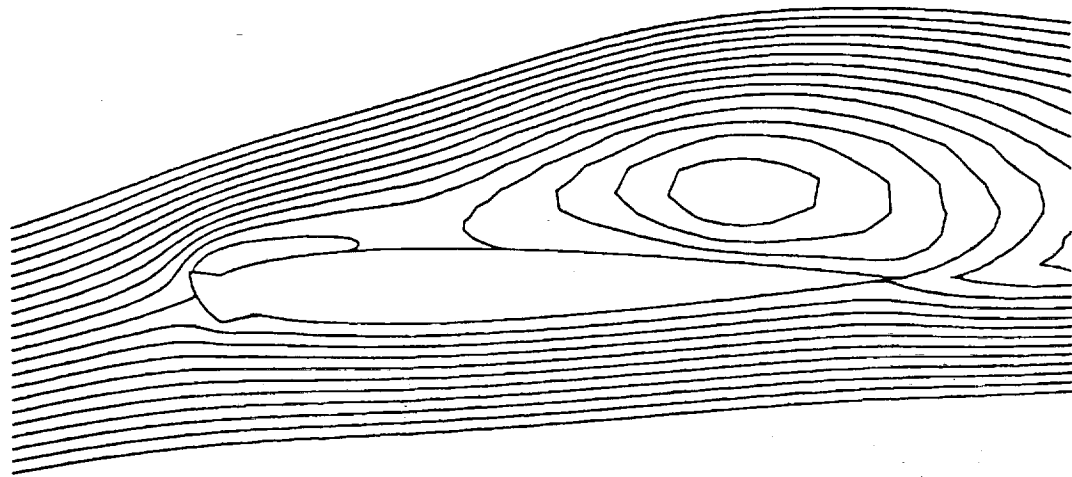
(a)
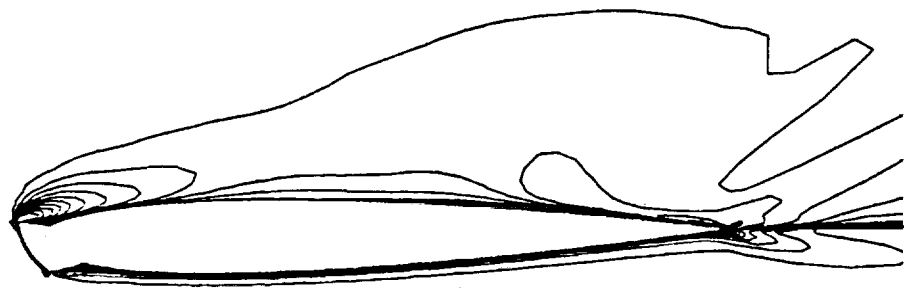
(b)

Figure 61   Vortex development on the NACA0012 airfoil with G1 ice shape; AOA=8°,

t=t$_0$ + 1500Δt ;   (a) stream function contours, (b) equi-vorticity contours
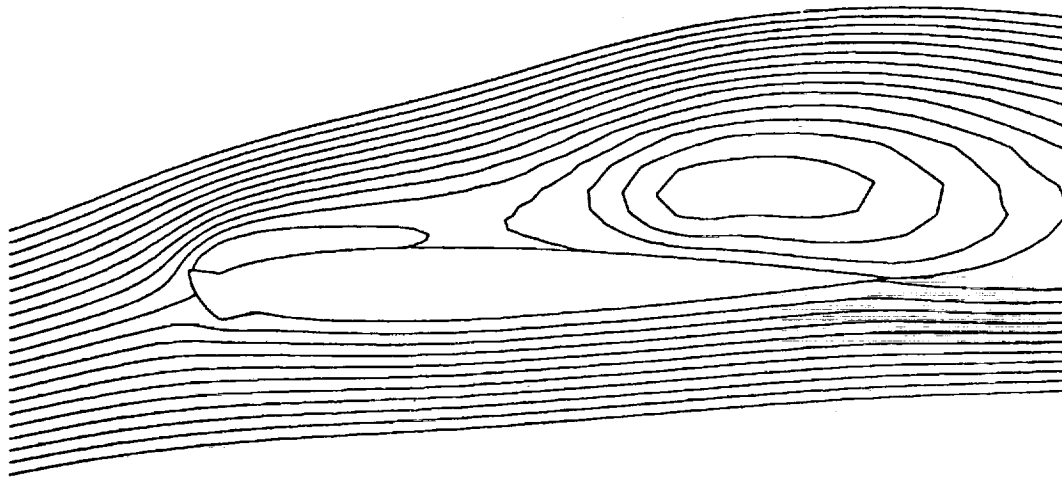
(a)
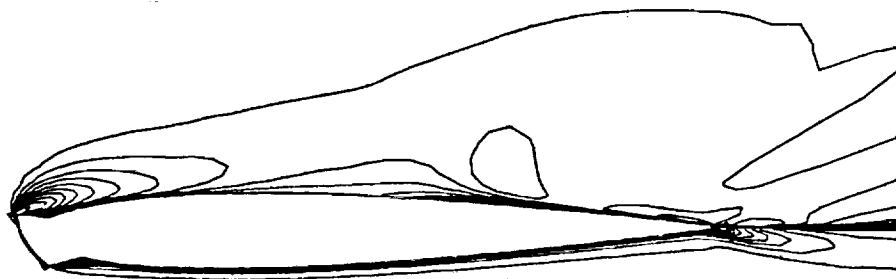
(b)

Figure 62   Vortex development on the NACA0012 airfoil with G1 ice shape; AOA=8°,

t=t_0 + 1600Δt ;   (a) stream function contours, (b) equi-vorticity contours
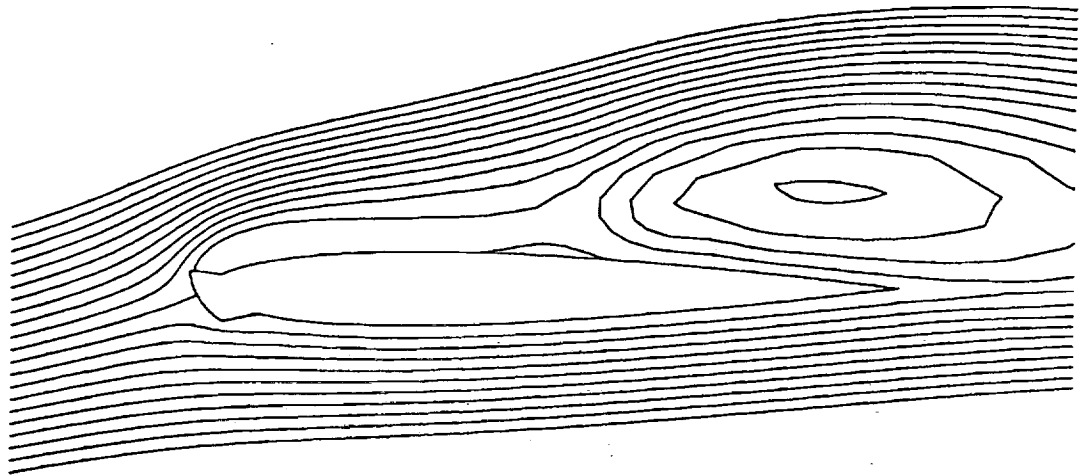
(a)
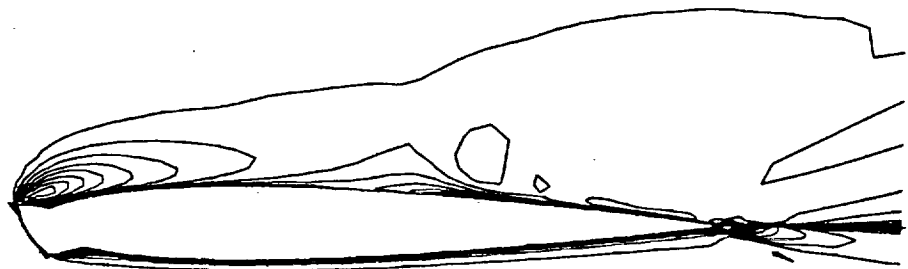
(b)

Figure 63   Vortex development on the NACA0012 airfoil with G1 ice shape; AOA=8°,

t=t_0+1700Δt; (a) stream function contours, (b) equi-vorticity contours
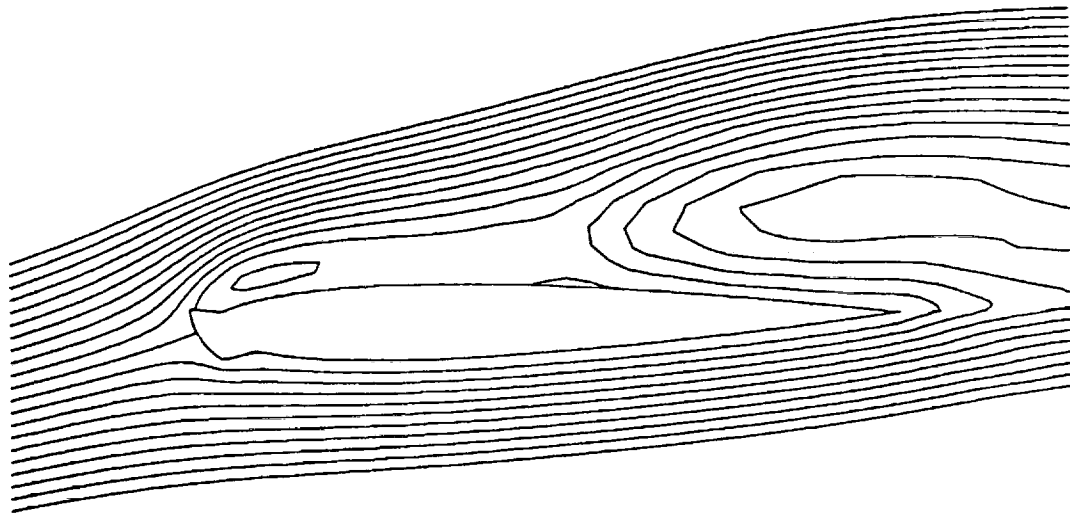
(a)
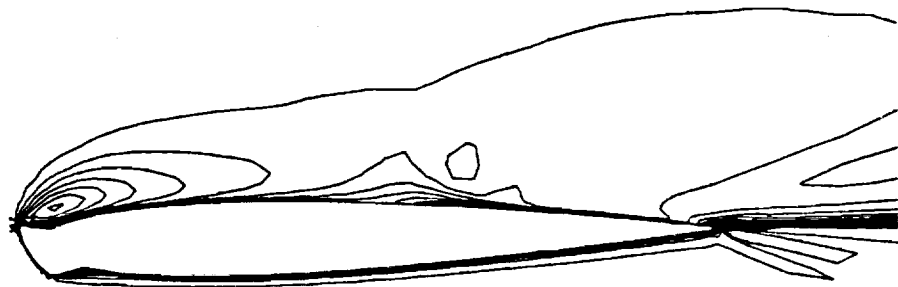
(b)

Figure 64   Vortex development on the NACA0012 airfoil with G1 ice shape; AOA=8°,

t=t$_0$+1800Δt; (a) stream function contours, (b) equi-vorticity contours
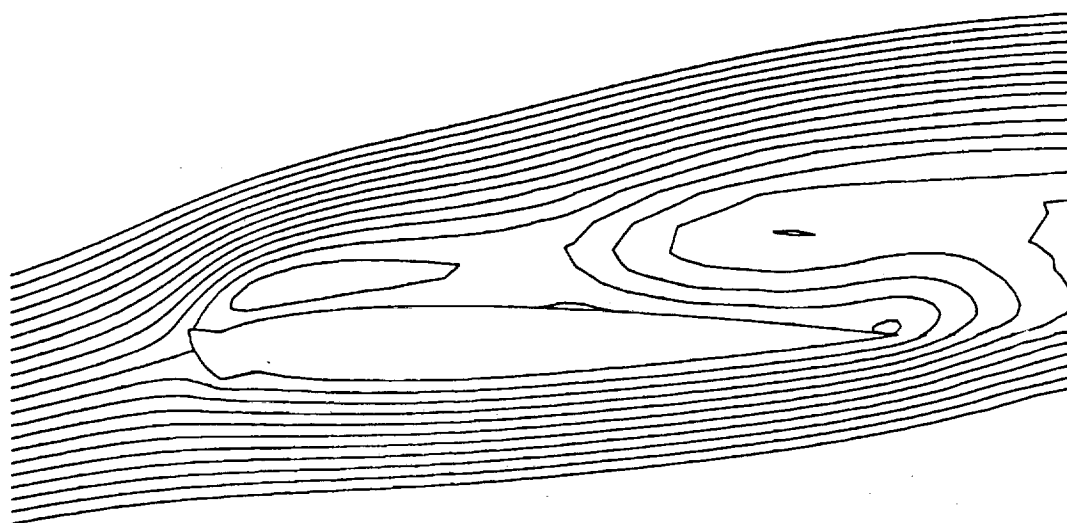
(a)
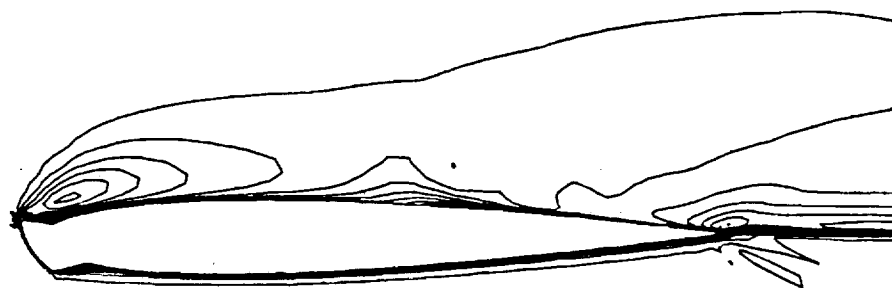
(b)

Figure 65   Vortex development on the NACA0012 airfoil with G1 ice shape; AOA=8°,

t=t$_0$+1900Δt; (a) stream function contours, (b) equi-vorticity contours
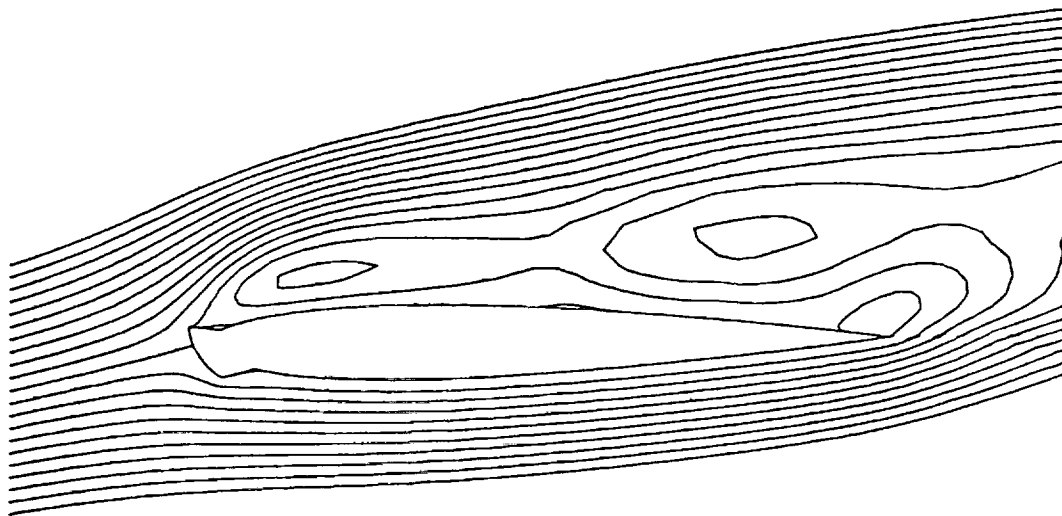
(a)

(b)

Figure 66   Vortex development on the NACA0012 airfoil with G1 ice shape; AOA=8°,

t=t$_0$+2000Δt; (a) stream function contours, (b) equi-vorticity contours

134
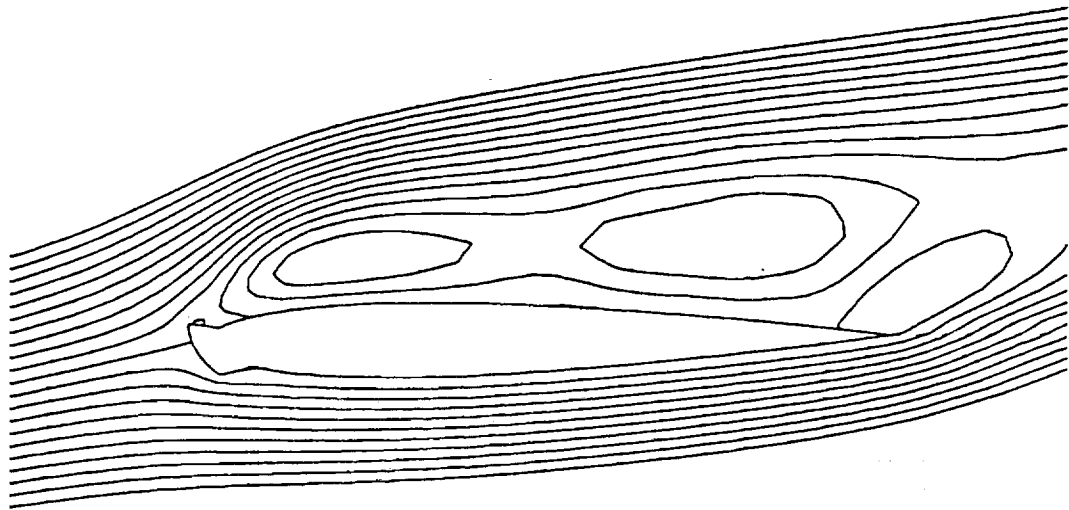
(a)
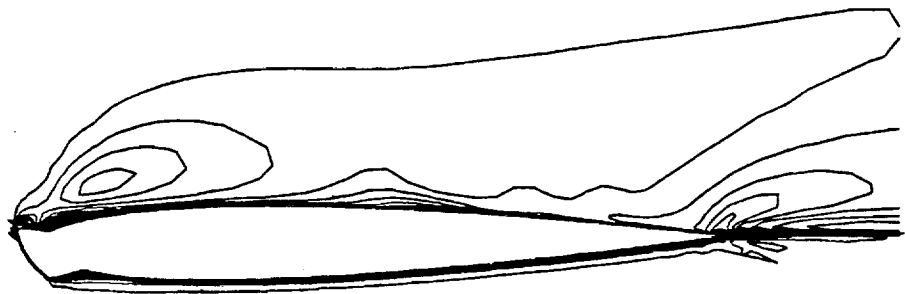
(b)

Figure 67   Vortex development on the NACA0012 airfoil with G1 ice shape; AOA=8°,

t=t$_0$+2100Δt; (a) stream function contours, (b) equi-vorticity contours
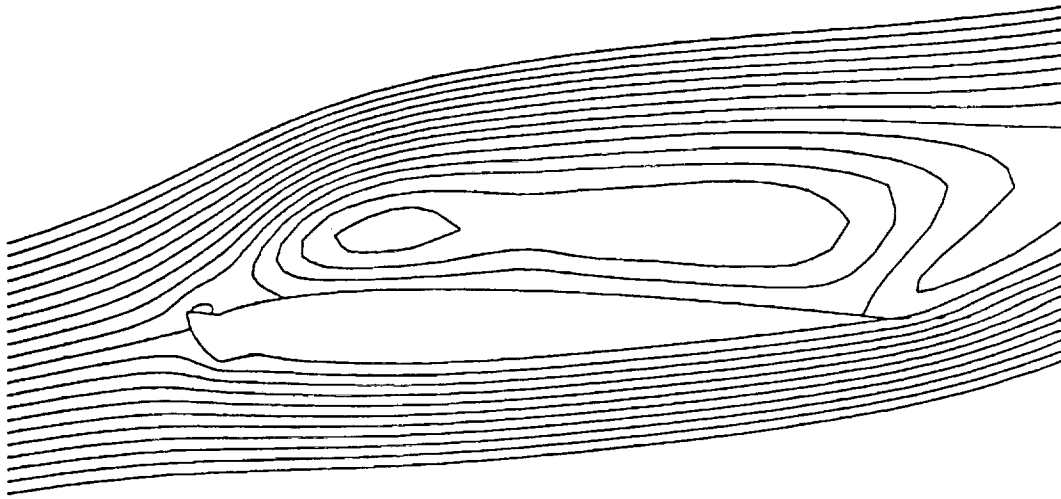
(a)
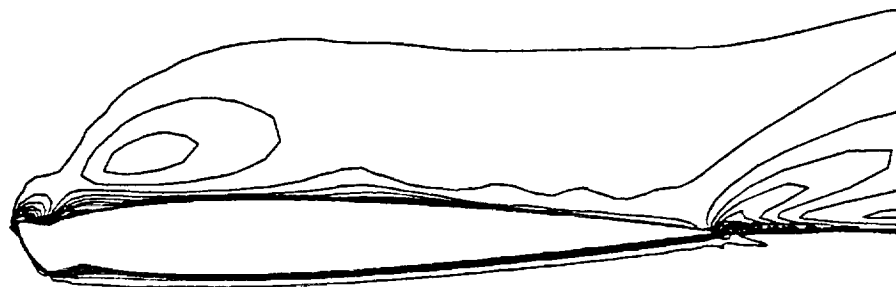
(b)

Figure 68   Vortex development on the NACA0012 airfoil with G1 ice shape; AOA=8°,

t=t₀+2200Δt; (a) stream function contours, (b) equi-vorticity contours
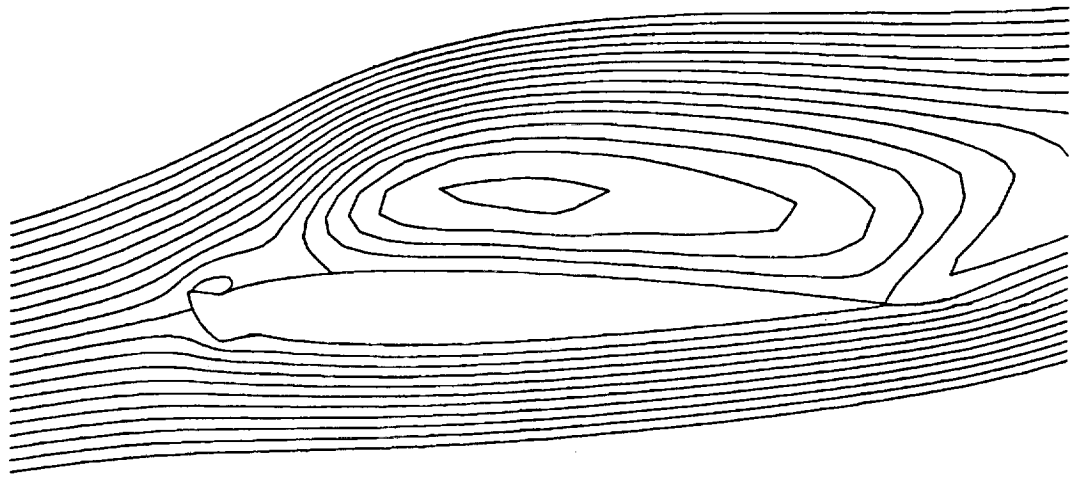
(a)
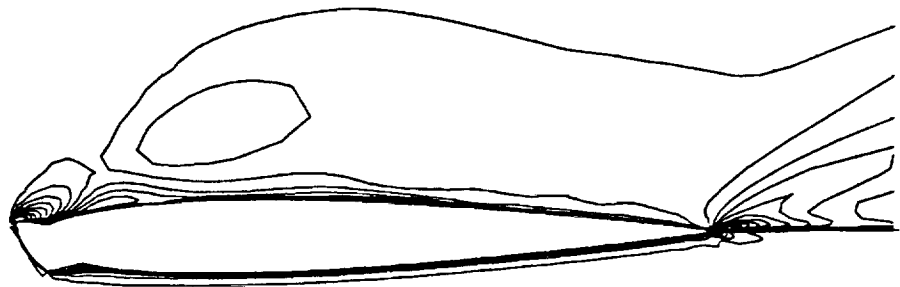
(b)

Figure 69   Vortex development on the NACA0012 airfoil with G1 ice shape; AOA=8°,

t=t_0+2300Δt; (a) stream function contours, (b) equi-vorticity contours
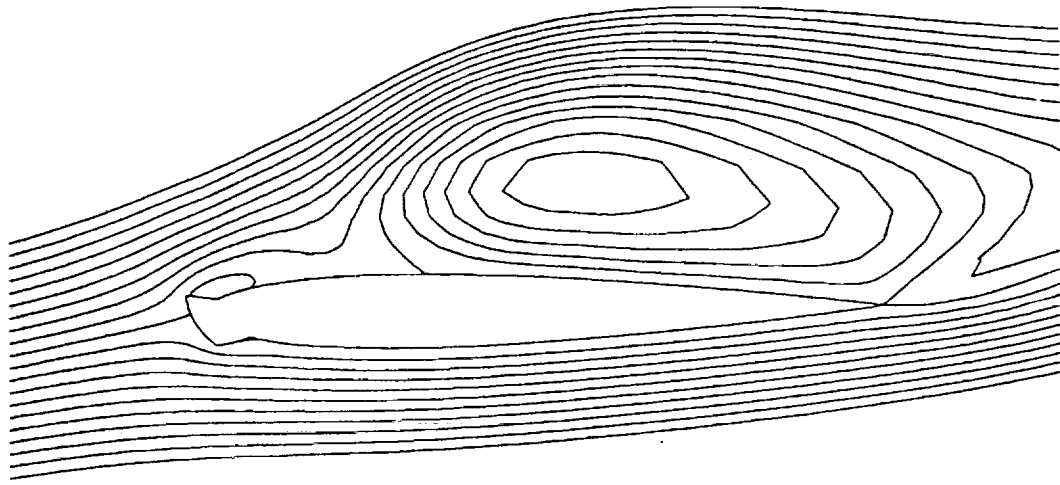
(a)
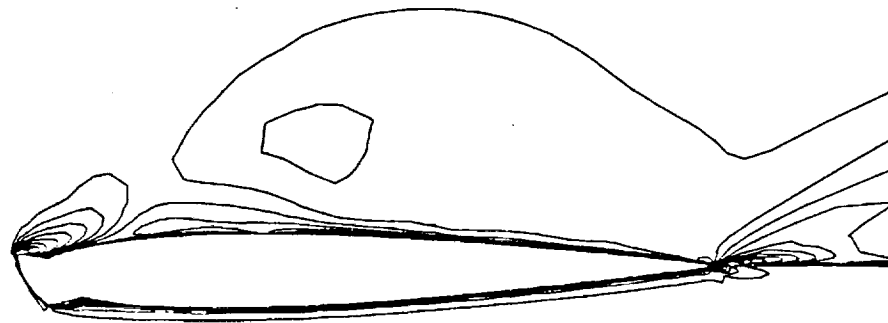
(b)

Figure 70   Vortex development on the NACA0012 airfoil with G1 ice shape; AOA=8°,

t=t$_0$+2400Δt; (a) stream function contours, (b) equi-vorticity contours
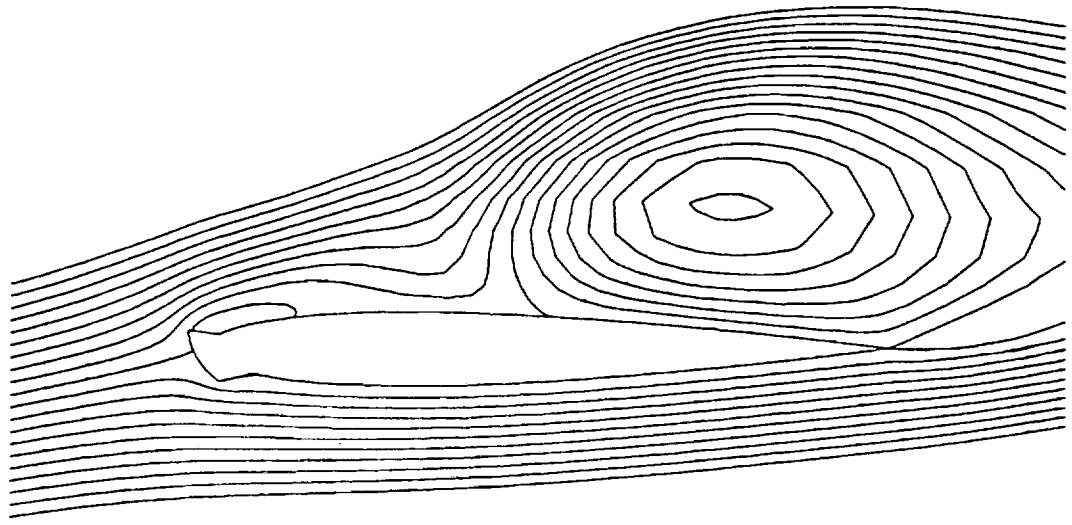
(a)
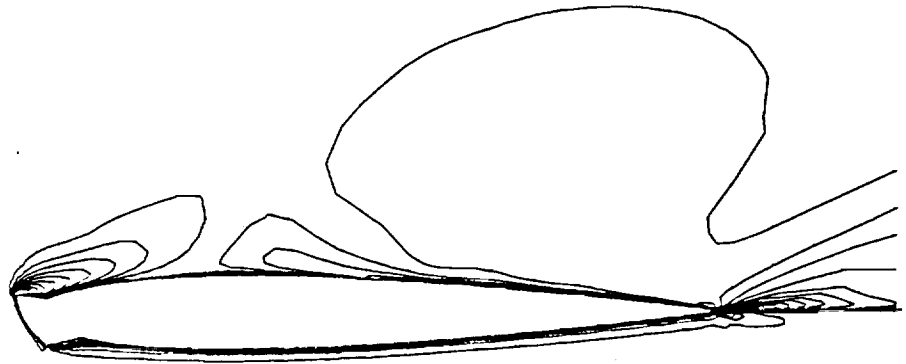
(b)

Figure 71   Vortex development on the NACA0012 airfoil with G1 ice shape; AOA=8°,

t=t$_0$+2500Δt; (a) stream function contours, (b) equi-vorticity contours
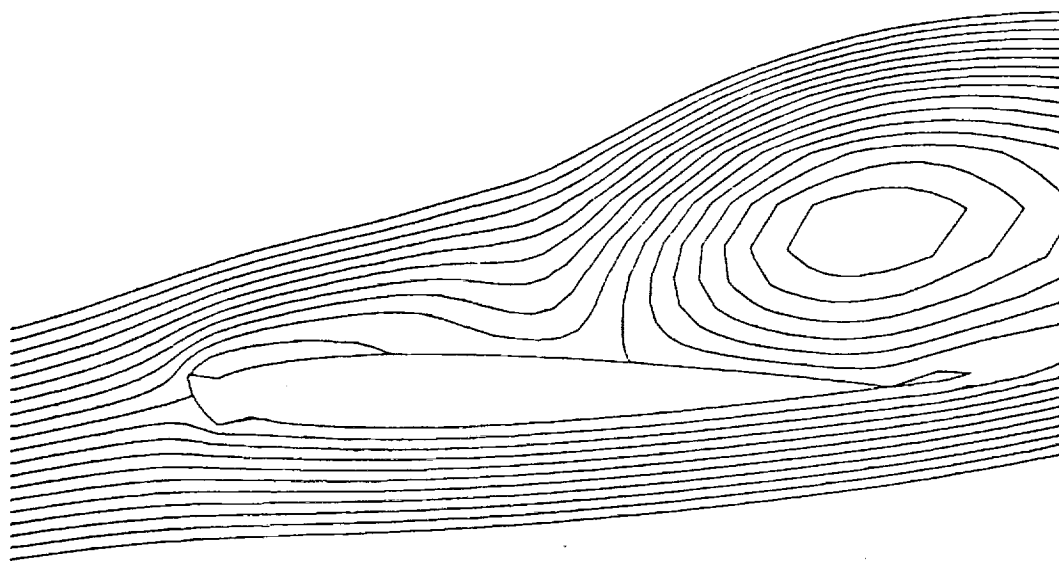
(a)
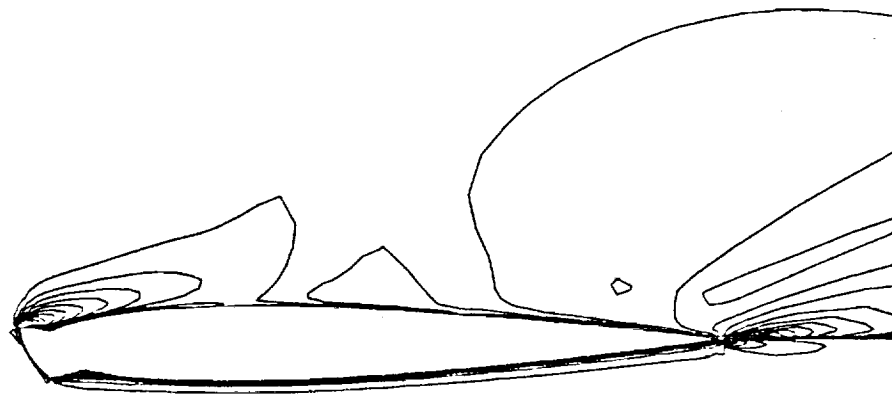
(b)

Figure 72   Vortex development and shedding on the NACA0012 airfoil with G1 ice shape;

t=t$_0$ + 2600Δt ;   (a) stream function contours, (b) equi-vorticity contours

140
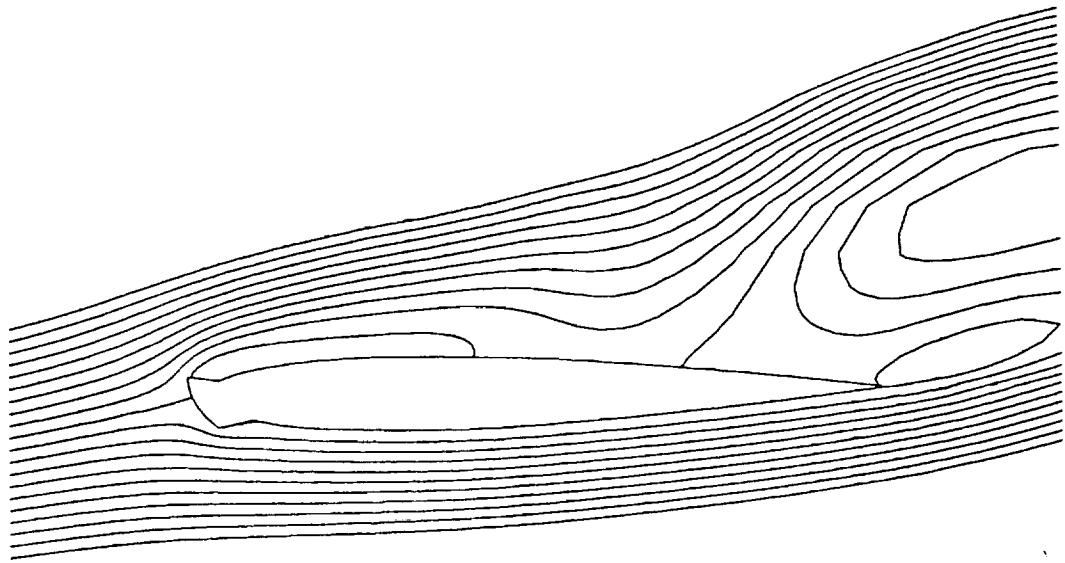
(a)
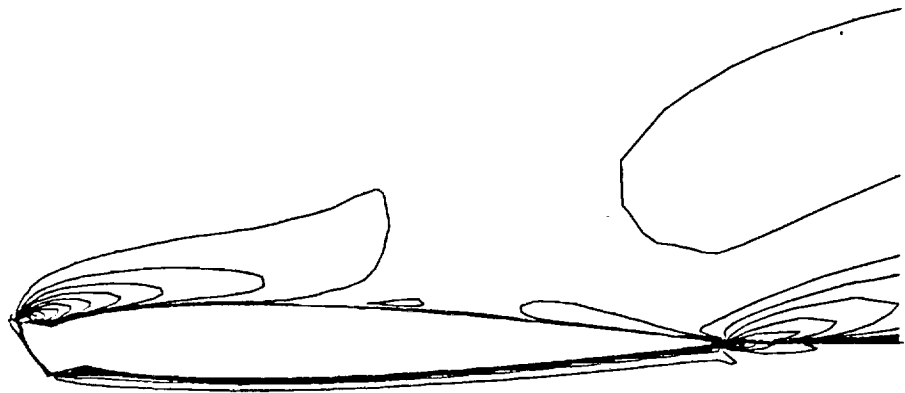
(b)

Figure 73   Vortex development and shedding on the NACA0012 airfoil with G1 ice shape;

$t=t_0 + 2700\Delta t$;   (a) stream function contours, (b) equi-vorticity contours
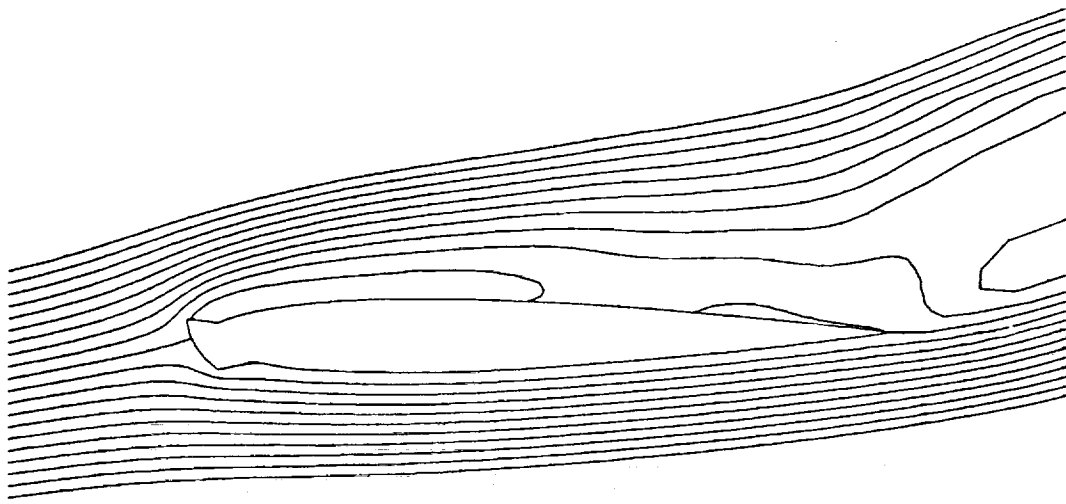
(a)
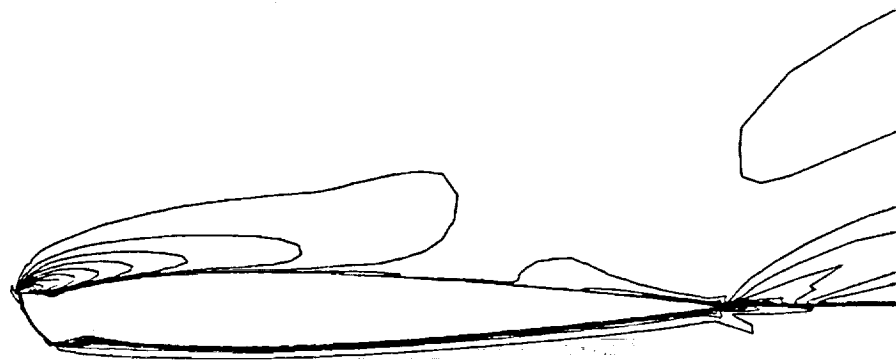
(b)

Figure 74   Vortex development on the NACA0012 airfoil with G1 ice shape; AOA=8°,

t=t₀+2800Δt; (a) stream function contours, (b) equi-vorticity contours

142
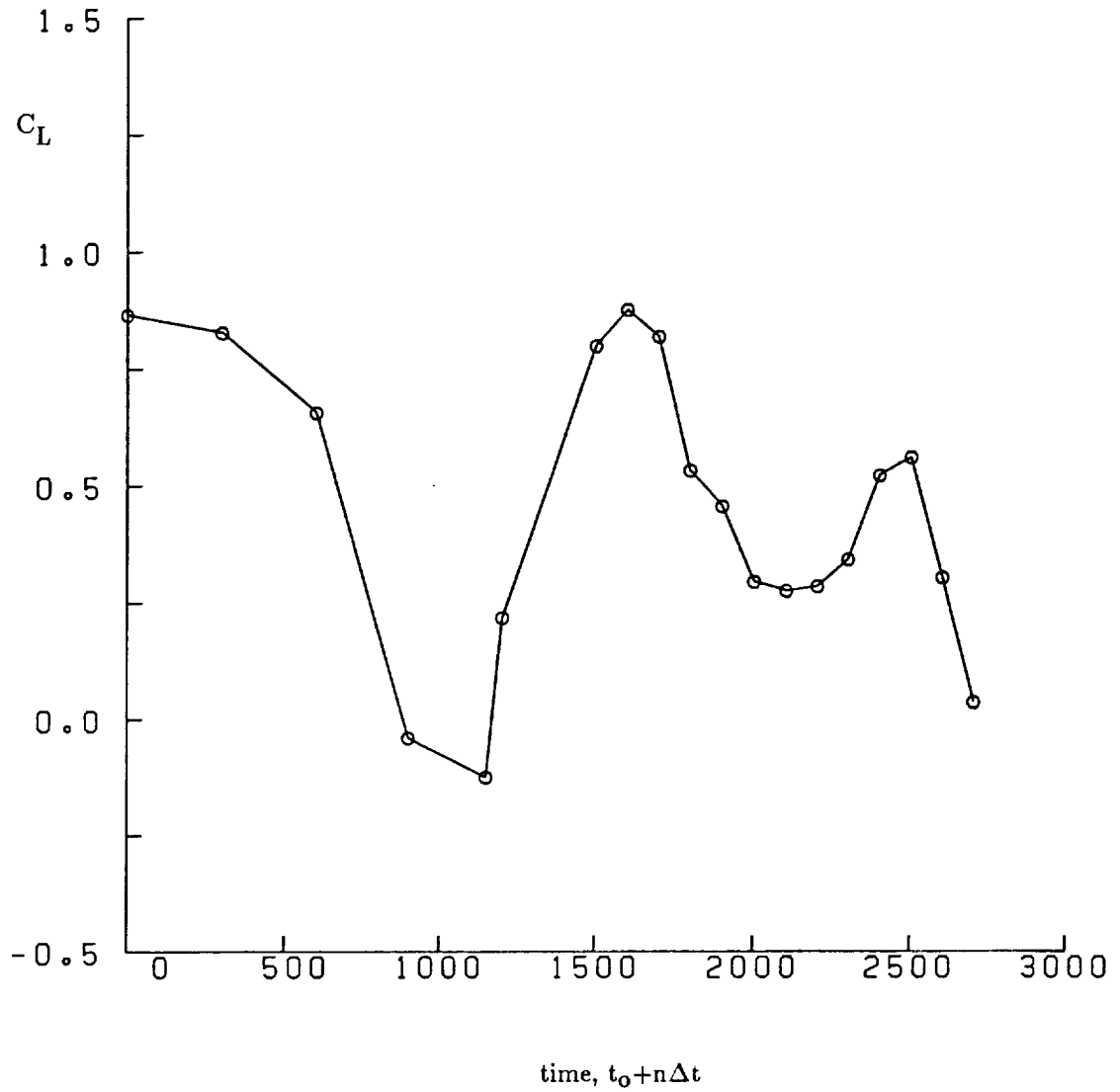
Figure 75   Lift history during vortex shedding process on NACA 0012 airfoil

with G1 ice shape

143

The next figure in the sequence has two significant features. The leading edge region exhibits a pinching off of the separation bubble and a gradual movement of the vortex center downstream and away from the surface. This coincides with a distinct shedding of vorticity from the surface toward the free stream. Also, the small bubble near the trailing edge has merged with the larger bubble and the resulting bubble has reattached to the surface. This second phenomenon is a residual adjustment to the previously shed vortex.

The bifurcation of the leading edge separation region can be attributed to the convection of vorticity away from the horn, where it is initially developed. As the process starts, a vortex is present just past the ice shape region. This vortex moves away, as time progresses, due to entrainment by the shear layer. It is replaced by vorticity which is constantly being generated at the horn itself. This last point is indicated by the constant vorticity level found at the horn, even as vorticity is being convected away. This is seen in figures 76-85, which show equi-vorticity contours near the horn. Thus, as one separation bubble moves along the airfoil surface another is being created at the horn to take its place. The timing of these two processes determines the amplitude and frequency of the lift and drag oscillations.

The reattachment of the bubble at the trailing edge keeps the separation bubble on the airfoil. This prevents the lift loss from being more severe. The vortex associated with this bubble can be clearly seen in figure 57. The drop in lift of the airfoil can be associated with the movement of this vortex away from the surface and into the wake, shown in figures 57-59. These figures show the growth of the negative and positive separation bubbles at the leading and trailing edges, respectively. These bubbles grow in strength and force the larger bubble to first separate from the surface (fig. 58) and then to flow into the wake (fig. 59). This vortex sustains lower pressures on the upper surface and when it leaves the surface these pressures increase. This collapse of the pressure peak produces the drop in lift.
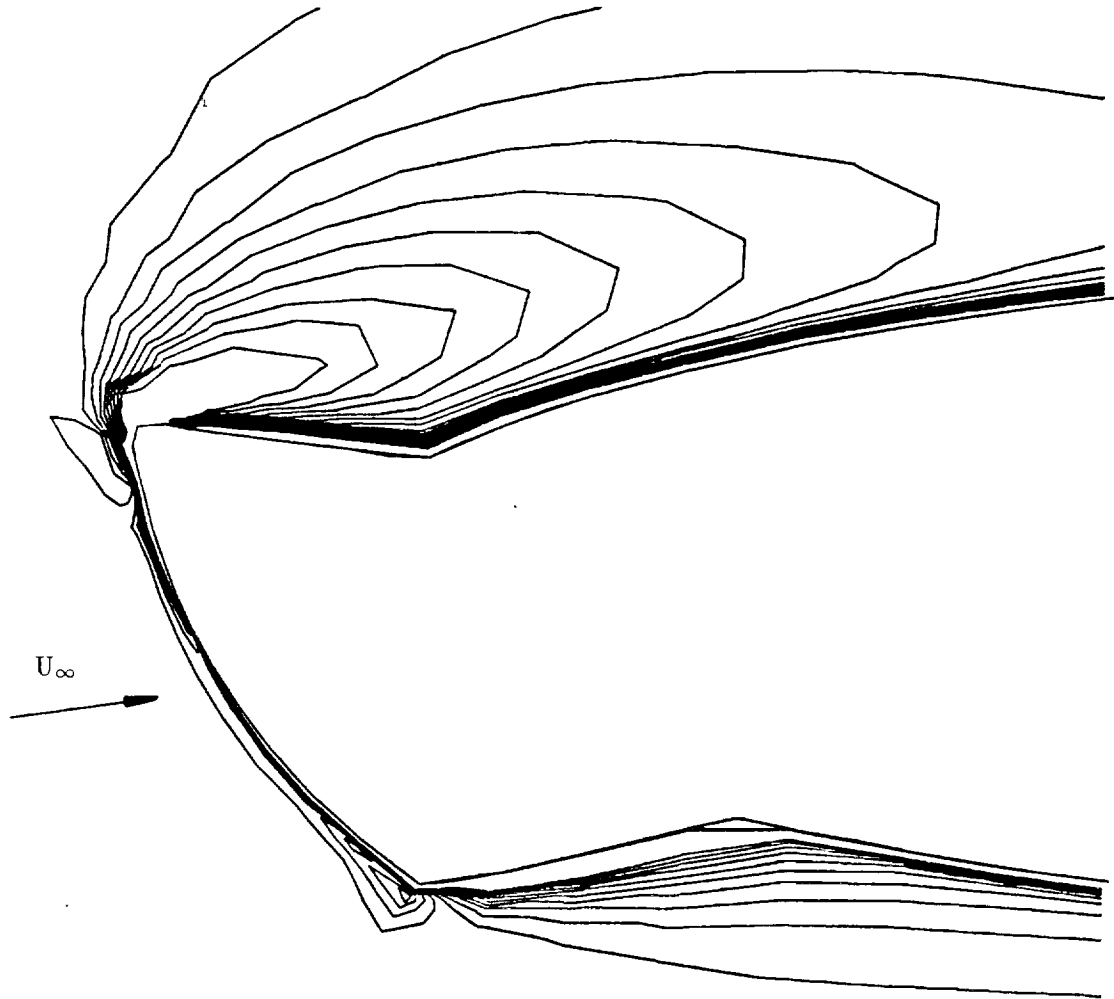
Figure 76   Equi-vorticity contours near the leading edge of the NACA0012 airfoil

with G1 ice shape; AOA=8°, t=t$_0$ + 1500Δt
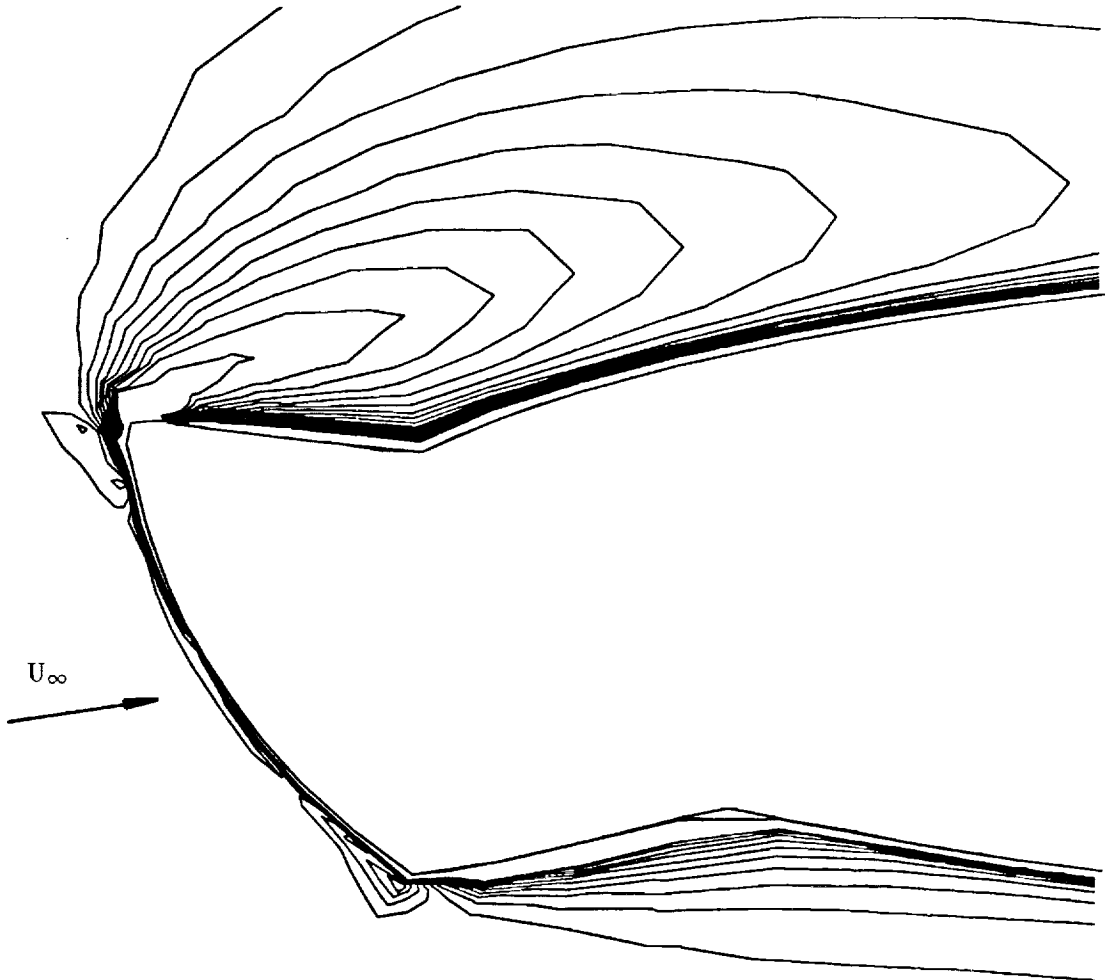
Figure 77   Equi-vorticity contours near the leading edge of the NACA0012 airfoil

with G1 ice shape; AOA=8°, t=t$_0$ + 1600Δt

146
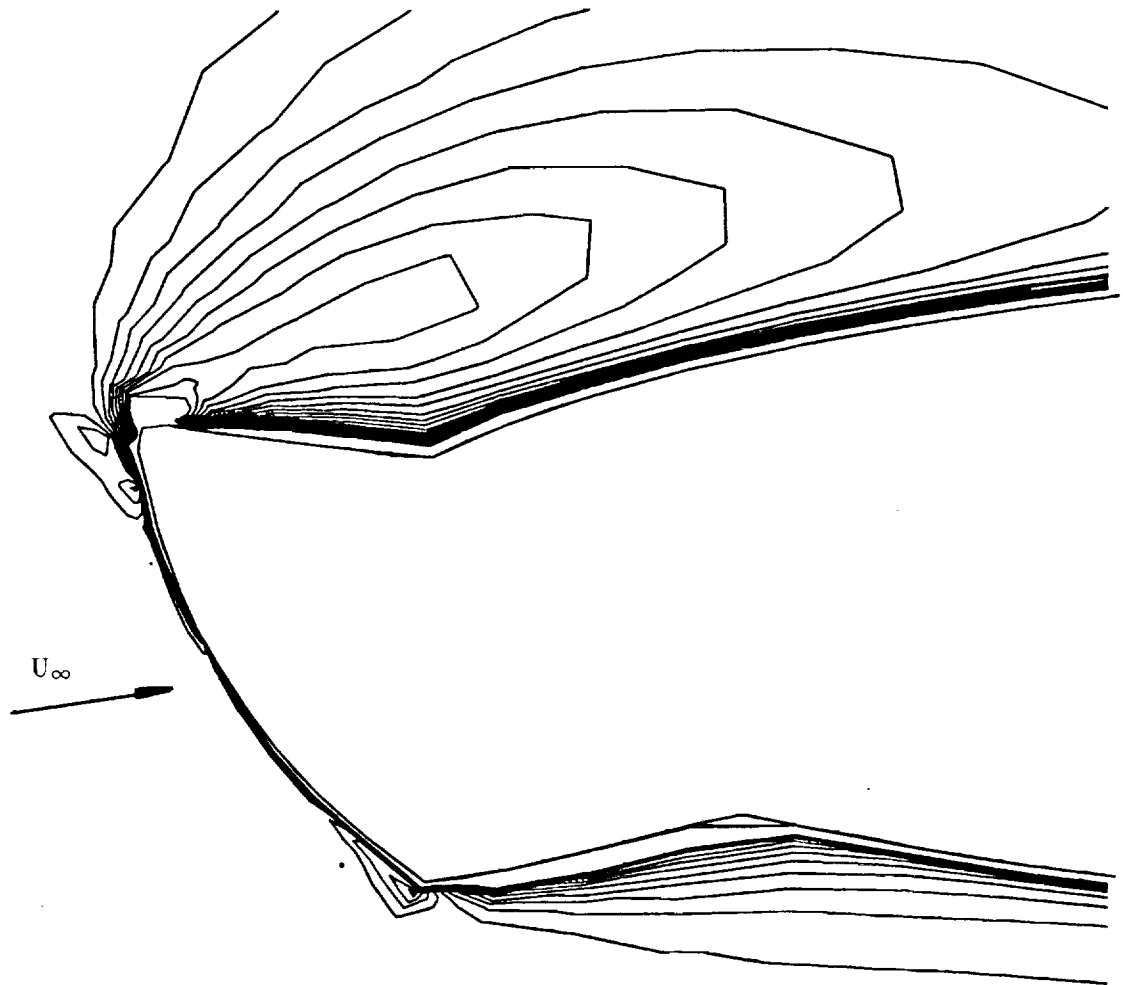
Figure 78   Equi-vorticity contours near the leading edge of the NACA0012 airfoil

with G1 ice shape; AOA=8°, t=t$_0$ + 1700Δt

147
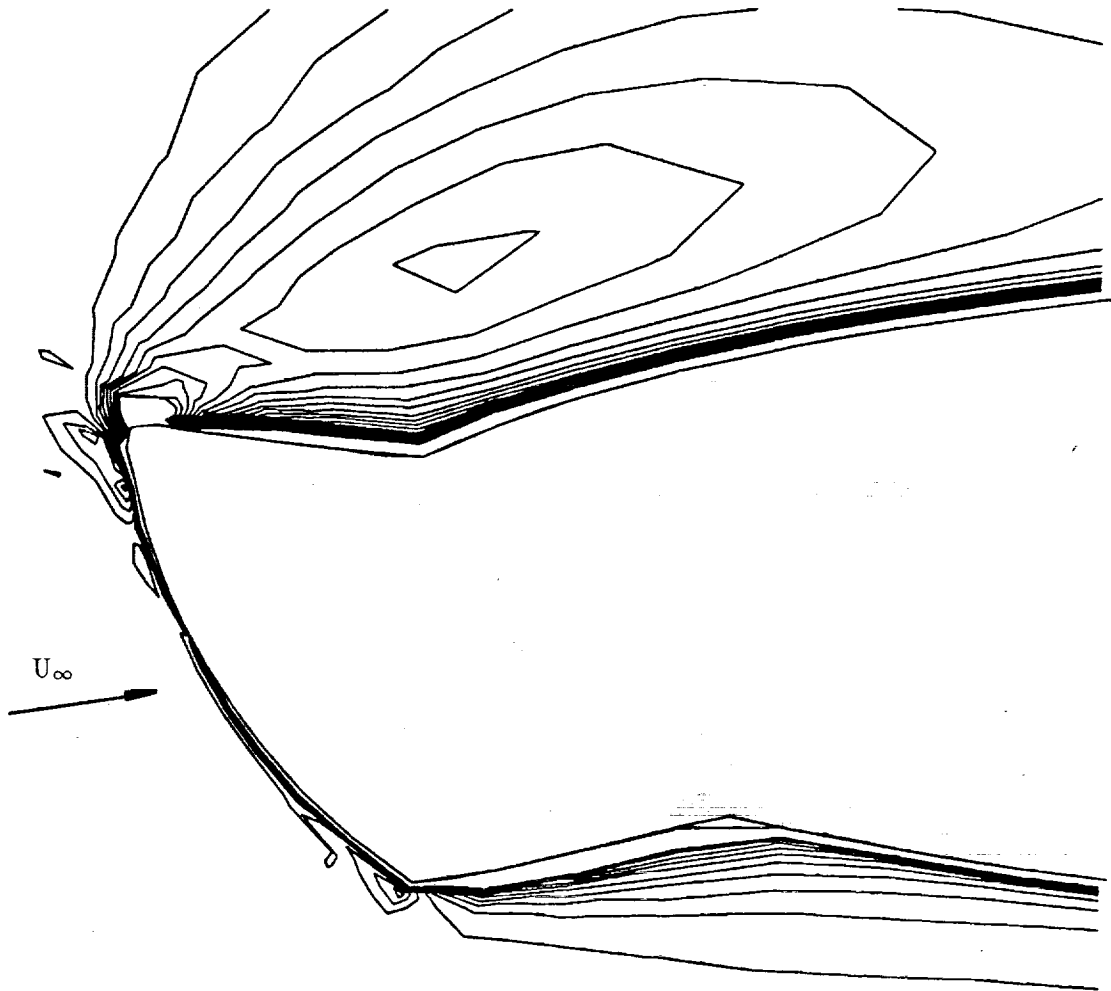
Figure 79   Equi-vorticity contours near the leading edge of the NACA0012 airfoil

with G1 ice shape; AOA=8°, t=t$_0$ + 1800Δt
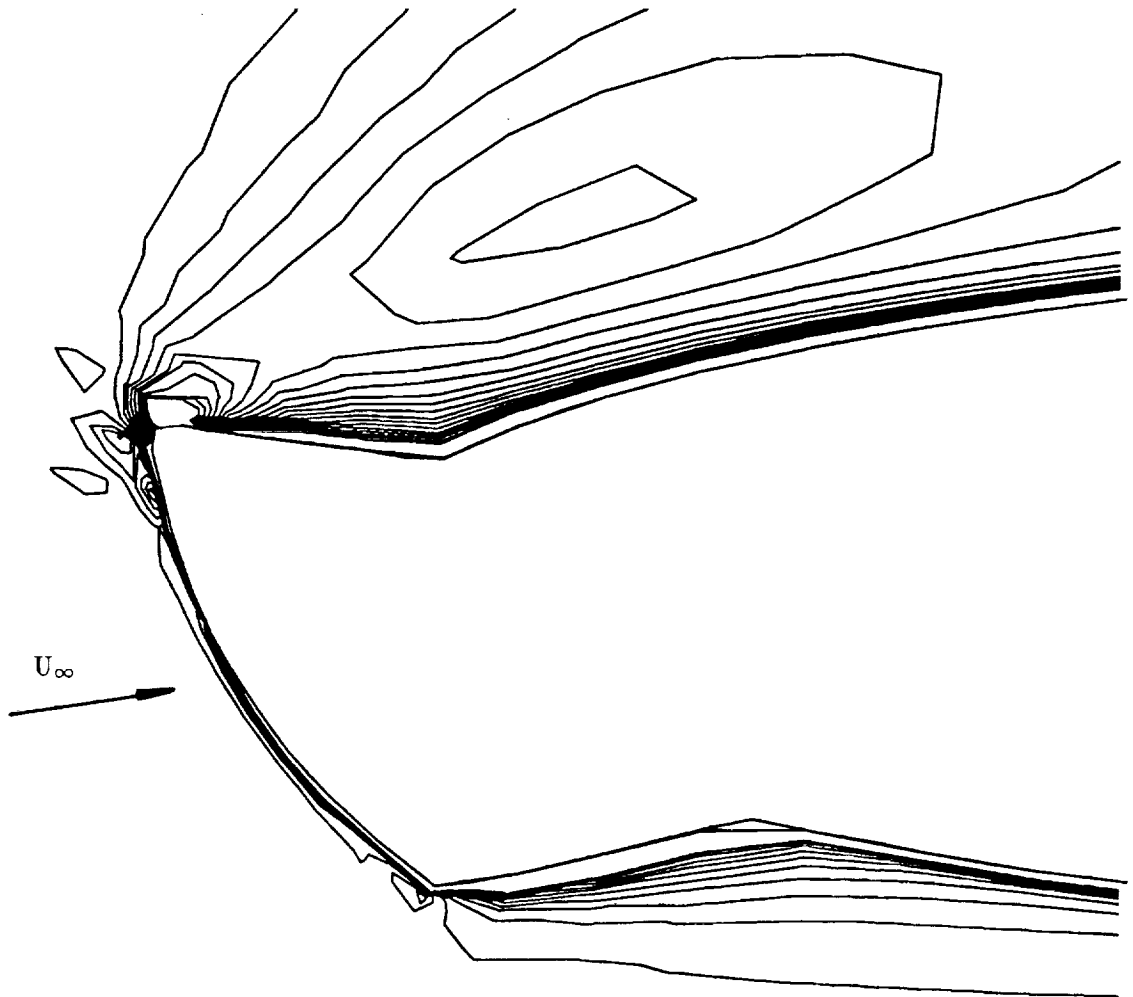
Figure 80   Equi-vorticity contours near the leading edge of the NACA0012 airfoil

with G1 ice shape; AOA=8°, t=t$_0$ + 1900Δt
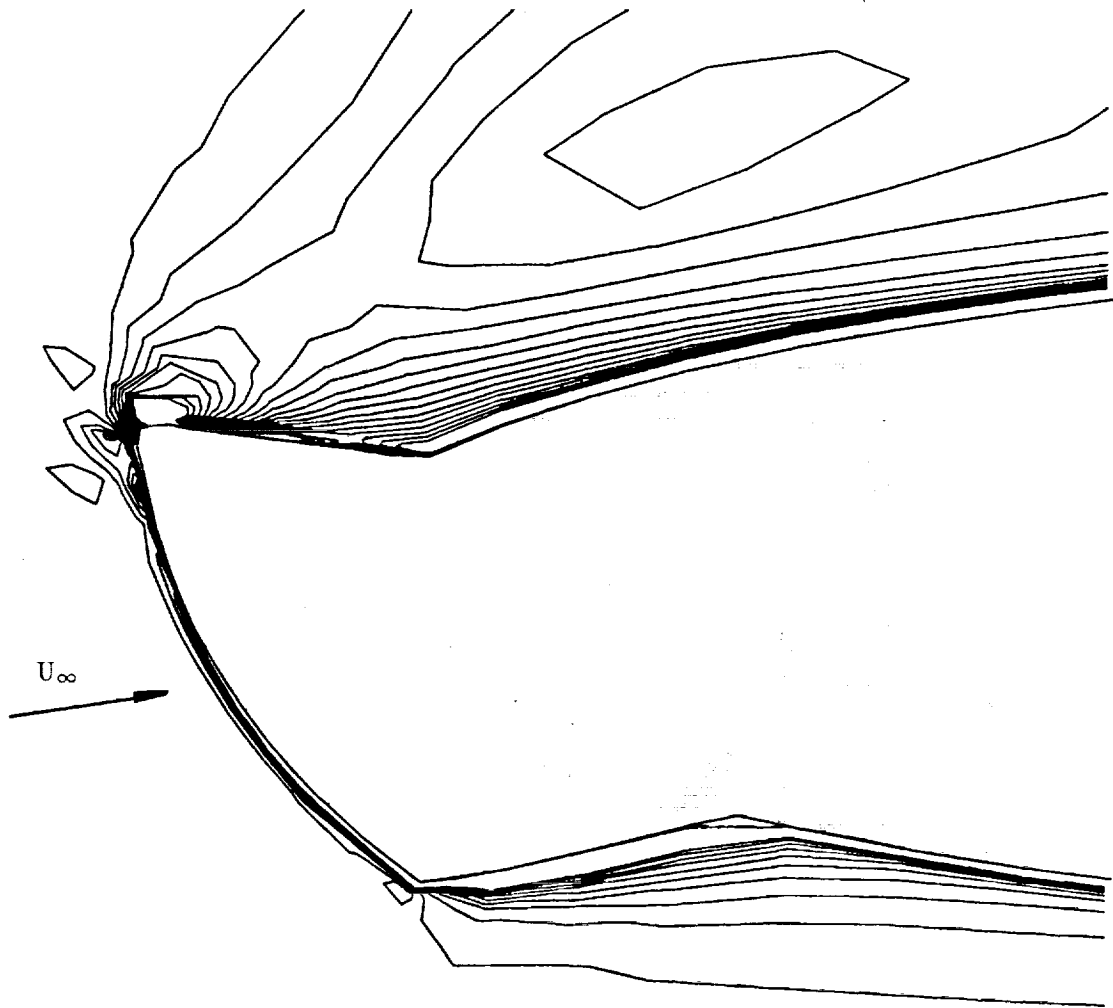
Figure 81   Equi-vorticity contours near the leading edge of the NACA0012 airfoil

with G1 ice shape; AOA=8°, t=t$_0$ + 2000Δt
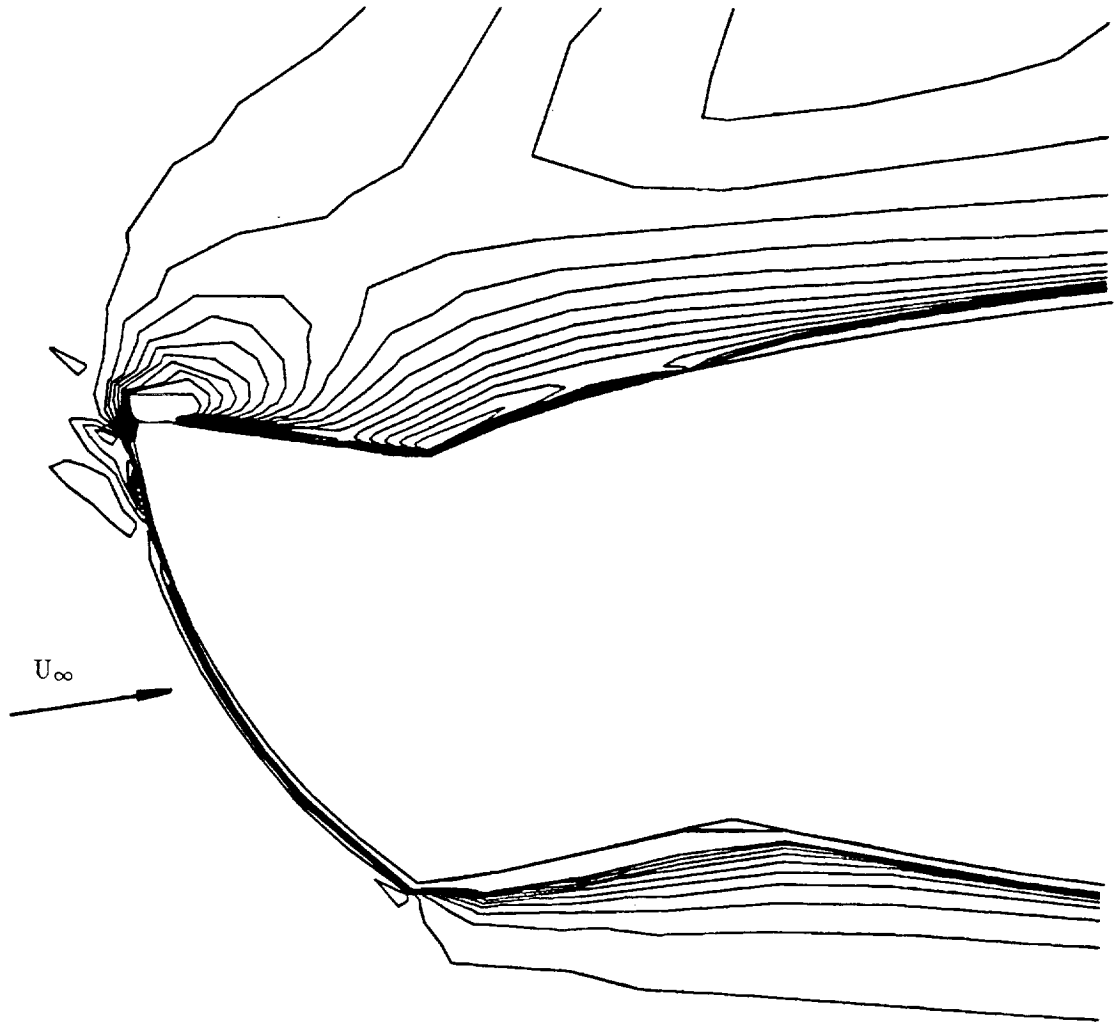
Figure 82   Equi-vorticity contours near the leading edge of the NACA0012 airfoil

with G1 ice shape; AOA=8°, t=t$_0$ + 2100Δt
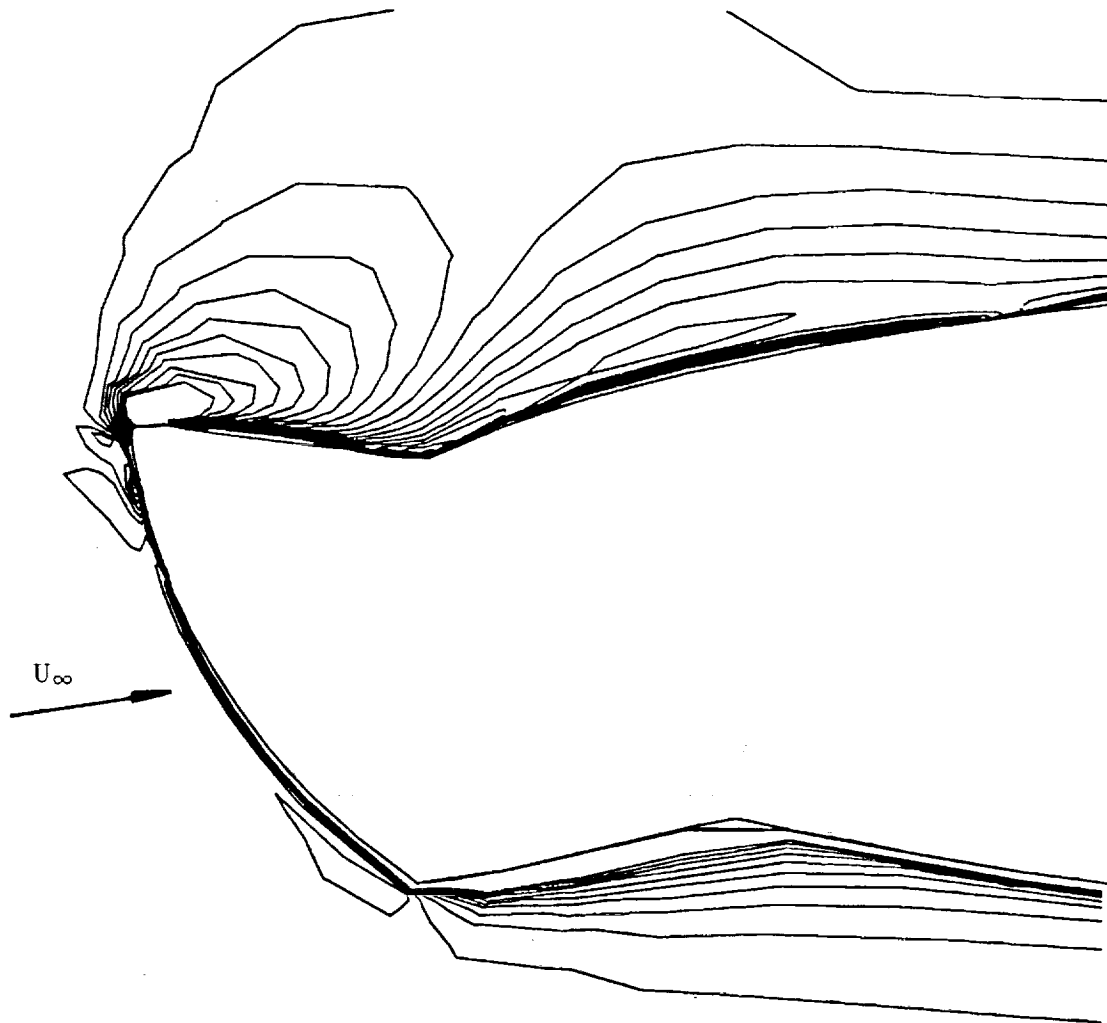
Figure 83   Equi-vorticity contours near the leading edge of the NACA0012 airfoil

with G1 ice shape; AOA=8°, t=t_0 + 2200Δt
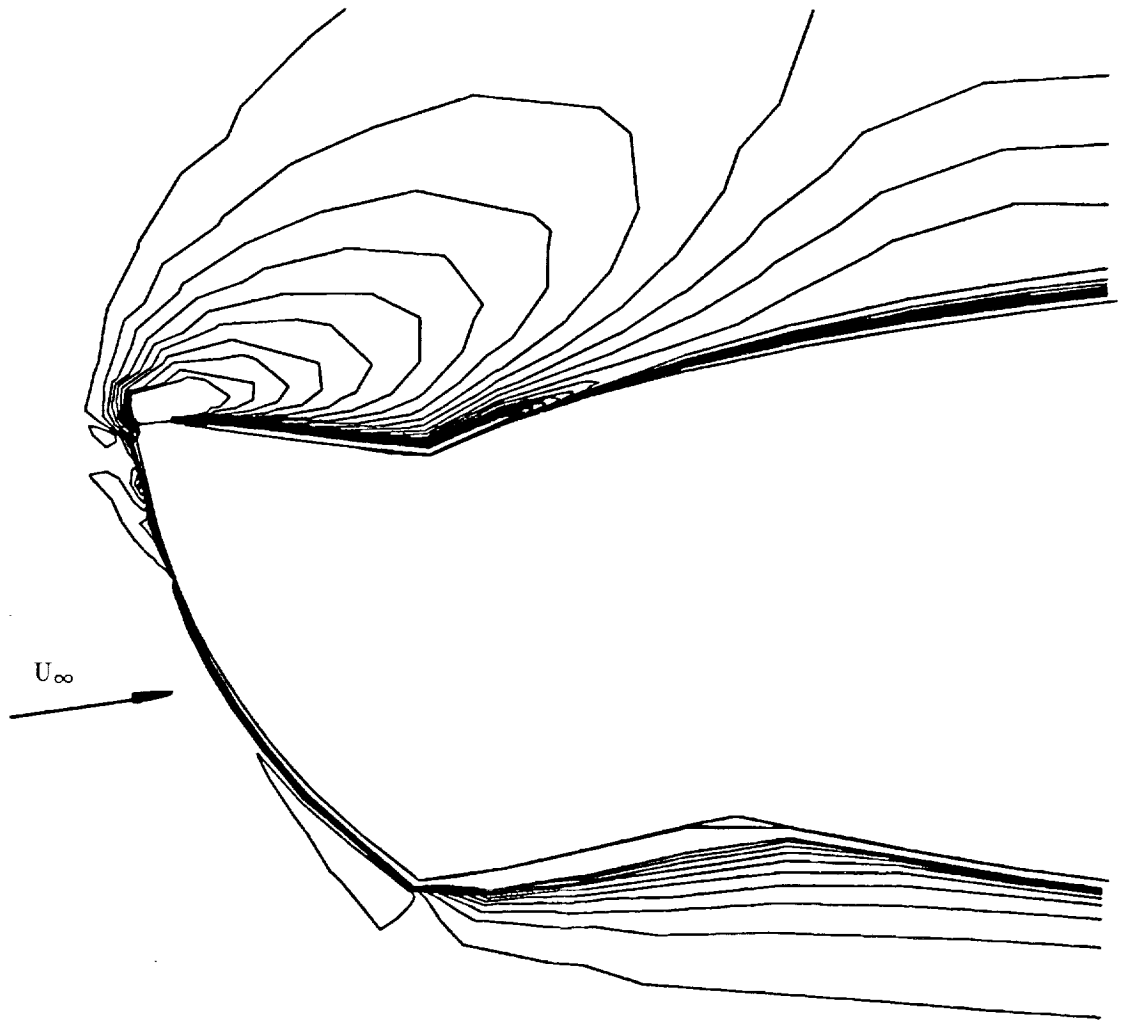
Figure 84   Equi-vorticity contours near the leading edge of the NACA0012 airfoil

with G1 ice shape; AOA=8°, t=t$_0$ + 2300Δt
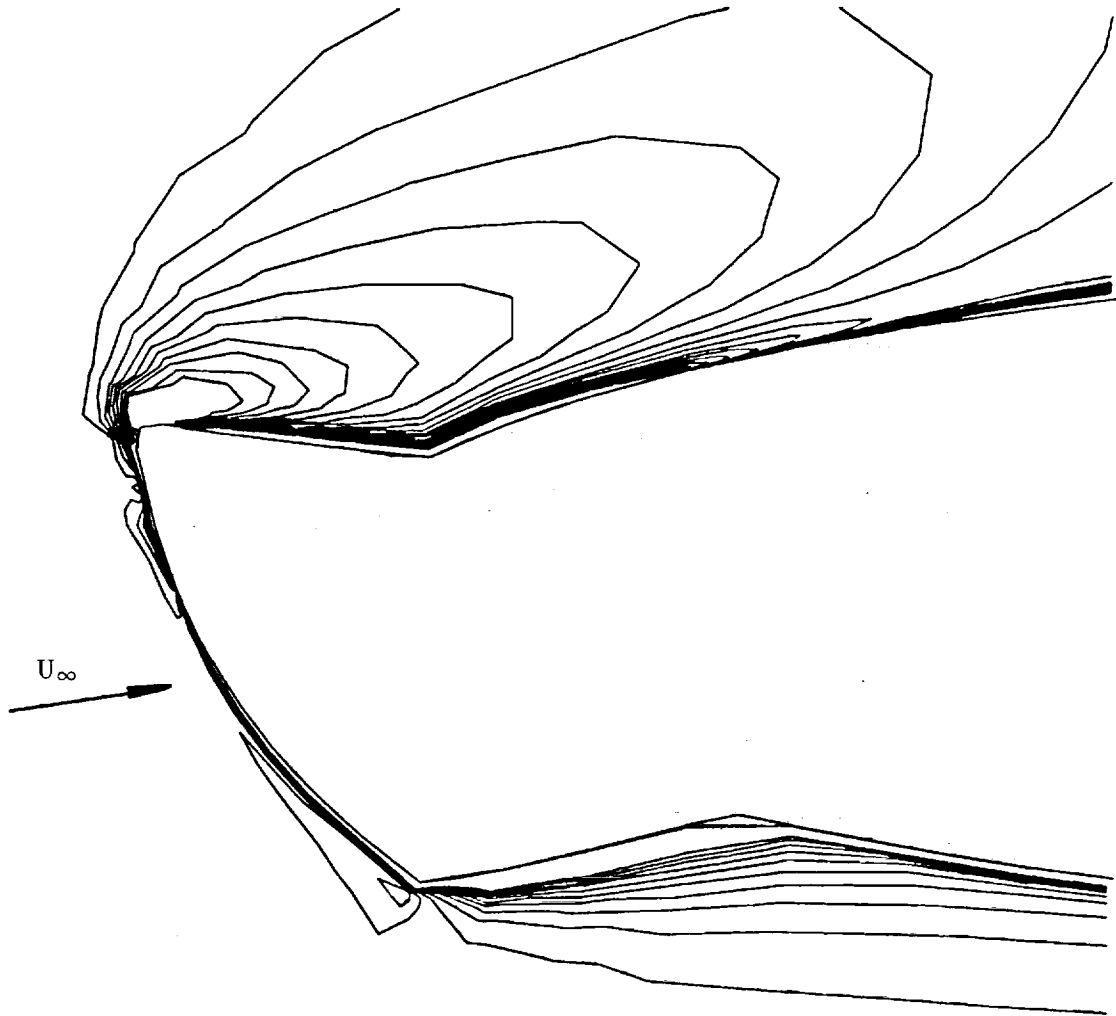
Figure 85   Equi-vorticity contours near the leading edge of the NACA0012 airfoil

with G1 ice shape; AOA=8°, t=t₀ + 2400Δt

There are two other interesting features of this shedding process. The vorticity on the lower surface remains undisturbed by the activity on the upper surface. The vorticity levels here are established by the airfoil/ice shape geometry and the angle of attack. Additionally, the leading edge stagnation point remains at the same location throughout the process. The stagnation region appears to be well isolated from the unsteady flow by the horn of the ice shape. This last point has significant consequences for the modeling of the ice accretion process itself. It appears that extreme accuracy in modeling of the flowfield downstream of the ice shape is not necessary for correct representation of the incoming flow. Some accounting for separation may be necessary, however, for establishing the correct limits of water droplet impingement. Certainly, further examination of the flow near the separation region should be undertaken in order to confirm this assertion.

Figure 60 indicates that the vorticity generated at the horn has again grown to encompass the entire upper surface of the airfoil. This occurs as a result of the movement of the previous bubble off the airfoil surface. The flowfield pattern is now similar to that of figure 56, however, there are significant differences which result in a slightly altered shedding sequence for this bubble. In this case, the bulge in the separation bubble is centered more toward the trailing edge. This would suggest a shorter shedding period, as the bubble is already further along the surface. Indeed, figures 61-65 show that half the bubble has moved into the wake before the positive bubble develops at the trailing edge. This produces a somewhat different shedding behavior and consequent changes in lift and drag.

During this shedding period, the large negative bubble is not shed completely but is pinched off by the positive bubble. Figures 65-67 show how the negative bubble is essentially cut in two with some fluid moving into the wake and some being forced back onto the airfoil surface. As a result, the circulation on the surface is restored as indicated by the reattachment

155

of the bubble seen in figure 68. This causes the decrease in lift to stop at a C_L value of approximately 0.3 as compared to the minimum C_L value of -0.1 from the previous shedding cycle.

Examination of figures 76-83 indicates that during this time a new negative vortex has developed at the horn. This vortex grows in size and strength until, during the interval from $t = t_o+1800\Delta t$ until $t = t_o+2200\Delta t$, the vortex separates from the horn and moves further back along the airfoil surface. This event corresponds to the detachment of the separation bubble from the horn. The vorticity level at the horn itself remains essentially constant, apparently independent of the shedding process occurring downstream. The vorticity level at the horn appears to be established by the horn geometry, the angle of attack, and the freestream conditions. Consequently, modeling the flow in this region is extremely important for establishing the correct size, strength, and timing of the vortex shedding process. How much detail of the horn geometry is required, what grid size and spacing is appropriate, and what type of flow modeling is appropriate are all pertinent questions when trying to capture the details of this process.

Figures 68-74 show the movement of the separation bubble along the airfoil surface and its subsequent shedding into the wake. This case is more like the first shedding event, in that the separation bubble is almost completely off the surface by the time the positive bubble develops. It is interesting to note the changes occuring to the separation bubble, as it moves along the airfoil surface. More fluid appears to enter the bubble as indicated by the larger number of stream function contours. At the same time, the vorticity levels do not seem to change considerably, thus indicating no significant change in the amount of circulation associated with this bubble. The lift increase must, therefore, be due to the vorticity being generated at the horn. When the bubble finally bursts (fig. 72), the drop in circulation is much greater than the amount being generated at the horn and hence the lift decreases rapidly.

The positive vorticity which develops at the trailing edge is seen to remain on the airfoil upper surface (i.e. figure 74). This further reduces the lift such that, at $t_0 + 2800\Delta t$, it is negative. This region of positive vorticity eventually merges with the leading edge vortex, as was the case in figures 59 and 60. This merging of the two regions and the continuing creation of negative vorticity at the leading edge leads to an eventual restoration of the lift, until the entire cycle repeats.

The turbulence model can have a significant impact on the development of the separation bubbles associated with this shedding process. As seen in the previous chapter, the Baldwin-Lomax model has some difficulties with separated flow due to the specification of the F_{max} parameter. The behavior of the MML model during the vortex shedding is seen in figures 86-91. The regions of highest turbulent dissipation correspond to locations of separation and reattachment. This insures that velocity levels in these regions remain low, consistent with expectations. These regions move along the surface, following the motion of the separation bubbles. As the bubble moves along the surface, the turbulence level decreases reflecting the lower mean flow velocities within these regions.

The other interesting feature of the turbulence model behavior during this sequence is the development of the leading edge region. The eddy viscosity levels just aft of the upper-surface horn remain consistently high throughout the shedding cycle. Thus, as vorticity is constantly generated at the horn the turbulence level remains correspondingly high. These μ_t levels can in turn influence the growth rate of the vorticity and some type of feedback mechanism is thus established. Accurate prediction of turbulence levels near the horn is therefore essential to the correct prediction of the vortex shedding time scales and hence of the integrated force coefficient values for this post-stall behavior.

Finally, examination of the lower-surface indicates steady flow behavior with associated constant eddy viscosity values. The vorticity generation rate at this horn must be

(a)

(b)
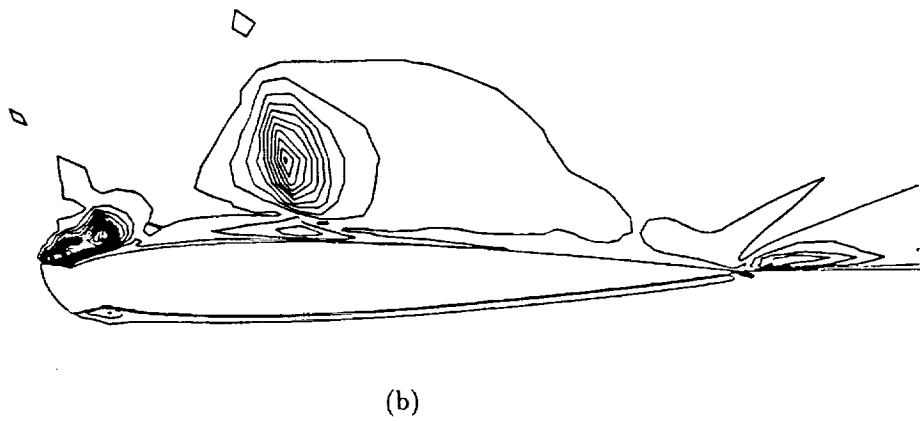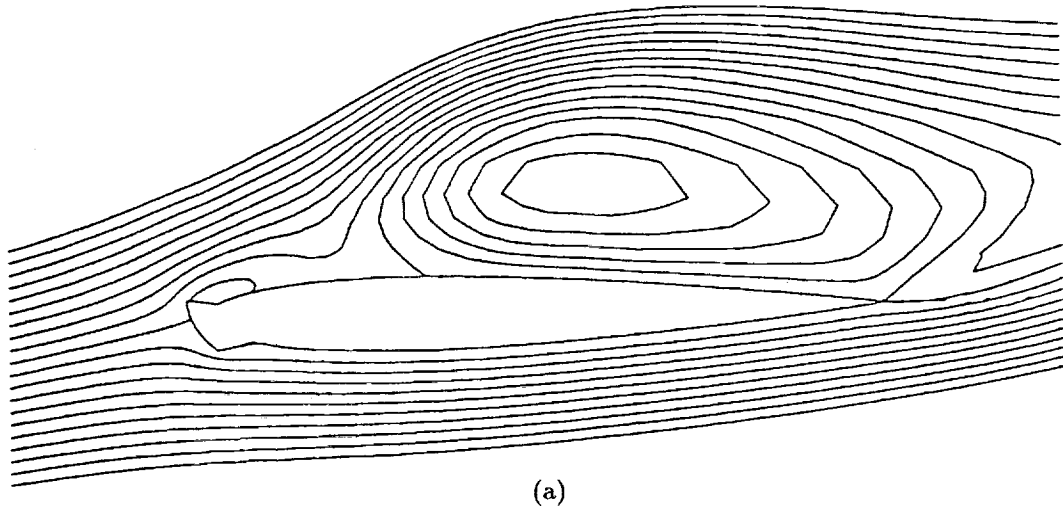
Figure 86   Turbulence model behavior during vortex shedding process; AOA=8°,

t=t₀+2400Δt; (a) stream function contours, (b) eddy-viscosity contours
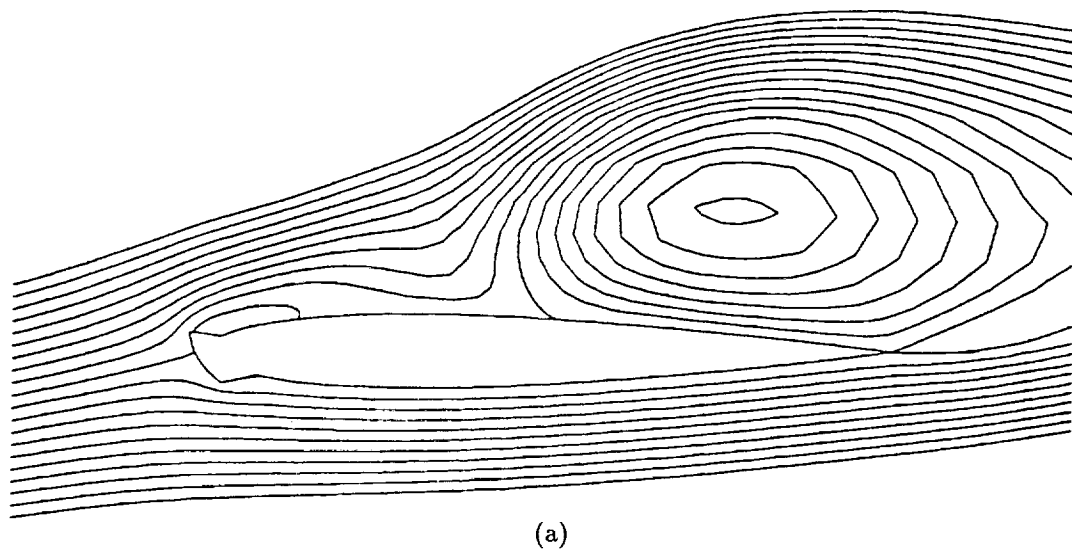
(a)
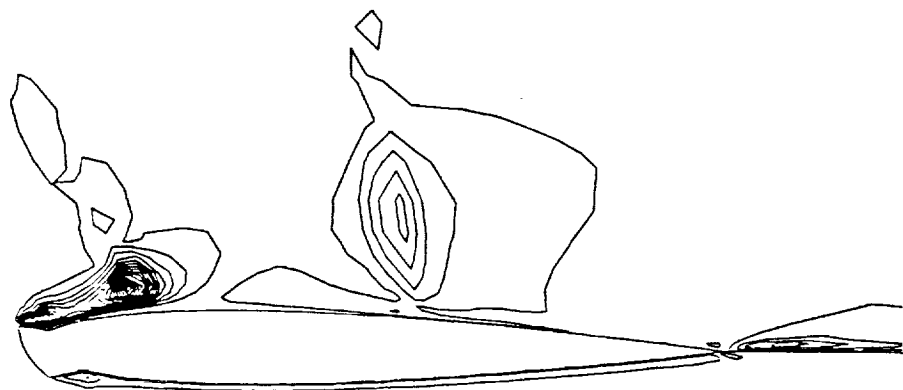
(b)

Figure 87   Turbulence model behavior during vortex shedding process; AOA=8°,

t=t$_0$+2500Δt; (a) stream function contours, (b) eddy-viscosity contours

(a)

(b)
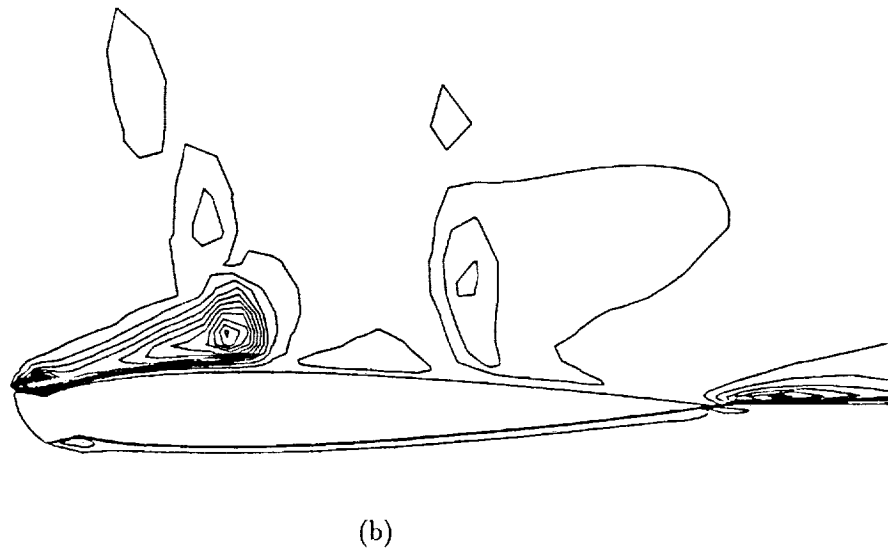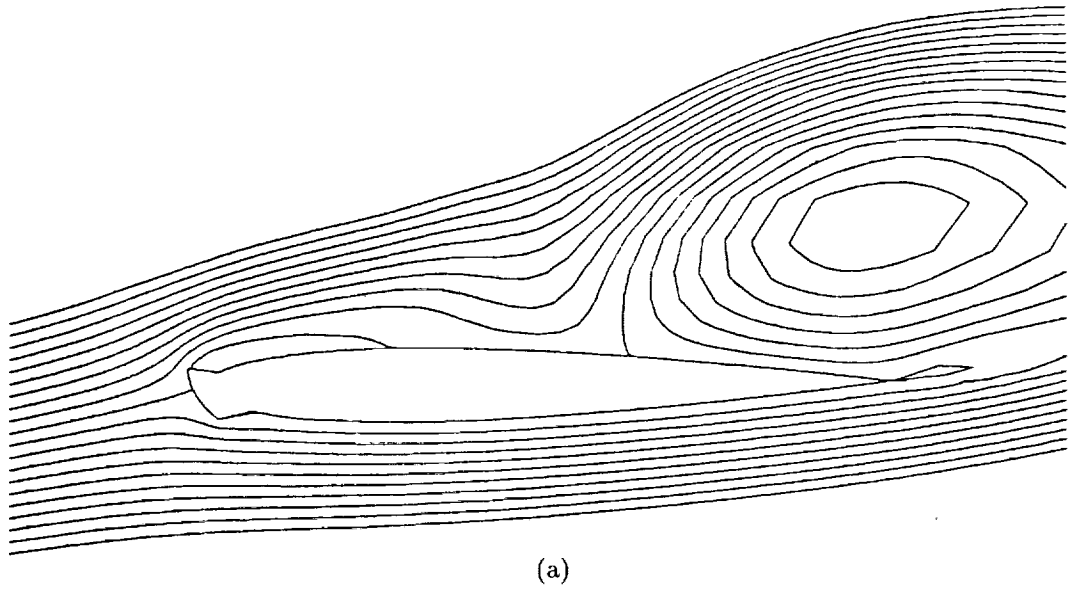
Figure 88   Turbulence model behavior during vortex shedding process; AOA=8°,

t=t₀+2600Δt; (a) stream function contours, (b) eddy-viscosity contours

160
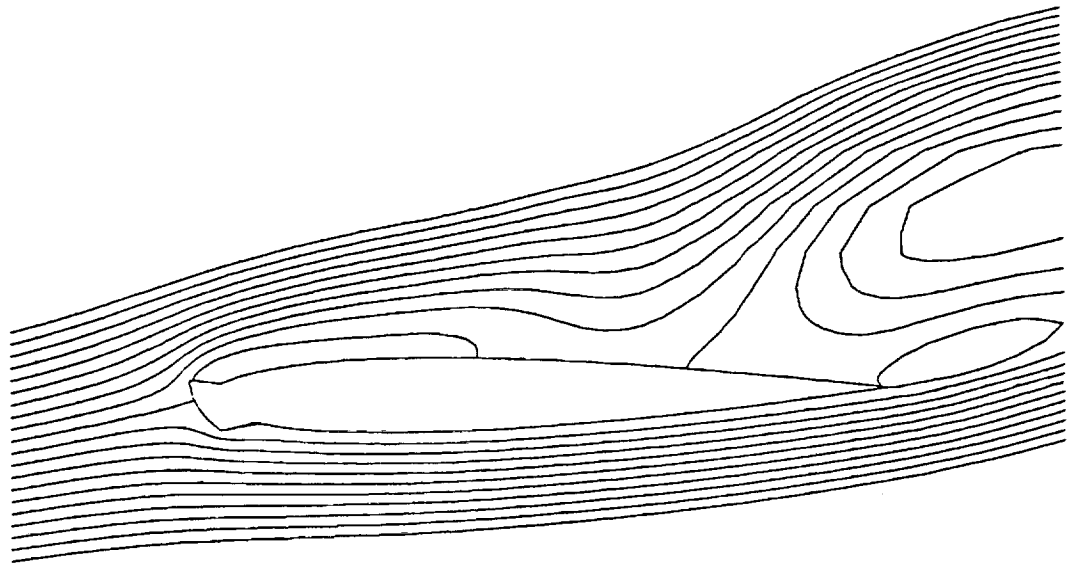
(a)
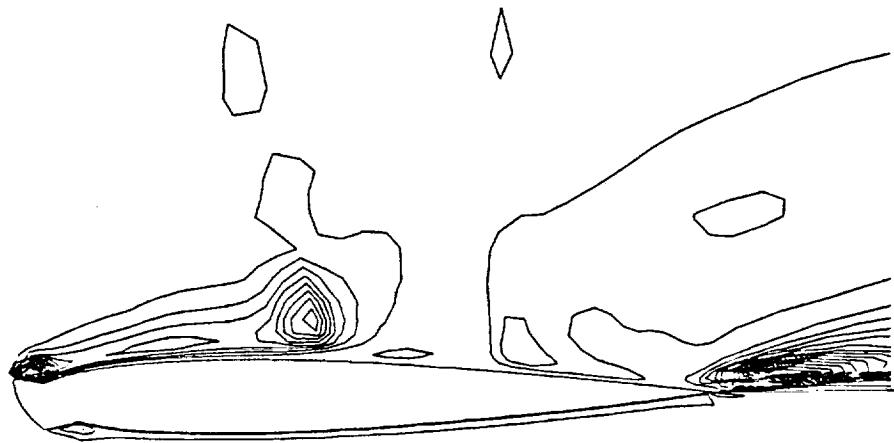
(b)

Figure 89   Turbulence model behavior during vortex shedding process; AOA=8°,

t=t₀+2700Δt; (a) stream function contours, (b) eddy-viscosity contours
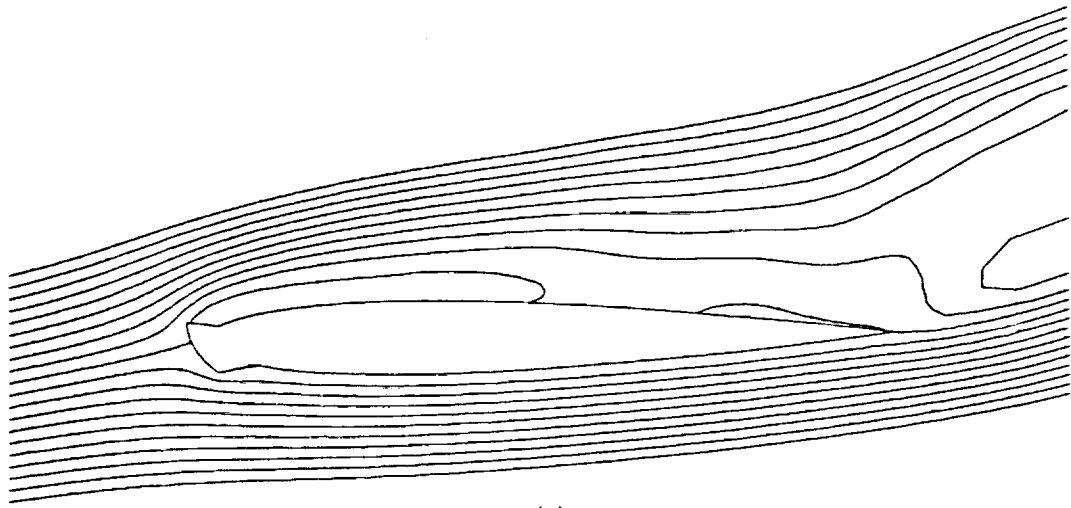
(a)
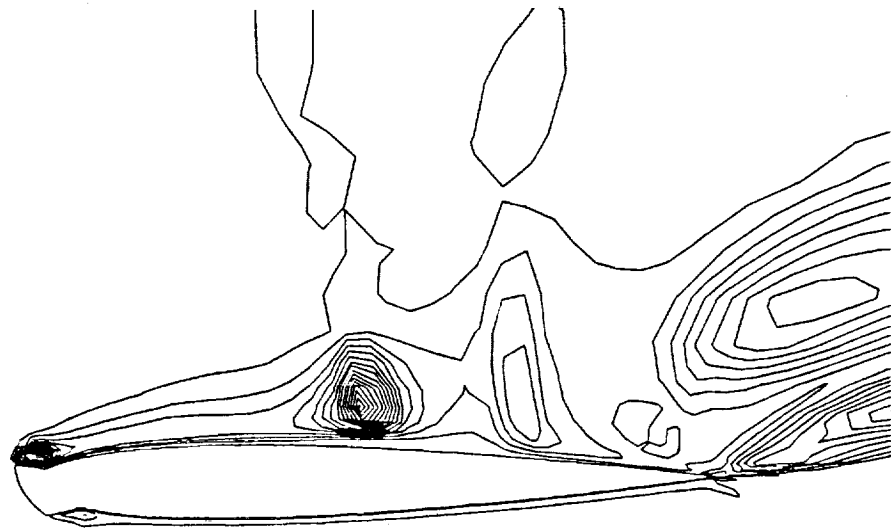
(b)

Figure 90   Turbulence model behavior during vortex shedding process; AOA=8°,

t=t₀+2800Δt; (a) stream function contours, (b) eddy-viscosity contours
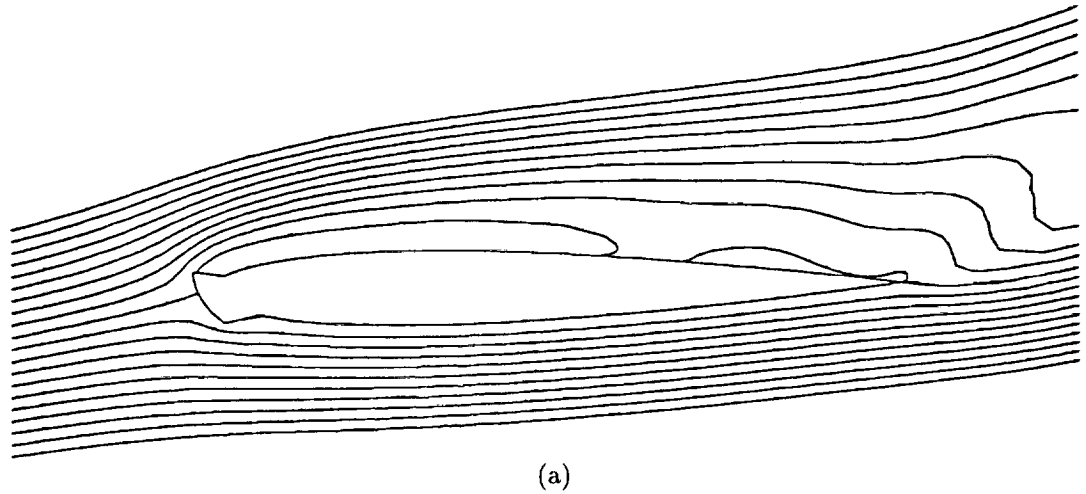
(a)
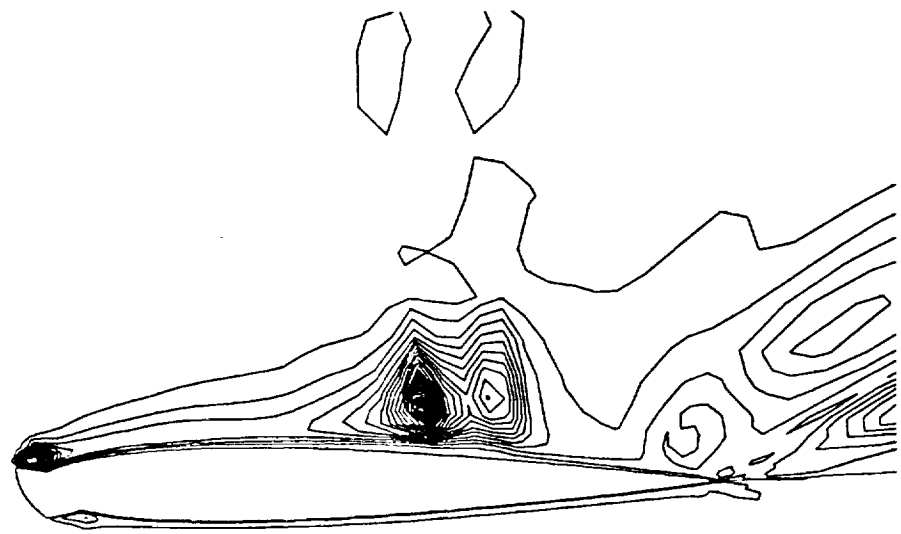
(b)

Figure 91   Turbulence model behavior during vortex shedding process; AOA=8°,

t=t_0 + 2900Δt; (a) stream function contours, (b) eddy-viscosity contours

lower than for the upper-surface and can be easily convected along the airfoil. This lower generation rate precludes the development of large regions of vorticity and hence the lower-surface does not experience the unsteady behavior seen on the upper-surface. The turbulence levels on this surface are substantially lower than those of the upper-surface. This is consistent with the near laminar behavior on the pressure surface of a clean airfoil. The favorable pressure gradient on the lower-surface does not promote the development of a large amount of vorticity away from the surface. This lower vorticity level in turn produces a lower eddy viscosity level. In fact, the turbulence on this surface appears to develop at the lower-surface horn and is then distributed along the airfoil.

As stated previously, the difference in time scales of vorticity generation and convection lead to alteration in frequency and amplitude of the force coefficient fluctuation. Since the eddy viscosity level can affect both of these time scales, the turbulence model can influence the temporal development of the lift, drag, and pitching moment. Correct representation of the turbulence level is therefore essential to the modeling of the post-stall behavior of an airfoil, either clean or with leading edge ice. While the MML model may not provide completely accurate predictions of turbulence level for a stalled airfoil, it can provide information on the appropriate turbulence levels and distributions for modeling of such behavior.

Further investigations will be required to determine the sensitivity of the MML model to different geometries and grid resolutions. Airfoil geometries can result in several types of stall behavior; leading-edge stall, trailing-edge stall, and combined leading and trailing edge stall. The ability of codes such as ARC2D to calculate stall behavior may also depend on which stall mechanism occurs. For the iced airfoil, the mechanism is more apparent than in most clean airfoil stalls. The iced airfoil case may result in a greater degree of two dimensionality due to the highly structured behavior near the horn. If this is the case, the iced

airfoil computations may be a truer representation of the actual physics. This is discussed, for the clean airfoil, by Zaman and McKinzie [68].

Grid sensitivity studies must be performed in order to determine requirements for capturing of the vortex shedding. Preliminary results have indicated a dependence of integrated force coefficients on the spacing near the surface and around the horn. It is necessary to determine the magnitude of this dependence and how fine a grid is required. Methods are presently being developed for adapting grids to the characteristics of the particular flowfield being studied. These may be required for unsteady flows such as those being studied here. Also, unstructured grids have the potential to provide a better representation of irregular geometries, such as the iced airfoil. These and other developments show great promise in providing better methods for iced airfoil analysis in the future.

CHAPTER 6

SUMMARY

Evaluation of the aerodynamic performance changes to an airfoil due to leading edge ice accretions has been performed using a 2D unsteady Navier-Stokes computer code. This code, along with appropriate grid generator and turbulence model, has provided considerable information on the aerodynamics of these highly complex geometries. Comparisons to experimental data have provided insight into the capabilities and limitations of this modeling method. Calculations indicate a high degree of confidence in the results for integrated force coefficients at pre-stall conditions. Discrepencies were noted in the separation bubble at pre-stall conditions and in the unsteady flowfield at post-stall conditions. A new turbulence model formulation was employed in order to address these difficulties and met with some degree of success. Further use of this turbulence model along with finer grids may help in evaluation of these conditions.

The MML turbulence model employed for this study is a zero-equation, eddy viscosity model with a Modified Mixing Length formulation which does not incorporate the F-function of the Baldwin-Lomax model and does not require the calculation of the displacement thickness. In this model, the mixing length is based on the local value of y^* and the velocity scale is based on the mixing length and the local value of the vorticity. In this way, the feedback existing between the wall shear and the turbulence level is not dependent on the distribution of the vorticity in the far field but rather on its value near the wall. This prevents large scale structures, which have essentially inviscid behavior, from unduly influencing the

turbulence level throughout the flowfield. In this model, the level of the turbulence is established by the fluid behavior near the wall, where vorticity generation takes place, and its distribution throughout the fluid is determined by the vorticity in the far field. This allows the development of the large vortices seen in the post-stall conditions examined and yet does not over-predict their size due to unrealistically low turbulent viscosity levels.

The use of the MML model was examined by evaluation of flow behavior on a clean airfoil. Calculations were performed for a clean NACA 0012 airfoil under attached and separated flow conditions. The attached flow results indicated that the Baldwin-Lomax model resulted in a more accurate representation of the drag. This was the result of better representation of near-wall behavior. The lift values were quite accurate for both models and did not have any impact on evaluation of their relative performance. The higher angle of attack calculations indicated qualitative differences between the two models. The MML model calculation indicated an unsteady flowfield with periodic vortex shedding. The Baldwin-Lomax model, on the other hand, indicated a steady, attached flow with a C_L value much higher than experiment. Additionally, a laminar flow calculation was performed and the unsteady flow behavior was again observed, albeit with a different shedding frequency. The MML model and laminar flow calculations had shedding frequencies both of which have been observed in experiment. Which one is appropriate, for this airfoil and under these flow conditions, will require further investigation.

The ability of the code, using either turbulence model, to predict the force coefficients for the iced airfoils is very good at angles of attack below stall. A rime condition and two glaze conditions were evaluated, with lift and drag values agreeing very well with experiment. Pressure distributions also indicated good agreement with the exception of the region in the immediate vicinity of the separation bubble aft of the glaze ice horn. Results in the separation bubble indicated an overprediction of the pressure peak in the forward part of the bubble and a lack of the constant pressure profile through the aft section of the bubble. This inablility to

capture the correct pressure profile resulted in poor representation of the velocity distribution within the bubble. Both turbulence models had difficulties in resolving this region and in fact the IBL approach of Cebeci [1] has also indicated similar difficulties.

The role of transition location was examined and found to significantly alter the velocity profiles. Setting transition at the midpoint of the bubble resulted in better prediction of the bubble height and reattachment location but also resulted in overprediction of the reverse flow velocities in the forward part of the bubble. Such limitations in the present implementation of the turbulence models prevented further investigation along these lines and further work is required. The role of grid spacing in modeling of the separation bubble is also being investigated. It is quite likely that the resolution in the shear layer, above the separation bubble, is not sufficient to capture the details of that flow, which could play a major role in prediction of reattachment location. Also, the streamwise resolution may not be sufficient to resolve the details of the separation and reattachment processes. This is presently being addressed by implementation of an unstructured grid scheme which would be more easily adapted to the irregular geometry of the iced airfoil.

At flow conditions near stall, the ability of the code to correctly predict lift and drag values is not as robust. There can be considerable differences in prediction of stall conditions and the AOA at which stall occurs. Several factors influence these calculations; grid spacing near the ice shape, transition location, and turbulence modeling all play a major role. The results indicate that the MML model appears to predict the $C_{L_{max}}$ values and stall angles better than the Baldwin-Lomax model. This is due to the lower μ_t values obtained with the MML model. These lower eddy viscosity values allow development of the vortex shedding process and yet alter the shedding frequency from the laminar-flow values. The frequencies obtained using the MML model correspond to the low frequency shedding observed by Zaman and McKinzie in experiments on another airfoil shape. Further examination of this unsteady behavior is presently underway in a joint computational and experimental study [72].

168

In summary, the approach of examining the performance degradation of an iced airfoil using a Navier-Stokes code has been shown to be feasible. Reasonably accurate results have been obtained for pre-stall conditions. Determination of the angle of attack of stall can be predicted using the MML turbulence model. The accurate calculation of post-stall behavior requires further development. The MML turbulence model was developed and tested for calculation of this post-stall behavior with positive results. Further refinement of this modeling procedure is required and recommendations for continued activities in this area are outlined below.

6.1 Future Activities

The need for accurate evaluation of the aerodynamics associated with iced airfoils is twofold. A representation of the velocity field surrounding the iced airfoil is important for use in conjunction with ice accretion prediction codes. The velocity field can impact particle trajectories and heat transfer calculations, which in turn affect the prediction of ice shape development. The use of a code such as this also allows the prediction of performance degradation and the onset of premature stall. These requirements serve as justification for futher research into the development of the correct methods for predicting the complex aerodynamics associated with iced airfoils. The present study has shown areas requiring further investigation which shall now be summarized.

i)   A grid refinement study is required to determine the sensitivity of force coefficient calculations to the number and distribution of grid nodes. This study should examine the attached separation bubble at low angles of attack and the region of vortex shedding activity at angles of attack past stall. The use of an unstructured and adaptive grid method may be appropriate. Additionally, grid refinement near the ice shape itself may improve pressure distribution and heat transfer calculations in these regions.

169

ii) The effects of transition location and the modeling of the transition process itself should be examined with regard to modeling of the attached separation bubble. Some method of allowing the code to determine the transition location should be examined. The method of Michel [75], presently used in many codes, was developed for attached flow transition and may require modification for the shear layer associated with the separation bubble.

iii) A reformulation of the turbulence model to account for the low flow conditions in the separation bubble and still provide for turbulent flow in the overlaying shear layer should be developed. This would allow for transition to turbulent flow in the shear layer without resulting in a relaminarization of the reverse flow region in the bubble. This should be coupled to experimental investigations of the turbulence characterisitics within the bubble which are presently underway [76].

iv) Further examination of the unsteady behavior predicted at high angles of attack is required utilizing the results of the investigations just described. Comparisons to experiment, especially the unsteady components such as shedding frequencies and amplitudes, can be used to provide insight on the applicability of the grid, of the turbulence modeling, and of the flowfield code itself. Such information can be used to further refine the implementation of these components for the iced airfoil geometry.

v) Implementation of a method for representing surface roughness will be required for investigation of its relative importance. Possibilities include an adjustment to the turbulence model to account for equivalent sand grain roughness or

170

implementation of a discrete roughness element model. The former requires a method of representing icing roughness by equivalent sand grain roughness and the latter requires the characterization of icing roughness heights, sizes, and spacing. Both approaches would require a correlation of the roughness to the environmental conditions prevalent during the accretion process.

vi)   Future analysis activities will require the evaluation of icing effects on multi-element airfoils, swept wings, stability and control parameters, and total aircraft configurations. This means that an ability to predict 3D effects will be important. Thus, the extension of present methods to 3D codes must be pursued while acknowledging the considerable amount of work still required in less complicated 2D analysis. The use of a zero-equation turbulence model will be all the more important for 3D analysis due to its simplicity and low computational overhead.

REFERENCES

172

1. Cebeci, T., "Prediction of Flow Over Airfoils with Leading Edge Ice," AIAA Paper 88-0112, 1988.

2. Reinmann, J.J., Shaw, R.J., and Olsen Jr., W.A., "NASA Lewis Research Center's Program on Icing Research," NASA TM 83031, 1983.

3. Gray, V.H., "Prediction of Aerodynamic Penalties Caused by Ice Formations on Various Airfoils," NASA TN D-2166, 1964.

4. Bragg, M.B., "Rime Ice Accretion and its Effects on Airfoil Performance," NASA CR-165599, March 1982.

5. Miller, T.L., Korkan, K.D., and Shaw, R.J., "Statistical Study of an Airfoil Glaze Ice Coefficient Correlation," SAE TP 830753, presented at the Business Aircraft Meeting and Exposition, Wichita, Kansas, April 12-15 1983.

6. Peterson, A.A. and Dadone, L.U., "Helicopter Icing Review," FAA-CT-80-210, Sept. 1980.

7. Bragg, M.B., Gregorek, G.M., and Shaw, R.J., "Wind Tunnel Investigation of Airfoil Performance Degradation Due to Icing," AIAA Paper 82-0582, 1982.

8. Eppler, R. and Somers, D.M., "A Computer Program for the Design and Analysis of Low-Speed Airfoils," NASA TM 80210, August 1980.

9. Bragg, M.B., "Predicting Airfoil Performance with Rime and Glaze Ice Accretions," AIAA Paper 84-0106, 1984.

10. Dvorak, F.A., "CLMAX Program Description," AMI Report 7965, 1979.

11. Bristow, D.R., "Multi-Element Airfoil Inviscid Analysis and Design Program (Version 1) User Instructions," McDonnell Aircraft Company, St. Louis MO, Dec. 1980.

12. Winslow, A.M., "Numerical Solution of the Quasilinear Poisson Equation in a Nonuniform Triangle Mesh," J. Comp Phys., vol. 1, 1966, pg. 149.

13. Chu, W., "Development of a General Finite Difference Approximation for a General Domain, Part I: Machine Transformation," J. Comp Phys., vol. 8, 1971, pp. 392-408.

14. Amsden, A. and Hirt, C., "A Simple Scheme for Generating General Curvilinear Grids," J. Comp Phys., vol. 11, 1973, pp. 348-359.

15. Thompson, J.F., Thames, F.C., and Mastin C.W., "Automatic Numerical Generation of Body-Fitted Curvilinear Coordinate System for Fields Containing Any Number of Arbitrary Two-Dimensional Bodies," J. Comp Phys., vol. 15, 1974, pp. 299-319.

16. Thompson, J.F., Thames, F.C., and Mastin C.W., "Boundary-Fitted Curvilinear Coordinate Systems for Solution of Partial Differential Equations on Fields Containing Any Number of Arbitrary Two-Dimensional Bodies," NASA CR-2729, 1977.

17. Thompson, J.F., Thames, F.C., and Mastin C.W., "TOMCAT -A Code for Numerical Generation of Boundary-Fitted Curvilinear Coordinate Systems on Fields Containing Any Number of Arbitrary Two-Dimensional Bodies," J. Comp Phys., vol. 24, 1977, pp. 274-302.

18. Steger, J.L. and Sorenson, R.L., "Automatic Mesh-Point Clustering Near a Boundary in Grid Generation with Elliptic Partial Differential Equations," J. Comp Phys., vol. 33, 1979, pp. 405-410.

19. Sorenson, R.L., "A Computer Program to Generate Two-Dimensional Grids About Airfoils and Other Shapes by the Use of Poisson's Equation," NASA TM 81198, 1980.

20. Barth, T., Pulliam, T., and Buning, P., "Navier-Stokes Calculations for Exotic Airfoils," AIAA Paper 85-1234, Jan. 1985.

21. Gibeling, H.J., Shamroth, S.J., and Eiseman, P.R., "Analysis of Strong-Interaction Dynamic Stall for Laminar Flow on Airfoils," NASA CR-2969, 1978.

22. Eiseman, P.R., "A Coordinate System for a Viscous Transonic Cascade Analysis," J. Comp Phys., vol. 26, 1978, pp. 307-338.

23. Shamroth, S.J., "Calculation of Steady and Unsteady Airfoil Flowfields Via the Navier-Stokes Equations," NASA CR-3899, August 1985.

24. Mehta, U.B. and Lavan, Z., "Starting Vortex, Separation Bubble and Stall: A Numerical Study of Laminar Unsteady Flow about an Airfoil," J. Fluid Mech., vol. 67, 1975, pp. 227-256.

25. Lugt, H.J. and Haussling, H.J., "Laminar Flow about an Abruptly Accelerated Elliptic Cylinder at 45° Incidence," J. Fluid Mech., vol. 65, 1975, pp. 711-734.

26. Reddy, R. and Thompson, J., "Numerical Solution of Incompressible Navier-Stokes Equations in the Integro-Differential Formulation Using Boundary-Fitted Coordinate Systems," AIAA Paper 77-650, 1977.

27. Wu, J.C., and Sampath, S., "A Numerical Study of Viscous Flow About an Airfoil," AIAA Paper 76-337, 1976.

28. Wu, J.C., Sampath, S., and Sankar, N.L., "A Numerical Study of Viscous Flows Around Airfoils," Proceedings of AGARD Conference on Unsteady Aerodynamics, September 1977.

29. Wu, J.C. and Thompson, J.F., "Numerical Solutions of Time-Dependent Incompressible Navier-Stokes Equations Using an Integro-Differential Formulation," Computers and Fluids, vol. 1, 1973, pp. 197-215.

30. Sugavanam, A. and Wu, J., "Numerical Study of Separated Turbulent Flow Over Airfoils," AIAA Paper 80-1441, 1980.

31. Harlow, F. and Welch, J., "Numerical Calculation of Time-Dependent Viscous Incompressible Flow of Fluid with Free Surface," Phys. of Fluids, vol. 8, 1965, pp. 2182-2189.

32. Hirt, C. and Harlow, F., "A General Corrective Procedure for the Numerical Solution of Initial-Value Problems," J. Comp. Phys., vol. 2, 1967, pp. 114-119.

33. Hodge, J.K., "Numerical Solution of Incompressible Laminar Flow About Arbitrary Bodies in Body-Fitted Curvilinear Coordinates," PhD Dissertation, Mississippi State University, 1975.

34. Hodge, J.K. and Stone, A.L., "Numerical Solution for Airfoils Near Stall in Optimized Body Fitted Curvilinear Coordinates," AIAA Paper 78-284, 1978.

35. Ghia, K., Hankey, W., and Hodge J., "Study of Incompressible Navier-Stokes Equations in Primitive Variables Using Implicit Numerical Technique," AIAA Paper 77-0648, 1977.

36. Verhoff, A., "Numerical Solution of Subsonic Inviscid Interacting Flows," AFFDL-TR-76-64, July 1976.

37. MacCormack, R.W., "The Effect of Viscosity in Hypervelocity Impact Cratering," AIAA Paper 69-354, 1969.

38. Diewert, G.S., "Recent Computation of Viscous Effects in Transonic Flow," Proceedings of the Fifth International Conference on Numerical Methods in Fluid Dynamics, Springer-Verlag, New York, 1976.

39. Briley, W.R. and McDonald, H., "Solution of the Multidimensional Compressible Navier-Stokes Equations by a Generalized Implicit Method," J. Comp. Phys., vol. 24, August 1977, pp. 372-397.

40. Sankar, N.L. and Tassa, Y., "Reynolds Number and Stability Effects on Dynamic Stall of an NACA0012 Airfoil," AIAA Paper 80-0010, 1980.

41. Johnson, D.A. and King, L.S., "A New Turbulence Closure Model for Boundary Layer Flows with Strong Adverse Pressure Gradients and Separation," AIAA Paper 84-0175, Jan. 1984.

42. Coakley, T.J., "Impact of Turbulence Modeling on Numerical Accuracy and Efficiency of Compressible Flow Simulations," NASA TM-88333, Sept. 1986.

43. Launder, B.E. and Spalding, D.B., "The Numerical Computation of Turbulent Flows," Computer Methods in Applied Mechanics and Engineering, vol. 3, 1974, pp. 269-289.

44. Launder, B.E. and Spalding, D.B., <u>Mathematical Models of Turbulence</u>, Academic Press, New York, 1972.

45. Cebeci, T. and Smith, A.M.O., article from <u>Computations of Turbulent Boundary Layers</u>, AFOSR-IFP Conf., vol. 1, 1968, Stanford University Press, pg. 356.

46. Baldwin, B.S. and Lomax, H., "Thin Layer Approximation and Algebraic Model for Separated Turbulent Flows," AIAA Paper 78-257, Jan. 1978.

47. Shamroth, S.J. and Gibeling, H.J., "A Compressible Solution of the Navier-Stokes Equations for Turbulent Flow About an Airfoil," NASA CR-3183, 1979.

48. Shamroth, S.J. and Gibeling, H.J., "Analysis of Turbulent Flow About an Isolated Airfoil Using a Time-Dependent Navier-Stokes Procedure," AGARD Conference on Boundary Layer Effects on Unsteady Airfoils, AGARDograph 296, 1980.

49. Shamroth, S.J., "A Turbulent Flow Navier-Stokes Analysis for an Airfoil Oscillating in Pitch," IUTAM Symposium on Turbulent Shear Flows, Springer-Verlag, NY, 1981.

50. Tassa, Y. and Sankar, N.L., "Dynamic Stall of an Oscillating Airfoil in Turbulent Flow Using Time-Dependent Navier-Stokes Solver," IUTAM Symposium on Turbulent Shear Flows, Springer-Verlag, New York, 1981.

51. Sankar, N.L. and Tang, W., "Numerical Solution of Unsteady Viscous Flow Past Rotor Sections," AIAA Paper 85-0129, 1985.

52. Steger, J.L., "Implicit Finite-Difference Simulation of Flow about Arbitrary Two-Dimensional Geometries," <u>AIAA Journal</u>, vol. 16, July 1978, pp. 679-686.

53. Beam, R. and Warming, R.F., "An Implicit Finite-Difference Algorithm for Hyperbolic Systems in Conservation Law Form," <u>Journal of Computational Physics</u>, vol. 22, Sept. 1976, pp. 87-110.

54. Pulliam, T.H., "Euler and Thin-Layer Navier-Stokes Codes: ARC2D, ARC3D," Notes for Computational Fluid Dynamics User's Workshop, UTSI Publication No. E02-4005-023-84, March 12-16, 1984.

55. Pulliam, T.H. and Barton, J.T., "Euler Computations of AGARD Working Group 07 Airfoil Test Cases," AIAA Paper 85-0018, 1985.

56. Vinokur, M., "Conservation Equations of Gas Dynamics in Curvilinear Coordinate Systems," <u>J. of Comp. Phys.</u>, vol. 14, 1974, pp. 105-125.

57. Jameson, A., Schmidt, W., and Turkel, E., "Numerical Solutions of the Euler Equations by Finite Volume Methods Using Runge-Kutta Time-Stepping Schemes," AIAA Paper 81-1259, 1981.

58. Degani, D. and Schiff, L.B., "Computation of Supersonic Viscous Flows Around Pointed Bodies at Large Incidence," AIAA Paper 83-0034, 1983.

59. Sankar, L.N. and Wu, J., "Studies of Unsteady Viscous Flows Using a Two-Equation Model of Turbulence," (Status Report for NASA Grant No. NAG 3-768.)

60. Gorski, J.J., "A New Near-Wall Formulation for the k-ϵ Equations of Turbulence," AIAA Paper 86-0556, 1986.

61. Prandtl, L., "Bericht über Untersuchungen zur ausgebideten Turbulenz," ZAMM, vol. 5, 1925, pp. 136-139.

62. Cebeci, T., and Smith, A.M.O., Analysis of Turbulent Boundary Layers, Academic Press, New York, 1974.

63. Simpson, R.L., Chew, Y.T., and Shivaprasad, B.G., "The Structure of a Separating Turbulent Boundary Layer. Part 1. Mean Flow and Reynolds Stresses," Journal of Fluid Mechanics, vol. 113, Dec. 1981, pp. 23-51.

64. Bradshaw, P., ed., Turbulence, 2nd Edition, Springer-Verlag, New York, 1978.

65. Gregory, N. and O'Reilly, C., "Low-Speed Aerodynamic Characteristics of NACA 0012 Airfoil Section, Including the Effects of Upper-Surface Roughness Simulating Hoar Frost," ARC-R/M-3726, 1973.

66. Bragg, M.B., "An Experimental Study of the Aerodynamics of a NACA 0012 Airfoil with a Simulated Glaze Ice Accretion," AARL Technical Report 8602, The Ohio State University, 1986.

67. Jacobs, E.N., "Airfoil Section Characteristics as Affected by Protuberences," NACA TR-446, 1933.

68. Zaman, K.B.M.Q. and McKinzie, D.J., "A Natural Low Frequency Oscillation in the Wake of an Airfoil Near Stalling Conditions," AIAA Paper 88-0131, Jan. 1988.

69. Chang, P.K., Separation of Flow , Pergamon Press, Oxford, 1970.

70. Bragg, M.B., Zaguli, R.J., and Gregorek, G.M., "Wind Tunnel Evaluation of Airfoil Performance Using Simulated Ice Shapes," NASA CR-167960, Nov. 1982.

71. Majumdar, S. and Rodi, W., "Numerical Calculations of Turbulent Flow Past Circular Cylinders," Third Symposium on Numerical and Physical Aspects of Aerodynamic Flows, ed. T. Cebeci, 1985.

72. Zaman, K.B.M.Q. and Potapczuk, M.G., "A Low Frequency Oscillation in the Flow Over a NACA 0012 Airfoil with an 'Iced' Leading Edge," Paper presented at the Conference on Low-Reynolds Number Phenomena, University of Notre Dame, June 1989.

73. Mehta, U., "Physical Aspects of Computing the Flow of a Viscous Fluid," NASA TM 85893, April 1984, pg. 8.

74. Olsen, W., Shaw, R., and Newton, J., "Ice Shapes and the Resulting Drag Increase for a NACA 0012 Airfoil," NASA TM 83556, 1984.

75. Michel, R., "Etude de la Transition sur les Profiles d'Aile; Establissement d'un Critere de Determination de Point de Transition et Calcul de la Trainee de Profile Incompressible," ONERA Rept. 1/1578A, 1951.

76. Bragg, M.B. and Khoudadoust, A., "Effect of Simulated Glaze Ice on a Rectangular Wing," AIAA Paper 89-0750, Jan. 1989.

APPENDICES

Appendix 1

Nomenclature

$\hat{A}$ = $\partial\hat{E}/\partial\hat{Q}$

A^+ = van Driest damping constant = 26

AOA = angle of attack

a = speed of sound

$\hat{B}$ = $\partial\hat{F}/\partial\hat{Q}$

C = airfoil chord length

C_1 = MML turbulence model constant; controls mixing length saturation level

C_2 = MML turbulence model constant; controls blending region curvature

C_{cp} = Baldwin-Lomax turbulence model constant = 1.6

C_D = coefficient of drag = $D/(0.5\rho U_\infty{}^2 s)$

C_f = friction coefficient = $\tau_w/(0.5\rho U_\infty{}^2)$

C_{kleb} = Klebanoff intermittancy factor constant = 0.3

C_L = coefficient of lift = $L/(0.5\rho U_\infty{}^2 s)$

C_p = pressure coefficient = $(P-P_\infty)/(0.5\rho U_\infty{}^2)$

C_{wk} = Baldwin-Lomax turbulence model outer region constant = 0.25

D = drag force

$\dfrac{D}{Dt}$ = substantial derivative

E = convection terms in Navier-Stokes equations; Cartesian coordinates (Eq. 3.14)

$\hat{E}$ = convection terms in Navier-Stokes equations; curvilinear coordinates (Eq. 3.22)

Ev = viscous terms in Navier-Stokes equations; Cartesian coordinates (Eq. 3.15)

$\hat{E}$v = viscous terms in Navier-Stokes equations; curvilinear coordinates (Eq. 3.23)

e = total energy

e_4 = viscous term in Ev matrix of energy equation

F = convection terms in Navier-Stokes equations; Cartesian coordinates (Eq. 3.14)

$\hat{F}$ = convection terms in Navier-Stokes equations; curvilinear coordinates (Eq. 3.22)

$F(y)$ = $y\,|\omega|\left[1 - \exp(-y^+/A^+)\right]$ in Baldwin-Lomax turbulence model

F_{kleb} = Klebanoff intermittancy factor

Fv = viscous terms in Navier-Stokes equations; Cartesian coordinates (Eq. 3.15)

$\hat{F}v$ = viscous terms in Navier-Stokes equations; curvilinear coordinates (Eq. 3.23)

F_{wake} = length × velocity scale in outer region of Baldwin-Lomax turbulence model

f = vortex shedding frequency

f_4 = viscous term in Fv matrix of energy equation

h = Δt

I = identity matrix

J = Jacobian of the coordinate transformation

K = Clauser constant = 0.0168

L = Lift force

$\mathcal{L}$ = characteristic length

ℓ = turbulence model length scale

$\tilde{M}$ = $\partial \hat{S}/\partial \hat{Q}$

P = pressure

$\tilde{P}$ = constant in Poisson equation used in GRAPE code

Pr = Prandtl number

Q = independent variables in Navier-Stokes equations; Cartesian coordinates

$\hat{Q}$ = independent variables in Navier-Stokes equations; curvilinear coordinates

$\tilde{Q}$ = constant in Poisson equation used in GRAPE code

Re = Reynolds number

$\hat{S}$ = viscous terms in thin-layer form of Navier-Stokes equations (Eq. 3.33)

S_t = Strouhal number

t = time

U = contravarient velocity in curvilinear coordinate system

$\bar{U}$ = velocity vector

U_{diff} = term in F_{wake} parameter of Baldwin-Lomax turbulence model (Eq. 3.45)

U_∞ = freestream velocity

u = velocity in x-direction

u_τ = wall shear velocity (Eq. 4.6)

V = contravarient velocity in curvilinear coordinate system

v = velocity in y-direction

v = velocity scale in turbulence models

x = Cartesian coordinate

y = Cartesian coordinate

y^+ = boundary layer coordinate; Baldwin-Lomax - Eq. 3.40; MML - Eq. 4.5

y^* = wall shear length scale (Eq. 4.10)

α = angle of attack

γ = ratio of specific heats = 1.4

δ = boundary layer thickness

η = curvilinear coordinate (nominally normal to body surface)

θ = constant in implicit time-differencing scheme

κ = von Karman constant = 0.4

λ = $-\frac{2}{3}\mu$

μ = viscosity

μ_t = turbulent viscosity

ν = kinematic viscosity; μ/ρ

ξ = curvilinear coordinate (nominally in streamwise direction)

ρ =   density

τ =   shear stress; time in curvilinear coordinate system

ϕ =   constant in implicit time-differencing scheme

$\bar{\Omega}$ =   vorticity vector

ω =   vorticity

Subscripts

i   =   grid index in ξ-direction

t   =   differentiation with respect to t

w   =   at the wall

x   =   differentiation with respect to x

y   =   differentiation with respect to y

η =   differentiation with respect to η

ξ =   differentiation with respect to ξ

τ =   differentiation with respect to τ

∞ =   freestream conditions

Superscripts

n   =   iteration number

Appendix 2

MML Turbulence Model Code Listing

The subroutine listed on the following pages calculates the turbulent viscosity level for the flowfield obtained from the ARC2D calculation on a user-specified two-dimensional grid system. The subroutine uses the velocities and grid coordinates to determine length and velocity scales according to the equations described in Chapter 4. These length and velocity scales are then used to find μ_t, which is then used in the subsequent iteration of the velocity calculation procedure. The pertinant variable names are described below in order to clarify the relationship of the code to the actual MML model equations.

APLUS = Van Driest damping factor; 26

C2B = Temperature ratio for Sutherland law $= \dfrac{198.6}{T_\infty}$

C2BP = 1. + C2B

DELTA(J) = Array of YSTAR values on the airfoil surface

FMUtmp(K) = Viscosity value at a K location

F1 = C_1

F2 = C_2

GAMMA = Ratio of specific heats; γ

J = Index in ξ-direction

JMAX = Maximum J value in grid

JTAIL1 = First J grid line on airfoil surface

JTAIL2 = Last J grid line on airfoil surface

JTRANLO = J grid line location for transition on lower surface

JTRANUP = J grid line location for transition on upper surface

K = Index in η-direction

KMAX = Maximum K value in grid

MXLNGTH = Mixing length; ℓ

NUMITER = Iteration number

PRESS = Pressure; GAMI*(Q(4) - 0.5*(Q(2)**2+Q(3)**2)/Q(1))

Q(J,K,M) = $\hat{Q}$; Conservative variables: M=1 $\Rightarrow \rho$

M=2 $\Rightarrow \rho u$

M=3 $\Rightarrow \rho v$

M=4 $\Rightarrow e$

$RA = 1/y^*$

$RE = $ Reynolds number

$SNOR = $ Distance normal to surface

$TAU = $ Vorticity at the surface; $|\omega|_w$

$TINF = T_\infty$

$TT = \gamma\left(\dfrac{P}{\rho}\right)$

$TURMU = \mu_t$

$VK = \kappa$

$VORT = $ Vorticity at a grid location

$WMU = \mu_w$

$X = $ x location of grid point

$XY(J,K,M) = $ Metrics of transformation: $M=1 \Rightarrow \xi_x$

$M=2 \Rightarrow \xi_y$

$M=3 \Rightarrow \eta_x$

$M=4 \Rightarrow \eta_y$

XYJ(J,K) = Jacobian

YSTAR = y^*

YPLUS = y^+

```
C**********************************************************************
C************************* TURBULENT VISCOSITY ************************
C**********************************************************************
      SUBROUTINE MUTUR(JDIM,KDIM,Q,PRESS,VORT,TURMU,X,Y,XY,XYJ)
      PARAMETER(MAXJ=260)
c
      COMMON/BASE/
     1 JMAX,      KMAX,       JM,          KM,          JBEGIN,    JEND,
     1 KBEGIN,    KEND,       jplus(999),  jminus(999), jlow,      jup,
     1 KLOW,      KUP,        JMAXOLD,     PERIODIC,    NP,        DT,
     1 FSMACH,    ALPHA,      GAMMA,       GAMI,        PI,
     1 IOPERXY,   DIS2X,      DIS2Y,       DIS4X,       DIS4Y,
     1 SMU,       SMUIM,      PHIDT,       THETADT,     METH,
     1 jacdt,     DTRATE,     nsuper,      maxres(2),   maxdq(2),
     1 RESID,     RESIDMX,    STRTIT,      BCAIRF,
     1 CPUTIME,   RESTART,    STORE,       IREAD,       IPRINT,
     1 JTAIL1,    JTAIL2,     dswall,      sobmax,      CIRCUL,
     1 SHARP,     CUSP,       totime,
     1 numiter,   istart,     ISPEC,       re,          VISCOUS,
     1 IVIS,      TURBULNT,   VISXI,       VISETA,      VISCROSS,
     1 TRANSUP,   TRANSLO,    JTRANUP,     JTRANLO,     NPCP
      LOGICAL RESTART,STORE,TURBULNT,VISCOUS,PERIODIC,CIRCUL
      LOGICAL SHARP,CUSP,BCAIRF
      LOGICAL VISXI,VISETA,VISCROSS
      REAL*4 MXLNGTH
      COMMON /TEMPT/TINF,TWALL,WTRAT,TMN
c
      DIMENSION Q(JDIM,KDIM,4),TURMU(JDIM,KDIM),VORT(JDIM,KDIM)
      DIMENSION PRESS(JDIM,KDIM),XY(JDIM,KDIM,4),XYJ(JDIM,KDIM)
      DIMENSION X(JDIM,KDIM),Y(JDIM,KDIM)
c
```

```fortran
      COMMON/WORKSP/SNOR(MAXJ),TMO(MAXJ),TMI(MAXJ),UU(MAXJ),
     * TAS(MAXJ),WORK(MAXJ,87)
      COMMON /FTURB/ FY(260,65),YMAXX(260),FMAXX(260),RYSM(260),YFMN
      COMMON/PLTDAT/ RESD(41000),CFPLT(MAXJ),CLPLT(41000),CDPLT(41000),
     & MXLNGTH(260,65),TMUI(260,65),TMUO(260,65),
     & DELTA(MAXJ)
c

      dimension FMUtmp( 2)


c
C

      DATA VK,APLUS/0.4,26./
      DATA F1,F2/2000.,5.0/
C

      IF(TURBULNT) THEN
      IF(NUMITER.LT.10) RETURN
      KEDGE = 0.75*KEND
      DO 40 J=JTAIL1,JTAIL2
C
C DETERMINE VORTICITY TAS(K)
C
      DO 5 K=KBEGIN,KUP
      TAS(K) = VORT(J,K)
      TURMU(J,K) = 0.0
 5       CONTINUE
C
C COMPUTE RA
c
      do 15 k = KBEGIN,KBEGIN+1
      C2B = 198.6/TINF
      C2BP = C2B + 1.
```

194

```fortran
          RINV = 1./Q(J,K,1)
          TT = GAMMA*PRESS(J,K)*RINV
          FMUtmp(K) = C2BP*TT**1.5/( C2B+TT)
15        continue
c

          K=KBEGIN
          WMU = .5*( FMUtmp(1) + FMUtmp(2))
          TAU = 0.10*ABS(VORT(J-2,K))+0.20*ABS(VORT(J-1,K))
        & + 0.40*ABS(VORT(J,K))+0.20*ABS(VORT(J+1,K))
        & + 0.10*ABS(VORT(J+2,K))
          RA = SQRT( RE*XYJ(J,K)*Q(J,K,1)*TAU/WMU)
C WRITE(6,1000) TAU,RA
C1000 FORMAT(1X,'TAU = ',E10.4,2X,'RA = ',E10.4)
C
C CALCULATE NORMAL DISTANCE AND YSTAR
C
          YSTAR = 1./RA
          DELTA(J) = YSTAR
          SNOR(1) = 0.0
          DO 10 K=KLOW,KUP
          SCIS = ABS(XY(J,K-1,3)*XY(J,K,3)+XY(J,K-1,4)*XY(J,K,4))
          SCAL = 1.0/SQRT(SCIS)
          SNOR(K) = SNOR(K-1) + SCAL
10        CONTINUE
C
C CALCULATE MIXING LENGTH
C
          DO 30 K=KBEGIN,KEDGE
          YPLUS = SNOR(K)/YSTAR
          IF(YPLUS .LE. F1) THEN
          MXLNGTH(J,K) = VK*(F1/F2)*YSTAR*(1.-(1.-YPLUS/F1)**F2)
```

```
      & *(1.-EXP(-YPLUS/APLUS))
      ELSE
      MXLNGTH(J,K) = VK*(F1/F2)*YSTAR
      ENDIF
      TLSQR = MXLNGTH(J,K)*MXLNGTH(J,K)
      TURMU(J,K) = Q(J,K,1)*XYJ(J,K)*RE*TLSQR*ABS(VORT(J,K))
30    CONTINUE
40    CONTINUE
C
C USE CONSTANT T.E. LENGTH SCALE IN WAKE
C
      DO 60 K=KLOW,KUP
      DO 50 J=1,JMAX
      IF(X(J,K) .GT. 1.0 .AND. Y(J,K) .LT. 0.0) JTELO=J
      IF(X(J,K) .LT. 1.0 .AND. Y(J,K) .GT. 0.0) JTEHI=J
50    CONTINUE
      DO 60 J=1,JMAX
      IF(X(J,K) .GT. 1.0 .AND. Y(J,K) .LT. 0.0) THEN
      MXLNGTH(J,K) = MXLNGTH(JTELO,K)
      TLSQR = MXLNGTH(J,K)*MXLNGTH(J,K)
      TURMU(J,K) = Q(J,K,1)*XYJ(J,K)*RE*TLSQR*ABS(VORT(J,K))
      ENDIF
      IF(X(J,K) .GT. 1.0 .AND. Y(J,K) .GT. 0.0) THEN
      MXLNGTH(J,K) = MXLNGTH(JTEHI,K)
      TLSQR = MXLNGTH(J,K)*MXLNGTH(J,K)
      TURMU(J,K) = Q(J,K,1)*XYJ(J,K)*RE*TLSQR*ABS(VORT(J,K))
      ENDIF
60    CONTINUE
C<<<<<<<<<<<<<<<<<<<<<<<<<<<<<<<<<<<<<<<<<<<<<<<<<<<<<<<<<<<<<<<<<<<<<
C
C**** PROVIDE FOR NONZERO LENGTH SCALE ACROSS CENTERLINE OF C-GRID
```

```
C
      JT1M1 = JTAIL1-1
      DO 70 J=1,JT1M1
      JMX2 = JMAX-J+1
      SLOPEML = (MXLNGTH(JMX2,5)-MXLNGTH(J,5))/(Y(JMX2,5)-Y(J,5))
      DO 70 K=1,4
C
C**** CALCULATE MIXING LENGTH BELOW CENTERLINE
C
      MXLNGTH(J,K) = SLOPEML*(Y(J,K)-Y(J,5))+MXLNGTH(J,5)
      TLSQR = MXLNGTH(J,K)*MXLNGTH(J,K)
      TURMU(J,K) = Q(J,K,1)*XYJ(J,K)*RE*TLSQR*ABS(VORT(J,K))
C
C**** CALCULATE MIXING LENGTH ABOVE CENTERLINE
C
      MXLNGTH(JMX2,K) = MXLNGTH(JMX2,5)-SLOPEML*(Y(JMX2,5)-Y(JMX2,K))
      TLSQR = MXLNGTH(JMX2,K)*MXLNGTH(JMX2,K)
      TURMU(JMX2,K)=Q(JMX2,K,1)*XYJ(JMX2,K)*RE*TLSQR*ABS(VORT(JMX2,K))
70    CONTINUE
C>>>>>>>>>>>>>>>>>>>>>>>>>>>>>>>>>>>>>>>>>>>>>>>>>>>>>>>>>>>>>>>>>>>>>
c
      if(TRANSLO.ne.0.0)then
c
c zero turmu from JTRANLO to JTRANUP
c
      do 455 j = JTRANLO,JTRANUP
      do 455 k = KBEGIN,KEND
      turmu(j,k) = 0.
455   continue
c
      endif
```

```
c
C IF NOT TURBULNT SET TURMU = 0.0
C
      ELSE
      DO 800 K = KBEGIN,KEND
      DO 800 J = JBEGIN,JEND
      TURMU(J,K) = 0.0
800   CONTINUE
C
      ENDIF
C
      RETURN
      END
```

Appendix 3

Coordinates of the Airfoil/Ice-Shape Geoemtries

This appendix contains the x-y coordinate pairs that define the surface of the three airfoil/ice-shape geometries used in this work. The coordinates are listed as they would appear for an input file to the GRAPE grid generation code. All the x-coordinates are listed first with their corresponding y-values listed afterward. Both sets are listed in the same order(i.e. starting at the trailing edge and proceeding in a clockwise direction until reaching the trailing edge again.) All coordinates have been normalized by the chord length with the leading edge at (0.0, 0.0) and the trailing edge at (1.0, 0.0). Since the ice shapes grow in the negative x-direction, some coordinate locations will have x-values less than zero.

Coordinates for the NACA 63$_A$- 415 airfoil and R7 ice shape

X=

1.0000000,	0.9497200,	0.8994100,	0.8491500,	0.7989800,	0.7489100,
0.6989400,	0.6490700,	0.5993000,	0.5496100,	0.5000000,	0.4504500,
0.4009500,	0.3514800,	0.3020000,	0.2525000,	0.2029500,	0.1533100,
0.1035300,	0.0785300,	0.0534000,	0.0280200,	0.0150900,	0.0099999,
0.0037000,	-0.0013900,	-0.0077790,	-0.0113000,	-0.0131500,	-0.0115700,
-0.0081500,	-0.0041700,	0.0000000,	0.0030000,	0.0052500,	0.0099100,
0.0219800,	0.0466000,	0.0714700,	0.0964700,	0.1466900,	0.1970500,
0.2475000,	0.2980000,	0.3485200,	0.3990500,	0.4495500,	0.5000000,
0.5503900,	0.6070000,	0.6509300,	0.7010600,	0.7510900,	0.8010200,
0.8508500,	0.9005900,	0.9502800,	1.0000000,		

Y=

0.0000000,	0.0033300,	0.0018400,	-0.0019300,	-0.0071600,	-0.0132700,
-0.0198900,	-0.0266000,	-0.0331100,	-0.0391800,	-0.0445900,	-0.0490900,
-0.0524300,	-0.0543900,	-0.0547400,	-0.0536100,	-0.0509500,	-0.0465600,
-0.0400900,	-0.0356500,	-0.0300000,	-0.0222000,	-0.0164600,	-0.0185200,
-0.0181500,	-0.0175900,	-0.0168500,	-0.0151900,	-0.0116700,	-0.0060200,
0.0000000,	0.0063000,	0.0115700,	0.0128700,	0.0158500,	0.0207400,
0.0296400,	0.0426400,	0.0526100,	0.0607700,	0.0734800,	0.0827900,
0.0894100,	0.0936200,	0.0955900,	0.0952700,	0.0928900,	0.0887100,
0.0829800,	0.0759500,	0.0678000,	0.0587700,	0.0490700,	0.0390000,
0.0288500,	0.0188400,	0.0093100,	0.0000000		

Coordinates for the NACA63$_A$-415 airfoil and G3 ice shape

X=

1.0000000,	0.9497200,	0.8994100,	0.8491500,	0.7989800,	0.7489100,
0.6989400,	0.6490700,	0.5993000,	0.5496100,	0.5000000,	0.4504500,
0.4009500,	0.3514800,	0.3020000,	0.2525000,	0.2029500,	0.1533100,
0.1035300,	0.0785300,	0.0534000,	0.0280200,	0.0116200,	0.0088810,
0.0065130,	0.0046010,	0.0022330,	-0.0000456,	-0.0028660,	-0.0046860,
-0.0069620,	-0.0081510,	-0.0085260,	-0.0079870,	-0.0070810,	-0.0055410,
-0.0049140,	-0.0046560,	-0.0048770,	-0.0051820,	-0.0056810,	-0.0062490,
-0.0069890,	-0.0077240,	-0.0084540,	-0.0094570,	-0.0111000,	-0.0132800,
-0.0150200,	-0.0166600,	-0.0184100,	-0.0187900,	-0.0178000,	-0.0155300,
-0.0112500,	-0.0070600,	-0.0030580,	0.0003970,	0.0030300,	0.0054740,
0.0106100,	0.0219800,	0.0466000,	0.0714700,	0.0964700,	0.1466900,
0.1970500,	0.2475000,	0.2980000,	0.3485200,	0.3990500,	0.4495500,
0.5000000,	0.5503900,	0.6070000,	0.6509300,	0.7010600,	0.7510900,
0.8010200,	0.8508500,	0.9005900,	0.9502800,	1.0000000,	

Y=

0.0000000,	0.0033300,	0.0018400,	-0.0019300,	-0.0071600,	-0.0132700,
-0.0198900,	-0.0266000,	-0.0331100,	-0.0391800,	-0.0445900,	-0.0490900,
-0.0524300,	-0.0543900,	-0.0547400,	-0.0536100,	-0.0509500,	-0.0465600,
-0.0400900,	-0.0356500,	-0.0300000,	-0.0222000,	-0.0148100,	-0.0140500,
-0.0139000,	-0.0138300,	-0.0135900,	-0.0132600,	-0.0132900,	-0.0133100,
-0.0132400,	-0.0126400,	-0.0116800,	-0.0109700,	-0.0106100,	-0.0099830,
-0.0090120,	-0.0076940,	-0.0040130,	-0.0010340,	0.0029950,	0.0050950,
0.0061400,	0.0068340,	0.0070020,	0.0071670,	0.0072390,	0.0073050,
0.0079010,	0.0088490,	0.0105000,	0.0120700,	0.0130500,	0.0131600,
0.0128500,	0.0128000,	0.0129300,	0.0132300,	0.0137800,	0.0149500,
0.0195600,	0.0296400,	0.0426400,	0.0526100,	0.0607700,	0.0734800,
0.0827900,	0.0894100,	0.0936200,	0.0955900,	0.0952700,	0.0928900,
0.0887100,	0.0829800,	0.0747735,	0.0678000,	0.0587700,	0.0490700,
0.0390000,	0.0288500,	0.0188400,	0.0093100,	0.0000000	

Coordinates for the NACA 0012 airfoil and G1 ice shape

X=

1.0000000,	0.9913444,	0.9809285,	0.9681920,	0.9523343,	0.9321911,
0.9060580,	0.8714901,	0.8252681,	0.7642254,	0.6882111,	0.6043302,
0.5252967,	0.4601904,	0.4103649,	0.3700089,	0.3300074,	0.2887478,
0.2051575,	0.0888420,	0.0851143,	0.0737720,	0.0695000,	0.0657206,
0.0619175,	0.0581143,	0.0543111,	0.0505079,	0.0467048,	0.0390984,
0.0352952,	0.0314291,	0.0309070,	0.0276889,	0.0238857,	0.0233862,
0.0228841,	0.0224050,	0.0219731,	0.0216107,	0.0213361,	0.0211634,
0.0188905,	0.0166191,	0.0143476,	0.0120762,	0.0098048,	0.0075333,
0.0052619,	0.0029905,	0.0007191,	-0.0015524,	-0.0038238,	-0.0060952,
-0.0083667,	-0.0106381,	-0.0129095,	-0.0151810,	-0.0174524,	-0.0197238,
-0.0219952,	-0.0242667,	-0.0265381,	-0.0268877,	-0.0269931,	-0.0268443,
-0.0264583,	-0.0258790,	-0.0251724,	-0.0244191,	-0.0213483,	-0.0182775,
-0.0152068,	-0.0121361,	-0.0090653,	-0.0059946,	-0.0029238,	0.0001469,
0.0032177,	0.0062884,	0.0093592,	0.0124299,	0.0155007,	0.0185714,
0.0737220,	0.0836666,	0.0965504,	0.1080990,	0.1285863,	0.1792650,
0.2023058,	0.3143436,	0.4387820,	0.5316864,	0.5894307,	0.6300145,
0.6700144,	0.7106869,	0.7707552,	0.8509442,	0.9156263,	0.9540105,
0.9764334,	0.9905078,	1.0000000,			

Y=

0.0000000,	-0.0012323,	-0.0026976,	-0.0044639,	-0.0066250,	-0.0093109,
-0.0127008,	-0.0170272,	-0.0225450,	-0.0293820,	-0.0371858,	-0.0448267,
-0.0509522,	-0.0550485,	-0.0574780,	-0.0589117,	-0.0597804,	-0.0600007,
-0.0577608,	-0.0449812,	-0.0441132,	-0.0417323,	-0.0407000,	-0.0416710,
-0.0426421,	-0.0436131,	-0.0445841,	-0.0455552,	-0.0465262,	-0.0474972,
-0.0484683,	-0.0494393,	-0.0504103,	-0.0513813,	-0.0523524,	-0.0524220,
-0.0523769,	-0.0522204,	-0.0519603,	-0.0516100,	-0.0511872,	-0.0507137,
-0.0490488,	-0.0472992,	-0.0454587,	-0.0435218,	-0.0414819,	-0.0393315,
-0.0370620,	-0.0346632,	-0.0321230,	-0.0294269,	-0.0265574,	-0.0234926,
-0.0202050,	-0.0166590,	-0.0128070,	-0.0085832,	-0.0038910,	0.0014202,
0.0076136,	0.0152347,	0.0259245,	0.0266049,	0.0269931,	0.0280895,

0.0287365, 0.0292182, 0.0294798, 0.0294914, 0.0290133, 0.0285361,

0.0280588, 0.0275816, 0.0271044, 0.0266272, 0.0261500, 0.0256728,

0.0251956, 0.0247184, 0.0242412, 0.0237640, 0.0232867, 0.0228095,

0.0417323, 0.0439715, 0.0462317, 0.0481440, 0.0511603, 0.0560180,

0.0576065, 0.0599511, 0.0561746, 0.0505007, 0.0460672, 0.0426025,

0.0389335, 0.0349618, 0.0286748, 0.0195168, 0.0114718, 0.0063985,

0.0033242, 0.0013507, 0.0000000

REPORT DOCUMENTATION PAGE

1. AGENCY USE ONLY (Leave blank)	2. REPORT DATE	3. REPORT TYPE AND DATES COVERED
	February 1993	Final Contractor Report

4. TITLE AND SUBTITLE

Navier-Stokes Analysis of Airfoils With Leading Edge Ice Accretions

5. FUNDING NUMBERS

WU-505-68-10
NAG3-416

6. AUTHOR(S)

Mark G. Potapczuk

7. PERFORMING ORGANIZATION NAME(S) AND ADDRESS(ES)

University of Akron
Akron, Ohio 44325

8. PERFORMING ORGANIZATION REPORT NUMBER

E-7580

9. SPONSORING/MONITORING AGENCY NAMES(S) AND ADDRESS(ES)

National Aeronautics and Space Administration
Lewis Research Center
Cleveland, Ohio 44135-3191

10. SPONSORING/MONITORING AGENCY REPORT NUMBER

NASA CR-191008

11. SUPPLEMENTARY NOTES

Project Manager, Robert J. Shaw, Propulsion Systems Division, NASA Lewis Research Center, (216) 433-3919.

12a. DISTRIBUTION/AVAILABILITY STATEMENT

Unclassified - Unlimited
Subject Category 02

12b. DISTRIBUTION CODE

13. ABSTRACT (Maximum 200 words)

A numerical analysis of the flowfield characteristics and the performance degradation of an airfoil with leading edge ice accretions was performed. The important fluid dynamic processes were identified and calculated. Among these were the leading edge separation bubble at low angles of attack, complete separation on the low pressure surface resulting in premature stall, drag rise due to the ice shape, and the effects of angle of attack on the separated flow field. Comparisons to experimental results were conducted to confirm these calculations. A computer code which solves the Navier-Stokes equations in two dimensions, ARC2D, was used to perform the calculations. A Modified Mixing Length turbulence model was developed to improve capabilities in calculating the separated flow phenomena. A grid generation code, GRAPE, was used to produce grids for several ice shape and airfoil combinations. Results indicate that the ability to predict overall performance characteristics, such as lift and drag, at low angles of attack is excellent. Transition location is important for accurately determining separation bubble shape. Details of the flowfield in and downstream of the separated regions requires some modifications. Calculations for the stalled airfoil indicate periodic shedding of vorticity that was generated aft of the ice accretion. Time averaged pressure values produce results which compare favorably with experimental information. A turbulence model which accounts for the history effects in the flow may be justified.

14. SUBJECT TERMS

Aircraft icing; Aerodynamics

15. NUMBER OF PAGES

205

16. PRICE CODE

A10

17. SECURITY CLASSIFICATION OF REPORT	18. SECURITY CLASSIFICATION OF THIS PAGE	19. SECURITY CLASSIFICATION OF ABSTRACT	20. LIMITATION OF ABSTRACT
Unclassified	Unclassified	Unclassified	